

UNIVERSITÉ DE MONTRÉAL

THE INFLUENCE OF GRAIN SIZE ON CREEP AND CREEP CRACK
GROWTH IN UDIMET 520, A FORGED NICKEL-BASE SUPERALLOY

SU XU

DÉPARTEMENT DE MÉTALLURGIE ET DE GÉNIE DES MATÉRIAUX
ÉCOLE POLYTECHNIQUE DE MONTRÉAL

THÈSE PRÉSENTÉE EN VUE DE L'OBTENTION DU DIPLÔME DE
PHILOSOPHIAE DOCTOR (Ph.D.)
(MÉTALLURGIE ET GÉNIE DES MATÉRIAUX)

NOVEMBRE 1997

© Su Xu, 1997.



National Library
of Canada

Acquisitions and
Bibliographic Services

395 Wellington Street
Ottawa ON K1A 0N4
Canada

Bibliothèque nationale
du Canada

Acquisitions et
services bibliographiques

395, rue Wellington
Ottawa ON K1A 0N4
Canada

Your file Votre référence

Our file Notre référence

The author has granted a non-exclusive licence allowing the National Library of Canada to reproduce, loan, distribute or sell copies of this thesis in microform, paper or electronic formats.

The author retains ownership of the copyright in this thesis. Neither the thesis nor substantial extracts from it may be printed or otherwise reproduced without the author's permission.

L'auteur a accordé une licence non exclusive permettant à la Bibliothèque nationale du Canada de reproduire, prêter, distribuer ou vendre des copies de cette thèse sous la forme de microfiche/film, de reproduction sur papier ou sur format électronique.

L'auteur conserve la propriété du droit d'auteur qui protège cette thèse. Ni la thèse ni des extraits substantiels de celle-ci ne doivent être imprimés ou autrement reproduits sans son autorisation.

0-612-33036-2

UNIVERSITÉ DE MONTRÉAL
ÉCOLE POLYTECHNIQUE DE MONTRÉAL

Cette thèse intitulée:

THE INFLUENCE OF GRAIN SIZE ON CREEP AND CREEP CRACK
GROWTH IN UDIMET 520, A FORGED NICKEL-BASE SUPERALLOY

présentée par: XU Su

en vue de l'obtention du diplôme de: Philosophiae Doctor

a été dûment acceptée par le jury d'examen constitué de:

M. MARCHAND Norman J., Ph.D., président

M. DICKSON John Ivan, Ph.D., membre et directeur de recherche

M. KOUL Ashok K., Ph.D., membre et co-directeur de recherche

M. VERREMAN Yves, Ph.d., membre

M. IMMARRIGEON Jean-Pierre, Ph.D., membre

ACKNOWLEDGMENTS

I would like to express my heartfelt thanks to my thesis advisor, Prof. J.Ivan Dickson, for providing me with the opportunity to study under his supervision and to do this project on superalloys. I am also very indebted to him for his guidance, motivation and help during my study. His accurate, practical and realistic attitude toward scientific research has influenced me very much.

I would like to sincerely thank my thesis co-supervisor Dr. Ashok K. Koul especially for providing me the opportunity to work in superalloys in a very good research environment and for providing me with a well defined thesis topic, and for guiding, motivating and encouraging me. I have appreciated his efficiency and ability to manage research at fundamental as well as applied fields.

I would like to thank Dr. X.J. Wu especially for his advice on the development of the creep crack growth model for many hours and days of time and useful discussions. These discussions certainly provide a deep insight into the modeling approaches and help to explain some of the experimental results.

Much of the work for this project was performed at the Structures, Materials and Propulsion Laboratory (SMPL) of Institute for Aerospace Research (IAR), National Research Council (NRC) under IAR-NRC project JHM05: Damage Tolerance of Aeroengine Materials. I would like to express my sincere gratitude to Dr. W. Wallace and Dr. J.P. Immarigeon for allowing me to work at SMPL-IAR, NRC and providing all necessary support.

I would like to thank Mr. Min Chang and Mr. Jason Dyer for their help in the DC-PD technique setup. I also would like to thank every member of the staff of the laboratory, especially Messrs. Tak Tereda, Dave Morphy and Ray Dainty for their patient and reliable technical support. Thanks also go to the technical staff in the department of metallurgical and materials engineering at Ecole Polytechnique de Montreal.

This thesis is dedicated to my parents. I would also like to express my gratefulness to my other family members for their understanding and support during my study. I also would like to express my thanks to some of my friends, especially Dr. Changzhun Zhou, Ms. Xiaozhu Wu and Dr. Jianguo Zhao, who encouraged and helped me to go through a period of personal difficulty.

RÉSUMÉ

Cette thèse porte sur l'étude du fluage et de la vitesse de fissuration lors du fluage de l'Udimet 520, un superalliage à base de nickel, en fonction des variables microstructurales. La principale étape expérimentale de cette recherche fut de caractériser et de quantifier l'influence de la taille de grains sur le comportement en fluage et sur la propagation d'une fissure sur du matériau traité pour avoir une absence de précipités aux joints de grains. La première partie de l'étude expérimentale avait pour but d'établir les cinétiques pour la croissance des grains, pour la précipitation de γ' dans la matrice et pour la précipitation de carbures aux joints de grains pour l'Udimet 520. Les résultats apportent les bases nécessaires à la modélisation microstructurale de la propagation d'une fissure en fluage.

Les vitesses de fissuration lors du fluage ont été étudiées en fonction de la taille des grains à une température légèrement inférieure à celle employée lors du vieillissement afin d'éviter la précipitation de carbures intergranulaires pendant les essais. Nous avons mis l'emphase à isoler l'effet de la taille des grains sur le fluage et sur la fissuration par fluage, en l'absence de précipités aux joints de grains dans un environnement d'air, avec quelques essais effectués dans l'argon. La technique de la chute du potentiel électrique a été employée pour mesurer la propagation des fissures en fonction de K , le facteur d'intensité de contrainte, à la température de 540°C. La vitesse

de propagation de la fissure en fluage ne dépendait pas de la taille des grains, pour une température de recuit au dessus ou en dessous de la température de mise en solution du carbure MC. Cependant la vitesse de fissuration dans les échantillons recuits au dessus de la température de mise en solution du carbure MC était environ 2,5 fois plus élevée que pour ceux recuits au dessous de la température de mise en solution du carbure MC.

Un modèle de la propagation d'une fissure en fluage a été développé en tenant compte de l'influence de l'environnement et des mécanismes de fissuration indiqués par les observations fractographiques. Ce modèle prévoit que la propagation des fissures contrôlée par le glissement de joints de grains est indépendante de la taille des grains (d) dans une structure planaire des joints de grains ne contenant pas de précipités intergranulaires; mais que la vitesse de fissuration lors du fluage est inversement proportionnelle à la taille des grains dans les échantillons contenant une distribution discontinue de précipités intergranulaires et incessamment proportionnelle au carré de la taille de grain dans les échantillons contenant une phase continue de précipités intergranulaires. Ce modèle prévoit aussi que le glissement des joints de grains varie avec K^2 , où K est le facteur d'intensité de la contrainte. L'importance de ce modèle est qu'il indique que le glissement des joints de grains est le facteur qui contrôle le mécanisme de la rupture lors de la fissuration en fluage dans ce matériau.

Nous discutons brièvement de l'influence de la taille des grains sur les discontinuités sur la courbe de traction à 540°C, qui sont semblables aux décrochements obtenus lors du vieillissement dynamique après écrouissage. Le comportement en fluage obtenu à 540°C est aussi décrit.

ABSTRACT

This thesis presents a study of the creep deformation and creep crack growth behaviors of a nickel-base superalloy, Udimet 520, as a function of microstructural variables. The focus was on the characterization and quantification of the influence of grain size on the creep and creep crack growth rate (CCGR) behavior in the absence of a grain boundary phase. A microstructural investigation on the forged Ni-base superalloy, Udimet 520 was first performed. This experimental study was used to establish the kinetics of grain growth, γ' precipitation and precipitation of carbides at grain boundaries for Udimet 520. The results provided the basis for obtaining the microstructure for the creep and creep crack growth testing program.

The creep crack growth rates were studied as a function of grain size at a temperature lower than that employed in aging in order to prevent the formation of grain boundary carbides during the test. Emphasis was placed on isolating the grain size effect on creep and creep crack growth rates from the effects of grain boundary precipitates and environment. A direct current potential drop technique was employed in order to measure the rate of crack propagation as a function of K , the stress intensity factor at a temperature of 540°C. The CCGRs were insensitive to the change in grain sizes in specimens solution treated either above or below the MC carbide solvus temperature (1190°C). However, the CCGRs in specimens solution treated above the MC carbide solvus temperature were about 2.5 times higher than those treated below the MC carbide

solvus temperature. Fractographic observations on the fracture surfaces and metallographic examinations on the cross-sections of the interrupted CCG specimens revealed formation of intergranular microcracks and an intergranular mode of fracture. The influence of the air environment was also studied by comparing the creep crack growth rates in air with those obtained in a high purity argon environment.

A mechanistic model describing the creep crack growth behavior was developed taking into account the influence of the environment and the cracking mechanisms indicated by fractographic and metallographic observations. This model predicts that the GBS-controlled CCGR is independent of grain size (d) in planar grain boundary structures containing no grain boundary precipitates; but CCGR is inversely proportional to the grain size in the presence of discrete grain boundary precipitates and inversely proportional to the square of the grain size in materials containing continuous grain boundary precipitate distribution. This model also predicts that the GBS-controlled CCGR has a dependence on stress intensity factor (K) to the power of 2. The significance of this model is that it indicates that GBS is the controlling fracture mechanism in CCG behavior.

The influence of grain size on tensile serration behavior in tensile tests at 540°C was briefly discussed and the creep tests at 540°C were documented.

CONDENSÉ EN FRANCAIS

Cette thèse porte sur l'étude du fluage et de la vitesse de fissuration lors du fluage de l'Udimet 520, un superalliage à base de nickel, en fonction des variables microstructurales. La principale étape expérimentale de cette recherche fut de caractériser et de quantifier l'influence de la taille de grains sur le comportement en fluage et sur la propagation d'une fissure dans du matériau traité pour avoir une absence de précipités aux joints de grains.

La première partie de l'étude expérimentale avait pour but d'établir les cinétiques pour la croissance des grains, pour la précipitation de la phase durcissante γ' dans la matrice et pour la précipitation de carbures aux joints de grains pour l'Udimet 520. Le but de ceci était d'identifier les conditions permettant d'obtenir une précipitation d'un montant important de γ' à l'intérieur des grains, mais sans précipitation de carbures aux joints de grains. Des courbes en forme de C pour la précipitation des carbures $M_{23}C_6$ aux joints de grains ont été obtenues. Pour chaque température de vieillissement, le logarithme du temps de vieillissement pour la précipitation des carbures a été déterminé et comparé au temps de vieillissement pour la précipitation de γ' , en employant des observations par microscopie électronique à transmission et des mesures de microdureté. Ceci a montré que pour obtenir une précipitation importante de γ' en absence de carbures aux joints de grains, il fallait employer des températures de vieillissement relativement basses, ce qui impliquait des longs temps de vieillissement. Nous avons obtenu une précipitation convenable de γ' en

absence de carbures intergranulaires en employant un vieillissement de 20 minutes à 700°C suivi d'un deuxième vieillissement de 92 heures à 600°C.

Les résultats de l'étude microstructurale indiquaient que peu de carbures $M_{23}C_6$ (identifiés au MET par son patron de diffraction) précipitait lors d'un vieillissement à 900°C, mais que la croissance de ces carbures était rapide à cette température. Suite à un long vieillissement, leur croissance produisait une couche de carbure continue aux joints de grains. Lors d'un vieillissement à 850°C, plus de carbures précipitaient mais leur croissance était plus lente. Des carbures en forme de plumes ont été observés à plusieurs endroits, avec cette forme indiquant que ces carbures étaient formés par un effet simultané de précipitations de carbures intergranulaires et de croissance des grains.

Les carbures intergranulaires $M_{23}C_6$ disparaissaient à une température de 1100°C. Cependant suite à une mise en solution à 1250°C, des carbures de type MC précipitaient sur les joints de grains lors de vieillissement à des températures entre 1100 et 1177°C, mais une telle précipitation ne se produisait pas à 1190°C.

Le graphique pour la taille des grains en fonction de la température de mise en solution présentait deux régions de forte augmentation, la première qui se trouve vers 1190°C s'explique par la mise en solution des carbures secondaires de composition MC et la deuxième qui se trouve vers 1240° s'explique par la mise en solution de carbonitrures. Le

graphique pour la microdureté en fonction de la température de mise en solution avait une forme semblable, indiquant un durcissement appréciable associé au carbone et à l'azote mis en solution.

Nous avons mis l'emphase à isoler l'effet de la taille des grains sur le fluage et sur la fissuration par fluage, en l'absence de précipités aux joints de grains dans un environnement d'air, avec quelques essais effectués dans l'argon. Ces essais ont été effectués à une température de 540°C, qui est de 60°C plus faible que la plus faible des deux températures de vieillissement employées pour la précipitation de la phase γ' lors des traitements thermiques. Cette température de 540°C a permis d'éviter la précipitation de carbures intergranulaires pendant les essais.

Nous avons effectué des essais de vitesse de fissuration en fluage en employant des éprouvettes CT ayant une largeur de 26 mm et une épaisseur de 13 mm sur une machine de fluage à charge constante. Tous les essais sauf un ont été effectués à une charge constante de 23.1 kN, donnant un facteur initial d'intensité de contrainte d'approximativement 71 MPa(m)^{1/2}. La chute du potentiel électrique en courant direct a été employée pour mesurer la longueur de fissure lors des essais et pour obtenir les vitesses de fissuration en fonction du facteur d'intensité de contrainte.

La vitesse de propagation de la fissure en fluage ne dépendait pas de la taille des grains, pour une température de recuit au dessus ou en dessous de la température de mise en solution du carbure MC, avec la taille des grains au dessus de cette température allant de 235 à 464 μm . Cependant la vitesse de fissuration dans les échantillons recuits au dessus de la température de mise en solution du carbure MC était environ 2,5 fois plus élevée que pour ceux recuits au dessous de cette température. Deux essais de fissuration effectués dans l'argon ont indiqué qu'à faible K la vitesse était semblable (possiblement légèrement plus faible) que celle à l'air mais, à K élevé, la vitesse était nettement plus faible que celle à l'air. Les observations fractographiques ont indiqué que la fissuration lors du fluage se produisait principalement de façon intergranulaire et que le glissement des joints de grains contribuait à cette fissuration. Nous proposons que les différences de vitesse de fissuration dans ces éprouvettes en fonction de la température de mise en solution sont, au moins en partie, le résultat de plus de ramification des fissures dans les éprouvettes ayant une taille de grains fine obtenue lors de la mise en solution en bas de 1190°C.

Un modèle de la propagation d'une fissure en fluage a été développé en tenant compte de l'influence de l'environnement et des mécanismes de fissuration indiqués par les observations fractographiques. Ce modèle est basé sur la fissuration se produisant principalement par l'effet de glissement des joints de grains. Il prévoit que la propagation des fissures contrôlées par le glissement de joints de grains est indépendante de la taille des grains (d) dans une structure planaire des joints de grains ne contenant pas de précipités

intergranulaires, mais que la vitesse de fissuration lors du fluage est inversement proportionnelle à la taille des grains dans du matériau contenant une distribution discontinue de précipités intergranulaires et inversement proportionnelle au carré de la taille de grain dans du matériau contenant une distribution continue de précipités intergranulaires. Ce modèle prévoit aussi que le glissement des joints de grains varie avec K^2 , où K est le facteur d'intensité de la contrainte. L'importance de ce modèle est qu'il indique que le glissement des joints de grains est le facteur qui contrôle le mécanisme de la rupture lors de la fissuration en fluage dans ce matériau.

Les résultats que nous avons obtenus sur les vitesses de fissuration en absence de précipités intergranulaires $M_{23}C_6$ concordent avec ce modèle pour les recuits de mises en solution effectués en haut de 1190°C. La fissuration plus lente pour les recuits effectués en bas de cette température s'explique par la ramification des fissures plus importantes dans le matériau à grains fins et par l'effet d'un montant de fissuration transgranulaire plus important lorsque les grains sont grossiers, qui sont des effets qui ne sont pas considérés dans ce modèle. Les différences entre les courbes de vitesses de fissuration obtenues dans l'air par rapport à celles obtenues dans l'argon s'expliquent en considérant l'effet de l'oxydation dans le modèle proposé.

Des discontinuités ont été observées sur la courbe de traction à 540°C, qui sont semblables aux décrochements obtenus lors du vieillissement dynamique après écrouissage.

Le comportement en fluage obtenu à 540°C est aussi décrit. Les déformations par fluage à cette température étaient faibles, mais une fissuration intergranulaire se produisait à partir de la surface, indiquant que cette fissuration était associée à un effet de l'environnement.

CONTENTS

	PAGE
ACKNOWLEDGMENTS	iv
RÉSUMÉ	vi
ABSTRACT	ix
CONDENSÉ EN FRANCAIS	xi
TABLE OF CONTENTS	xvii
LIST OF TABLES	xxiii
LIST OF FIGURES	xxiv
1. INTRODUCTION	1
1.1 Background	1
1.2 Project Objectives	3
2. LITERATURE REVIEW	5

2.1 Creep Deformation and Damage Accumulation in Superalloys	6
2.1.1 Statement of the polycrystal Creep deformation	6
2.1.2 The Phenomenology of Creep	8
2.1.3 Creep Deformation Mechanisms	14
2.1.3.1 Creep Deformation Mechanism Map	14
2.1.3.2 Relative Importance of Creep Mechanisms	15
2.1.3.3 Role of Grain Boundary Sliding (GBS) in Superalloy Creep	17
2.1.3.4 Intragranular Dislocation Creep	22
2.1.4 The Importance of Grain Size and Grain Boundary Precipitates on Creep in Ni-Base Superalloys	23
2.1.4.1 Grain Size Effects on Creep Deformation	24
2.1.4.2 Effect of Carbides on Creep in Ni-Base Superalloys	31
2.1.5 Intergranular Creep Fracture	34
2.1.5.1 Types of Intergranular Cracks	34
2.1.5.2 Grain Size Effects	35
2.1.5.3 Grain Boundary Precipitate Effects	36
2.1.5.4 Environmental Effects	37
2.2 Creep Crack Growth in Ni-Base Superalloys	41

2.2.1. Fracture Parameters to Describe Creep Crack Growth Behavior	42
2.2.2. Creep Crack Growth Process	46
2.2.2.1 Initial Stage of CCG	47
2.2.2.2 The Effect of Temperature on CCGR	50
2.2.2.3 The Effect of Side-Grooves on CCGR	50
2.2.2.4 The Effect of Microstructure on CCGR	51
2.2.2.5 The Effect of Environment on CCGR	52
2.2.2.6 Long Term CCG	55
2.2.2.7 The Fracture Mode During CCG	56
2.2.3 Creep Crack Growth Rate Models	58
2.2.3.1 Stress Intensity Factor (K) Based Models	59
2.2.3.2 Deformation Based Models	61
2.2.3.3 Diffusion Based Models	64
2.2.3.4 Combined Deformation and Diffusion Models	66
3. EXPERIMENTAL MATERIALS AND METHODS	71
3.1 Materials	71
3.2 Microstructural Characterization	72
3.3 Heat Treatment Procedures	74

3.4 Hardness Testing	74
3.5 CCGR Testing	75
3.6 Tensile and Creep Testing	79
4. RESULTS	81
4.1 Grain Growth, Carbide Precipitation and γ' Precipitation in Udimet 520	81
4.1.1 Influence of Solution Treatment on Grain Size and Carbide Precipitation	81
4.1.2 Grain Boundary $M_{23}C_6$ Carbide Precipitation Kinetics	85
4.1.3 The Morphology of Grain Boundary $M_{23}C_6$ Carbides	87
4.1.4 Secondary MC Carbide Precipitation and MC Carbide Solvus Temperature	89
4.1.5 Gamma Prime Precipitation	92
4.2 The Effect of Grain Size on Creep Crack Growth in Udimet 520	93
4.2.1 Creep Crack Growth Rate	93
4.2.2 Fracture Surface Observations	95
4.2.3 Metallographic Observations	98

4.3 The Effect of Grain Size on Tensile and Creep Properties	98
4.3.1 Tensile Properties	98
4.3.2 Tensile Specimen Surface Observations	100
4.3.3 Creep-Rupture Properties	101
4.3.4 Creep Fractographic Observations	102
4.3.5 Creep Specimen Surface Observations and Metallographic Cross- Section Observations	103
5. DISCUSSION	105
5.1 Grain Growth, Carbide and γ' Precipitation in Udimet 520	106
5.2 The Effect of Grain Size on CCG Behavior in Udimet 520	111
5.2.1 Initiation Stage of the Creep Crack Growth Process	112
5.2.2 Effect of Grain Size on CCGR in the Absence of Grain Boundary Precipitates	112
5.2.3 Fracture and Deformation Mechanisms During CCG	113
5.3 A Grain Boundary Sliding-Controlled Intergranular CCGR Model	116

5.3.1 Effective Stress Distribution Ahead of the Crack Tip	117
5.3.2 The Proposed Model	120
5.3.3 Model Prediction and Verification	123
5.3.3.1 The Effect of Grain Size on CCGR	124
5.3.3.2 The CCGR Dependence on Stress Intensity Factor	127
5.3.3.3 Oxidation Effect on CCGRs	129
5.4 Tensile and Creep Behavior of Udimet 520	132
5.4.1 Tensile Serrated Flow Mechanism	132
5.4.2 Creep Mechanisms	134
5.4.3 Effect of Grain Size and Environment on Creep Life	135
6. Summary and Conclusions	137
Recommendations for Further Work	142
Figure	163
References	207

LIST OF TABLES

Table 2.1 Approximate temperatures at which creep behavior becomes significant for different metals and alloys	6
Table 2.2 Minimum creep rate equations of different creep mechanisms	26
Table 3.1 Chemical composition of the alloy investigated (wt%)	71
Table 4.1 Microstructural details and microhardness results from different heat treatments	82
Table 4.2 Parametric results obtained from different CCG tests in air on U-520 material at 540°C	94
Table 4.3 Parametric results obtained from different CCG tests in argon on U-520 material at 540°C	94
Table 4.4 Tensile properties of Udimet 520 after different treatments	99
Table 4.5 Features of tensile serrations of different heat treatments	100
Table 4.6 Creep-rupture results on Udimet 520 at 540°C	102

LIST OF FIGURES

- Figure 2.1 Schematic creep curves for (A) constant tensile stress and (B) constant tensile load [7]. 143
- Figure 2.2 Effective shear strain rate vs time of Nimonic 80. Torsion and constant stress uniaxial tension at same effective stress [9]. (The effective stress $\sigma = \sqrt{3/2}$ * octahedral shear stress. In uniaxial tension σ is numerically equal to the applied tensile stress. The effective strain ϵ (=octahedral shear strain/ $\sqrt{2}$) is equal to the tensile strain in a uniaxial tensile test.). 143
- Figure 2.3 An example of creep strain vs time relationship of IN-800H alloy [10]. 144
- Figure 2.4 Primary and secondary creep properties of new and service exposed blades, creep tested at 350 MPa at 830°C. Superimposed is the rejuvenated turbine blade data [11]. 144
- Figure 2.5 Minimum creep rate for aluminum over a wide range of stresses [16]. 145
- Figure 2.6 A deformation mechanism map for IN738LC blades indicating typical operational stress and temperature regimes for industrial and aero engine blades [28]. 145
- Figure 2.7 The predicted curves for diffusional creep and GBS compared with experimental data for fine-grained copper at 820°C [33]. 146
- Figure 2.8 The minimum creep rate vs the multiplication of $(\sigma - \sigma_{ig})$ and $(\sigma - \sigma_{ic})$ in Nimonic 115. For the material with grain boundary carbides, $\sigma_{ig} = \sigma/b$, $b = 1.3$, and $\sigma_{ic} = 487$ MPa.

The minimum creep rate data are taken from ref. 23. The solid lines represent the regression lines [29].	146
Figure 2.9 Creep strain vs time relationship for new and service exposed IN738LC blades tested at 899° C and 90MPa. The symbols represent the test data [36]. The solid lines represent the predictions [29].	147
Figure 2.10 Schematics of the creep curve [3].	147
Figure 2.11 Existence of an optimal grain size for which the minimal creep rate is lowest in a superalloy with $f_v = 20\%$ tested at 800°C at a stress of 150 MPa [47].	148
Figure 2.12 Variation of steady state creep rate with grain size at various stresses at 873 K in type 316 stainless steel [49].	148
Figure 2.13 Variation of steady state creep rate with grain size at various stresses at 973 K, in type 316 stainless steel [49].	149
Figure 2.14 The effect of grain size on the minimum creep rate for a series of Ni-based alloys tested at 800°C [50].	149
Figure 2.15 The secondary creep rate vs. grain size test at 700°C in Inconel X-750 [51].	150
Figure 2.16 The variation of secondary creep rate with average grain diameter tested at 600°C in Nimonic 80A [52].	150
Figure 2.17 The effect of grain size on minimum creep rate for different mismatch and volume fraction of γ' in Ni-20 Cr carbon free alloys at 154.4 MPa at 750°C [55].	151

Figure 2.18 Variation of the rupture life as a function of grain size test at 900°C in a cast superalloy IN-100 [58].	151
Figure 2.19 Carbide density vs. grain size for cast In-100 superalloy. There is a strong similarity between this curve and that of Fig. 2.18 [58].	152
Figure 2.20 Effect of grain boundary carbides on the minimum creep rate of Nimonic 115 over a range of temperatures at 517 MPa [23].	152
Figure 2.21 Relative tendencies for wedge (w) and cavity (r) voids as a function of stress and grain size [70].	153
Figure 2.22 (a) Minimum creep rate data and (b) rupture life data for Udimet 700 at 927°C and 172MPa, in air and vacuum [78], as replotted in [3].	153
Figure 2.23 Creep crack growth rate data for various superalloys at 704°C [92].	154
Figure 2.24 Effect of temperature on creep crack growth behavior in Inconel 718 [93].	155
Figure 2.25 Effect of side groove depth on CCGR in an aluminum alloy [116].	156
Figure 2.26 Initial stress intensity to produce failure in 100 h at 704°C vs grain size [90].	156
Figure 2.27 Creep crack growth rate as a function of microstructure (◆, necklace structure; ▼, coarse grain (L-S); ▲, coarse grain (S-L) ●, fine grain; ✱, fine grain (β)) [118].	157
Figure 2.28 Effect of grain boundary structure on CCG [90].	158
(a) Serrated grain boundary microstructure of IN-792	158

(b) Time to failure vs stress intensity factor with either smooth or serrated grain boundaries for IN- 792 at 704°C	158
Figure 2.29 Time to failure vs stress intensity factor with various heat treatments for Inconel 718 at 649°C [92].	159
Figure 2.30 Creep crack growth rates in air and helium for Inconel 718 at 650°C [123].	159
Figure 2.31 Comparison between creep crack growth rates in superalloys in air and in vacuum at 927°C [134].	160
Figure 2.32 Interlinked cavities at the creep crack tip, $\times 720$ [138].	161
Figure 2.33 Grain boundary sliding contributing to crack growth [152].	161
Figure 2.34 Comparison of measured and calculated creep crack growth rates at 704°C of PM HIP MERL 76, an advanced disc alloy [122].	162
Figure 3.1 The CT specimen for CCGR testing.	163
Fig. 3.1 (a) Specifications of the AGARD CT specimen.	163
Fig. 3.1 (b) A CT specimen with current & potential leads attached to it (with fiberglass insulator sleeves around the leads), $\times 1.5$:.....	164
Figure 3.2 The setup of CCG testing in argon.	165
Figure 3.3 Schematic of the DC-PD used to monitor crack length.	167
Figure 3.4 The tensile and creep specimen geometries employed.	168
Figure 4.1 Microstructure of the forged Udimet 520 (as received).	169
Figure 4.2 Microstructure of an U-520 specimen after 1050°C /4h/AC solution treatment.	

.....	190
Figure 4.3 Effect of solution treatments on the mean intercept length of grains for Udimet 520.	191
Figure 4.4 Grain coarsening curve for Udimet 520.	191
Figure 4.5 Microstructure of a specimen after 1090°C /4h/AC solution treatment and the normal two-stage aging treatment.	192
Figure 4.6 Microstructure of a specimen after 1235°C /2h/AC solution treatment and the normal two stage aging treatment.	192
Figure 4.7 TEM replica micrograph of a specimen after solution treatment at 1135°C for 2 hours and air cooling.	193
Figure 4.8 A representative X-ray spectrum of $M_{23}C_6$ carbides from a replica.	193
Figure 4.9 Replica TEM micrograph of a specimen aged at 1050°C for 15 minutes and water quenched, following a solution treatment of 4 hours at 1135°C and air cooled.	
(a) Grain boundary $M_{23}C_6$ morphology	194
(b) Electron diffraction pattern and index from a carbide in Fig. 4(a)	194
Figure 4.10 The C-curve for the start of the grain boundary $M_{23}C_6$ carbide formation in Udimet 520.	195
Figure 4.11 Microstructure of a specimen annealed for 2 hours at 1100°C, following an aging treatment of 30 minutes at 850°C performed after a first solution treatment at 1250°C for 2 hours.	196

Figure 4.12 Microstructure of a specimen aged for 30 minutes at 850°C and water cooled after the 1250°C solution treatment.	175
Figure 4.13 Replica TEM micrographs of specimens aged for the indicated time at 900°C after the 1135°C solution treatment: (a) 40 minutes (b) 24 hours (c) 48 hours (d) 90 hours	176
Figure 4.14 Replica TEM micrographs of a specimen aged at 700°C for 100 hours and water cooled after an 1135°C solution treatment.	177
Figure 4.15 Replica TEM micrograph of a specimen after an 1135°C/4h/AC solution treatment followed by the normal two-stage aging treatment.	177
Figure 4.16 Feather-like grain boundary $M_{23}C_6$ carbides in a specimen aged at 900°C for 40 minutes and water cooled following an 1135°C C/4h/AC solution treatment.	178
Figure 4.17 Microstructure of a specimen annealing at 1177°C for two hours and water cooled after a 1250°C solution treatment (polished only).	178
Figure 4.18 Matrix Vicker microhardness vs solution temperature relationship.	279
Figure 4.19 TEM micrograph of grain boundaries and γ' phases of a specimen solution treated at 1135°C.	279
Figure 4.20 Creep crack length vs time relation of an CCG specimen solution treated at 1200°C and CCG tested in air at 540°C.	180
Figure 4.21 CCGR and stress intensity factor relations for specimens subjected to different heat treatments and tested in air at 540°C.	181

Figure 4.22 CCGR and stress intensity factor relations of the specimen solution treated at 1135°C and tested at 540°C.	182
Figure 4.23 CCGR and stress intensity factor relations of the specimen solution treated at 1135°C and 1120°C tested at 540°C in argon.	183
Figure 4.24 Interface of the pre-fatigued region and CCG region of an CCG specimen solution treated at 1135°C and CCG tested in air at 540°C.	184
Figure 4.25 SEM micrographs of CCG region of a specimen solution treated at 1135°C and tested in air at 540°C.	185
Figure 4.26 SEM micrographs of CCG region of an CCG specimen solution treated at 1200°C and tested in air at 540°C.	186
Figure 4.27 SEM micrographs of CCG region of a specimen solution treated at 1250°C and tested in air at 540°C.	187
Figure 4.28 Interface of slow CCG region and fast fracture region of an CCG specimen solution treated at 1135°C and tested in air at 540°C.	188
Figure 4.29 SEM micrograph of fast fracture region of an CCG specimen solution treated at 1135°C and tested in air at 540°C.	188
Figure 4.30 SEM micrographs of CCG regions tested in argon at 540°C.	189
Fig. 4.30 (a) Specimen solution treated at 1135°C	189
Fig. 4.30 (b) Specimen solution treated at 1200°C	189
Figure 4.31 Metallographic cross section of an CCG specimen solution treated at 1135°C and tested in air at 540°C (crack propagation from top to bottom).	190

Figure 4.32 Polished cross section of an interrupted CCG specimen solution treated at 1200°C and tested in air at 540°C (crack propagation from top to bottom).	191
Figure 4.33 Tensile strength vs grain size relationship at 540°C.	192
Figure 4.34 Tensile engineering strain vs load curve (part).	192
Figure 4.35 Surface morphology after tensile tests.	193
Figure 4.35 (a) 1110°C solution treatment	193
Figure 4.35 (b) 1190°C solution treatment	194
Figure 4.35 (c) 1250°C solution treatment	194
Figure 4.36 Surface morphology close to the tensile fracture surface of the specimen solution treated at 1250°C.	195
Figure 4.36 (a) Surface microcracks	194
Figure 4.36 (b) Surface deformation bands and microcracks	195
Figure 4.37 Creep strain vs time relationship in Udimet 520 solution treated at 1135°C.	195
Figure 4.38 Creep fracture surface of specimen solution treated at 1135°C and tested in air.	196
Figure 4.39 Creep fracture surface of specimen solution treated at 1190°C and tested in air.	197
Figure 4.40 Creep fracture surface of specimen solution treated at 1250°C and tested in flowing argon.	197
Figure 4.41 Intergranular fracture of creep specimen solution treated at 1135°C and tested	

in air.	198
Figure 4.42 Transgranular fracture of creep specimen solution treated at 1135°C and tested in air.	198
Figure 4.43 Intergranular fracture of creep specimen solution treated at 1135°C and tested in flowing argon.	199
Figure 4.44 Surface of specimen solution treated at 1135°C and creep tested at 540°C.	199
Figure 4.45 Surface of specimen solution treated at 1250°C and creep tested at 540°C.	200
Figure 4.46 Grain boundary cracks at free surface in specimen solution treated at 1135°C and creep tested at 540°C.	201
Figure 4.46 (a) Tested in air.	200
Figure 4.46 (b) Tested in flowing argon.	201
Figure 4.47 Profile of fracture surface of specimen solution treated at 1190°C.	201
Figure 5.1 A schematic summary of heat treatment time-temperature-microstructure relationship in Udimet 520.	202
Figure 5.2 Proposed mechanisms for the local transgranular fracture caused by the stress concentration ahead of w-type cracks.	203
Fig. 5.2 (a) Local transgranular cracking at a grain boundary imperfection.	
Fig. 5.2 (b) Local transgranular cracking by high local stress.	
Figure 5.3 Effective stress versus distance ahead of the creep crack tip.	204

Figure 5.4 The predicted CCGR vs K relation on the specimens solution treated at 1135°C and tested at 540°C. 205

Figure 5.5 The intergranular cracks on the surface of an specimen interrupted just after creep loading (solution treated at 1110°C). 206

1. INTRODUCTION

1.1 Background

Superalloy microstructures have traditionally been designed to optimize high temperature tensile strength, creep resistance, and more recently low cycle fatigue (LCF) or thermal mechanical fatigue (TMF) properties. Damage tolerance or tolerance to flaw is also assuming an increasing importance in new superalloys design specifications [1], as well for engine maintenance [2] for rotating components. To satisfy these new damage tolerance requirements, crack growth properties under creep, fatigue or combined loading conditions must be controlled. Thus, designing microstructures for the critical rotating components in order to meet both the crack growth rate resistance and the traditional LCF crack initiation life requirements is a challenging task.

Numerous researchers have studied the effect of microstructural features on creep crack growth rates (CCGRs) and fatigue crack growth rates (FCGRs) of superalloys in the past 20 years. It has been shown that grain size, grain boundary carbides and grain boundary morphology are the controlling microstructural features for creep and crack growth resistances in Ni-base superalloys strengthened by gamma prime precipitates. Since grain boundaries are often the weak links of the material at high temperatures, and especially in aggressive environments, the grain boundary related microstructural features often govern the critical properties of precipitation-strengthened superalloys. However,

the effect of grain size in the absence of grain boundary carbides in complex superalloys, and the influence of grain boundary carbides at constant grain size on creep crack growth, have not been systematically explored either experimentally or analytically. To isolate the effect of grain size on the minimum creep rate or on the CCGR is experimentally difficult. This is because these microstructural features in superalloys are interrelated and, upon changing the grain size through material processing, the grain boundary precipitate size and spacing also change simultaneously. The same aging treatments usually produces different grain boundary precipitate distributions (size (r) and spacing (h)) in different grain size specimens. The grain size effect is further overshadowed or hidden by environmental effects, especially at high temperatures.

1.2 Project Objectives

The primary objective of this study was to characterize and quantify the influence of grain size on the creep crack growth rate and the creep behavior of a Ni-base superalloy, Udimet 520, in the absence of a grain boundary phase. Since the commercial alloy Udimet 520 contains $M_{23}C_6$ carbides at the grain boundaries and intragranular γ' precipitates, the kinetics of intragranular γ' nucleation and growth and the formation of grain boundary carbides, was also studied in order to obtain similar precipitate hardening in different grain size materials as in the commercial alloy but without forming any grain boundary precipitates. The objective was to select heat treatment conditions for varying the grain size without precipitating grain boundary carbides.

The creep crack growth rates and the creep behavior were studied as a function of grain size at a temperature somewhat lower than that employed in aging in order to prevent the formation of grain boundary carbides during the test. The influence of the air environment was also studied by comparing the creep crack growth rates with those obtained in a high purity argon environment. One of the objectives of the experiments was to implement a direct current potential drop technique using dead weight creep machine to measure the crack propagation as a function of K , the stress intensity factor.

From a theoretical perspective, an important objective of the project was to develop constitutive model(s) for describing the creep crack growth behavior in complex

engineering alloys taking into account the influence of the environment and the cracking mechanisms observed fractographically and metallographically.

A review of superalloy creep deformation and creep crack growth in Ni-base superalloys as well as the importance of grain size and grain boundary precipitates on creep and creep crack growth in Ni-base superalloys is presented in Section 2 in this thesis. Sections 3 and 4 present the experimental methods and results of the microstructural investigation respectively, the latter combined with a brief discussion. The effects of grain size and environment on creep crack growth behavior as well as on creep are discussed in Section 4. The discussion and the mechanistic CCGR model are presented in Section 5. Finally, the general conclusions are stated in Section 6.

2. LITERATURE REVIEW

The first part of the review presents some important aspects of creep deformation in Ni-base superalloys. Grain boundary sliding (GBS) is shown to be a key deformation mechanism operative during superalloy creep and the supporting metallurgical evidence for this phenomenon is also reviewed. The effect of grain size and the presence of carbides, the primary as well as secondary carbides at the grain boundaries on creep is also considered in some detail. Intergranular creep fracture is discussed.

The second part of the review concentrates on mechanical and metallurgical aspects, including testing aspects of creep crack growth in complex engineering alloys including Ni-base superalloys. The fracture mechanics parameters used to correlate the creep crack growth rates are discussed. The influence of microstructures and test conditions on the creep crack growth behavior is reviewed. Modeling work on the creep crack growth process is reviewed and classified.

2.1 Creep Deformation and Damage Accumulation in Superalloys

2.1.1 Statement of the polycrystal Creep deformation

Creep is the response of a material subjected to a stress (constant or slowly changing) and at $T > 0.3 T_M$. Thus, microstructure (including dislocation structures) might first change to produce viscous flow. Of course, creep can frequently accelerate the change of microstructure, although it is the microstructure that changes first. Creep is usually regarded as the time-dependent mode of anelastic deformation that occurs under stress at high temperature [3]. This time-dependent deformation is related to thermal activation processes which occur, e.g. thermally activated dislocation glide, cross slip, climb and the diffusion of vacancies and atoms. The temperature above which substantial creep deformation occurs after the application of the load is of the order of $0.3 T_m$. Table 2.1 shows the approximate temperatures at which creep behavior becomes significant in engineering alloys [4].

Table 2.1 Approximate temperatures at which creep behavior becomes significant for different metals and alloys

Material type	Temperatures		
	°C	°F	T/T_m
Aluminum alloys	205	400	0.54
Titanium alloys	315	600	0.30
Low alloy steels	370	700	0.36
Austenitic iron-base alloys	540	1000	0.49
Nickel- and cobalt-base superalloys	650	1200	0.56
Refractory metals	980-1540	1800-2000	0.40-0.45

Superalloys are used in heat exchangers, furnace linings, boiler baffles, high-temperature bolts and springs, jet-engine burner liners and exhaust systems, components for gas turbines etc. Ni- or Co-base superalloys are often used under high stress conditions at temperatures up to about 1100°C leading to creep deformation. Probably the most demanding application for creep resistance exists in aircraft gas turbine engines. Superalloy components in gas turbine engines include turbine blades, vanes, discs, combustion cans, ducts, cases and liners. Turbine blades operate at metal temperatures ranging between 650-1100°C and under longitudinal stresses of up to approximately 150 MPa in the airfoil region. In the blade root, temperatures are lower while tensile stresses are higher (250-560 MPa) [5]. These conditions require materials which provide high temperature strength, resistance to creep and microstructural stability at high temperatures. Turbine nozzle guide vanes, which are non-rotating components, are subjected to relatively low steady-state stresses (70 MPa) but extremely high gaseous temperatures up to 1600°C or higher [6]. The basic material requirements are therefore creep resistance at high temperatures as well as resistance to thermal and mechanical fatigue, oxidation, erosion and hot corrosion. Turbine discs operate at temperatures up to 800°C in the outer rim, and are subject to very high stresses and creep as well as creep crack growth resistance are considered important. Towards the center of discs, creep becomes less important since the temperature is lower, but stresses are of the order of 480 MPa and high low cycle fatigue and tensile strengths are therefore necessary.

Through 60 years of research and development of superalloys, a large amount of

creep data was generated for different superalloys, microstructure and microstructural evolution effects on creep have been demonstrated in different composition superalloys, and creep mechanisms have been proposed and studied extensively. With the development of superalloys and related technologies, metallurgists are now more capable of meeting high temperature tensile stress and creep property requirements through γ' and γ'' precipitation control. The understanding and explanation of existing creep data are still developing, but extensive research will be required before the creep crack propagation is completely understood.

2.1.2 The Phenomenology of Creep

The engineering creep tests are usually conducted at a constant load or constant stress. Figure 2.1 illustrates schematically the creep behavior of a material subjected to a constant tensile load (curve A) and a constant tensile stress (curve B) [7]. Both stress and, in particular, temperature increase the creep strain rate ($d\varepsilon/dt$). Under constant load conditions, the creep curves are conventionally divided into three stages: a primary stage I, a secondary constant or steady-state stage, stage II and a tertiary stage III. The first application of a creep stress will produce an elastic strain, and may generate an initial plastic strain if dislocation sources can be activated athermally. The stage I creep rate $\dot{\varepsilon}_I$ decreases continuously with time (and strain) in an annealed material. The stage II creep rate $\dot{\varepsilon}_{II}$ is also known as the minimum creep rate. In stage III there is an acceleration in the creep rate, leading to the eventual fracture of the specimen. The extent of the tertiary creep stage may

be limited in some relatively brittle materials but it can be very extensive in ductile materials.

If the creep curve is obtained under constant stress (not constant load) conditions, the transition between primary and secondary creep often disappears and the transient creep is directly followed by tertiary creep. Garofalo [8] observed this behavior in an austenitic stainless steel and later Dyson and McLean [9] also observed similar behavior during short-term creep test in Ni-base superalloy Nimonic 80A (Fig. 2.2 [9]). These observations indicate that creep is a continuous process where a decreasing creep rate regime is followed by an accelerating creep rate regime beyond a minimum creep rate. In fact, the strain rate vs time curve does not always have a plateau in constant load creep. An example is shown in Fig. 2.3 [10]. In a study on service induced microstructural damage and the rejuvenation of investment cast IN738LC turbine blades, Koul and Castillo [11] have pointed out that, in constant load tests, it is more appropriate to consider the primary as well as the secondary creep stages together as part of a transient creep regime (Fig. 2.4).

Creep properties refer to creep resistance and creep fracture properties. Creep resistance of different materials is often compared by comparing their minimum creep rates, the rupture times and the primary and secondary creep strains. Creep fracture is often characterized by the creep strain at rupture. The creep resistance (or strength parameters) are often defined in terms of the observed minimum creep rate $(d\epsilon/dt)_{II}$ and rupture life (t_r) at a given stress and temperature [12]. When reference is made to an increase in creep

resistance or strength, it is invariably accompanied by an increase in rupture life and a decrease in creep rate [13]. A commonly used test in the industry is the stress rupture (creep-rupture or rupture) test and the important parameters obtained from this test are the time to rupture (t_r) and fracture strain (ϵ_r). In a creep test, in addition to t_r and ϵ_r the minimum creep rate is also determined experimentally. If the concept of creep strain limit is used for design, the primary strain or primary plus secondary strain are also important, since materials may process different transient strains but the same minimum creep rate. For example, the maximum overall strain allowed in civilian aircraft engines is approximately 1 per cent in 10 000 hours (a strain rate of $3 \times 10^{-10} \text{ s}^{-1}$) [14]. As a result, transient creep phenomena must be taken into account in these cases.

The steady-state creep rate, sometimes approximated by the minimum creep rate, can be correlated to grain size (d), applied stress (σ) and temperature (T) by a power law (“power law creep”) equation often presented in the following form:

$$\dot{\epsilon} = \frac{AEbD}{kT} \left(\frac{b}{d}\right)^p \left(\frac{\sigma}{E}\right)^n \quad (2.1)$$

where D is the diffusion coefficient, E is the Young’s modulus, b is the Burgers vector, k is Boltzman’s constant, A is a material constant and n is the apparent stress exponent. This equation can fit creep rates generated from different creep mechanisms. Usually, “power-law” is a term employed for a phenomenological description of intragranular dislocation creep phenomena with $n=4$ to 7. The apparent stress exponent depends on a combination of external effects (applied stress, creep temperature) and internal effects (material,

microstructure). Although the apparent stress exponent *per se* does not provide much physical meaning, it is still used to reflect the stress sensitivity of the dominant creep phenomenon in the material. An increase stress exponent with increasing stress may indicate a transition [15] from diffusional creep or Harper-Dorn creep at low stress to dislocation controlled creep or power law breakdown (dislocation glide creep). Figure 2.5 [16] shows the minimum creep rate for aluminum over a wide range of stresses.

At intermediate stresses, power law creep often gives rise to $n=3$ to 5 , $p=0$ and $D=D_L$, where D_L is the lattice diffusivity in pure metals and solid solution alloys. This indicates that at intermediate stress levels intragranular creep dominates creep deformation. Sherby and Burke [17] pointed out that solid solution alloys depict two types of creep behavior. Some alloys exhibit exponents n about 3 which are different from pure metals; Other alloys show a power law dependence with n equal to 5 which is similar to that of pure metals. The alloys which show a similar behavior to that of pure metals do not have significant primary creep and are not influenced by changes in stacking fault energy or subgrain size changes. The alloys showing a different behavior to that of pure metals show large primary creep characteristics and are influenced by changes in stacking fault energy and subgrain size. Nickel has a stress exponent of 5 and Ni-Cr solid solution alloys have n values of the order of 5.2 [18].

At higher stresses, a power law breakdown behavior is observed where the creep rate increases rapidly with stress. This is associated with the ability of matrix dislocations to

pass athermally through sub-boundaries [3]. Power-law breakdown may also result from a process of dynamic recrystallisation [19].

At low stress levels, a transition to Newtonian viscous flow occurs where $n=1$ is observed, and this has been summarized by Wang [20]. Three distinct mechanisms could produce this behavior. Two involve the stress-directed flow of vacancies from the free surfaces and grain boundaries under a tensile stress to those under relative compression with the vacancy flow occurring through the crystal lattice (Nabarro-Herring creep) or along the grain boundaries (Coble creep); and for which the creep rate is grain size dependent. The third process involves dislocation generation, multiplication and motion within the grains (Harper-Dorn creep), where the grain size dependence disappears. Although all three mechanisms can be described by the same power-law equation, the creep rates produced by each mechanism are different. As will be discussed later, the existence of purely diffusional creep mechanism has been challenged because the theoretical diffusional creep rates are several orders of magnitude lower than the experimental data.

At stress levels ranging between Harper-Dorn creep ($n \approx 1$) and typical power-law creep ($4 \leq n \leq 7$), GBS is the dominant mechanism. A stress exponent of 2 can be observed with $p=1-2$ in Eq. (2.1). At this stress level, the grain size has a significant effect on the creep rate. A stress exponent of 2 is also predicted by Langdon's GBS model [21]. Although creep rate from GBS also fits the form of Eq. (2.1), it is worth noting that the term "power-law creep" is mainly used to describe intragranular creep with $n=3-5$.

Most engineering multi-phase materials show a very different creep behavior than that described for simple solution strengthened alloys at intermediate stress levels. When the minimum creep rates are analyzed in terms of equation (2.1), much higher values of n and Q are obtained compared to simple single-phase alloys. The concepts of back stress or friction stress were used to rationalize the minimum creep rate data of engineering alloys under these conditions. In an analysis of the steady state creep behavior of various γ' strengthened nickel-base superalloys, Purushothaman and Tien [22] described dislocation creep through a modulus-normalized effective stress including a microstructurally related back stress. The creep equation then takes the form

$$\dot{\epsilon}_{II} = A' \left(\frac{\sigma - \sigma_B}{E(T)} \right)^{n_0} \exp\left(\frac{-Q^*}{RT}\right) \quad (2.2)$$

where σ is the applied stress, σ_B is the average back stress, $E(T)$ is the temperature-sensitive Young's modulus in the applied stress direction, n_0 is the true stress sensitivity exponent, Q^* is the true creep activation energy and A' is the material- and structure-dependent parameter. They incorporated a threshold stress which is of the order of the Orowan stress. A similar analysis has been employed for grain-boundary-related creep in Nimonic 115 [23]. The back stress σ_B can be estimated from equation (2.8) through iterative back calculations using isothermal creep rate data [22].

As McLean [24] pointed out in an early survey, a metal with melting temperature T_m usually shows three or four ranges of behavior: (i) $0 < T < 0.3 T_m$ (transient logarithmic creep), (ii) $0.3 T_m < T < 0.5 T_m$ and $0.5 T_m < T < 0.9 T_m$ (the range or ranges which are usually important

in engineering), and (iii) $0.9 T_m < T < T_m$ (diffusional creep). Mclean suggested that cross slip of dislocations would be more important than climb in the lower of these ranges; in this case the activation energy would no longer be the activation energy for self-diffusion as it is in the ranges above $0.5T_m$. Nabarro and de Villiers [25] estimated that an atom will make one diffusional jump about every 500 seconds at $T=T_m$. In order to influence the creep process by causing dislocations to climb, diffusion must occur over distances of the order of 10^2 atomic spacings, which requires about 10^4 random diffusional jumps, taking 5×10^6 s = 2 months. Therefore, in a test duration of 2 months, dislocation climb will be important at temperatures above $0.5T_m$ and unimportant below this temperature.

2.1.3 Creep Deformation Mechanisms

2.1.3.1 Creep Deformation Mechanism Map

Generally, creep mechanisms can be divided into four major groups: diffusion creep, dislocation creep involving glide and climb, pure dislocation glide and grain-boundary sliding (GBS). Normally, there is a dominant creep mechanism in operation for a certain test condition, which depends on test temperature, stress and material. The regions of dominance of each mechanism are often displayed in a log σ/G (G is the shear modulus) vs T/T_m (T_m is the melting point in degree Kelvin) plot called a deformation mechanism map. The deformation mechanism map concept was first developed by Ashby [26] and later extended by Luthy, White and Sherby [27] to include GBS. Figure 2.6 presents an example

of a deformation mechanism map for cast IN738LC turbine blade/vane material [28]. The blade operational stress/temperature ranges for typical aircraft and land based turbines are represented by the hatched regions on the map. This deformation mechanism map indicates that grain boundary sliding and diffusional creep predominate during creep in aircraft blades and land based turbine blades, respectively.

2.1.3.2 Relative Importance of Creep Mechanisms

From a more fundamental point of view, there have been two advances recently in the understanding of creep mechanisms, one is the recognition that GBS in superalloy controls the overall creep behavior, while the second concerns the challenge to the existence of pure diffusional creep.

It is recognized that GBS itself contributes significantly to superplastic flow and the role of GBS during creep is also well recognized. Wu and Koul [29] considered that GBS always contributes significantly to the transient creep strain in polycrystalline materials. This is because the stress at geometrical discontinuities, such as the grain boundaries, will be higher than within the grain interiors, and dislocations at these locations will be activated immediately upon the application of a load during a creep test. Following this rationale, GBS is expected to contribute to the creep deformation process much earlier than other deformation mechanisms. However, at any point of time, the total deformation is always the sum of GBS and intragranular strain according to the deformation decomposition rule. If

the stress is high, creep deformation within the grain interiors by dislocation glide plus climb may provide the most part of total creep deformation since intragranular deformation is more sensitive to stress in the presence of a three-dimension dislocation network. In superalloys strengthened by a high volume fraction of γ' phase, GBS controls the long term creep (i.e. under conditions of practical importance). In addition, GBS as been shown to play a key role in the creep fracture process because intergranular fracture is often one of the characteristics of creep fracture.

The existence of diffusional creep was challenged by Ruano, Sherby, Wadsworth and Wolfenstine [30-32] who also provided their phenomenological approach to understanding the creep behavior. In a recent paper [31], they brought the following arguments to support their claims: (i) Denuded zones, universally considered as direct evidence for diffusional creep, are seen only under conditions where a high stress exponent (as opposed to a value of 1 in Nabarro-Herring diffusional creep) is observed, indicating that diffusion-controlled dislocation creep is the operative deformation process; (ii) The creep rate of fine-grained superplastic materials is invariably orders of magnitude greater than predicted by diffusion creep, as shown in Figure 2.7 [31] in which cases, the deformation process has been established to be GBS accommodated by slip rather than diffusion creep. (iii) The creep behavior of fine-grained copper measured by Burton and Greenwood [33] can be described by a diffusion-controlled dislocation creep mechanism at high stresses, by GBS at intermediate stresses, and by Harper-Dorn creep at low stresses, with no clear evidence for diffusion creep. It is however not clear

whether these authors considered interface reaction controlled diffusional creep in any detail.

2.1.3.3 Role of Grain Boundary Sliding (GBS) in Superalloy Creep

There are two types of GBS [34], respectively the Lifshitz and the Rachinger type. Lifshitz grain boundary sliding is a process related to diffusion creep. With the Lifshitz GBS, grains are elongated and displaced with respect to each other during the process. With the Rachinger GBS on the other hand, the grains retain essentially their original shape, i.e. this mechanism is independent of the deformation occurring in the grain interiors. The literature review which is presented here will be concerned with the role and effects of Rachinger GBS in superalloys.

Creep fractographic studies have revealed that intergranular fracture is the dominant feature in failed creep rupture and creep crack growth specimens. This indicates that GBS is an important creep deformation mechanism during superalloy creep. Therefore, grain size, grain boundary structure and grain boundary precipitate distributions all need to be evaluated in superalloys and optimized to obtain better creep properties in superalloys. Some experimental results are presented below.

Since GBS here is considered a process of dislocation movement along or adjacent to grain boundaries, direct observations of dislocations near grain boundaries is important.

Howell and Dunlop [35] have shown that grain boundary dislocations are always mobile whether the creep behavior is governed by diffusional creep or power-law creep according to the deformation mechanisms maps.

There is much evidence in the literature that grain boundary carbides decrease the creep rate by suppressing GBS in Ni-base superalloys [23, 36, 37]. Low stress creep test data generated on new and service-exposed IN738LC blades over a wide range of temperatures [36] indicate that upon changing the fine intragranular γ' and discrete grain boundary carbide distributions to an overaged γ' size and an almost continuous grain boundary carbide network (as a result of service induced γ' coarsening and MC carbide degeneration respectively), both the primary creep strain and the secondary creep strain are significantly reduced relative to that of new blades. These observations indicate that GBS deformation control the evolution of creep strain during transient creep, since overaging of intragranular γ' precipitates decreases rather than increases the resistance to creep deformation.

Furrillo *et al.* [23] found that grain boundary carbides increase the apparent stress exponent from approximately 2.2 to 14.6 with and without grain boundary carbides in Nimonic 115. They also observed the activation energy increases from 334 KJ/mol which is approximately that for volume diffusion to an apparent activation energy of 390 KJ/mol. They rationalized this increase in stress exponent in terms of the back stress caused by grain boundary carbides opposing dislocation motion in the grain boundary plane. This

interpretation indicates that creep strain rate up to the minimum creep rate is also strongly influenced by GBS in superalloys.

The improvement in creep-rupture properties by serrated grain boundaries has also been demonstrated in superalloys [38-40]. That serrated grain boundaries improve both the rupture life and the ductility. These results indicates that GBS also played an important role in determining rupture life and ductility and that GBS is suppressed by the serrated grain boundary structure by redistributing stresses.

Langdon [21] modeled GBS in which sliding occurs by the movement of dislocations along, or adjacent to, the boundary by a combination of climb and glide. The theoretical analysis by Langdon revealed that the strain rate due to sliding is proportional to σ^2/d . The shear strain rate in a climb-glide process is controlled by the rate of climb but produces strain through glide. The rate of climb (\dot{s}) along the boundary, is

$$\dot{s} = Nbv_c \quad (2.3)$$

where N is the number of grain boundary dislocations per unit length, b is the Burgers vector and v_c is the frequency of climb. The shear strain rate by GBS is

$$\dot{\gamma}_{\text{gbs}} = MAbs\dot{s} \quad (2.4)$$

where M is the number of boundaries per unit volume and A is the total area swept out by dislocations moving along a boundary. Since dislocations come into the boundary region from slip on either side of the boundary, M and A can be expressed as $6/\pi d^3$ and πd^2 , respectively, where d is the average grain diameter. So, strain rate by GBS is

$$\dot{\gamma}_{\text{gbs}} \propto \frac{b^2 \sigma^2}{\mu kT d} \quad (2.5)$$

With Langdon's model, the contribution of grain boundary sliding to the total strain ($\epsilon_{\text{gbs}}/\epsilon_t$) increases with decreasing grain size at a high constant stress while this trend is reversed at a constant low stress and the maximum value attainable by $\epsilon_{\text{gbs}}/\epsilon_t$ increases with increasing grain size.

Wu and Koul [29] modified the Langdon's grain boundary sliding model, developed for clean grain boundaries, to account for the presence of grain boundary precipitates by incorporating internal stresses opposing dislocation glide (τ_{ig}) and climb (τ_{ic}). In their model, they considered that the transient creep was operative during both the primary and the secondary creep stages in a constant load creep test. This model assumes that GBS governs transient creep in superalloys. Their modified rate equation for GBS is shown in Eq. (2.6)

$$\dot{\gamma}_{\text{gbs}} = \frac{A_1 D \mu b}{kT} \left(\frac{b}{d}\right)^q \left(\frac{\lambda + r}{b}\right)^{q-1} \frac{(\tau - \tau_{\text{ig}})(\tau - \tau_{\text{ic}})}{\mu^2} \quad (2.6)$$

where q is the grain size index which assumes values of 2 for a discrete grain boundary precipitate distribution and 3 for an almost continuous grain boundary precipitate network, b is the Burgers vector and μ is the shear modulus. They also predicted that in Eq. (2.6) in the absence of grain boundary precipitates, λ will be equal to the interledge spacing and r will approach the average grain boundary ledge height. This rate equation accurately describes the stress dependence of minimum creep rate in superalloys containing grain boundary precipitates. Figure 2.8 shows the minimum creep rate vs $(\sigma - \sigma_{\text{ig}})(\sigma - \sigma_{\text{ic}})$ in Nimonic 115

(data from [38]).

The rate equation, along with the mathematical formulations for internal stresses, is employed to derive a transient creep model by Wu and Koul in terms of strain (γ) as a function of time (t). The transient creep equation for a given temperature takes the form

$$\gamma = \gamma_0 + \dot{\gamma}_{ss} t + \frac{\tau}{H\beta^2} [1 - \exp(-\eta\beta t)] \quad (2.7)$$

where γ_0 is the initial strain, $\dot{\gamma}_{ss}$ is the steady-state creep rate, β is a material constant, H is the work-hardening coefficient, and η is a parameter related to the rate of dislocation climb. This transient strain equation is very similar to Garofalo's empirical equation [8]. Upon transforming the shear components (τ , γ , μ) into tensile components (σ , ε , E), Eq. (2.7) takes the form

$$\varepsilon = \varepsilon_0 + \dot{\varepsilon}_m t + \frac{\sigma}{\beta^2 H} \left[1 - \exp\left(-\frac{\beta^2 H \dot{\varepsilon}_m t}{\sigma(\beta - 1)}\right) \right] \quad (2.8)$$

This equation accurately predicts the transient creep behavior of IN738LC Ni-base superalloy material containing a discrete carbide distribution or a continuous network of carbides. Figure 2.9 shows the creep strain vs time relationship for new and service-exposed IN738LC blades tested at 899°C and 90MPa [29]. Their model focuses on the prediction of the basic creep parameters such as creep strain and time.

2.1.3.4 Intragranular Dislocation Creep

As mentioned earlier, the climb-plus-glide mechanism is considered the most important cause of creep at intermediate stresses. This type of creep is known as “power-law creep” or “Weertman creep”. Based on dislocation theory, Weertman’s model [41, 42] describes the creep rate as being proportional to the diffusion coefficient and depending on stress to the fourth power. In engineering alloys, it was proposed [43] that an effective stress should be substituted into Weertman’s power-law equation to account for the high power observed in the presence of second phase particles [43]. It is worth noting that the term “power-law” is generally employed to describe intragranular creep. Recently, Wu and Koul [3] developed an intragranular creep deformation model having the following form,

$$\dot{\gamma} = (\alpha b \rho v) \exp\left(-\frac{\Delta G_l^*}{kT}\right) \left[\frac{b}{h} \exp\left(\frac{V \tau_{\text{eff}} + \Omega \sigma}{kT}\right) - \exp\left(-\frac{\Omega \sigma}{kT}\right) \right] \quad (2.9)$$

where σ is the stress, ρ is the mobile dislocation density, $v = kT/h$, V is the activation volume, Ω is the atomic volume, l is the sliding distance, τ_{eff} is the effective stress and ΔG_l^* is the activation energy for lattice diffusion. This model successfully described the creep rate dependence on stress over a wide range of creep rate from Harper-Dorn and power-law creep to power-law breakdown. This model indicates that intragranular creep has the same base mechanism, i.e. climb plus glide.

Assuming that the pseudo steady state creep rate, $\dot{\epsilon}_i$, is described by Eq. (2.9), the intragranular creep with dislocation multiplication can be expressed as

$$\dot{\varepsilon}_g = (1 + B\varepsilon_g)\dot{\varepsilon}_i \quad (2.10)$$

where B is the dislocation multiplication factor. Integration of Eq. (2.10) leads to the following strain-time relation

$$\varepsilon_g = \frac{1}{B} \left(\exp(B\varepsilon_g t) - 1 \right) \quad (2.11)$$

The total creep strain at any point in time is equal to the sum of the GBS strain given by Eq. (2.8) and the intragranular strain given by Eq. (2.11), as schematically shown in Figure 2.10.

2.1.4 The Importance of Grain Size and Grain Boundary Precipitates on Creep in Ni-Base Superalloys

The microstructural features that control the properties of superalloys are the grain size, the size, morphology and distribution of carbides (i.e., grain boundary carbides and the primary carbides), the grain boundary morphology, the size, shape and volume fraction of intragranular γ' and γ'' and the type of dislocation substructure. In this review, the controlling microstructural features related to grain boundaries of superalloys are highlighted.

2.1.4.1 Grain Size Effects on Creep Deformation

Grain size ranges can be divided in four categories and these are the macroscopic ($>1000\ \mu\text{m}$), the mesoscopic (typically $10\text{-}1000\ \mu\text{m}$), the microscopic ($0.01\text{-}10\ \mu\text{m}$) and the nanoscopic (typically of the order of only a few nanometers in at least one dimension) [44]. The mesoscopic grain size range is most common in metals and alloys used in normal engineering practice. In this grain size range, grain boundaries make a substantial contribution to the flow strength of the material. Grain boundaries act as barrier to dislocation motion below $0.25T_M$ but grain boundary sliding (GBS) facilitates deformation during high temperature creep. GBS plays an important role in creep deformation in the medium temperature and stress range as indicated in deformation mechanism maps. Furthermore, the boundaries may play a dominant role in the ultimate rupture of a test piece or a component. An important characteristic of this range of grain size is the formation of subgrains within the grains during high temperature deformation.

Malakondaiah et al [45] have analyzed the transient (primary) stage of creep at low stress in $\alpha\text{-Ti}$, $\alpha\text{-Zr}$, $\beta\text{-Co}$ and zircaloy-2. They showed that time associated with the primary stage of the creep curve increased with increasing grain size up to a grain size of nearly $100\ \mu\text{m}$. However, transient strain, normalized with respect to the elastic strain, appeared generally to be independent of grain size.

Wu and Koul [29] emphasized grain boundary sliding (GBS) role in the transient

(primary plus secondary) creep of complex engineering alloys. Their mechanistic model showed that the creep rate is related to the grain boundary precipitate size, shape and distribution and grain boundary morphology.

In a review on grain size dependence of the minimum creep rate, Li [46] summarised the experimental results on the effect of grain size on minimum creep rate. Two types of creep rate-grain size relationships are commonly observed. In one relationship, there is a critical grain size above which the creep rate is independent of the grain size, but below which the creep rate increases with a decrease in grain size. In the other relationship, there is an intermediate grain size at which the creep resistance is optimum. The first relationship is usually observed at higher temperatures ($> 0.5 T_m$), and intermediate stress ranges, while the second relationship was usually seen at intermediate temperature ranges ($0.4-0.5 T_m$) and higher stresses. In both types of creep rate-grain size relations, the increase in creep rates with a decrease in grain size for small grain sizes is related to GBS. For very large grain sizes, an intragranular dislocation climb mechanism dominates during creep deformation for the first relationship, whereas a Hall-Petch grain boundary strengthening effect, associated with dislocation glide mechanism, is believed to play an important role in the second type of relationship.

To predict the critical or optimum grain size where the minimum creep rate has the lowest value, Lasalmonie and Strudel [47] in their review article presented considerations of creep mechanisms and the equations for the description of the U-shape curve in the

minimum creep rate versus grain size relationship. In consideration of grain size, two types of creep mechanisms are considered: firstly by a purely diffusional mechanisms such as Nabarro-Herring and Coble creep, and, secondly, grain boundary sliding. The creep rate is then shown to be a decreasing function of the grain size ($\propto Ad^{-m}$) where $m=2$ for bulk diffusion and $m=3$ for grain boundary in accordance with the constitutive equations for creep listed in Table 2.2 [47].

Table 2.2 Minimum creep rate equations of different creep mechanisms

Mechanisms	Equation for $\dot{\epsilon}$ (sec ⁻¹)	Remarks
Dislocation climb	$\dot{\epsilon} = AD \frac{Gb}{kT} \left(\frac{\sigma}{G}\right)^{4.5}$ (1)	$A \approx 10^8$ G = shear modulus
Diffusional creep		
Nabarro-Herring (bulk)	$\dot{\epsilon} = BD \frac{Gb}{kT} \left(\frac{b}{d}\right)^2 \frac{\sigma}{G}$ (2a)	$B \approx 30$ Threshold stress $\approx 10^{-2} G$
Coble (grain boundaries)	$\dot{\epsilon} = C \left(\frac{D_{GB} Gh}{kT}\right) \left(\frac{b}{d}\right)^3 \frac{\sigma}{G}$ (2b)	$C \approx 70$ Threshold stress $G \frac{b}{d}$
Ashby-Verrall (diffusion accommodated flow)	$\dot{\epsilon} = FD \frac{b}{kT} \left(\frac{b}{d}\right)^2 (\sigma - \sigma_c) \left[1 + \frac{\delta}{d} \left(\frac{D_{GB}}{D}\right)\right]$ (2c)	$F \approx 100$ δ = GB thickness Threshold stress $\sigma_c = \frac{0.7\Gamma}{d}$ Γ = GB free energy
GB sliding		
Controlled by GB diffusion	$\dot{\epsilon} = HD_{GB} \frac{Gb}{kT} \left(\frac{b}{d}\right)^3 \left(\frac{\sigma}{G}\right)^2$ (3a)	$H \approx 8 \times 10^7$
Controlled by lattice diffusion	$\dot{\epsilon} = LD \frac{Gh}{kT} \left(\frac{b}{d}\right)^2 \left(\frac{\sigma}{G}\right)^2$ (3b)	$L \approx 10^7$
Harper-Dorn	$\dot{\epsilon} = MD \frac{Gh \sigma}{kT G}$ (4)	$M \approx 10^{-11}$

Lasalmonie and Strudel offered the following equation for the description of the U-shape relationship between the steady-state creep rate and grain size (d)

$$\dot{\epsilon}_m = 10^7 D \frac{Gb}{kT} \left(\frac{b}{d}\right)^2 \left(\frac{\sigma_a}{G}\right)^2 + 10^6 D \frac{Gb}{kT} \left(\frac{\sigma_c}{G}\right)^{4.5} \quad (2.12)$$

where D is the bulk diffusion coefficient at temperature T , k is Boltzmann's constant, σ_c is

the effective stress experienced by the dislocations, and is equal to the applied stress σ_a minus the internal stress σ_i , G is the shear modulus and b is the Burgers vector. In Eq. (2.12), the first term on the right represents the contribution of grain boundary sliding controlled by lattice diffusion and corresponds to curve 1 in Figure 2.11 [47]. The second term in Eq. (2.12) is the contribution of dislocation climb and corresponds to curve 2 in Fig. 2.11.

Lasalmonie and Strudel [47] have also included the Hall-Petch relationship into Eq. (2.12) to predict the optimum grain size

$$\sigma_e = \sigma_s - \sigma_0 - k_{HP} d^{-1/2} \quad (2.13)$$

where σ_0 is associated with microstructural hardening, k_{HP} is the Hall-Petch constant. Setting $\partial \epsilon_s / \partial d = 0$, the following relationship is obtained for the optimum grain size (d_0)

$$d_0 = 4 \left[\frac{G(b)^{1/2}}{k_{HP}} \right]^{2/3} \left(\frac{\sigma_s}{\sigma_e} \right)^{4/3} \left(\frac{Gb}{\sigma_e} \right). \quad (2.14)$$

In a recent publication on creep behavior of a Ni-15Cr solid solution alloy, a “U” type steady state creep rate dependence on grain size was observed by Kloc, Fiala and Cadek [48]. The creep data were generated at low stress and intermediate temperatures and the intercept grain size ranged between 47 μm and 254 μm . Their experimental data can be most satisfactorily represented by considering a transition in mechanisms with a creep rate proportional to grain size d^3 (Coble diffusional creep) to the mechanism with a creep rate independent of d (Harper-Dorn dislocation creep controlled by dislocation core diffusion). With the “U” type dependence of steady state creep rate on grain size, this indicates that

creep is not controlled by a single mechanism over the full range of possible grain sizes.

Mannan and Rodriguez [49] studied the influence of grain size on the creep rate in AISI type 316 stainless steel at 873 and 973 K over a wide range of applied stresses. Grain boundaries contributed to strengthening at high stresses ($180\text{-}260 \text{ MN m}^{-2}$) at 873 K, as shown in Figure 2.12. The importance of loading strain in determining the creep rate was indicated. The creep rate was generally constant at 973 K (shown in Figure 2.13) but increased for small grain sizes and for lower stresses. This was attributed to an increased contribution of grain boundary sliding in fine grain size materials.

Figure 2.14 [50] gives an example for a series of alloys containing various γ' volume fractions, f_v . At small grain sizes, the steady state creep rate is proportional to d^{-2} which indicates that the deformation rate is controlled by lattice diffusion [50]. Above $0.5 T_m$, the secondary creep rate in most superalloys is generally a decreasing function of d for $d < 200 \mu\text{m}$. The decrease of creep resistance of small grain materials is usually attributed to more intense GB sliding in these materials. Figure 2.15 [51] shows a typical minimum creep rate at a critical grain size of Inconel alloy X-750 at 700°C using four grain sizes ranging from 9 to $200 \mu\text{m}$ over a range of stresses varying between 207 and 414 N/mm^2 .

White [52] reported reaching the lowest minimum creep rate at a grain size of about $140 \mu\text{m}$ in Nimonic 80A at 750°C . However, Brownsword and Hoar [53] observed that the secondary creep rate in Nimonic 80A tested at 600°C decreased with an increase in grain

size (as shown in Fig. 2.16). The main feature of Fig. 2.16 is that the minimum creep rate is grain-size dependent, at a small grain size value, for the low temperature ($0.5T_m$) and high stress conditions employed. Under these conditions a significant contribution from Coble creep to the total creep deformation would be unlikely and it is apparent that some grain boundary process other than diffusion creep played an important role during creep deformation [53].

In a study on the effect of grain size (10-100 μm) on minimum creep rate of Inconel 718, Han, Chaturvedi and Cahoon [54] have suggested that the creep rate for power law creep varies as $d^{0.42}$, whereas, the creep rate for diffusional creep varies as $d^{-0.19}$ at temperatures ranging between 467 and 495°C. In the region between those in which diffusional creep and power law creep dominate, it is suggested that both mechanisms contribute to the creep rate, which gives rise to an optimum grain size exhibiting a minimum creep rate.

Gibbons and Hopkins [55] investigated the influence of grain size and γ' phase on the creep properties of Ni-20Cr alloys free of carbides. Figure 2.17, which illustrates the effect of grain size on the minimum creep rate of the alloys hardened with (Ti+Al), reveals a number of features. In the solid-solution alloy and in that containing 5 vol.-% fraction of precipitate, there was a fairly small effect of increasing the grain size on the minimum creep rate. On the other hand, in the alloy with 19 vol.-% fraction of precipitate, an increase in grain size had a large proportional effect in reducing the minimum creep but there was little

further effect at a larger volume fraction of 31 vol.-%.

From the above review, it has been shown that the grain size effect on the minimum creep rate depends on the temperature and stress at which different creep mechanisms apply. At high stress levels, the grain size effect is small because deformation within the grains dominates. At low stress level, grain size effect is also small since the Harper-Dorn creep mechanism dominates. The grain size effect also depends on the presence of grain boundary precipitates, their amount, and their distribution. When the grain size effect is investigated, all of these factors should be taken into consideration.

Tertiary creep is often considered to involve the most severe damage accumulation processes. Grain boundary cavitation, wedge-cracking or oxidation cracking would most probably be caused or enhanced by GBS and vacancy diffusion which may also be a process related to grain boundaries.

Koul and Wallace [56] have shown that the rupture life of a wrought nickel base superalloy is primarily governed by grain size and grain boundary carbide morphology. Generally, a large grain size improves creep rupture properties. However, large grains especially in relation to the section size, can cause grain boundary sliding and lead to premature failure. Richards [57] found that rupture life and creep resistance increased as the component thickness-to-grain-size ratio increased. With a wrought superalloy, provided the ratio was kept constant, life and creep resistance increased with grain size. Cast superalloys

show the same dependence of life and creep resistance on thickness-to-grain-size ratio. This effect can be very obvious when large grains occur in thin section. Thin sections usually exhibit reduced creep rupture resistance; the thinner the section, the lower the rupture strength compared to thick sections. For a given specimen size, the rupture life and creep resistance should increase with an increase in grain size as long as the grain size is below a critical size, but will decrease if the grain size is above this critical value. In their study on the microstructural dependence of creep strength in Inconel 700, Koul and Wallace [56] showed that rupture life decreases with increasing grain size (grain size: 200-500 μm) in all their experiments.

The grain size effect is associated with grain boundary carbide distribution. In a study on the effect of grain size and carbides on the creep resistance and rupture properties of a conventionally cast nickel-base superalloy, Baldan [58] showed that the optimum values of creep strength and rupture properties are obtained at a specific grain size (Fig. 2.18). This optimum grain size for their alloy was around 545 μm . For this critical grain size the grain boundary carbide particle density is the highest, whereas above and below the this critical grain size the carbide density decreases (Fig. 2.19).

2.1.4.2 Effect of Carbides on Creep in Ni-Base Superalloys

Early investigators noted detrimental effects on ductility from certain grain boundary carbide morphologies and took the logical step of reducing carbon to very low levels.

However, this direction was found to sharply reduce the creep life and creep ductility when the carbon content was less than 0.03% C in Nimonic 80A [59] and Udimet 500 [60]. Betteridge and Franklin [61] were the first to identify the critical role of $M_{23}C_6$ carbides in Ni-base alloy properties, finding that discrete globular $M_{23}C_6$ carbides at grain boundaries optimize the creep-rupture life.

The most popular method of strengthening the grain boundaries in Ni-base superalloys has been through the precipitation of carbides which decrease the creep rate by suppressing grain boundary sliding, as shown in Figure 2.20 [23].

Short term stress rupture tests generally reveal a reduction in rupture life if continuous $M_{23}C_6$ networks are present [62]. It was also reported that impact resistance can be severely degraded if the carbides precipitate as a continuous $M_{23}C_6$ grain boundary film [63]. The presence of a continuous carbide film provides an easy fracture path. Although the grain boundary carbides tend to promote creep resistance by inhibiting GBS, the deformation that must be transferred from grain to grain is eventually accommodated either by cracking of these carbides or by interfacial decohesion leading to intergranular fracture. In other word, grain boundary sliding restricted by grain boundary carbides will lead to excessive stress build-up [64].

The deleterious effects of carbide network were also related to other microstructure degradations, such as denuded regions of γ' or Cr. It has also been suggested that the $M_{23}C_6$

and γ' form an interconnected grain boundary network which is very susceptible to environmental attack and which reduces ductility [65]. Chromium depletion near grain boundaries was observed to be caused by the precipitation of chromium grain boundary carbides [66]. Grain boundary Ti/Nb carbides were also observed to reduce the creep resistance of X-750 alloy [67].

However, the effect of carbides on long term creep properties is different from short term creep properties. Investigations on new and service exposed IN738LC blades indicate that continuous networks have no detrimental effect on rupture life during long-term (10,000 hour) creep tests and they reduce the minimum creep rate by suppressing grain boundary sliding [36].

The rupture life and especially the ductility have been found to improve in the presence of grain boundary serration [68]. The increase in rupture ductility may be a direct consequence of the difficulties associated with cavity nucleation and linkage along a serrated grain boundary [69].

2.1.5 Intergranular Creep Fracture

While a large grain size is generally beneficial to creep resistance, it is usually deleterious to the creep fracture properties in terms of the creep ductility. In superalloys, the overall behavior during creep fracture has been summarised by Wu and Koul [3]. There are three fracture criteria which can be applied to creep fracture according to them: (i). If intragranular dislocation accumulation alone leads to the point of structural instability, the fracture event may be linked to the exhaustion of tensile ductility, i.e., $\epsilon_{\text{creep}} = \epsilon_f$, where ϵ_f is the fracture strain; (ii). If extensive intergranular cavitation occurs before individual grains are severely crept, fracture is mainly caused by intergranular separation. At fracture, a critical cavity density may be reached such that $\sigma/(1 - \omega_{\text{creep}}) = \sigma_u$, where ω_{creep} is the area fraction damage, σ_u is the material's fracture strength; (iii). If fracture occurs due to a dominant crack propagating, coupled with environmental attack, cavity growth and microcrack linkage, the fracture criterion $K = K_c$ (fracture toughness) may apply.

2.1.5.1 Types of Intergranular Cracks

In wrought engineering materials under small loads at high temperatures, (typically under 10^{-3} to 10^{-4} G at 0.4 to $0.6 T_m^*$), creep and ultimately rupture occur by the nucleation, growth and inter-linkage of creep cavities along the grain boundaries. Generally, cracking

* where G and T_m refer to the shear modulus and the melting point.

at grain boundaries is related to either cracking at grain-boundary triple points or to the formation of cavities (or voids) on grain boundaries which lie approximately normal to the applied stress. These two types of defects are often referred to [8] as w-type cracks and r-type voids (r) respectively. It is the development of the latter type of defects which leads to premature creep failure with limited ductility, which is termed creep cavitation [64]. Figure 2.21 illustrates the relative tendencies for the formation of wedge (w) and cavity voids in a stainless steel [70] as a function of grain size. Cavitation forms preferentially at lower stress levels; whereas, triple-point cracking is the preferred mode at higher stresses. It is also evident that cavities form preferentially when the grain size is small.

2.1.5.2 Grain Size Effect

Grain size effects on creep fracture [71] (including the slow strain rate high-temperature tensile testing employed to save time in studies of creep-type fracture [71-75]) have been studied in stainless steels [71-73], copper [74] and a copper alloy [75]. With a decrease in grain size there is usually a transition from wedge cracks to voids. In large grain size material, GBS causes wedge crack formation at grain boundary triple points. However, triple points are usually considered to inhibit the propagation of wedge cracks [73].

In a typical study on creep failure in type 316 austenitic steel [71], Morris found that

increasing the grain size, at a given stress, leads to a maximum in rupture ductility at a grain size of approximately 25 μm . At small grain sizes there is a low density of small cracks, which are elongated in the applied stress direction. He concluded that failure was consistent with the operation of the so-called intergranular void sheet mechanism. In this mechanism, failure occurs by the formation of intense shear bands between neighboring cracks or holes, with intragranular failure occurring within these shear bands. In the case of fine grain sizes and at high temperatures, failure is controlled by the volume fraction of cavities so that decreasing the grain size decreases ductility. With large grain sizes, there is a greater density of larger cracks and failure occurs after a certain amount of crack growth. It has been suggested that failure depends on the stress concentration developed at the tips of the largest cracks, i.e., by a Griffith-Orowan mechanism. This mechanism indicates that the onset of final rupture is controlled by critical crack length criterion. Increasing the grain size increases the crack length and decreases ductility.

2.1.5.3 Grain Boundary Precipitate Effect

The influence of grain boundary δ phase precipitates on creep fracture was studied in Inconel 718 by Chen and Chaturvedi [76]. They found that both the rupture time and total creep strain decreased with an increase in δ phase when its area percentage in grain boundaries was below approximately 45%. However, when this percentage was greater than 45%, both the rupture time and creep strain increased with an increase in δ phase to a

value much higher than that observed in the material with no such precipitates at the grain boundaries. SEM observations of the crept samples and their fracture surfaces have shown that the presence of delta precipitates at grain boundaries results in the formation of creep voids in all specimens. They considered that the effect of creep voids on the final fracture of the material is dependent upon the amount of δ phase. For lower amount of δ phase, creep voids were observed to be isolated, and the fracture was considered to occur due to the propagation of wedge cracks initiated at triple points at the grain boundaries. In the presence of a higher amount of δ phase, the probability of wedge crack formation should be reduced. The fracture will then be controlled by the growth rate and propagation of voids at grain boundaries normal to stress axis. This is a much slower process than the formation of wedge cracks at triple points. Their test results provide good evidence that grain boundary precipitates affect the creep behavior. Our understanding of the role of grain boundary precipitates on creep fracture still leaves much to be explored.

2.1.5.4 Environmental Effects

Environment attack is an important type of damage since it often contributes to further reduce rupture life and rupture strain. This has been summarized by Ashby and Dyson [77].

The effect of environment on the creep/rupture behavior of Ni-base superalloys

appears complicated. For example, The rupture life in both new and service exposed IN-738LC [36] blades appear to be governed by stress-assisted environmental cracking rather than by any deformation mechanisms *'per se'*. Fracture in both materials occurs through the link-up of environmentally induced surface cracks with creep-induced internal cracks. Final fracture occurs by transgranular shear. On the other hand, for some single crystal superalloys, longer rupture lives and lower creep minimum rates were reported in air than in vacuum [78, 79]. In the air environment, oxide forms on the surface of superalloys. The thick oxide cracks during the extension of the specimen, and these cracks become blunted and grow slowly into the alloying element denuded soft surface layer. The surface oxide played a hardening role in the material deformation. This is considered to be the beneficial effect of environment associated with the matrix material behavior, i.e., in the absence of grain boundaries.

In polycrystalline materials, a longer rupture life and lower minimum creep rate are generally reported in large grain size material compared to small grain size material in air [78-81]. The reverse behavior has also been reported in some cases [80, 82], in particular, for coarse-grained specimens [81]. In vacuum, a longer rupture life and lower minimum creep rate has been reported in small grain size material [78].

Two types of damage are usually caused by environmental attack, namely, internal oxidation and failure of the external oxide. In Ni-base superalloys, damage by failure of the external oxide is often the cause of environmental attack which may dominate the rupture

life [36, 78]. Ashby and Dyson [77] has provided a simple model to account for the fracture of the oxide scale. In this model, they consider a brittle, external oxide, of thickness h , on the surface of a creeping metal. The fracture strain (or spalling strain) of the oxide is ε^* . Creep of the underlying metal stretches the film until it fractures or spalls. This increases the oxidation rate locally until the crack or gap heals; the time constant for healing is t^* . The time taken for the new oxide film to crack is:

$$t^* = \frac{\varepsilon^*}{\dot{\varepsilon}} \quad (2.15)$$

During this time, the film has grown (assuming parabolic kinetics) to a thickness:

$$X^* = \sqrt{2K_p t^*} \quad (2.16)$$

where K_p is the parabolic rate constant (units: m^2/s). If the oxide spalls when it fractures, the rate of loss of thickness of the sample, dX/dt , is:

$$\frac{dX}{dt} = \frac{X^*}{t^*} = \left(\frac{2K_p \varepsilon^*}{\dot{\varepsilon}} \right)^{\frac{1}{2}} \quad (2.17)$$

Wu and Koul [3] considered the case of surface cracks formed at oxides propagating towards the material interior along grain boundaries, as is often observed in cast Ni-base superalloys [36, 78]. They assumed that the growth of the oxidation damage is assisted by GBS, thus, cracks propagate along the grain boundaries by repeated breaking of previously formed oxide layers. Then, similar to the treatment of surface film rupture given above, the oxide crack propagation rate is

$$\left. \frac{dX}{dt} \right|_{\text{oxidation}} = \left(\frac{2D\varepsilon}{\varepsilon^*} \right)^{\frac{1}{2}} \quad (2.18)$$

where X is the oxide crack length, D is a diffusion constant, and ε^* is the fracture strain of the oxide. This model is also consistent with data on Udimet 700 [78] as shown in Fig. 2.22 [3].

2.2 Creep Crack Growth in Ni-base Superalloys

Industrial components often have non-uniform stress distribution which may result in the formation of discrete cracks, especially from some pre-existing defects. Growth of such discrete cracks is considered important in thick-sectioned components (such as those found in electricity-generating and petrochemical plants) where the existing stresses are low and the expected design lives are long. This kind of single crack growth under creep conditions is known as creep crack growth (CCG) process. Although creep crack growth is a type of creep damage, it is often treated as an independent subject from creep.

In the past two decades, the creep crack growth (CCG) behaviors of a number of materials, such as low alloy steels [83-86], stainless steels [87-89] and superalloys [90-95] have been widely studied. In early studies on CCG, a large numbers of studies attempted to determine which fracture mechanics parameter best correlates the crack growth rates under creep loading conditions. Although the stress intensity factor K is suitable for describing slow crack growth behavior in many structural materials under fatigue (for example, see the literature review on the fatigue of superalloys [96]), several fracture parameters such as the stress intensity factor K , the net section stress σ_{net} , the C^* integral and the crack-tip-opening displacement (CTOD) δ have been proposed for describing the CCG behavior. In this review, the usefulness of these parameters is briefly discussed and the experimental and theoretical basis for the applicability of K are reviewed. Another aspect of research on CCG is the crack initiation stage and the propagation behavior which are controlled by the applied

stress conditions, the metallurgical variables and the environmental effects. The present section summarizes the important CCG experimental aspects such as the initial stage of CCG, the microstructural influence on CCGR, the fracture mode of CCG, environment effects and long term CCG as revealed from the literature. The modeling aspects of CCG are also classified and summarized.

It is important to note that the CCG specimens employed are often precracked in fatigue. These specimens are different from the notch rupture tests in which the specimens are notched by mechanical methods. The latter tests were often used in earlier studies on superalloys to display the effects of composition, microstructure, etc., on the notch sensitivity, but these results differ from those obtained using the fracture mechanics approach.

2.2.1 Fracture Parameters to Describe Creep Crack Behavior

Several relevant parameters such as the stress intensity factor K [97], the path-independent C^* integral, originally proposed by Landes and Begley [98], the net section stress σ_{net} [99, 100] and the crack-tip opening displacement (CTOD) δ [101, 102] has been employed for the phenomenological characterization of creep crack growth. One of the aims of many CCG studies is to determine whether or not creep fracture can be analyzed by conventional fracture mechanics techniques or whether other parameters should be employed to better describe the CCG test results.

In an “ideal” brittle material, the stress intensity factor K can uniquely define the stress field ahead of a crack tip. The K can then be clearly considered as the driving force for crack growth.

If the material ahead of the crack is under steady state creep, C^* can be employed to describe its stress state. There are two properties of C^* [103], the first being its energy rate interpretation, whereby, C^* is the energy rate or power difference between two identically loaded bodies having incrementally differing crack lengths. The other property of C^* is its ability to uniquely characterize the stress distribution at the crack tip. For a power-law creeping material, the crack tip stress is given by Hutchinson [104, 105] and Rice and

Rosengren [106]: $\sigma_{ij} = \left[\frac{C^*}{AI_n r} \right]^{\frac{1}{1+n}} \tilde{\sigma}_{ij}(\theta, n)$, where $\tilde{\sigma}_{ij}(\theta, n)$ is an angular function and I_n is

a nondimensional constant with a value ranging between 3.8 and 6.3 for a range of n values.

The C^* represents the amplitude of the crack-tip stress fields and is defined by analogy to

the J-integral: $C^* = \int_{\Gamma} W^* - T_i \frac{\partial u_i}{\partial x} ds$; where Γ is the line contour taken from the lower crack

surface to upper crack surface, W^* is the strain energy rate (or power) density associated

with point stress, σ_{ij} , and strain rate, $\dot{\epsilon}_{ij}$, T_i is the traction vector defined by the outward

normal, n_j , along Γ and $T_i = \sigma_{ij} n_j$. The displacement vector is denoted by u_i .

Riedel and Rice [107] first theoretically analyzed the applicability of the fracture

parameters K and C^* . In the creep brittle case, the elastic strains dominate almost everywhere except in a small "creep zone" around the crack tip. If the crack grows while this creep zone is still small compared with the crack length and the specimen size, the creep crack growth rate can be described by the stress intensity factor K . In the creep ductile case, the calculated creep zone becomes larger than the specimen size, the stresses become time-independent and the elastic strain rates can be neglected. In this case, the creep crack growth rate can be correlated with the C^* integral. Five criteria for the creep ductile or the creep brittle cases have been proposed, either experimentally or theoretically. For example, the characteristic time t_1 for the transition is defined as

$$t_1 = \frac{K_I^2 (1 - \nu^2) / E}{(n + 1) C^*} \quad (2.19)$$

for plane strain, where E is Young's modulus, and ν is Poisson's ratio in Eq. (2.19). For plane stress, the term $(1 - \nu^2)$ is replaced by 1. Small-scale yielding prevails if the time for the crack tip region to approach the steady-state creep stage is sufficiently small compared with the characteristic time t_1 . The characteristic time t_1 can also be simply compared with the test time or the hold-time (in creep-fatigue interaction tests) to decide whether small scale yielding or large scale yielding occurs.

In creep or under a sustained load, crack tip blunting may occur (in the cases of using δ). Large scale creep deformation may proceed before the crack can advance by a noticeable increment (in the case of C^*). Even, creep might occur over the whole specimen cross-section and the net section stress can be applied to predict the rupture life.

Floreen [92] tested the CCG behavior of a series of typical superalloys in the 500 to 704°C temperature range. The curves of the crack growth rate vs stress intensity factor in various superalloys are shown in Figure 2.23 [92]. As can be seen, the crack growth rates are proportional to a power of the stress intensity factor. Later, Floreen [108] in a study on Alloy 718 over temperature range of 595 to 704°C, used center-notched specimens and specimen thicknesses of 0.5 to 3.1 mm. He concluded that thickness had no apparent effect on the CCG characteristics. Slow crack growth during creep loading was intergranular in character, and the fractures were flat in appearance with no shear lips present. No changes in specimen thickness at the fracture surface could be detected. These results suggest that with nickel-base superalloys at temperatures of the order of one-half their melting point, fracture mechanics can be used to study creep crack growth.

It has been shown that the creep crack growth behavior of superalloys at temperatures between 538-760°C [90-94] can be well described in terms of K , while that of alloy steels and stainless steels [83-89] can be best represented by the C^* integral. Other parameters were also found to be useful in some cases. Jones and Tetelman [109] in a study on the elevated temperature static load crack extension behavior of type 304 stainless steel showed that the stress intensity correlation is strongly dependent on specimen geometry; whereas, the net section stress correlation appears to be generally valid. Wells and McBride [110] were the first to propose that creep crack growth is controlled by the local displacement at the crack tip (δ). Several investigators [101, 111] have correlated creep crack growth with δ using indirect techniques.

The choice of parameters becomes crucial only when trying to predict service behavior or for comparison with other experimental results. If the CCG tests are designed to compare different materials, heat treatments, etc., the choice of parameters is not important as long as identical specimens are employed. This is because K , C^* , and the net section stress (σ_{net}) are proportional to each other for a certain geometry and crack length.

The K and the C^* integral are the most commonly employed fracture parameters in CCGR because of their convenience and effectiveness. In superalloys, possessing high toughness and ductility at high temperatures, it has been demonstrated experimentally that K adequately correlates the CCG behavior. The K has also been employed to correlate CCGR data in aluminum alloys over a temperature range of 175-316°C [112] and titanium aluminides over a temperature range of 600-800°C [113]. In stainless steels and heat-resistant alloys that are not age hardened, C^* appears to be a more appropriate parameter.

2.2.2 The Creep Crack Growth Process

Under creep conditions, the crack does not start to propagate immediately upon loading. There is an apparent incubation period before the crack starts to grow. The crack then grows at an accelerating rate until a fast, overload fracture takes place. The general type of curve for crack growth rate vs the stress intensity factor is shown in Figure 2.23 [92]. At K values above the apparent threshold the creep crack growth rates da/dt often can be expressed in a power law form,

$$\frac{da}{dt} = AK^m \quad (2.20)$$

where A and m are constants in this equation. Values for m vary from 2 to 8 but are not the same as the power law creep stress exponents for a given material. The CCG behavior is influenced by test procedures and temperature, microstructural variables and environmental effects. Creep fracture generally occurs by an intergranular crack growth process involving the formation of microcracks at grain boundaries ahead of the main crack. The CCG behavior and the associated fracture mode at the crack tip are discussed below.

2.2.2.1 Initial Stage of CCG

The initial stage of CCG is influenced by the loading procedure, the precracking method and the specimen geometry. Specimens employed for CCG tests are usually fatigue precracked CT specimens [92-94, 112], machine-saw-cut single edge notched (SEN) specimens [87] or electrical discharge notched CT specimens [114]. Most investigators use fatigue precracked CT specimens at room temperature for their CCG investigation. A load shedding procedure is widely employed in fatigue precracking to get a sharp crack, as well as to obtain a final ΔK as low as possible to facilitate creep crack initiation. Then the specimens are creep tested under sustained load at a fixed test temperature. The load at which the CCG test is started is higher than the maximum load employed during the last stage of fatigue precracking. The load might be increased if creep crack growth does not occur in a certain period of time, for example, 24 hours

[112] or 100 hours [92, 94].

In the study of CCG, the initiation time and threshold stress intensity factor are of interest. Many investigators have shown that there is a period during which no detectable surface crack growth occurs, with this period increasing with decreasing initial stress intensity. The incubation time is defined as the period necessary to detect crack initiation and growth over a certain distance by using the direct current potential drop technique [87, 94]. This critical distance is chosen in relation to the accuracy of the potential drop technique. This distance is often practically equal to approximately the size of a single grain. Unlike the fatigue crack growth threshold, the threshold in creep crack growth has less meaning since the threshold related stage I is only a transient regime, which is strongly dependent on the experimental procedure employed. As demonstrated by Diboine and Pineau [94], the threshold stress intensity factor increases with an increase in the initial load level. The threshold stress for multiple loads is higher than that for a single load. The threshold stress intensity is often reported to be of the order of a CCG rate of 10^{-2} mm/hr. Sadananda and Shahinian [93], in a study of creep crack growth in alloy 718, examined the fracture surface of a specimen alternately fatigue cracked and creep loaded for different intervals of time. Although the crack length measurements based on the specimen side surfaces showed no crack growth at 1 and 3 h intervals and very small growth at a 15 h interval, definite crack growth for all three intervals was observed inside the specimen. Based on these observations, they claimed the non-existence of any incubation period during creep crack growth.

From a practical point of view, how the crack grows under creep conditions is also important. The nature of cracks has an effect on the initiation of the CCG process. Bain and Pelloux [115] in their study on CCG in PM/HIP René 95 compared the notched stress rupture (NSR) and single edge notched (SEN) specimens at different stress concentration factors (k_t) of 3.18 and 10, respectively. They found that the crack initiation time was a strong function of notch root radius and the creep crack initiation times increased with notch root radius. No incubation time was observed for creep crack growth from fatigue precracked specimens in air for their test conditions. The test temperatures also had a strong effect on the initiation of CCG. At relatively low temperatures, the initial stress intensity required is usually so high that it approaches the K_{IC} value of the material. Consequently the CCG data is difficult to obtain. Such a temperature effect has been noticed in aluminum aluminide by Khobaib [110] with very high initial stress intensity factor at low temperatures. It is noteworthy that both the cavitation process and the environment-crack tip interactions during CCG are dependent on test temperatures and dependent on time.

Specimen thickness also affects the initiation period of CCG because the thicker the specimens, the more closely the plane strain conditions are approximated. As well, side grooves in CT specimens can ensure that the plane strain conditions are maintained [116]. In many cases, side grooves must be used to prevent severe crack tip curvature and shear lips at the lateral edges.

2.2.2.2 The Effect of Temperature on CCGR

Higher temperatures usually lead to higher creep crack growth rates. Sadananda and Shahinian [93] considered that creep crack growth occurs as a result of two competing processes, (i) diffusion of point defects which contributes to crack growth, and (ii) a power-law creep deformation process which causes retardation of crack growth. This can explain their research of the temperature effect on creep crack growth in Inconel 718. Figure 2.24 [93] shows their results as well as those obtained by Floreen [92]. The results show that for a given stress intensity value the crack growth rate increases significantly with an increase in temperature from 538 to 649°C but it either decreases or increases only slightly with a further increase in temperature to 760°C.

2.2.2.3 The Effect of Side-Grooves on CCGR

Side grooves in CT specimens are used to ensure plane strain conditions for the cracking and to reduce or avoid crack tip tunneling. Figure 2.25 shows that the crack growth rates in specimens without side grooves are 10 times lower than those measured in specimens with side grooves in 2219-T851 aluminum alloy at 175°C [116]. Side groove effect was investigated with 40 pct, 20 pct or 0 pct width side grooves. The crack growth rates in specimens with 40 pct side grooves were slightly higher than in specimens with 20 pct side grooves at a given stress intensity factor. Severe crack bowing occurred and shear lips were observed in the CT specimen without side grooves. Side grooves have also been

found to be especially useful to in reducing crack tunneling during CCG tests on Udimet 700 [117].

2.2.2.4 The Effect of Microstructure on the CCGR

Unlike the complex dependence of minimum creep rate on grain sizes, creep crack growth rate dependence on grain sizes appears relatively simple in superalloys [90, 118]. Figure 2.26 and 2.27 present the effect of grain size on CCGR in IN-792 and IN-718 superalloys. The CCGR is roughly inversely proportional to grain sizes. This indicates that the micromechanisms of CCG in the superalloys reported are generally cavitation coupled with environmental effect ahead of the crack tip. Larson and Floreen [90], in a study of metallurgical factors affecting the crack growth resistance of a superalloy IN-792, have pointed out that the primary factors influencing the crack growth behaviour were the grain size and grain boundary morphology. Increasing the grain size or having serrated grain boundaries markedly improved the "creep toughness". By slow cooling through the gamma prime solvus, a serrated grain boundary structure was developed, which also improved the cracking resistance as shown in Figure 2.28 [90]. However, the grain size effect in the absence of grain boundary carbides in superalloys and the effect of grain boundary carbides have generally not been well explored.

In contrast, Zhu et al. [114, 119] in a study on creep crack growth behaviour of Fe-15Cr-25Ni austenitic steels concluded that the creep crack growth rate increased with

increasing grain size. Grain boundary triple points were identified as the main barriers to crack propagation and, with an increase in grain size, the number of triple points decreased and therefore the crack growth rates increased. Again, the grain boundary related microstructure strongly influences the CCGR.

It is also known that overaging tends to improve the CCG characteristics of many alloys, and typical results are shown in Figure 2.29 [92] for Inconel 718 at 649°C. The alloy in overaged condition shows a much higher threshold stress intensity and lower growth rates. The explanation is probably that overaging tends to change the slip mode from dislocation shearing to looping (planar to wavy) [120]. Wavy slip allow the back stress to reduce more quickly. As a result, the effective stress at boundaries and near crack tip relaxes more quickly. The dislocation looping mode promotes slip homogeneity, the maximum stresses associated with slip bands are reduced at grain boundaries, and cracking should be less likely.

The beneficial effect of grain boundary carbides on the creep crack growth rates has also been reported for superalloys [90, 118] and steels [121, 122].

2.2.2.5 The Effect of Environment on CCGR

The environment has a strong effect on CCG behavior. Environmental corrosive

process at the crack tip is one of the reported micromechanisms responsible for the obtained CCGR. The effects of environment on CCG in Inconel 718 have been investigated by Floreen and Kane as shown in Figure 2.30 [123]. Although cavity formation and transgranular cracking were observed for both the air and helium environments, the crack growth rate was almost 100 times higher in air than it was in helium. Bain and Pelloux [101, 124] observed that the creep crack growth rates were strongly environment sensitive in PM/HIP René 95. It was reported that the CCGR in air were up to 1000 times faster in air than in argon for a given value of K . The effect of environment on the CCG varies with the type of alloys. It has been reported [95, 125] that Udimet 700 and austenitic stainless steels (type 304 and 316) were less sensitive environmentally, while Inconel 718 and Inconel X-750 were significantly more sensitive in air, with the crack growth rates one or two orders of magnitude greater than those obtained in vacuum.

Pelloux and coworkers [101, 124-126] showed that, for tests carried out in air, the environmental effects seem to be principally due to oxidation at the crack tip. Oxidation plays a prominent role in creep crack growth. Superalloys, even though they have good creep rupture strengths, may have very poor resistance to creep crack growth. This is because superalloys are designed to develop protective surface oxide layers (usually Al_2O_3 and Cr_2O_3) in oxidizing environments. The depth of oxygen penetration in a high temperature tensile test is usually small when compared to the dimension of the tensile specimen, but it is a significant portion of the plastic zone size near the crack tip of a fracture mechanics specimen. At a crack tip under stress, moreover, the layer breaks continuously

and oxygen atoms can penetrate into the material, preferably along grain boundaries. It is speculated that the diffusion of oxygen into the base metal along grain boundaries leads to the formation of complex oxides which embrittle the grain boundaries [127]. These fine oxide particles may act as the nucleation sites for creep cavities, thus increasing the cracking rate. Gas bubbles may also be created along grain boundaries in nickel-base alloys containing carbon, due to the chemical reaction by which oxygen combines with carbon to form carbon dioxide [128]. It has been shown that oxygen diffusing along the grain boundaries in nickel-base alloys causes a decrease of ductility and of tensile strength at test temperatures between 600°C and 800°C [129-131]. Oxidation effects on crack growth rates were also noted for single crystals of nickel-base superalloys [132, 133]. These results of environmental effects on CCG behavior indicate that oxidation attack is an very important, or even controlling, factor for creep crack growth. Any approach to CCG should take into account environmental effects.

Although environmental effects should be taken into consideration when trying to understand CCG tests, there is no simple rule that can be employed. An air environment does not always accelerate creep crack growth compared to vacuum. In a study on crack growth behavior of some cast nickel-base superalloys (IN-738, In-792 and René 80), Shahinian and Sadananda [134] showed that these three cast superalloys had higher apparent resistance to creep crack growth in air than in vacuum (shown in Fig. 2.31 [134]). They explained this as being probably due to oxidation blunting the crack tip and further denuding

the crack tip region of alloying elements, making it more ductile and susceptible to blunting and thereby retarding crack growth compared with that in vacuum. The environmental effect is also associated with another micromechanism, e.g. cavitation. Although a difference in CCGRs between air and vacuum at 650°C was observed in Astroloy [135], the contribution of oxidation to creep crack growth was small compared to the creep cavitation damage at 760°C. This result is in agreement with the data obtained by Sadananda [117] on Udimet 700, which is an alloy very similar to Astroloy.

Some interesting aspects were found in a study on the CCG behavior of titanium aluminides (Ti-24Al-11Nb) [113]. At 650°C, the CCG behavior became very sensitive to the K value and therefore it was very difficult to generate data over a wide range of CCGRs. The failure mode in air was observed to be transgranular at all temperatures except at 800°C, where the fracture appeared to change to partially intergranular. However, the failure mode of specimens tested in vacuum appeared intergranular at all temperatures. The CCGRs and fracture behaviors at different temperatures and atmospheres were again related to environmental effects.

2.2.2.6 Long term CCG

Long term creep crack growth rate data is of interest for practical engineering applications. Crack growth rates of 10^{-9} m/s (3.6×10^{-3} mm/hr) or less are characteristic of the long term CCG growth data which are needed for practical applications. However, they

require tests lasting 1000 hours or more in duration. Of no surprise, there is little data reported in this regime for superalloys, although such data has been obtained in type 316 stainless steel [136, 137].

2.2.2.7 The Fracture Mode During CCG

The use of fractography and metallography of cross-sections are the two methods usually employed for studying the fracture modes associated with CCG. The macroscopic features of fractured surfaces include (1) the surface flatness, (2) the extent of crack tip curvature and (3) surface oxidation color. It is interesting to note that extensive crack tip branching with no crack tip tunneling was found during CCG tests on PM/HIP René 95 [115] in air. On the other hand, no significant crack tip branching and a slight crack tip tunneling were observed in tests in high purity argon. This further indicated strong environmental effects on the CCG behavior in air.

The microscopic features often found on the fractured surfaces include (1) the fracture path, (2) the presence of cavities and (3) the presence of crack tip branching. The fracture mode of CCG is primarily intergranular with a small fraction of transgranular cracking in superalloys [92] and stainless steels [87, 102]. The fraction of transgranular cracking decreases with increasing temperature [93]. Sometimes, the fracture surface details are not clear due to severe oxidation. This makes it difficult to observe the cavities on the fractured surface, although cavitation is observed in many cases. Figure 2.32 [138] shows

some cavities on the fracture surface of a 0.5Cr-0.5Mo-0.25V steel. From a microscopic point of view, most CCG results reported in wrought alloys involve ductile fracture with cavity formation. The shape of the microvoids is usually spherical, at least in two dimensions.

Cavity nucleation and growth is one mechanism by which CCG operates in many cases. The distribution of cavities ahead of the creep crack, which can also be observed on metallographic cross sections, as shown in reference [92], provides important information in understanding the micromechanism of CCG. Some materials nucleate microcracks ahead of the main crack, with the subsequent joining of the more favorably oriented cracks with the main crack, while other materials do not have observable microcrack nucleation ahead of the main crack. For example, Udimet 700 follows the first category, while Inconel 718 and Inconel X-750 belong to the second category, as discussed by Sadananda and Shahinian [95]. Sections of creep fractured specimens can also be used for displaying surface layer denuded by the environment [134].

In a study on long-term creep crack growth behavior (>10000 h) of 316 stainless steel, Tabuchi, Kubo and Yagi [136] observed a relationship between the creep crack growth rates and the fracture mode. The crack growth rates obtained using CT specimens were faster at 750°C than those in short-term tests at 650°C. The creep crack which gave wedge-type or cavity-type intergranular fracture showed higher growth rates than that which produced transgranular fracture. The difference in the crack growth rates between the

wedge-type intergranular and transgranular fracture modes was attributed to the effect of creep ductility. The crack growth with cavity-type fracture was observed for higher temperatures and longer term creep tests.

2.2.3 Creep Crack Growth Rate Models

Understanding the creep crack growth behavior and establishing mathematical relationships between microstructure and the CCG properties is an active area of research in nickel-base superalloys. There are a considerable number of models available in the literature for modeling the creep crack growth behavior. The following summarizes some important aspects of two distinct approaches and in developing models. Two types of approaches, one at the macroscopic viewpoint, and the other using the concept of cavity nucleation and growth of cavities, both of which use the stress intensity factor K in their formulation, will be presented because the CCGR in nickel-base superalloys are to be correlated well with the stress intensity factor K . CCG has been analyzed assuming that the crack extension is controlled by diffusion, by deformation or by a combination of these two processes. These will be discussed in turn. Wu and Koul [139] developed an intergranular creep crack growth model which also provides a physical description of the region ahead of the crack tip. Their model will also be presented. The effect of environment on the creep crack growth behavior and the model related to this effect will be discussed subsequently.

2.2.3.1 Stress Intensity Factor (K) Based Models

Purushothaman and Tien [140] considered K as a parameter for correlating the CCGRs and proposed a continuous rupture model. In their model, the Orowan-Irwin expression is used to estimate the stress distribution in the vicinity of the crack tip. They also employed an empirical time-to-rupture expression is used to describe the fracture event. The final expression for CCG rate is:

$$da/dt = B K^{\alpha m} \exp(-\alpha Q_c^* / RT) \quad (2.21)$$

where B and α are material constants, with α equal to or slightly less than unity, m is the steady state creep stress exponent, and Q_c is the activation energy for steady state creep. This model entails that the activation energy for crack growth is less than that for creep (Q_c). The authors used the activation energy data for Inconel 718 [92] to support their contention. On the other hand, the results by Sadananda and Shahinian [95] indicate that most of this energy is related to environmental interactions. This analytical equation also assumes a power law dependence of da/dt on the applied stress through the stress intensity factor K with a power exponent αm . This power exponent is found to be close to the value of the stress exponent for the steady state or minimum creep rate with $\alpha = 0.7 - 0.8$ for superalloys [92].

Although the stress provided by the Orowan-Irwin elastic expression only approximates the actual stress near the crack tip, Purushothaman and Tien's model is simple and clear. Actually, the model considers the plastic deformation zone ahead of the crack tip

as zero, and this assumption may not be true but not far from the small-scale yielding condition applicable in superalloys. In their model grain boundary sliding was not considered as a creep crack growth mechanism.

Dimelfi and Nix [141] proposed a CCGR model also based on the K as a driving force. They noticed that cavitation damage is often nucleated in the early stages of creep and that the mean density of the cavities increases with increasing applied stress. They postulated that the stress field ahead of the crack tip is the same as that predicted by linear elasticity. They also ignored the effect of cavities on the stress distribution. They also assumed that the material deforms under a constant applied stress in accordance with power law creep and that the grain boundary cavities grow by the same process within an intensified stress field ahead of the crack tip, as during power-law creep. Therefore, the steady-state crack growth rate can be calculated by considering that the crack grows one cavity spacing when the nearest cavity grows large enough to intersect the crack tip.

Their formula to express the growth rate in terms of the rate of growth of a spherical cavity ahead of a crack, is written as

$$\frac{1}{C} \frac{dC}{dt} = A \left[\frac{2}{\sqrt{3}} \right]^{n-1} \left[\frac{3K}{2n\sqrt{2X}} \right]^n X^{n/2} \quad (2.22)$$

where A is a constant, C is the cavity diameter, n is the exponent in the power-law equation, X is the distance ahead of the crack tip and K is the stress-intensity factor.

As compared to Purushothaman and Tien's model, Dimelfi and Nix's model is more mechanistic, because it tries to model grain boundary cavity nucleation and growth ahead of a macroscopic crack. The model also relates the grain size effect to the CCG process. They assume that when creep flow is associated with cavity growth, the deformation is highly localized, and intergranular fracture can occur with very little plastic deformation. Thus, the stress field ahead of the crack tip is closely approximated by the elastic field. However, they also assume that the cavities further suffer creep deformation. It is further assumed that the nucleation of cavities ahead of the crack is homogeneous and that interactions between cavities can be ignored. The model also suggests that creep ductility depends very much on the intercavity spacing.

2.2.3.2 Deformation Based Models

Deformation based models describe the so-called “steady-state” of CCG process. Creep crack growth process can be considered involving two processes: one is deformation of the material ahead of the crack tip causing crack-tip blunting; the other is damage accumulation in terms of microcracks or voids. While the first process can decrease the crack-tip stress field, the other can increase it by coalescence of microvoids with the crack tip. The steady state of creep crack growth behavior should be related to the balance between these two competing processes. The deformation models thus developed provide a basis for understanding how it affects the creep crack growth behavior. The model of

Purushothaman and Tien and that of Dimelfi and Nix discussed above can also be viewed as deformation-based models.

Barnby [142] developed a model which assumes that under steady state conditions, the creep rates are inversely proportional to the rupture time, and that the crack growth rates are proportional to the creep rates. An expression for the crack growth rate in terms of K^m (m has a value of 3 or more) and σ_{net} was deduced from the limited cases of low and high values of creep exponents. It should be noted that the first assumption is empirical while the second assumption is not necessarily valid, since materials with high creep rates do not always have high creep crack growth rates and vice versa. Although this model relates the creep crack growth rate to creep deformation, it does not provide a clear physical description of the phenomenon.

One similarity among all the deformation models is that some criterion for crack growth such as a critical strain, a critical displacement, or the time for fracture of a critical size ligament ahead of the crack tip is assumed in all cases.

In the critical strain model of Floreen and Kane [91], intergranular creep fracture propagates when the local strain ahead of the crack tip reaches a critical value. The value of the critical strain appears to be related to the microstructure of the grain boundary as well as the internal structure of the grains. Examination by Floreen [92] of the test results in a number of different nickel-base superalloys indicated that the stress intensity required to

produce failure in 100 hours at 704°C could be expressed as

$$K = [3\delta_0\sigma_{ys}E + 0.3\sigma_{ys}Ed\epsilon^*]^{1/2} \quad (2.23)$$

where δ_0 is the initial crack tip displacement, σ_{ys} is the yield strength, E is Young's modulus, ϵ^* is the critical strain and d is the grain diameter. In this formula, it is noteworthy that creep cracking rate is accelerated in the presence of a large grain. The model is based on the critical strain model of McClintock and Irwin [143]. Some of the assumptions made are very similar to those of Barnby [142], and therefore the same limitations also apply to this model. While the critical strain models help in understanding the CCG mechanism, they cannot be easily used to predict the CCG rates because of the uncertainty associated with the actual critical strain value.

Walker and Wilson [144] analyzed the creep crack growth process using a unified viscoplastic constitutive formulation [145] to determine the time dependent material behavior in the vicinity of the crack tip. A continuum damage equation, proposed by Chaboche [146], was also employed to predict the time required to fail a particular point in the crack tip area. The proposed viscoplastic/continuum damage model can predict the CCGRs using material constants obtained from uniaxial bar specimens. This is a great advantage of the model over other models. Their model prediction fits well the creep crack growth rate data obtained from experiments on CT specimens of Inconel 718 at 649°C.

2.2.3.3 Diffusion Based Models

In the temperature ranges of interest for many applications, diffusion always occurs. The operating diffusion mechanism can be an important factor in determining the actual CCG rates. Creep crack growth is essentially intergranular. Cracks grow by diffusion because of the chemical potential gradient set up by the stress field near the crack tip. Growth can occur either by volume or grain-boundary diffusion of vacancies towards the crack tip, which is equivalent to diffusion of atoms away from the crack tip. Diffusion models assume that creep crack growth is purely controlled by diffusion or diffusion caused by deformation. This provides a framework to understand and predict creep crack growth rates. The available activation energies for CCG, which have not been extensively measured, appear to be within the range of grain boundary diffusion energies for some materials [92, 95]. These observations indicate that the CCG process is associated with grain boundary diffusion.

Vitek [147] provided a detailed diffusion analysis using numerical techniques. He proposed a model for intergranular creep crack growth rates controlled by diffusional flow of material along grain boundaries in certain alloys [93, 148, 149]. The proposed mechanism of crack propagation was grain boundary diffusion of atoms away from the crack tip, with the atoms deposited at the grain boundaries, assumed to be ideal sinks for atoms. The driving force for this atomic diffusion is the chemical potential of atoms at the grain boundary subjected to a normal tensile stress. The numerically calculated crack

growth rates were obtained from the following equation:

$$\frac{da}{dt} = \frac{0.516D_b \delta \Omega G}{kTd^4} \left(\frac{K}{G} \right)^4 \quad (2.24)$$

where Ω is the atomic volume, G the shear modulus, k Boltzmann's constant, δ the grain-boundary thickness and d the crack-tip displacement. The fourth-power dependence on K is predicted for steady-state crack growth. For K smaller than some minimum value, Vitek shows that the growth rate decreases, reaches a minimum, and then increases when steady-state conditions are established.

Vitek's theory of intergranular crack growth at elevated temperatures is somewhat analogous to the theory of the growth of homogeneously distributed r-type voids. He considered the effect of stress relaxation due to the deposition of matter from the crack tip. However, this model does not take into account the deformation and grain boundary sliding effects near the crack tip. Although the K^4 dependence of steady-state rate is absolute, the transient regime predicted by this model satisfies the observation that the initial creep crack growth rate decreases with an increase in stress intensity in some cases. This model predicts a very sensitive dependence of the CCGRs on crack width.

The diffusion model developed by Sadananda [150] provides a different perspective of creep crack growth, even though the assumption of crack growth occurring by the diffusion of vacancies along the grain boundaries is similar to that of Vitek [147]. It is suggested that creep crack growth results from a balance between two competing processes,

namely the diffusion of point defects which contributes to crack growth and creep deformation which tends to retard growth. It is also suggested that grain boundary associated crack growth should occur within a limited temperature range. Crack growth occurs if $D_g d > 2D_b r_p$ where D_g and D_b are the grain boundary and bulk diffusion coefficients respectively, and d and r_p are the grain boundary thickness and the plastic zone size respectively. The upper limiting temperature is determined by the bulk diffusion processes which can cause vacancies that are diffusing to the crack tip to be dispersed into the plastic zone ahead of the crack. This model's predictions and the upper limiting temperature correlate well with Inconel 718 data [93]. As noted in Figure 2.24, for a given stress intensity value, the crack growth rates in Inconel 718 increased significantly with increasing temperature from 540 to 650°C but decreased or increased very little with further increase in temperature to 760°C (Fig. 2.24 [93]).

2.2.3.4 Combined Deformation and Diffusion Models

There are models developed to consider both the effect of deformation and diffusion on creep crack growth.

Beere and Speight [151] studied the diffusive intergranular creep crack growth in a plastically deforming solid. The diffusion of atoms can locally relieve the high stresses at the crack tip. An equilibrium stress profile increases continuously with increasing distance from the crack tip. The crack moves essentially by diffusional creep between the crack and

the boundaries around the crack. Ahead of the crack, this displacement is matched by dislocation creep. The crack growth rate under steady-state conditions is given by

$$\frac{da}{dt} \propto \frac{\dot{\epsilon}^{1/2} D_g \sigma_a}{D_s^{1/2}} \quad (2.25)$$

where $\dot{\epsilon}$ is the creep rate in the plastic zone, D_s is the surface diffusion coefficient, D_g is the grain boundary diffusion coefficient and σ_a is the applied stress. In Beere and Speight's analysis, the diffusion and deformation are coupled, but the deformation is only considered to accommodate the incompatibilities in deformation. The stress is assumed to be a minimum at the crack tip in the model.

Wu and Koul [139] developed an intergranular creep growth model which provides a physical description of the region ahead of the crack tip. According to their review, cavitation ahead of the main crack is recognized in most CCG models. The analytical treatments available are largely based on continuum mechanics or continuum damage mechanics concepts and, therefore, do not provide a physical description for the grain boundary cavitation process, which causes intergranular crack growth under creep conditions.

Wu and Koul [139] consider that under the conditions of steady-state creep, where elastic deformation can be neglected, the total strain rate ahead of the crack tip can be written as:

$$\dot{\epsilon} = \dot{\epsilon}_g + \dot{\epsilon}_{gbs} + \dot{\epsilon}_{diff} \quad (2.26)$$

where $\dot{\epsilon}_g$ refers to creep deformation due to the motion of dislocations within the grains, $\dot{\epsilon}_{gbs}$ refers to creep deformation due to grain boundary sliding, and $\dot{\epsilon}_{diff}$ refers to creep deformation due to diffusional creep. This model describes the creep crack growth as a combination of deformation, diffusion and grain boundary sliding events. In this combined model, however, GBS is considered to be the critical and dominant factor. The stress distribution ahead of the crack tip is assumed to be properly described by the HRR field [104, 105, 106]. Therefore, the model assumes the stress-dependence of creep crack growth rate to be of the form

$$\dot{\epsilon} \propto C^* \quad (2.27)$$

a relation which has been observed experimentally in many cases.

Sadananda and Shahinian's combined model [152] relates the creep crack growth rate to matrix creep and grain boundary sliding. Figure 2.33 [152] schematically shows how grain boundary sliding can lead to nucleation of a microcrack and its growth. From geometric considerations, they consider the coalescence of the microcrack as an event requiring a sliding displacement (d) equals to $L/2$ where L is indicated in Fig. 2.38. The resulting crack growth rate takes the simple form

$$da/dt = 2L \dot{u}_g \quad (2.28)$$

where is \dot{u}_g the strain rate due to grain boundary sliding.

Sadananda and Shahinian applied to their model the Crossman and Ashby's [153]

finite element analysis of the sliding rate as a function of the matrix creep rate. For the case where grain boundary sliding is accommodated by power law creep, the crack growth rate is given by

$$da/dt = 2L\alpha \dot{u}_T \quad (2.29)$$

where \dot{u}_T is the total deformation rate of the aggregate and $\dot{u}_T = \dot{u}_m + \dot{u}_g$ (\dot{u}_m is the matrix deformation rate). This equation indicates that the sliding rate and the creep rate are competing processes. An optimum condition exists where crack growth rate reaches a maximum. If the creep rate is very high, either because of a high loading rates or high stress index n , creep crack growth should not occur.

Few studies have tried to model the effect of environment on the creep crack growth rates. Bain, Pelloux and Bensussan [124, 125] have linked the environmental effect on CCG in several disc alloys successfully. Their model is based on the concept of critical strain often used in deformation models, coupled with an oxidation effect at the crack tip. The creep strain accumulated ahead of crack-tip is given by

$$\varepsilon_c(t) = \left(\left(\frac{0.29K^2}{E\Gamma} \right)^{N_c} B_c (N_c + 1) t \right)^{\left(\frac{1}{N_c + 1} \right)} \quad (2.30)$$

where $\varepsilon_c(t)$ is the creep strain as a function of time, E is the Young's modulus, B_c and N_c are material constants defined in Norton's Law. The damage accumulated ahead of the crack tip was treated as creep strain in elements equal in size to the critical microstructural parameters (i.e. grain size, or prior particle size). The proposed model requires only

information on the microstructure and data from smooth bar tensile and creep tests to generate a prediction of the time dependent crack growth rates. The effect of the environment was taken into account by reducing the allowable creep strain and/or by changing the critical microstructural parameters (e.g. grain size for tests in air and prior power particle size for tests in argon). A comparison [125] between the predicted and measured growth rates for PM HIP MERL 76 tested in air and in argon at 704°C is shown in Figure 2.34.

3. EXPERIMENTAL MATERIALS AND METHODS

This section presents the material used, heat treatments conducted and testing methods employed in this project.

3.1 Materials

The material used in this study was a wrought Udimet[®] 520 (U-520) nickel-base superalloy produced by Special Metal Corporation, and subsequently hot rolled and centerline ground into reforging stock by Kelsey Hayes Inc. Table 3.1 lists the chemical composition of the material investigated.

Table 3.1 Chemical composition of the alloy investigated (wt%)

Ni	Cr	Co	Mo	Ti	Al	W	C	B	S
bal.	18.9	11.9	6.00	3.21	2.22	1.05	0.06	0.006	0.002

3.2 Microstructural Characterization

In order to establish the optimum range of grain sizes for creep and creep crack growth studies, several preliminary solution treatments were applied to the forging stock materials. The influence of solution treatments was studied on specimens solution-treated at 1050°C, 1090°C, 1135°C, 1185°C and 1235°C for 1, 2 and 4 hours followed by air-cooling (AC) as well as at 1190°C, 1200°C, 1210°C, and 1250°C for 2 hours followed by water-quenching. An immersion etchant containing 10 ml HNO₃, 10 ml acetic acid, 15 ml HCl and 2-5 drops glycerol was employed to reveal the grain structure of solution treated specimens. The mean linear intercept length of the grain structure was measured by the Heyn intercept method [154] and enough numbers of grains were measured so that the results were within the 95 percent confidence limits in all cases.

In order to select aging treatments for obtaining carbide-free grain boundaries in specimens with different grain sizes, a series of carbide precipitation kinetics experiments were performed. The M₂₃C₆ grain boundary carbide precipitation kinetics studies were conducted on two separate batches of specimens subjected to two different solution treatment conditions. In one batch, the solution treatment was carried out at 1135°C for 4 hours followed by air cooling (AC) and, in the other, a solution treatment of 1250°C for 2 hours followed by water cooling (WC) was employed. The two solution treatment conditions produced significantly different grain sizes. The aging experiments were

* Udimet is a registered trademark of Special Metals Inc..

conducted on cube-shaped specimens, 5 mm x 5 mm x 5 mm, in a radiation type electric furnace. All specimens were polished and immersion etched following standard metallographic procedures. The etchant employed was 3 parts glycerol, 2-3 parts HCl and 1 part HNO₃. At room temperature, M₂₃C₆ grain boundary carbides, if present, were revealed after etching for about 60-90 seconds. This rapid method of gauging the presence or absence of grain boundary M₂₃C₆ carbides was initially calibrated against scanning electron microscopy (SEM) observations, using energy dispersive X-ray (EDX) microanalysis, and transmission electron microscopy (TEM) replica observations. After etching for 90-120 seconds, the γ' phase was also easily revealed. First stage carbon replicas from the metallographic specimens were examined in a JEM-2000FX transmission electron microscope. Carbides were identified by SEM or TEM using EDX analysis and by TEM using the electron diffraction method. Vickers microhardness measurements at a load of 0.98N or 100 gram-force were also performed on metallographically polished surfaces which had been cut slowly with a diamond-coated saw.

Specimens solution treated at 1250°C for 2 hours were employed to determine the secondary MC carbide precipitation temperature range. Metallography and SEM observations with EDX microanalyses were employed to identify the carbides.

TEM specimens were electro-polished in a 5% HClO₃ methanol solution at temperatures ranging between -60 and -70°C at a voltage of 30 to 40 mV.

3.3 Heat Treatment Procedures

The heat treatments were designed on the basis of the results obtained from preliminary heat treatments studies performed on Udimet 520 materials, to obtain different grain sizes while precipitating certain amounts of γ' phase within the grain interiors but without precipitating any grain boundary carbides. The heat treatments employed for different specimen batches included solution treating at (i) 1110°C, (ii) 1135°C, (iii) 1190°C, (iv) 1200°C and (v) 1250°C which was followed by the same two step aging treatment in all cases. The actual heat treatment conditions employed are listed below,

1110°C, 4h, A C
 1135°C, 4h, A C
 1190°C, 4h, W C + 700°C, 20min, A C + 600°C, 92h, A C.
 1200°C, 2h, W C
 1250°C, 2h, W C

TEM thin film samples were prepared to measure γ' volume fractions and to observe grain boundary morphology. Approximate γ' volume fractions ($V_{\gamma'}$) were determined on the basis of enlarged areas fraction measurements on TEM micrographs.

3.4 Hardness Testing

The load employed for the Vickers microhardness was 0.98 N. The specimens

were cut by diamond saw slowly and the hardness testings were performed on metallographic surfaces.

3.5 CCGR Testing

Compact tension (CT) specimens with dimensions shown in Figure 3.1 (a) were machined from the heat treated plates. This CT specimen is a standard AGARD** specimen geometry with a width (W) of 26 mm and thickness (B) of 13 mm.

Fatigue precracking prior to actual CCGR testing provides a sharp crack for fracture mechanics testing purposes. The CT specimens were fatigue precracked in an MTS 810 material test system at room temperature up to a crack length to width ratio (a/W) of approximately 0.35. The load shedding method was employed during fatigue precracking in order to shorten the test time. The load change was smaller than 20% of maximum load (P_{max}) based on the recommendation contained in ASTM E647 [155]. The final maximum stress intensity during precracking is significantly lower (< 25%) than the initial stress intensity for creep crack growth testing.

The CCG tests were conducted in an ATS (Applied Test Systems, Inc.) standard creep machine with deadweight loading and automatic lever balance in load control. All the tests except one were conducted at a constant load of 23.1 KN (initial stress intensity

factor of about $71 \text{ MPam}^{1/2}$). The first CCG test performed, which was on an 1135°C solution treated specimen, was loaded using a multiple-step load increase procedure with at least 48h between each load increase. This test was finally conducted at an initial stress intensity factor (K) of $79.2 \text{ MPam}^{1/2}$. The CCGRs obtained from this first CCG test showed the same rates as those obtained from the CCG test at an initial K of $71 \text{ MPam}^{1/2}$. This trend suggests that the use of K is appropriate to quantify the crack propagation results in the present tests, even though plane strain conditions are not strictly met. It should also be keep in mind that the crack propagation results obtained on different specimens serve particular for comparative purposes.

Constant load CCG tests were also conducted in 99.9 pct ultra-high-purity (UHP) argon environment. A retort was used in the argon tests on an MTS 810 testing frame. Argon tests were conducted at an over pressure of 0.006894 MPa (1 p.s.i.) in order to ensure no back streaming of air. The setup for CCG tests in argon is shown in Figure 3.2.

Crack lengths during precracking and CCGR testing were monitored by a direct current (DC) potential drop (PD) technique implemented at the Institute for Aerospace Research (IAR), of the National Research Council of Canada (NRC) [156]. A constant DC current of 10 A was supplied to the CT specimens using a stabilized power supply and 1.15 mm (0.045 in.) diameter type 302 stainless steel current leads. Wires were welded directly to the specimens. The potential change was monitored with 0.5 mm

** Advisory Group for Aerospace Research & Development, North Atlantic Treaty Organization.

(0.02 in.) diameter stainless steel lead wires spot welded to the opposite corners of the CT specimens, as shown in Figure 3.1 (b). Potential drop data acquisition system was computer-controlled using a QB language program in a personal computer system written during the course of this research program. The precision of the crack length increment determined by this DC-PD system is 0.08 mm. The other specifications of the DC-PD technique used can be found in an NRC technical report by Pishva, Bellinger, Terada and Koul [157]. The schematic illustration of DC-PD setup is shown in Figure 3.3. The calibration equation for crack length as a function of change in normalized voltage ratio was the same as that developed for the standard AGARD CT specimens [158], which is given by,

$$\frac{a}{W} = -0.5051 + 0.8857 \beta - 0.1398 \beta^2 + 2.398 \times 10^{-4} \beta^3$$

where a is the crack length, W is the width of the CT specimen (26 mm), and β is the normalized voltage ratio.

The test temperature was chosen to be 540°C (close to 1000°F). This temperature is significantly lower than the final aging temperature of 600°C and was chosen to suppress material overaging and grain boundary carbide precipitation during testing. As well, a number of creep and CCG tests have been performed at this temperature on other Ni-base alloys [e.g. 93]. It has been reported that crack growth rates under static loads at 538°C was a critical property for optimizing low expansion superalloys for commercial usage [159]. Specimens were heated to the test temperature and homogenized for 2 hours

before applying the dead weight load.

The potential drop data were processed using Excel software in an external computer system to generate the crack length vs time curves and to calculate the stress intensity factors. The stress intensity factors were calculated as follows (ASTM E 647):

$$K = \frac{P}{B\sqrt{W}} \frac{(2+\alpha)}{(1-\alpha)^{3/2}} (0.886 + 4.64\alpha - 13.32\alpha^2 + 14.72\alpha^3 - 5.6\alpha^4)$$

Where $\alpha = 2a/W$.

Creep crack growth rate was then determined from the crack length vs time relationship obtained from the DC-PD measurements. The secant method [160] was used to calculate the crack growth rate (da/dt) with the minimum crack extension between successive data points being ≥ 0.08 mm. Sudden jumps in the DC-PD reading were caused by environmental disturbance near the recording systems, such as electric welding in the lab or movement of the setup of the DC-PD equipment. These jumps were not considered in CCGR calculations.

Fracture surfaces were examined in a SEM. Microstructures before and after the creep crack growth tests were also examined using thin film specimens in a TEM.

3.6 Tensile and Creep Testing

The dimensions of tensile and creep specimens are shown in Figure 3.4. All specimens were ground longitudinally using 600 grit silicon carbide paper and then polished with 600 grit soft microcut paper sheets (Buehler corporation products).

The tensile specimens were threaded into MAR-M-246 grips. The high temperature tensile tests were performed at an engineering strain rate of $1.67 \times 10^{-4} \text{ s}^{-1}$ to a total strain value of 2% using an MTS 810 test frame with a 100 KN load cell. An MTS series 632.61C.04 high temperature extensometer with a gage length of 21 mm was employed to obtain engineering strain-load curves.

The creep specimens were threaded into MAR-M-246 grips. Creep tests were conducted in an ATS dead weight lever-type creep frame. The specimens were heated to 540°C and homogenized for 2 hours before creep loading. Most tests were carried out in an air environment. In order to observe the effect of oxidation on creep, one creep test was also conducted in vacuum and some tests were also carried out in a “flowing argon” environment. In the flowing argon tests, a creep specimen size cubic chamber was made by fiberfrax around the creep specimen in the ATS split type resistance high temperature furnace where other parts of the furnace employed for the creep tests were filled with the fiberfrax to reduce the space in the furnace chamber as much as possible. The argon was directly tubed to the fiberfrax chamber. This “flowing argon” environment was actually

an argon plus air environment.

A stereo-microscope was also used for observing the specimen surfaces before and after testing. Fractographic observations and the observations of the specimen surfaces after testing were studied using a SEM. Longitudinal cross-sections after testing were observed metallographically.

4. RESULTS

This section presents the experimental results of the testing program. First the results of the microstructural investigation on Udimet 520 are presented. This is followed sequentially by the results on CCG tests, tensile and creep tests.

4.1 Grain Growth, Carbide Precipitation and γ' Precipitation in Udimet 520

In this study, different solution treatments and aging treatments were employed to investigate grain growth behavior and carbide precipitation in Udimet 520. This subsection presents results on the grain growth behavior, the $M_{23}C_6$ grain boundary carbide precipitation kinetics, the morphologies of such carbides, related microstructural changes, the secondary MC carbide precipitation behavior and γ' precipitation in Udimet 520.

4.1.1 Influence of Solution Treatment on Grain Size and on Carbide Precipitation

Figure 4.1 shows the as-received microstructure of the forged alloy. A necklace-type microstructure, consisting of small grains approximately 12 μm in diameter amongst arrays of larger grains approximately 82 μm in diameter, was observed. Primary MC carbides were present as massive grey particles and some carbonitrides with an

approximately cubic morphology were also present.

The grain sizes (in terms of mean linear intercept length) after solution treatment are shown in Table 4.1. Other microstructural details before and after the two step aging treatment will be discussed in the subsection 4.1.5

Table 4.1 Microstructural details and microhardness results from different heat treatments

Treatment	Mean intercept length (μm)	V_{γ} (%)	d_{γ} (nm)	H_v (after HT)	H_v (after aging)	ΔH
"1110"	100 ± 8	9.2	21.0	396	426	30
"1135"	106 ± 4	8.9	21.7	385	410	25
"1190"	235 ± 7	10.5	22.1	275	315	40
"1200"	245 ± 9	13.6	22.8	305	345	40
"1250"	464 ± 10	13.1	23.0	355	385	30

After solution treatments at temperatures of 1050°C and 1090°C for four hours, the necklace microstructure still remained, (see Figure 4.2), and the average grain size values were therefore not employed for comparison. The necklace structure of the forged material began to disappear at 1110°C. This suggests that the change starts near 1100°C with the dissolution of grain boundary $M_{23}C_6$ carbides which is discussed in detail in subsection 4.1.2. The grain size is heterogeneous even after solution treatment at 1250°C for two hours due to the inhomogeneous distribution of the original grain structure. The effect of the

1135°C, 1185°C and 1235°C solution treatments on the mean intercept lengths of the grain structures is shown in Figure 4.3. The effect of the solution temperature on the mean intercept length of the grain structure is shown in Figure 4.4. At a given solution temperature, the mean intercept length increases with solution time in a slow, but approximately linear, manner (Fig. 4.3), while for a given solution time the mean intercept length increases with solution temperature in the manner shown in Fig. 4.4. The solution temperature has a more important effect on the grain size of Udimet 520 alloy than the solution time. The grain coarsening behavior, for a solution time of two hours of the Udimet 520 investigated is also indicated in Figure 4.4. The grain size increases rapidly at 1190°C compared with the grain size obtained after a solution treatment below 1190°C. The grain size again increases slowly in the temperature range of 1190-1235°C, until another phase of rapid grain growth occurs above 1235°C. This indicates that two grain coarsening temperatures (GCT) for Udimet 520 can be defined as 1190°C and 1250°C. The lower of these two temperatures is actually higher than the coarsening temperature of 1150°C reported for Udimet 500 [161]. The rapid increase in grain size at 1190°C appears to be associated with the solvus temperature of the MC carbides in Udimet 520, which is close to 1190°C (this is further discussed in subsection 4.1.4). The rapid grain growth at 1250°C is associated with the dissolution of carbonitrides. Carbon in the as-received alloy is tied up in large chunky MC carbides and cubic carbonitrides, with the remaining carbon in solution. It is observed that MC carbides in the matrix become less numerous when the solution temperature is higher and the solution time is longer. After solutionizing at 1135°C for 4 hours, most MC carbides are about 4-10 μm in width, while after solutionizing

at 1190°C for 2 hours, most MC carbides are below 5 μm in width. These results indicate that the grain coarsening behavior of Udimet 520 is controlled by MC carbide dissolution. The grain growth kinetics at 1190°C and 1250°C indicate that significant MC carbides dissolution begins at 1190°C, with important M(C,N) dissolution occurring above 1250°C.

Grain size has an indirect effect on M_{23}C_6 carbide precipitation. The larger the grain size, the smaller is the grain boundary area available for precipitate formation. A given volume of precipitates will therefore form a thicker and more continuous film as the grain size increases or even form intragranular carbides. Figure 4.5 shows the microstructure of the specimen after 1090°C solution and the normal two-stage aging treatments. Significant grain growth was not observed during solution treatment at 1090°C for four hours. The necklace structure remained present. Annealing twins were observed in the specimen but no M_{23}C_6 precipitate was observed in the grains. Figure 4.6 shows the microstructure of the specimen after 1235°C solution and the normal two-stage aging treatments. In this higher temperature solution condition, the grain size is larger than that after the 1090°C solution treatment. No annealing twins were observed but M_{23}C_6 precipitates were present both at grain boundaries and within grains. The star-shape precipitates within grains are considered to be M_{23}C_6 carbides since they are rich in Cr. Such a grain size effect on M_{23}C_6 carbides has also been reported in Udimet 500 [162].

4.1.2 Grain Boundary $M_{23}C_6$ Carbide Precipitation Kinetics

A Vickers microhardness of 385 and a mean grain boundary intercept length of $106 \pm 4 \mu\text{m}$ were obtained after solution treatment of four hours at 1135°C followed by air-cooling. A Vickers microhardness of 365 and a mean grain boundary intercept length of $464 \pm 10 \mu\text{m}$ was obtained after solution treatment of two hours at 1250°C followed by water-quenching, to avoid possible carbide precipitation during cooling. The microhardness difference between the water-quenched and air-cooled solution treated specimens indicates that some γ' phase is nucleated and precipitated during air cooling. This was confirmed by TEM replica observations. As seen in Figure 4.7, spherical γ' phase and no grain boundary carbides were observed after solutioning at 1135°C for four hours and air cooling.

Energy dispersive X-ray microanalyses of the grain boundary carbides formed during aging at temperatures in the range from 600 to 1050°C showed that chromium was a major component and a significant amount of molybdenum was also present (Figure 4.8). This agrees with the typical chemical composition expected for $M_{23}C_6$. Figure 4.9 (a) shows a micrograph of a first-stage replica of a specimen aged at 1050°C for 15 minutes and water-quenched following a solution treatment of four hours at 1135°C . Figure 4.9 (b) shows the diffraction pattern and index from a grain boundary carbide in Figure 4.9 (a). The lattice parameter (a) calculated from the diffraction pattern is 1.07 nm , which agrees well with that of Cr_{23}C_6 ($a = 1.06599 \text{ nm}$). These results indicate that the grain boundary

carbides precipitated at 600-1050°C were $M_{23}C_6$ carbides.

The TTT diagram (C-curve) established by metallography, for the start of the formation of grain boundary $M_{23}C_6$ carbides is shown in Figure 4.10. These carbides form very quickly in the temperature range 760°C - 1050°C. Their precipitation kinetics after the 1250°C solution treatment are more rapid than after the 1135°C solution treatment, in agreement with the higher dissolved carbon content available for precipitation after the former treatment. This difference in precipitation kinetics is more pronounced at higher aging temperatures.

At 1100°C, the grain boundary $M_{23}C_6$ carbides dissolved because specimens originally with such carbides showed no $M_{23}C_6$ carbides after annealing for 2 hours at 1100°C. However, at 1100°C the specimens solution treated at 1250°C reprecipitated discrete MC carbides along grain boundaries as well as within the grains as shown in Figure 4.11. These were identified to be MC carbides because of the large amount of titanium and/or molybdenum present. It was easy to distinguish primary MC and carbonitrides from the secondary precipitated MC carbides. The large primary MC carbides and carbonitrides were often aligned along the forming direction and were generally blocky and cubic in shape, while the secondary precipitated MC carbides were small and spherical in shape. Such secondary MC precipitation was not observed after annealing at 1100°C for two hours in specimens solution treated at 1135°C. These results indicate that $M_{23}C_6$ carbide precipitation dominates at temperatures below 1100°C while MC carbide precipitation may

occur at temperatures, approximately equal to or greater than 1100°C, if there is enough free carbon in solution in the matrix.

$M_{23}C_6$ carbide precipitation occurs first at the grain boundaries and then within the grains when sufficiently large amounts of $M_{23}C_6$ are precipitated during aging. Figure 4.12 shows the microstructure of a specimen aged for 30 minutes at 850°C after a 1250°C solution treatment. Such intragranular $M_{23}C_6$ carbides were not observed in specimens solution-treated at 1135°C. These observations suggested that microstructures resulting from low solution temperature treatments contain a lower amount of free carbon in the matrix and more grain boundaries (i.e., smaller grain size) for $M_{23}C_6$ precipitation as compared to conditions following high solution temperature treatments. Intragranular $M_{23}C_6$ appeared along certain crystallographic planes as shown in Fig. 4.12. Needle-like intragranular $M_{23}C_6$ carbides have been reported in Ni-Fe-Cr alloys [163], nickel-base superalloys [164, 165] and other nickel alloys [166] and have a cube-cube orientation relationship with the matrix [163-166].

4.1.3 The Morphology of Grain Boundary $M_{23}C_6$ Carbides

A variety of grain boundary carbide morphologies was observed after the different aging treatments. The nucleation and growth of grain boundary carbides occur as a function of time and temperature. Figures 4.13-4.15 provide some examples of grain boundary

$M_{23}C_6$ carbides observed in replicas. In 900°C temperature range, high aging temperatures produced fewer carbide nucleation sites, and carbides then spread quickly along the grain boundaries and even overlapped each other to form continuous grain boundary carbide networks after long aging times. Semi-continuous grain boundary carbide networks formed at shorter aging times, with the width of the carbides perpendicular to the grain boundary being narrow. Figure 4.13 shows replica micrographs of specimens aged at 900°C for 40 min, 24h, 48h and 90h after an 1135°C solution treatment. The grain boundary carbides grow very quickly at many sites after their formation (Figure 4.13a) and aging for long time at 900°C produces a nearly continuous carbide film in the grain boundary. The width of the grain boundary carbides is approximately 0.2-0.5 μm , with the growth in width occurring slowly with time.

Aging at temperatures below 850°C produced more numerous grain boundary carbide nucleation sites, as observed from the close spacing of discrete carbide particles (Figs. 4.14 and 4.15). Figure 4.14 shows a replica micrograph of a specimen aged at 700°C for 100 hours after an 1135°C solution treatment. In Figure 4.14, discrete grain boundary carbides have a size of 0.2-0.35 μm and an approximate spacing of 0.1 μm . TEM observations of the specimen solution-treated at 1135°C for 4 h and air cooled and then given the standard two-stage aging treatment indicated that the grain boundary $M_{23}C_6$ precipitates had sizes ranging between 0.2 and 0.4 μm and were almost in contact with each other (Figure 4.15). The γ' precipitates were 0.05-0.08 μm in diameter. The Vickers

microhardness of the matrix was 454.

The carbide morphology varied even within the same specimen, which indicates heterogeneous grain boundary precipitation. Grain boundary $M_{23}C_6$ carbides with a feather-like shape are shown in Figure 4.16 and were observed in localized small regions. Such a carbide shape, which develops on one side of the grain boundary, has been reported during precipitation in other nickel alloys [167] and nickel-based superalloys [168]. The growth of these precipitates in one direction indicates that this growth occurs during grain boundary migration [169].

4.1.4 Secondary MC Carbide Precipitation and MC Carbide Solvus Temperature

The EDX analyses of MC type carbides in as-polished specimens indicated that three types of MC carbides TiC, (Ti, Mo)C and (Ti, Mo, W)C were present. Most of the MC carbides conformed to TiC and (Ti, Mo)C compositions. This microanalyses also indicated that dissolution of MC carbide would increase the solute C and Ti contents of the matrix.

As mentioned previously, grain boundary $M_{23}C_6$ carbides dissolved at 1100°C. However, at 1100°C the specimens solution-treated at 1250°C precipitated discrete MC carbides at grain boundaries as well as within the grains (see Fig. 4.11). The secondary MC carbide precipitation occurs very rapidly at 1100°C, and was observed for specimens aged

10 minutes or longer. Grain boundary and intragranular MC precipitates were also observed in a specimen annealed at 1150°C for 2 hours, but only grain boundary MC precipitates (Figure 4.17) were observed in the specimen annealed at 1177°C for 2 hours. In a specimen annealed at 1190°C for 2 hours, this type of MC precipitates was not observed. These results indicate that secondary MC carbide precipitation occurred in the temperature range between 1100°C and 1177°C. Secondary MC precipitation did not occur at 1190°C, suggesting that MC carbides dissolve at this temperature.

Secondary MC precipitation was not observed after annealing at 1100°C for 2 hours in the specimens solution treated at a temperature of 1185°C or less. The specimens annealed at 1100°C for 2 hours after solution treatment at 1190 to 1210°C, however, showed secondary MC precipitation along grain boundaries. These observations show that secondary MC precipitation occurs in the temperature range of 1100 to 1177°C if the specimens were solution treated at temperatures above 1190°C, so as to have enough solute C in the matrix. The fact that a specimen solution treated at 1185°C for 2 hours did not undergo secondary MC precipitation at 1100°C indicates that MC carbide solvus temperature is probably between 1185 and 1190°C.

The matrix Vickers microhardness vs solution temperature relationship for water-quenched specimens is shown in Figure 4.18. The matrix Vickers microhardness of the specimen after solutionizing at 1190°C for 2 hours and water-quenched was about 300 while that after solutionizing at 1185°C for 2 hours and water-quenching was about 260.

Although the microhardness difference between specimens solution treated at 1190°C and at 1235°C and water-quenched was small, a more obvious difference in microhardness resulted between solution treatments at 1235°C and at 1250°C. The shape of the curve of matrix Vickers microhardness after quenching versus the solution temperature (Fig. 4.18) is similar to that of the grain size versus the solution temperature (Fig. 4.4). This suggests that the shape of Fig. 4.5 is largely associated with an increase in hardness due to increasing the solute content associated with dissolving the MC carbides and carbonitrides. This result suggests that there is much more carbonitride dissolution at 1250°C than at 1235°C. It is noted that the Vickers microhardness of a specimen solution treated at 1250°C for 4 hours and water-quenched was only slightly higher than that of the specimen solution-treated for 2 hours. These microhardness differences appear to be attributable to the difference in the C, N and Ti solute contents in the matrix since the higher the solution temperature, the more C, N and Ti solute are present in the matrix. The results also indicate that the MC solvus temperature in the Udimet 520 investigated was close to 1190°C and that the carbonitrides dissolve between 1235-1250°C.

Additional microhardness measurements made on the water-quenched specimens approximately 5 months after the original measurements indicated that the microhardness values of all specimens had decreased by 10-15 Vickers below the values originally measured, but that the shape of the microhardness curve remained the same. These results indicate that the shape of the curve obtained was not the result of hardening due to excess vacancies being quenched in.

4.1.5 Gamma Prime Precipitation

Figure 4.19 showed an example of a TEM micrograph of a specimen solution treated at 1135°C for 4 hours followed by the two step aging treatment. No grain boundary carbides were visible and the grain boundary ledge height was also very small and not visible. The γ' diameters ($d_{\gamma'}$), the microhardness after solution treatment (ST) and subsequent aging and the net microhardness increase after the aging treatments (ΔH) are summarized in Table 4.1. The main difference between specimens subjected to different heat treatments is the grain sizes which vary between 100 and 464 μm , whereas the γ' volume fractions are similar in all cases. The net increase in microhardness is relatively similar in most cases, but the overall hardness appears to vary from one batch of specimens to another in a complex manner.

It is interesting to note that microhardness measurements showed little increase with aging time before grain boundary carbide formation. After grain boundary carbide formation, there was a substantial increase (often going above 400 Hv) in the microhardness of the matrix, far from the grain boundaries. For aging at 600°C, there is little increase in the microhardness in the approximately first 200 hours of aging and then a substantial increase in the next 15-20 hours. This indicates that the γ' phase precipitation resulting in high microhardness occurred somewhat after the formation of the grain boundary carbides, although the two should not be related. Small increases in microhardness near grain

boundary carbides were generally noted. These results indicated that the grain boundary carbides tended to form before substantial formation of the γ' , at least for aging temperatures above 600°C.

4.2 The Effect of Grain Size on Creep Crack Growth in Udimet 520

4.2.1 Creep Crack Growth Rate

A typical example of the creep crack length vs time curve obtained during a CCG test is shown in Figure 4.20. The creep crack length increments in most cases were about 5 to 7 mm before fast fracture commenced. The incubation time t_i in Table 4.2 (air) and Table 4.2 (argon) are defined as the period necessary to detect creep crack growth over a distance of 500 μm (larger than the largest grain size employed in this study) in precracked specimens. The total rupture times to fracture the CT specimens t_r and the critical intensity factors (K_{crit}) at which fast fractures commenced during the CCG tests are also listed in Table 4.2 and Table 4.3.

The CCGR vs stress intensity factor relations for different grain size materials tested in air are illustrated in Figure 4.21. The CCGRs do not vary dramatically with grain size except that the two small grain size materials solution treated at 1110°C and 1135°C showed lower CCGRs than other three larger grain size materials by a factor of

Table 4.2 Parametric results obtained from different CCG tests in air on U-520 material at 540°C

Solution Temperature (°C)	Mean intercept length (μm)	m	t _i (h)	t _r (h)	K _{crit.} (MPa m ^{1/2})	K _{ini.} (MPa m ^{1/2})
1110	100 ± 8	-(2.3)	190	280	~97	~71
1135	106 ± 4	6.2 (2.5)	210	720	~113	~72
1190	235 ± 7	4	48	230	~130	~71
1200	245 ± 9	5.27	96	250	~112 to 124	~71
1250	464 ± 10	6.42	68	250.3	~105 to 121	~72.9

Table 4.3 Parametric results obtained from different CCG tests in argon on U-520 material at 540°C

Solution Temperature (°C)	Mean intercept length (μm)	m	t _i (h)	t _r (h)	K _{crit.} (MPa m ^{1/2})	K _{ini.} (MPa m ^{1/2})
1135	106 ± 4	~2	106	1035	~135	~72
1200	245 ± 9	~2.55	150	>600	~145	~72

about 2.5. In these two small grain size materials, CCGRs increased slowly with increasing K at the beginning of the tests and this was followed by a faster crack growth regime in the material solution treated at 1135°C. The steady state creep crack growth

regimes in all cases were found to follow an approximately straight line relationship on a log-log scale, although in materials solution treated at 1110°C and 1135°C, there appeared to be two such regions corresponding to slow and fast crack growth region, Fig. 4.21. The materials with grain sizes of 235–464 μm showed a very narrow slow crack growth regime but a wide faster crack growth regime with a slope of 4–6.42. In all cases, the slope m is shown in Table 4.2. The initial stress intensity factor employed was 70–72 $\text{MPam}^{1/2}$ and when K approached 113 $\text{MPam}^{1/2}$ (or higher), the fast fracture mode commenced. The CCGRs are of the order of 10^{-3} - 10^1 mm/h. The CCG experimental data were reproducible although the plots in Fig. 4.21 only show a single test result for each grain size material.

Figure 4.22 shows the CCGR vs K relationship for the specimens solution treated at 1135°C in different test environments. Figure 4.23 shows the CCGR vs K relation of the specimens solution treated at 1135°C and 1200°C in argon. The CCGRs in argon are lower than those in air and the CCGRs are closer to each other in argon than in air.

4.2.2 Fracture Surface Observations

Fractography and metallography of cross-sections are the usual two methods employed to study the fracture mode during CCG. The macroscopic features of the fracture surface include the surface flatness, the extent of crack tip curvature and the surface color.

The microscopic features of the fracture surface include the fracture path, the presence of creep cavities and the presence of crack tip branching. The distribution of cavities ahead of the creep crack tip or ahead of intergranular facets and the formation of oxidation layer provide important information on operative fracture and deformation mechanisms during CCG. Evidence for these phenomena can also be observed on metallographic cross sections.

Macroscopic observations showed that creep crack tips followed the tip of the fatigue precrack and that the fracture surface was not flat. There were three distinct fracture regions visible: fatigue precracked region, slow creep crack growth region and fast fracture region. Figure 4.24 shows the micrograph of the interface of fatigue precracking and creep crack growth region. The transition from the transgranular fracture in the precracking fatigue region to intergranular cracking in the creep crack growth region is clearly observable.

Typical fractographic features observed by scanning electron microscopy in slow CCG regions in different grain size specimens are presented in Figures 4.25-4.27. In these figures, the macroscopic direction of crack growth is always from right to left. Clean grain boundaries and secondary cracks are the main features in the slow creep crack growth regions in all cases (Figs. 4.25 a, 4.26 a and 4.27 a). The grain boundary separation as a result of crack tip branching is more abundant in small grain size specimens than in large grain size specimens (Fig. 4.25 b, 4.26 b and 4.27 b). A very

small fraction of localized transgranular fracture was also observed in specimens solution treated at 1110°C and 1135°C (Fig. 4.25 b), with the area fraction of local transgranular fracture increasing with an increase in grain size. No cavities were observed on grain boundary facets at high magnifications (Fig. 4.26 c). Some sparse imperfections appeared placed at some grain boundaries (Fig. 4.25 a). The EDX analysis showed that these sparsely distributed particles at the grain boundaries were rich in Ti and Mo, which indicates that they were MC type carbides. It was noted that these MC particles were much less abundant on fracture surfaces of specimen solution treated at 1200°C and 1250°C than on specimens solution treated at 1110°C and 1135°C. In some regions, fracture features strongly suggested that crack arrest lines were observed on the grain boundary facets of all fracture surfaces, (e.g., Fig. 4.26 b).

Figure 4.28 shows typical fractographic features at the interface between the CCG and the fast fracture regions. The fast fracture regions showed ductile fracture features. Figure 4.29 illustrates details of the fracture features in the fast fracture region.

The fractographic features of CCG in argon are similar to those observed in air. Figure 4.30 shows the typical fractographic features of CCG in argon. Local crack-arrest lines were again observed.

4.2.3 Metallographic Observations

Figure 4.31 shows an optical micrograph of the cross-section of a CCG specimen which had been solution treated at 1135°C. Some deep secondary cracks are clearly discernible, but no signs of creep cavitation were visible in the vicinity of the creep fracture surfaces. The intergranular secondary cracks are 2-5 grains deep relative to the fracture surface. Figure 4.32 depicts the profile of the crack tip region of an interrupted CCG specimen which had been solution treated at 1200°C. The creep crack is clearly seen to propagate along the grain boundaries which are lightly oxidized. Grain boundary cracks at triple point junctions are always branched although the main crack finally follows only one of these crack branches. The intergranular microcracks are observed to form at triple-point junctions along the macroscopic crack path. No crack was observed too far away from the main crack.

4.3 The Effect of Grain Size on Tensile and Creep Properties

4.3.1 Tensile Properties

Table 4.4 lists the tensile properties of Udimet 520 solution treated at 1110°C, 1190°C, 1250°C and after the “standard” treatment [170], where δ is the total elongation

and ψ is the reduction in area. It is expected that the specimens in this study would produce lower strengths and higher elongations than the standard treatment, because the former three treatments do not provide sufficient aging. All the tensile elongations were over 20%. Figure 4.33 shows the tensile strength vs grain size relationship in this test program.

Table 4.4 Tensile properties of Udimet 520 after different treatments

Treatment	Mean intercept length (μm)	σ_{UTS} (MPa)	$\sigma_{0.2}$ (MPa)	δ (%)	ψ (%)
"1110"	100 ± 8	1019	749	26*	27
"1190"	235 ± 7	925	741	23.1	24.6
"1250"	464 ± 10	829	640	28.8	25
"Standard" [170]	N.A.**	1240	825	20	N.A.

* Gauge length for elongation measurement in this test: 6.35d.

** N.A. –Not available

Figure 4.34 shows the primary portions of the engineering strain-load curves of the specimens solution treated at 1110°C and 1190°C and tensile tested at 540°C. The stress increased continuously in the strain-load curve until serrations occurred. The serrations started at approximately 1.1% engineering strain in the specimen solution treated at 1110°C and 0.7% in the specimen solution treated at 1190°C. The serrations occurred by the stress slowly dropping and then rapidly rising, and the serrations can be characterized as successive oscillations of stress in the load-strain curve. The serration features such as the length, height and time interval for one serration are shown in Table

4.5, with these corresponding to measurements made below 1.8% strain. The height of the individual serration is also termed as the stress decrement (σ_b) [171]. The serrations in the 1110°C treated specimen, which has a relatively small grain size, have a large stress decrement as well as wavelength. The serration features of the specimens solution treated at 1200°C and 1250°C are similar.

Table 4.5 Features of tensile serrations at 540°C for different heatment treatments

Treatment	Strain to start serrated flow ϵ_c (%)	σ_b (MPa)	Wave length (%)	Time interval (s)
“1110”	1.1	31	0.16	10
“1190”	0.7	16	0.06	5
“1250”	0.72	15.9	0.05	5

4.3.2 Tensile Specimen Surface Observations

The external surfaces of the tensile specimens tested at 540°C appear macroscopically wavy. Intergranular surface cracks were clearly observed in stereographic optical microscopic examinations, since the grains were tinted slightly differently from each other during the tests. Figure 4.35 shows the surface intergranular cracks and some transgranular cracks (Fig. 4.35 c) observed by SEM (with the tensile stress axis being the vertical direction). One side of the surface grain boundary cracks often offset out of the specimen surface, which makes this side appear bright during SEM observations. Grain distortion was also observed in the specimen surfaces. The degree of this grain distortion increased as the grain size increased. The grain boundaries on the

surfaces had a “hill-and-valley” morphology, especially in the largest grain size specimens (Fig. 4.35 c). This indicated that important surface grain boundary sliding occurred during the tests. The grain boundary cracks were observed in “valleys” where stress concentration occurred. Surface microcracks that did not occur along grain boundaries were generally observed close to the tensile fracture surface as shown in Figure 4.36. Such surface transgranular cracks were not observed far from the fracture surface, where the mainly intergranular cracks were always present.

4.3.3 Creep-Rupture Properties

Figure 4.37 shows a typical creep strain vs time curve for the Udimet 520 material solution treated at 1135°C and aged following the two-step aging treatment generally employed in this study. The specimens solution treated at other temperatures showed similar curves as in Fig. 4.37. The transient (primary plus secondary) creep strain is very small. The instant strain upon creep loading is higher in the creep specimen tested in flowing argon than that in air. The rupture life and testing details are listed in Table 4.6. Small grain size material had longer rupture lives than larger grain size material for the same creep conditions (see creep lives of specimens solution treated at 1135°C, 1190°C and 1200°C). Since the stress level of 815 MPa is close to the tensile strength of the material

Table 4.6 Creep-rupture results on Udimet 520 at 540°C

Solution Temperature	Mean intercept length (μm)	Stress level (MPa)	Surface polishing	Environment	Rupture time (h)
1135	106 \pm 4	815	Yes	Air	1196.8
				Flow argon	761/516.1
				Vacuum	570
1190	235 \pm 7	815	Yes	Air	136
1200	245 \pm 9	815	Yes	Air	97.4
1250	464 \pm 10	730	No	Air	61
			Yes	Flow argon	32.6

solution treated at 1250°C, the maximum creep stress employed was 730 MPa for this material. The rupture lives in air were observed to be longer than those in flowing argon for the same grain size material. One creep test was conducted in vacuum and the rupture life and deformation features are similar to those tested in flowing argon.

4.3.4 Creep Fractographic Observations

The macro-fractographic observations showed that two regions existed on the fracture surfaces: an intergranular region and a region of transgranular fracture. The fractured grain boundaries were tainted by the typical oxidation color observed in the slow creep crack growth regions in the CCG tests for Udimet 520 at 540°C. This color is

very different from that of the fast fracture region. Figures 4.38 to 4.40 illustrate the fracture surfaces of creep rupture specimens. The intergranular fracture initiated at the specimen surface and usually one of these intergranular cracks grew deeper than others. Fine grain size materials were noted to have larger intergranular fracture areas than coarse grain materials (Figs. 4.38 and 4.39). Microfractographic observations of fracture surfaces on creep specimens (rather than CCG specimens) tested in air are presented in Figures 4.41 and 4.42. Figure 4.43 shows a fracture surface of a creep-ruptured specimen tested in flowing argon. Intergranular fracture initiated at the surface and fast transgranular fracture was also observed in this relatively inert environment. The fractographic characteristics tested in air and flow argon environment are similar, but the specimens tested in flowing argon revealed more surface grain boundary deformation characteristics than the creep specimens tested in air. These observations indicate that cavitation is not the mechanism for creep fracture in this material under the test conditions employed.

4.3.5 Creep Specimen Surface Observations and Metallographic Cross-Section Observations

Intergranular surface cracks were observed clearly in a stereographic optical microscope since different grains became tinted by slightly different colors during the creep tests. The crack appeared along the grain boundaries perpendicular to the stress axis. Figures 4.44 and 4.45 show the specimen surfaces of creep ruptured specimens. The dimension of the surface cracks increased with an increase in grain size.

Metallographic observations on longitudinal cross-sectioned creep specimens showed that there are only micro-cracks at the specimen surface, as shown in Figure 4.46. No voids or microcracks within the specimen employed were evident, and oxide penetration along microcracks was also observed. Figure 4.47 shows the profile of fracture surface of the creep specimen solution treated at 1190°C. The portions of the fracture surface other than the intergranular fracture region exhibited the features of typical over-load shear fracture.

5. DISCUSSION

This section first presents a short introduction and a schematic summary of the heat treatment versus time-temperature-microstructure relationships in Udimet 520. The effect of grain size on CCG behavior is then discussed. An intergranular crack growth model based on grain boundary sliding (GBS) is developed which is a modification of an earlier model proposed by Wu and Koul [139]. The model agrees with the observations that intergranular cracking is observed in most CCG tests in superalloys. The model which uses the stress intensity factor K as the mechanical driving force takes into account the influence of grain size, grain boundary precipitates, grain boundary morphology and environment on the CCGRs. A brief discussion of the effects of grain size on tensile and creep properties in Udimet 520 is also presented.

5.1 Grain Growth, Carbide and γ' Precipitation in Udimet 520

Microstructural features in superalloys, such as the grain size and the precipitate size and distribution, are controlled by closely adjusting the solution and aging treatment temperatures and times. Grain growth in low γ' volume fraction forged alloys usually begins when the solution temperature is high enough to dissolve the primary carbides in the grain boundary regions. As the temperature approaches the MC carbide solvus temperature, a large amount of primary MC carbides dissolves and this is accompanied by rapid grain coarsening. The solution temperature in most Ni-base superalloys is usually in the range of 1040-1230°C [172]. Solutioning, which controls the grain size, is generally followed by a series of aging heat treatments to control the precipitation of grain boundary carbides as well as intragranular γ' phase. The morphology of the grain boundary carbides is controlled by varying aging temperatures and times as well as the material grain size. The precipitation kinetics of both $M_{23}C_6$ and MC phases are mainly influenced by the chemical compositions and the microstructural state prior to aging [161]. The primary purpose for the microstructural investigation undertaken for the study was to select heat treatment conditions for varying the grain size without precipitating grain boundary carbides.

The conventional heat treatment for wrought Udimet 520 alloy involves a three step treatment consisting of 1121°C/4h/AC, 843°C/24h/AC, 760°C/16h/AC, (where AC indicates air-cooling) [173, 174]. In some applications, a fourth stress relief step of 8h at 816°C followed by air cooling may also be used [175]. After either heat treatment, Udimet

520 microstructure is composed of a Ni-Cr-Co (γ) rich matrix which is hardened by fine (approximately 0.1 μm size) $\text{Ni}_3(\text{Al,Ti})$, gamma prime (γ') precipitates. Grain boundaries are strengthened by M_{23}C_6 carbides [173]. Stringer-like MC carbides may also be present within the grains. Little information has been published on the grain growth and grain boundary carbide precipitation kinetics in Udimet 520, although some work has been conducted on the effect of γ' size and volume fraction on strength [176-178], on the effect of long-term aging on the microstructure and properties (including strengths at room and elevated temperatures and thermal fatigue) and on the deleterious effects of topologically close-packed σ phase [173, 175, 116, 179].

Results gathered from the microstructural investigation have helped establish the phase reactions kinetics, especially for grain boundary M_{23}C_6 precipitation and related microstructural changes, including secondary MC carbide precipitation, in Udimet-520. The relationship of heat treatment versus time-temperature-microstructure in Udimet 520 is summarized schematically in Figure 5.1.

Two interesting features were observed while investigating the grain coarsening behavior. A grain coarsening temperature of 1190°C was identified as expected from MC carbide solvus temperature. However, another grain coarsening temperature was also observed at 1235-1250°C, which is related to the carbonitride solution temperature for the alloy. Another interesting aspect was that the microhardness increase followed the same

trend as the grain growth curve with an increase in solution temperature. The microhardness differences appear to be attributed to differences in the free C, N and Ti solute contents in the matrix, which affect the degree of solid solution hardening of the alloy.

As expected, there are two types of carbides in this alloy and these include MC carbides and primary as well as secondary $M_{23}C_6$ carbides. Below 1100°C , $M_{23}C_6$ can precipitate both at the grain boundaries (GBs) and within the grain interiors given sufficient time at high enough temperature. Secondary MC can reprecipitate at and above 1100°C if enough C is available in the matrix as a result of primary MC dissolution. $M_{23}C_6$ dissolves at 1100°C because specimens with these carbides showed no $M_{23}C_6$ after annealing at 1100°C .

Since grain boundary $M_{23}C_6$ is an important microstructural feature in Ni-base superalloys, a C-curve for the start of such $M_{23}C_6$ carbide formation in Udimet 520 was determined. Material that was solution treated at higher temperature exhibited faster grain boundary carbide (GBC) precipitation kinetics. The reason for this is that at higher solution treatment temperatures, a greater amount of dissolved carbon is available in the matrix as a result of primary MC carbides dissolution. When the aging temperature was below 850°C , discrete grain boundary carbides were often observed and above 850°C , semi-continuous or continuous grain boundary carbides formed.

Two critical temperatures were noted for secondary MC precipitation, 1100°C and 1190°C. Secondary precipitation occurred in the temperature range between 1100°C and 1177°C if the specimen had been solution treated at temperatures above 1190°C. However, at aging temperatures below 1100°C, $M_{23}C_6$ carbide precipitate preferentially at grain boundaries and the secondary MC precipitation does not occur. If the annealing temperature is above 1190°C, the MC carbides dissolve and this secondary MC precipitation does not form. This secondary MC precipitation behavior indicates that the MC carbide solvus temperature is close to 1190°C.

The relationship between grain size, grain boundary carbide distribution, and morphology is quite complex in the alloy. The same aging treatment can produce different grain boundary carbide distributions in terms of their size and spacing and in some cases it can even produce intragranular carbides. The primary reason for this difference is the decreased grain boundary area available for precipitation in coarse-grained materials which vary as a function of solution treatment temperatures as already discussed briefly in section 4.1.1. A given volume of precipitates produced by an aging treatment will therefore form a thicker or more continuous film as grain size increases. As well, at a higher solution temperature, more MC carbides dissolve in the matrix, and more free carbon is available for $M_{23}C_6$ precipitation.

Based on the observation made in the microstructural investigation, solution treatment temperatures of 1110°C, 1135°C, 1190°C, 1200°C and 1250°C were selected to

vary the grain sizes from about 100 μm to 464 μm , i.e. by a factor of greater than 4.5. Furthermore, two step aging treatments were selected to ensure that enough γ' precipitate phase formed during aging and the grain interiors were reasonably well strengthened. The volume fraction of γ' varied slightly, increasing with increasing grain size as shown in Table 4.1. In addition, materials with three different ranges (small, medium and large) were also produced, as planned, to contain no grain boundary carbides. This was important if one aimed to document the effect of grain size of CCG rate independently from the effect of grain boundary carbides, as discussed in the next section.

5.2 The Effect of Grain Size on CCG Behavior in Udimet 520

Several reasons exist for quantifying the effect of microstructure on the creep crack growth behavior of superalloys. First, the creep crack growth rate is a basic consideration in damage tolerance design for materials which operate at temperatures $\geq 0.25 T_M$ and developing quantitative microstructural design relationships for complex alloys is essential. Secondly, it has been reported [84] that failure by creep crack growth (CCG) can occur at temperatures and stresses below those normally considered significant from a creep design point of view. Several alloys such as Alloy 718 and cold-worked stainless steels show very poor resistance to creep crack growth [95] even though they possess good creep rupture strengths. Thirdly, since the fracture mode under CCG condition is essentially intergranular, the CCG tests provide a convenient way of quantifying the effects of grain size and grain boundary microstructural features on high temperature mechanical properties in complex alloys.

In superalloys, the effect of grain size on CCGRs were studied without removing grain boundary precipitates [90, 118, 180]. This is why heat treatments were specifically designed to vary the grain size without precipitating grain boundary carbides in the present study.

5.2.1 Initiation Stage of the Creep Crack Growth Process

It was found that the initial stress intensity factors required to initiate the CCG process in precracked specimens within a reasonable period were quite high (approximately $71 \text{ MPa m}^{1/2}$) in all CCG tests. Test temperature is known to have a strong influence on crack initiation in CCG specimens. In the present case, the test temperature (540°C) was relatively low and a creep crack could be expected to initiate at a high initial K value. The initiation times (t_i) in different grain size Udimet 520 for a stress intensity factor of $71 \text{ MPa m}^{1/2}$ are given in Tables 4.2 and 4.3. The small grain size materials ($100\text{-}106 \mu\text{m}$) had two to four times longer initiation lives than the larger grain size materials ($234\text{-}464 \mu\text{m}$).

5.2.2 Effect of Grain Size on CCGR in the Absence of Grain Boundary Precipitates

The experimental results (Figure 4.21) showed that the CCGR of the specimen solution-treated at 1110°C ($100 \mu\text{m}$ grain size) follows the approximately plot of creep crack growth rate vs K of that treated at 1135°C ($106 \mu\text{m}$ grain size). A CCG test of the specimen solution-treated 1110°C was interrupted by an early fast fracture. An important observation in Fig. 4.21 is that there is little difference in the CCGR vs K relations for the specimens solution treated at 1190°C ($235 \mu\text{m}$ grain size), 1200°C ($245 \mu\text{m}$ grain

size) and 1250°C (464 μm grain size) despite a grain size variation by a factor of 2 among the specimens. In addition, the CCGRs in the smaller grain size specimens, solution treated at 1110°C and 1135°C, are lower than those in larger grain size materials. It is noteworthy that the solution treatment temperatures of 1190°C, 1200°C and 1250°C lie above the MC carbide solvus temperature (1190°C) of Udimet 520; whereas, the solution treatment temperatures of 1110°C and 1135°C lie below this temperature. As a result, some minor differences in the primary MC carbide distribution in the grain boundary region exist between the coarse and fine-grained materials. The effects of grain size on CCGRs in the present investigation are almost opposite to the CCGR results reported by other workers for superalloys [90, 118, 180]. These results are rationalized quantitatively in the section dealing with the mechanistic modeling of CCG.

The CCG test in argon of the specimen solution treated at 1135°C showed lower CCGRs at a given K than in air (Figure 4.22). On a double logarithm scale, the CCGR vs K curve is approximately linear with a slope of about 2. Comparing the results in Figs. 4.21 and 4.22, it is evident that the CCGRs are influenced strongly by oxidation and this results in a higher power to K than 2 in air in the faster CCG region. This oxidation effect becomes stronger with increasing K value.

5.2.3 Fracture and Deformation Mechanisms during CCG

Fractographic observations clearly show that the main features associated with creep

crack surfaces are dominant intergranular fracture, clean grain boundaries with no cavitation damage, and extensive crack branching along the grain boundaries. These secondary grain boundary cracks are more extensive in smaller grain size specimens. While the creep crack growth was predominantly intergranular, a small fraction of localized transgranular fracture occurred on some grain boundary facets, with the average fraction of transgranular cracking increasing with an increase in grain size. The fracture surface was not flat and no severe crack tip tunneling was observed. The observations on polished cross section from interrupted CCG specimens indicated that the formation and growth of intergranular microcracks along the grain boundaries is one of the main deformation and fracture mechanisms operative during CCG and this conclusion is fully supported by the fractographic results.

Although cavitation during creep crack growth has been observed in a wide range of materials, the absence of grain boundary cavities in our creep crack growth studies could be related to the combination of the low test temperature (about $0.5 T/T_m$) and the absence of grain boundary $M_{23}C_6$ carbides in the test materials. A low test temperature would limit vacancy diffusion and the absence of grain boundary $M_{23}C_6$ carbides would suppress cavity nucleation because these precipitates are often reported to be the void nucleation sites [135, 138]. If a creep crack fracture with sufficient cavitation features is regarded as a microscopically ductile fracture, the fracture features in our materials suggest that a microscopic *brittle* intergranular fracture predominates at 540°C in the absence of grain boundary $M_{23}C_6$ carbides. The presence of crack arrest lines in some regions of creep

fracture surfaces (for example, in Fig. 4.26 b) indicates that creep crack tip blunting and crack arrests also occurred during the CCG tests.

Environmental damage due to oxidation is one of the dominant damage mechanisms operative during CCG. Environmental attack along the grain boundaries coupled with GBS was expected to occur during CCG in air.

The localized transgranular fracture features at fractured grain boundary facets are observed to be related to the grain size. This is because the grain boundary facet size and intergranular crack dimensions are proportional to grain sizes. Large grain sizes increase the intergranular crack sizes. Therefore, the stress concentration at the crack tip is usually higher in large grain size specimens when the cracks meet obstacles or when these cracks arrest due to orientation effects. In these cases, the stress concentration may cause localized transgranular fracture as illustrated in Figure 5.2. According to this proposed local stress concentration mechanism, a greater percentage of localized transgranular fracture is expected to be present in large grain size specimens than in small grain size specimens.

Fractographic observations showed that the fracture features for the tests in argon were similar to those in air. Local deformation features on the fracture surface as indicated by crack arrest lines were also observed in specimens tested in argon showed more.

5.3 A Grain Boundary Sliding Controlled Intergranular CCGR Model

As indicated in the literature survey, the CCGR vs K relations are commonly used to rationalize the CCG behavior for high strength heat resistant alloys such as superalloys [90-95, 118, 180], titanium aluminides [113] and aluminum alloys [112]. For example, the following relationship [137] is often observed in superalloys,

$$\frac{da}{dt} = \alpha K^n \exp\left(-\frac{Q}{RT}\right) \quad (5.1)$$

where Q (apparent activation energy), α and m are experimentally determined constants, R is the universal gas constant and T is the absolute temperature. The exponent m often falls in the range of 2 to 8, but it is not equal to the creep stress exponent for the same material. The proportional constant α is often found to vary with microstructure, especially the grain size [e.g. 90, 114, 118, 180] and grain boundary morphology [90].

Most researchers have recognized that the formation and linkage of creep cavities coupled with the environmental effect are the two main micromechanisms involved in CCG. Although intergranular wedge cracks are often observed in CCG tests [119, 180], their contribution to CCG has not been studied thoroughly from a micro-mechanistic point of view. In creep fracture, on the other hand, the formation and propagation of intergranular cracks have been said to be the preferred cracking mode at higher stresses and in large grain size materials [70]. Our results clearly demonstrate that intergranular cracking plays a dominant role in the CCG process in Udimet 520.

Numerous models have already been proposed [e.g. 125, 141, 142, 147, 150, 151, 152, 153, 181, 182, 183, 184] to describe creep crack growth. However, the role of GBS in creep crack growth has not received the attention it deserves. Since CCGRs in engineering alloys are quite sensitive to the grain size and the grain boundary microstructure, GBS coupled with environmental effects are combined to be the main cause of cavity nucleation and growth, wedge cracking, and/or oxide penetration, leading to intergranular fracture, which is the predominant mode of creep crack growth generally observed in numerous experiments, including the present work. Therefore, GBS should be considered to be an important, and possibly rate-controlling, factor in CCG models. The following sections thus focus on modeling creep crack growth by GBS. The analysis incorporates some fracture mechanics considerations in order to derive creep crack growth rates in the crack-tip stress field in the presence of several competing deformation mechanisms.

5.3.1 Effective Stress Distribution Ahead of the Crack Tip

In this analysis, it is assumed that GBS plays a key role in producing creep crack growth in most superalloys. In the present approach, simple and effective stress distributions ahead of the creep crack tip are employed to modify a model proposed by Wu and Koul's unpublished research [139] with a view to establishing the grain size dependence of CCGR in materials with a planar grain boundary structure in the absence of grain boundary precipitates.

At a crack tip, an elastic stress distribution with a singularity builds up when a load is applied. It is generally agreed that the stress singularity can be treated within a small scale yielding region in superalloys operating in laboratory air or other environments. Here, GBS is considered to be the key deformation mechanism which is operative in the small-scale-yielding region defined by r_d (see Figure 5.3). The distance r_d is the location at which the elastic stress is equal to the lower bound of the stress caused by GBS. In the area $r > r_d$, the elastic stress dominates and the effective stress field ahead of the creep crack tip is also shown in Figure 5.3.

The basic form of the elastic stress field is defined according to Westergaard [185]

$$\sigma_x = \frac{K_I}{\sqrt{2\pi r}} \cos\frac{\theta}{2} \left(1 + \sin\frac{\theta}{2} \sin\frac{3\theta}{2}\right) = \frac{K_I}{\sqrt{2\pi r}} f(\theta) \quad (5.2)$$

where

$$f(\theta) = \cos\frac{\theta}{2} \left(1 + \sin\frac{\theta}{2} \sin\frac{3\theta}{2}\right)$$

The value of $f(\theta)$ equals to 1 when only the stress distribution along the assumed crack propagation plane, where the y axis is normal to the crack plane stress, is considered.

In the GBS dominant region, the shear strain rate produced by GBS is assumed to be satisfactorily described by [29]

$$\dot{\epsilon}_{gbs} = B\sigma^p = \frac{D_{gb}\mu b}{kT} \left(\frac{b}{d}\right)^q \left(\frac{l+h}{b}\right)^{q-1} \left(\frac{\sigma}{\mu}\right)^p ; \quad (5.3)$$

where D_{gb} is the vacancy diffusion coefficient along the grain boundaries, b is the Burgers vector, μ is the elastic shear modulus, k is Boltzman constant, T is the absolute temperature ($^{\circ}\text{K}$), l is the dislocation glide distance and q is the grain size index, which has the same meaning as in Eq. [2.6] described in the section 2.1.2.3. The parameter p takes a value of 2 for the grain boundary sliding deformation mechanism [21].

By analogy with the HHR field (see section 2.2.3.4, page 66) [104-106], the stress distribution along an assumed crack propagation plane is described by

$$\sigma_{res} = \left[\frac{C^*}{I_n B r} \right]^{\frac{1}{n+1}} ; \quad (5.4)$$

where I_n is a function of n , B is the constant in Eq. (5.3) and r is the distance from the crack tip. In equation (5.4), C^* is defined by an integral as the form in section 2.2.3.4.

As discussed above, the elastic stress equals the lower bound of the GBS stress operative at a distance r_d ahead of the crack tip as shown in Figure 5.3. That is

$$\left[\frac{C^*}{I_n B r_d} \right]^{\frac{1}{n+1}} = \frac{K_I}{\sqrt{2\pi r_d}} \quad (5.5)$$

From Eq. (5.5) the expression is obtained for r_d :

$$r_d = B^{\frac{2}{n-1}} I_n^{\frac{2}{n-1}} \left[\frac{1}{\sqrt{2\pi}} \right]^{\frac{2(n+1)}{n-1}} C^{\frac{-2}{n-1}} K_I^{\frac{2(n+1)}{n-1}} \quad (5.6)$$

5.3.2 The Proposed Model

By considering that the small scale damage assumption is valid, and that GBS controls the fracture process, we can obtain a relationship for the CCG rate (da/dt) as a function of grain size d , grain boundary geometry λ and the average strain rate caused by GBS $\dot{\epsilon}_{gbs}$. The following derivation is similar to the critical strain model derived by Cocks and Ashby [181].

Let the time $t = 0$ when an element of material at a distance $r = r_d$ ahead of the crack tip begin to experience GBS. Then, after a time increment of Δt , this element is at a distance $r = r_d - \dot{a} \Delta t$ ahead of the crack tip. Here \dot{a} is the creep crack growth rate and is a constant under steady state CCG. The strain caused by GBS outside this element is negligible. The displacement by GBS rate at the element is

$$S = \epsilon_{gbs} d; \quad (5.7)$$

where d is the grain size.

As the crack grows, the GBS strain accumulated in the element is

$$\varepsilon_{\text{gbs}} = \int_0^{\frac{r_d}{\dot{a}}} \dot{\gamma}_{\text{gbs}}(r) dt = \int_{r=r_d}^0 \dot{\gamma}_{\text{gbs}}(r) d\left(\frac{r}{\dot{a}}\right) = \frac{1}{\dot{a}} \int_0^{r_d} \dot{\gamma}_{\text{gbs}}(r) dr \quad (5.8)$$

Assume that the fracture process zone ruptures when the critical GBS displacement S equals to a physical distance λ , i.e.,

$$\lambda = S_{\text{critical}} = \varepsilon_{\text{gbs}} d = \frac{d}{\dot{a}} \int_0^{r_d} \dot{\gamma}_{\text{gbs}}(r) dr \quad (5.9)$$

After rearrangement, the creep crack growth rate is found to be

$$\frac{da}{dt} = \left[\frac{d}{\lambda}\right] \dot{\varepsilon}_{\text{gbs}} r_d \quad (5.10)$$

where, the average strain rate caused by GBS is defined as

$$\dot{\varepsilon}_{\text{gbs}} = \frac{1}{r_d} \int_0^{r_d} \dot{\gamma}_{\text{gbs}}(r) dr \quad (5.11)$$

If CCG occurs as a result of the growth and coalescence of voids which lie on the grain boundaries, the critical displacement can be taken as the spacing between the crack tip and the cavity just ahead of the crack tip. The crack moves ahead one element and the entire process is repeated until the stress intensity reaches the critical stress intensity for fast fracture. It is possible to provide physical meaning for this critical displacement according to the grain boundary structure and morphology. For a planar grain boundary without any precipitates on the grain boundary plane, λ equals the grain size d and for grain boundaries containing grain boundary precipitates, λ equals the precipitate spacing.

Upon combining Eqs. (5.3), (5.4) and (5.11), the average strain rate caused by GBS

can be written as,

$$\begin{aligned}
 \dot{\epsilon}_{gbs} &= \frac{1}{r_d} \int_0^{r_d} (B \sigma^n) dr \\
 &= \frac{1}{r_d} \int_0^{r_d} B \left[\frac{C^*}{I_n Br} \right]^{\frac{n}{n+1}} dr \\
 &= \frac{B}{r_d} \left[\frac{C^*}{I_p B} \right]^{\frac{n}{n+1}} \int_0^{r_d} r^{\frac{n}{n+1}} dr \\
 &= (n+1) r_d^{\frac{n}{n+1}} B^{\frac{1}{n+1}} I_n^{\frac{n}{n+1}} C^{*\frac{n}{n+1}}
 \end{aligned} \tag{5.12}$$

Substituting Eq. (5.12) into Eq. (5.10), the creep crack growth rate can be obtained as,

$$\frac{da}{dt} = \frac{(n+1)d}{\lambda} B^{\frac{1}{n+1}} I_n^{\frac{n}{n+1}} r_d^{\frac{1}{n+1}} C^{*\frac{n}{n+1}} \tag{5.13}$$

Substituting Eq. (5.6) into Eq. (5.13), the steady state creep crack growth rate in terms of K_I and C^* is given by

$$\frac{da}{dt} = \frac{(n+1)d}{\lambda} \left[\frac{1}{\sqrt{2\pi}} \right]^{\frac{2n}{n-1}} B^{\frac{1}{n-1}} I_n^{\frac{2+n-n^2}{(n-1)(n+1)}} K_I^{\frac{2}{n-1}} C^{*\frac{n^2-n-2}{(n-1)(n+1)}} \tag{5.14}$$

This creep crack growth rate equation shows a rather complicated dependence on K and C^* ; however, for ideal cases where grain boundaries are clean and planar, $n=p=2$. Eq. (5.14) then reduces to

$$\frac{da}{dt} = \frac{3}{4\pi^2} \frac{d}{\lambda} BK^2 \tag{5.15}$$

In Eq. (5.15), only the term B is related to the grain size d . From Eq. (5.3),

$$B = \frac{D_{gb} \mu b}{kT} \left(\frac{b}{d} \right)^q \left(\frac{l+h}{b} \right)^{q-1} \propto d^{-q} \tag{5.16}$$

Taking, as discussed in connection with Eq. (5.3), that $q = 1, 2$ or 3 depending on grain boundary morphology, we can predict from Eq. (5.15) the grain size dependence of the CCGR as follows:

$$\frac{da}{dt} \propto \begin{array}{ll} d^0 & (\text{no GB precipitates, } q = 1) \\ \frac{1}{d} & (\text{discrete GB precipitates, } q = 2) \\ \frac{1}{d^2} & (\text{continuous GB precipitates, } q = 3) \end{array} \quad (5.17)$$

Another result obtained from Eq. (5.15) is that for GBS, the CCGR is given by

$$\frac{da}{dt} \propto K^2 \quad (5.18)$$

5.3.3 Model Predictions and Verifications

The CCG tests conducted in this work project serve a useful purpose for verifying the proposed model. The materials had been heat treated to possess different grain sizes, all containing a volume fraction of 8.9-13.6 % intragranular γ' , but without $M_{23}C_6$ grain boundary precipitates. During the CCG tests, no precipitates formed at the grain boundaries. Fractographic studies revealed that predominantly intergranular fracture and extensive crack branching had occurred both in air and in argon. This metallurgical evidence thus suggests that GBS is the controlling deformation and fracture mechanism. Furthermore, intragranular deformation by dislocation climb via volume diffusion should be small in

superalloys at this temperature. Therefore, diffusion creep mechanisms played a minor role in CCG process. Environmental effect is an important factor influencing CCGRs which will be taken into consideration in the subsection 5.3.3.3. The test and material conditions therefore satisfy the assumptions made in the model, and hence the CCGR data are considered to be useful for the verification of the model, as will become evident in the following subsections.

5.3.3.1 The Effect of Grain Size on CCGR

A successful model for CCG should be based on an understanding of the underlying micromechanisms combined with an analysis of the effective macroscopic stress state ahead of a crack tip. Unlike the CCG models generally based on nucleation and growth of cavitation damage, GBS is considered here to be the controlling mechanism responsible for intergranular creep crack growth, whether cavitation damage contributes to the crack growth or not. A critical GBS condition is applied to the model to allow the crack to grow. The critical GBS strain provides a physical parameter which can be related to microstructural features and this model also considers the CCGR dependence on the grain boundary microstructure and morphology.

The present CCGR model predicts that the grain size dependence of CCGR is also influenced by the grain boundary microstructural features as described by Eq. (5.17). The creep crack growth rate is independent of grain size (d) in materials containing planar

grain boundaries with no grain boundary precipitates. The present work on Udimet 520 with planar and clean grain boundaries revealed that the CCGR data were not sensitive to grain size variation over a grain size range of 235–464 μm . These test results thus agree well with the model prediction.

An inverse grain size dependence of CCGR is predicted by the model for a discrete grain boundary precipitate distribution. In superalloys, a discrete distribution of grain boundary precipitates (e.g. M_{23}C_6 or δ phase) is usually present and this presence favors good creep-rupture properties by decreasing GBS. This is why large grain size specimens always were previously reported to have lower CCGRs in superalloys [90, 118, 180]. In IN-792 [90] at 704°C, CCGRs can be roughly estimated to be inversely proportional to $d^{1/2}$ by assuming that the rupture life is inversely proportional to the CCGR. An inversely proportional relationship between CCGRs and grain size has been reported for Alloy 718 (after standard heat treatment) at 650°C [180]. Generally, the CCGRs are roughly inversely proportional to grain size in superalloys and however, the exact grain boundary precipitate distributions are rarely shown in technical reports dealing with grain size effects. In most cases, both the size (h) and spacing (l) of grain boundary precipitates are expected to be different when the same aging heat treatments are employed after obtaining different grain sizes. Therefore, such test results did not express the “pure” grain size effect on CCGRs. The model predictions in the presence of discrete grain boundary carbides are thus generally supported by the results reported in the literature.

A stronger grain size dependence is predicted by the model for materials with a continuous grain boundary precipitate network. Such network may result from overaging or service exposure. No experimental results are presently available on materials containing continuous carbide network in the open literature with which these theoretical predictions could be compared.

In Udimet 520 material, the small grain size (100 μm) material did show slower CCGR compared with the large grain size (235-464 μm) materials, in the absence of grain boundary M_{23}C_6 precipitates. That large grain size specimens have higher CCGRs than small grain size specimens has also been reported for a stainless steel without grain boundary precipitates [111]. These differences between the test results and the predictions of the proposed model can be rationalized as follows. It is reasonable to assume that small grain size specimens reveal lower CCGRs than coarse grain size specimens because more energy is expended in the former during crack tip branching. Fractographic observations also showed that coarse grain size specimens also fractured by local transgranular fracture during CCG. Therefore, a combination of crack tip branching and transgranular fracture is believed to cause the difference in CCGRs between the two groups of specimens of Udimet 520. During solution treatments, grain boundaries moved and naturally encountered some MC carbides. Fractographic observations showed that there were more MC carbides at the grain boundaries in the specimens solution treated at 1110°C and 1135°C (below the MC solvus) than the specimens solution treated at 1190°C, 1200°C and 1250°C (above the solvus). The

differences in CCGRs between the two groups of specimens may therefore be related to a minor difference in MC carbide distribution. Amongst the coarse-grained specimens, the grain sizes vary almost by a factor of two between specimens solution treated at 1190°C and 1250°C, yet there is no difference in CCGRs. This might suggest that the differences in CCGRs most likely occurred as results of difference in grain boundary primary MC carbide distribution than crack tip branching effects.

5.3.3.2 The CCGR Dependence on Stress Intensity Factor

As depicted by the model in section 5.3.1, the creep crack growth in Udimet 520 at 540°C is influenced by the near crack-tip grain boundary HRR stress and by the far-field elastic stress. The CCGRs, plotted in a double logarithm scale against the stress intensity factor K , exhibits a linear behavior with a slope of 2 in an argon environment. The controlling mechanism in this case is believed to be GBS, because this crack growth occurred at a temperature where volume diffusion is negligible. Secondly it was accompanied by intergranular cracking and thirdly the observed K -dependence of the CCGRs agrees with the model's prediction for a GBS mechanism operating in materials with planar grain boundaries. In this case, the stress dependence index of the GBS mechanism is 2 and hence, as predicted by Eq. (5.18), the CCGR depends on the square of the stress intensity factor (i.e., on K^2), but has no dependence on C^* . The fact that various relations of K -dependence, rather than C^* -dependence, have been observed for CCGRs in superalloys may support the argument that GBS plays an important role in

CCG in polycrystalline materials. Particularly, when environmental effects are present, K can still be the appropriate fracture controlling parameter, because environmental effects usually embrittle the material. However, the K -dependence may change from a power of 2 to higher power, as discussed in the next subsection.

In previous CCG models, the m value in deformation controlled CCG models (Eq. 2.20 and Eq. 5.1) has been predicted to be the same as the creep stress exponent n ($n > 2$) in deformation controlled models [138, 139, 182]. These models often consider cavity growth by power law creep in the HHR field or even in the elastic crack tip stress field. Consequently, the logarithmic CCGR vs stress intensity factor curves must show a slope of $m = n$. As mentioned earlier, the m value in CCG tests is rarely reported to be the same as the n value in creep tests. This is because the assumptions that, (1) under steady state, creep rates are inversely proportional to the rupture time, and (2) the crack growth rates are simply proportional to the creep rates do not hold all the time. Another reason for this discrepancy is that grain boundary deformation is responsible for the CCGR and not the creep mechanism occurring expressing creep within the grain interiors. In pure diffusion controlled model, the m value has been predicted to be 3 considering cavity surface diffusion [182] or 4 considering a mechanism of crack propagation by the removal of atoms from the crack tip by stress induced grain boundary diffusion [147]. However, these models do not take into account the deformation and especially the grain boundary sliding effects near the creep crack tip. The m value predicted by diffusion models are absolute and do not fit most CCG test conditions. This is why m has often been treated as

an experimentally determined constant.

5.3.3.3 Oxidation Effect on CCGRs

As shown in Fig. 4.22, the CCGRs in argon are slower than those in air. The materials with grain sizes of 100-106 μm revealed, at relative low K , a slow creep crack growth regime with a slope of 2.3-2.5 and at higher K a faster crack growth regime with a slope of approximately 6.5. However, the materials tested in argon showed only a slow crack growth regime with a slope of approximately 2 over the entire range of K (Fig. 4.22). This change in the K -dependence of CCGR with the environment, i.e. argon versus air, suggests that oxidation has a strong influence on the CCG process. These results suggest that the CCGR is influenced by an oxidation effect to produce the faster CCG regime. The results also indicate that this oxidation effect becomes stronger as the K value increases.

The deviation between the CCGR curves obtained in air and those obtained in argon can be explained by considering the effect of oxidation on Eq. (5.15). If the effect of the environment is taken into account, the critical physical distance λ for fracture will be reduced to $\lambda'=\lambda-X$, where λ is the critical GBS distance in the absence of oxidation effects, and X is the penetrating oxide depth measured from the external oxide surface. For localized oxidation at grain boundaries controlled by the reaction rate at the metal-oxide or oxide-gas interfaces, the oxidation kinetics are described by [186]

$$X = kt \quad (5.19)$$

where k is the oxidation rate constant and t is the time. The time t in Eq. (5.19) can be taken as

$$t = \int \frac{da}{\dot{a}} \quad (5.20)$$

where a is the crack length and \dot{a} is the creep crack growth rate. Combining Eq. (5.15) with Eq. (5.20), the time t is given by

$$t = \int \frac{da}{\frac{3}{4\pi^2} \frac{d}{\lambda} BK^2} \quad (5.21)$$

If we ignore the specimen geometry factor and take the simple form of $K = \sigma\sqrt{\pi a}$ and substitute it into Eq. (5.21), t can be expressed as

$$t = C \log K \quad (5.22)$$

where $C = 8\pi\lambda / (3d\sigma^2 B)$. Therefore, the penetrating oxide depth is approximately given by

$$X = kC \log K \quad (5.23)$$

To a first approximation, the effect of oxidation on CCGR can be expressed by introducing a correction factor to the CCGR given by Eq. (5.15). Substituting Eq. (5.23) for X in Eq. (5.15), while replacing λ by $\lambda - X$, leads to,

$$\left(\frac{da}{dt} \right)_{\text{oxidation}} = \phi(K) \left(\frac{da}{dt} \right)_{\text{no ox}} \quad (5.24)$$

where the correction function takes the form,

$$\phi = \frac{F_1}{F_1 - \log K} \quad (5.25)$$

The predicted trends of CCGR dependence on K before and after the correction are shown in Fig. 5.4 and the curve fitting constants F_1 and F_2 in Eq. (5.25) were determined to be 0.268 and 2.11.

The m values (Eq. 5.1) ranging from 4 to 6 range obtained for the present tests in air are experimentally determined constants. These m values include both oxidation-assisted crack growth and the contribution of local transgranular fracture in coarse grained materials in the overall crack growth process. The difference between the experimental CCGR curves and those predicted from Eq. (5.15) should be able to be depicted by different controlling oxidation mechanisms in the different test/material conditions. The CCGRs of Inconel 718 are reported to be very sensitive to environmental effects [95, 123]. An m value of 8 has been reported for Inconel 718 at 540°C by some workers [93]. The higher m values obtained directly from the CCGR curves and the deviation from the prediction of Eq. (5.18) are therefore not totally unexpected.

5.4 Tensile and Creep Behavior of Udimet 520

5.4.1 Tensile Serrated Flow Mechanism

The primary aim of the tensile experiments at 540°C was to study the influence of the grain size on the high temperature tensile strength and ductility of the Udimet 520 material. The tensile strength decreased with an increase in grain size. A large tensile elongation (>20%) was obtained in the tensile tests, which indicates a large amount of intragranular deformation. Surface intergranular cracks were always present. The tensile curves obtained at 540°C showed serrated flow. The stress dips are approximately 15 and 30 MPa. The time intervals for each serration were approximately 10 or 5 seconds. The critical plastic strains for the onset of the serrated flows were observed to be larger than that for the engineering yield strength ($\sigma_{0.2}$). The specimen with larger grain size had a smaller critical plastic strain. A critical amount of plastic strain (ϵ_c) for the initiation of serrations is well known [187-190]. Nakada and Keh [187] found that the critical plastic strain was related to the serrations, the smaller the critical strain (the higher the carbon content), the more pronounced were the serrations. In the present tests, the specimen with the larger grain size, which was treated at a higher solution temperature, should have a higher solute carbon content within the grains than the specimen with smaller grain size. The result that the specimen with larger grain size has a smaller ϵ_c is consistent with the observations of Nakada and Keh [187]. However, in the present tests the smaller ϵ_c was associated with less pronounced serrations. This

observation suggests that the operating mechanism causing serrated flow in the present specimens may be different from that by classic dynamic strain aging.

The specimen solution treated at higher temperatures are expected to have a higher quenched-in dislocation density. Based on the mechanisms proposed by Mulford and Kocks [191], the theoretical strain required for the onset of serrated flow would be expected to be lower in coarse grained materials. As regard, the difference in the serration amplitude between fine and coarse grained materials, these differences are related to the amount of free Ti available in the matrices after the solution and aging treatments. The fine grained materials contain lower gamma prime volume fraction (Table 4.1) because the quenched-in vacancy contribution in the specimens solution treated at lower temperatures is lower. The higher the vacancy contribution, the higher the nucleation and growth rate of γ' in Ni-base superalloys. As a consequence of this difference, the free Ti in the matrix is higher in fine grained Udimet 520. Again in accordance with the mechanism proposed by Mulford and Kocks [191] and Koul and Pickering [192], higher concentration of elements which reduce the matrix stacking fault energy also increase the amplitude of serrations during tensile testing. This is because a higher driving force is required to move the mobile dislocations through dislocation planes in lower stacking fault circumstances. Therefore, the onset of serrated flow and the amplitude of serrations can be rationalized on the basis of theories proposed by Mulford and Kocks [191] and Koul and Picking [192].

5.4.2 Creep Mechanisms

The creep fracture process has a dominant effect on controlling the creep life and identifying and understanding the operative creep fracture modes are of particular interest. Figure 5.5 shows intergranular cracks already present on the surface of a specimen unloaded just after creep loading. Therefore, the growth of these surface intergranular cracks with the help of GBS and environmental attack is believed to be the dominant fracture mechanism operating during creep. It was shown that there is usually a dominant intergranular crack develops during each creep test (Figs. 4.38 to 4.40) and final fracture always occurs by transgranular shear. The similar intergranular fracture features suggest that the same operative fracture mechanisms observed in creep tests are the same as those observed in early creep crack growth tests. Many workers have demonstrated that, when environmental effects are pronounced, at least for the size of the specimens employed, intergranular cracking can initiate at or close to the specimen surface and can cause creep fracture, in complex creep and corrosion resistant engineering alloys such as cast IN-738LC [36], cast Udimet 720 [78, 81], cast René 80 [193] and wrought Udimet 720 [81]. These observations suggest that oxidation is the controlling mechanism in the above creep fracture cases. Such cases were reported more often for cast superalloys than for wrought superalloys. This type of creep fracture has also been noticed in turbine discs at relatively low temperatures.

At the present creep test temperature of 540°C, the intragranular creep

deformation is expected to be very small. However, considering that matrix creep contribution to total deformation is also very small at this low test temperature, environment attack along the grain boundaries assisted by GBS could be the main deformation mechanism operative in all the experiments. This is why limited creep deformation was observed during the creep tests.

Fig. 4.37 shows that both the instantaneous strain obtained on loading and the creep rupture strain obtained in the inert argon environment are higher than those obtained in air. These results indicate that the environment plays an important role in influencing both the creep strain and the creep rate.

5.4.3 Effect of Grain Size and Environment on Creep life

The creep lives for a given grain size specimen in flowing argon and vacuum experiments were similar. These observations suggested that environmental effect can be easily minimized in argon flow. Longer creep lives were observed with a decreasing grain size. According to the fracture mechanism operative, the growth of the surface intergranular cracks produced at the start of testing occurred with the help of GBS and environmental attack during creep and caused the final fracture. The stress intensity factor at the surface crack can be taken as [194]

$$K_1 = 1.12\sigma\sqrt{\pi a}$$

where σ is load stress and $2a$ is the size of the surface cracks. The stress intensity factor for

the surface cracks is proportional to crack size \sqrt{a} and stress σ . It would be expected that the fine grain size materials had smaller initial surface microcracks than the coarse grain size specimens. When one of the surface cracks grew to a critical dimension the material fracture toughness was exceeded, and fast fracture was expected to occur. Therefore, the grain size effect on creep life is rationalized on the basis of difference in surface microcracks. Unfortunately, no meaningful minimum creep rate information could be obtained because the creep curves were very flat in short term tests. Long term tests of the order of 1000 hours and over would be required to obtain any meaningful data.

For the same grain size material, the creep lives in air were longer than those in a relatively inert environment such as flowing argon or vacuum. These results suggest an oxidation hardening effect on the creep properties where the surface oxide becomes load bearing and suppresses further environmental attack until the oxide spalls or fractures. An indirect consequence of the oxidation, the initial hardening effect can be observed in flowing argon tests where higher instant strain accumulates upon loading in flowing argon than in air.

6. SUMMARY AND CONCLUSIONS

A microstructural investigation was carried out and the results are summarized as below,

1. The grain coarsening behavior in Udimet 520 is controlled by the dissolution of primary MC carbides and M(C, N) carbonitrides. There are two distinct grain coarsening temperatures (GCTs) in Udimet 520 corresponding to a MC solvus temperature of 1190°C and a M(C, N) solvus temperature of 1235-1250°C.
2. The grain boundary as well as the intragranular $M_{23}C_6$ carbide precipitates form in this alloy over a temperature range of 600-1050°C. Different types of $M_{23}C_6$ precipitation reactions were observed leading to different precipitate morphologies. The presence of discrete grain boundary carbides was observed at aging temperatures below 850°C; whereas, a continuous grain boundary network of carbides resulted from higher aging temperatures. Intragranular $M_{23}C_6$ precipitates are strongly influenced by the dissolution of primary MC carbides in this alloy. A TTT diagram (C-curve) for the start of the grain boundary $M_{23}C_6$ carbide formation in Udimet 520 alloy was determined experimentally.
3. A high solution treatment temperature induces intragranular $M_{23}C_6$ carbide precipitation upon aging due to increased free C content and reduced grain boundary area available

for accommodating the precipitates.

4. Secondary MC carbide precipitation is observed in the range of 1100-1177°C after solutionizing at a temperature equal to or greater than 1190°C. The MC carbide solvus temperature of Udimet 520 heat investigated is close to 1190°C and M(C, N) carbonitrides dissolve above approximately 1250°C. No secondary MC carbides were observed in specimens solution treated below 1190°C. Therefore, primary MC carbide dissolution appears to be a precondition for the precipitation of secondary MC carbides in the alloy.

5. The sequence of carbide precipitation reactions and grain coarsening behavior are presented in the form of a time-temperature-microstructure relationship (Figure 5.1). Based on the understanding of the kinetics of carbide precipitation, γ' precipitation and grain growth, heat treatments were designed for Udimet 520 Ni-base superalloy to obtain different grain sizes in the absence of grain boundary carbides but containing 9 to 13% volume fraction of γ' within the grains.

6. The effect of grain size on creep crack growth (CCG) in the absence of grain boundary carbides was studied at 540°C. The fractographic studies and crack tip region profile of interrupted CCG specimens indicated that intergranular fracture was the dominant fracture mechanism and grain boundary sliding (GBS) coupled with environment attack are the main causes responsible for CCG in air under the test conditions employed. In argon environment, the test/material conditions are suitable for the validation of the proposed

GBS-based CCGR model.

7. The creep crack growth rates were insensitive to the changes in grain sizes in specimens solution treated either above (the middle and large grain sizes) or below (the small grain size) the MC carbide solvus temperature in air. However, the CCGR of specimens solution treated above the MC carbide solvus temperature was about 2.5 time higher than those treated below the MC carbide solvus temperature. The reason for higher CCGRs in specimens solutionized above the MC carbide solvus temperature than those below the MC carbide solvus temperature is believed to be mainly related to the differences in crack tip branching behavior and also primary MC carbide distribution along the grain boundaries.

8. The oxidation effect increased the CCGRs and the phenomenological slope of the da/dt vs K relation.

9. A GBS-controlled intergranular crack growth model has been developed with the assumption that the creep crack growth in superalloys is mainly controlled by GBS. In creep brittle materials, such as superalloys, the effective stress zones are considered consisting of the GBS zone and the elastic zone. The model predicts that the GBS-controlled CCGR has a dependence on the stress intensity factor (K) to the power of 2 and this slope value was confirmed experimentally. The deviation between CCGR curves tested in air and those in argon can be explained by considering oxidation effect in the

proposed model. The model also predicts that the GBS-controlled CCGR is independent of grain size (d) for planar grain boundary structures containing no grain boundary precipitates. The developed equation showed that the CCGR is inversely proportional to the grain size in the presence of discrete grain boundary precipitates, which generally agrees with the available superalloy results in the literature. And, for continuous precipitate grain boundary distribution, the CCGR is predicted to be inversely proportional to d^2 . The CCG tests of planar grain boundary structure without grain boundary precipitates generally showed higher CCGRs in larger grained materials than smaller grained materials. The reasons for the increasing CCGR with increase of grain size in planar grain boundary structure are suggested to result from the occurrence of be the more crack branching in small grained materials and more local transgranular cracking in large grained materials.

10. The high temperature tensile results showed that the serrated flow features are related to the quenched-in dislocation density, and the amount of free Ti in the matrix which reduces its stacking fault energy in Udimet 520 at 540°C. The height and wave length of the serrations of the small grain size specimen are about 2.3 times those of the middle grain size specimen. The serration features of middle and large grain size specimens are similar. The large grain size specimens have low critical strain. These results can be rationalized on the basis of mobile dislocation interaction with dislocation forests which are influenced by the quenching process and the matrix stacking fault energy

11. The macro-fractographic observations in the creep test program showed that there two regions existed in the fractured surfaces, intergranular region and fast transgranular fracture region. The intergranular fracture initiated at specimen surface and the growth of these surface intergranular cracks controlled the rupture life during creep. Fine grained materials showed longer creep lives than coarse grained materials under similar creep testing conditions. For the same grain size material, creep lives in air were longer than those tested in relatively inert environment such as flow argon or vacuum. These results suggested that an oxidation hardening effect is operative during creep.

Recommendations for Further Work

Further work is recommended to better understand the effect of microstructural features on creep and creep crack growth behavior of Udimet 520 at intermediate temperature (540°C):

1. Long-term creep tests are recommended to obtain meaningful creep minimum rate data.
2. More CCG tests in inert environment are recommended to investigate the environmental effect on CCG process.
3. More CCG tests as a function of microstructural features, for example in the materials with different grain sizes containing continuous grain boundary precipitates, are recommended to validate the proposed GBS-based CCGR model.

FIGURES

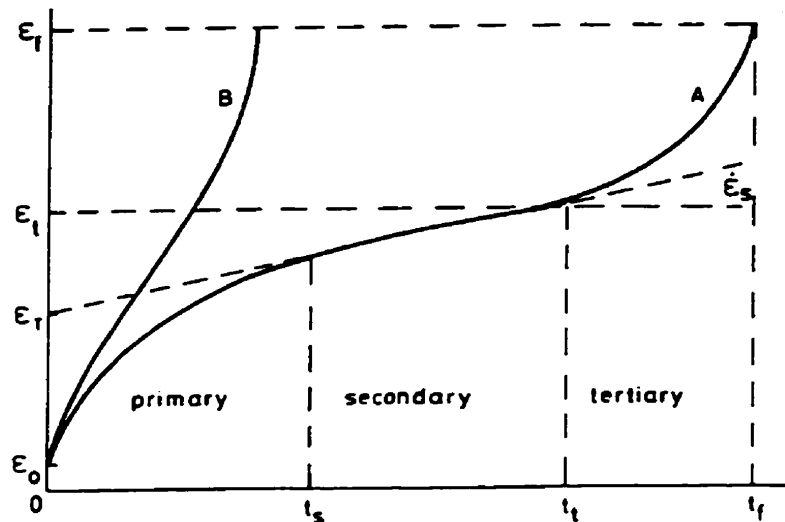


Figure 2.1 Schematic creep curves for constant (A) tensile stress and (B) tensile load [7].

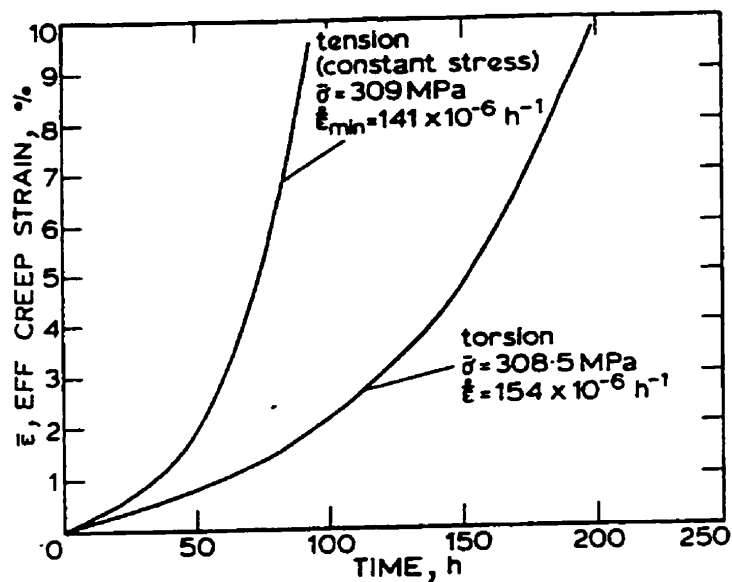


Figure 2.2 Effective shear strain rate vs. time. Torsion and constant stress uniaxial tension at same effective stress [9]. The effective stress $\sigma = 3/2^{1/2} \times$ octahedral shear stress. In uniaxial tension σ is numerically equal to the applied tensile stress. The effective strain ϵ ($=$ octahedral shear strain/ $2^{1/2}$) is equal to the tensile strain in a uniaxial tensile test.)

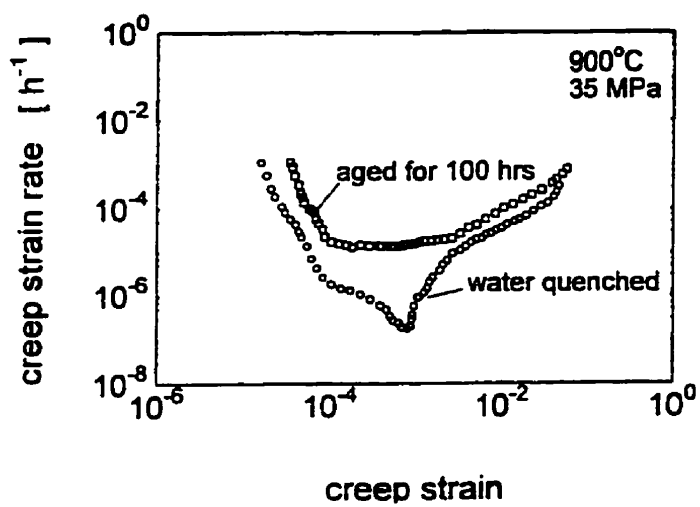


Figure 2.3 An example of creep strain vs time relationship of IN-800H alloy [10].

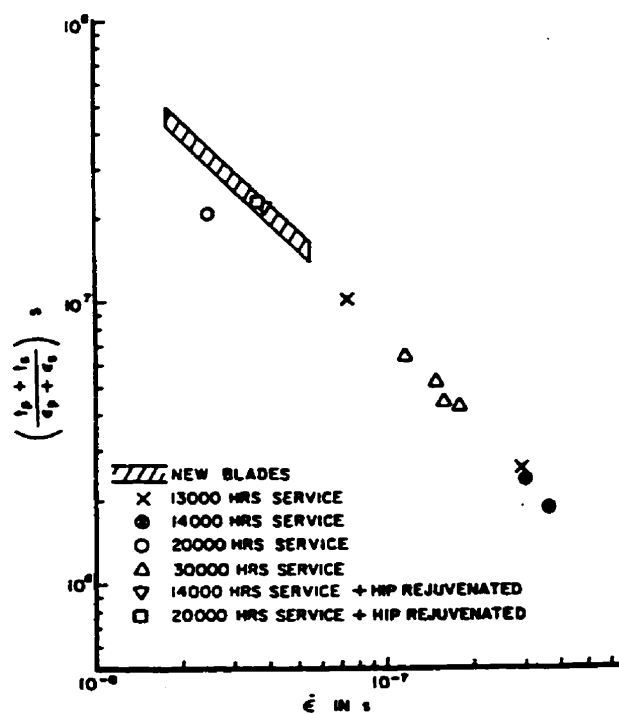


Figure 2.4 Primary and secondary creep properties of new and service exposed blades, creep tested at 350 MPa at 830°C. Superimposed is the rejuvenated turbine blade data [11].

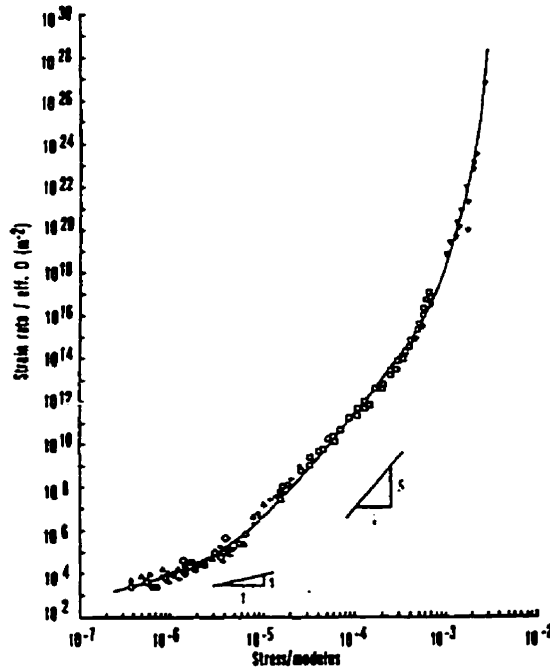


Figure 2.5 Minimum creep rate for aluminum over a wide range of stresses [16].

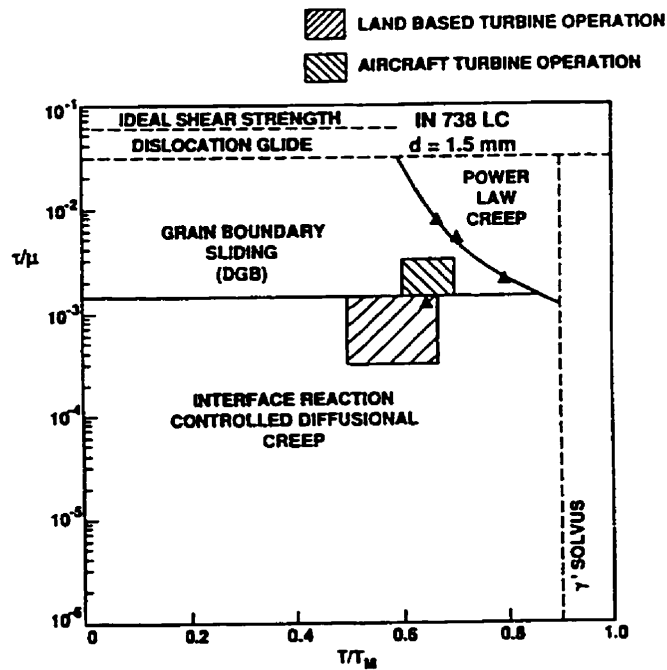


Figure 2.6 A deformation mechanism map for IN738LC blades indicating typical operational stress and temperature regimes for industrial and aero engine blades [28].

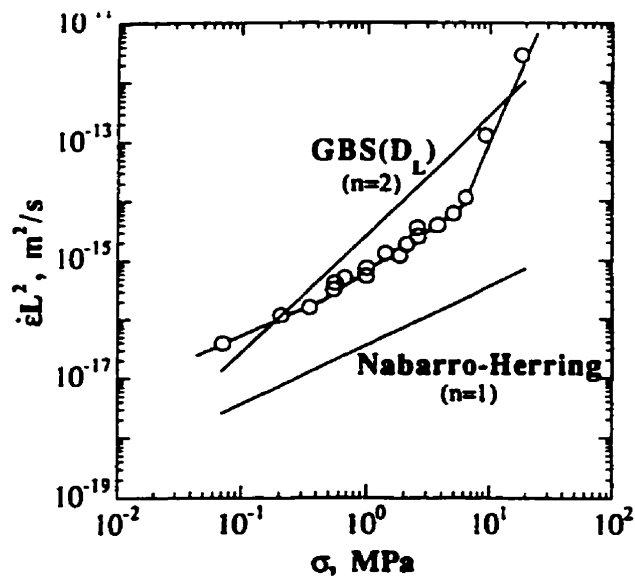


Figure 2.7 The predicted curves for diffusional creep and GBS compared with experimental data for fine-grained copper at 820°C of Burton and Greenwood [33].

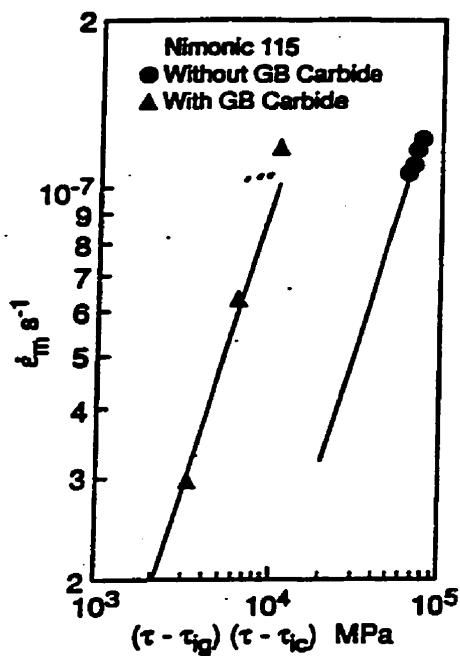


Figure 2.8 The minimum creep rate vs the multiplication of $(\sigma - \sigma_{ig})$ and $(\sigma - \sigma_{ic})$ in Nimonic 115. For the material with grain boundary carbides, $\sigma_{ig} = \sigma/b$, $b = 1.3$, and $\sigma_{ic} = 487$ MPa. The minimum creep rate data are taken from ref. 23. The solid lines represent the line of regressions [29].

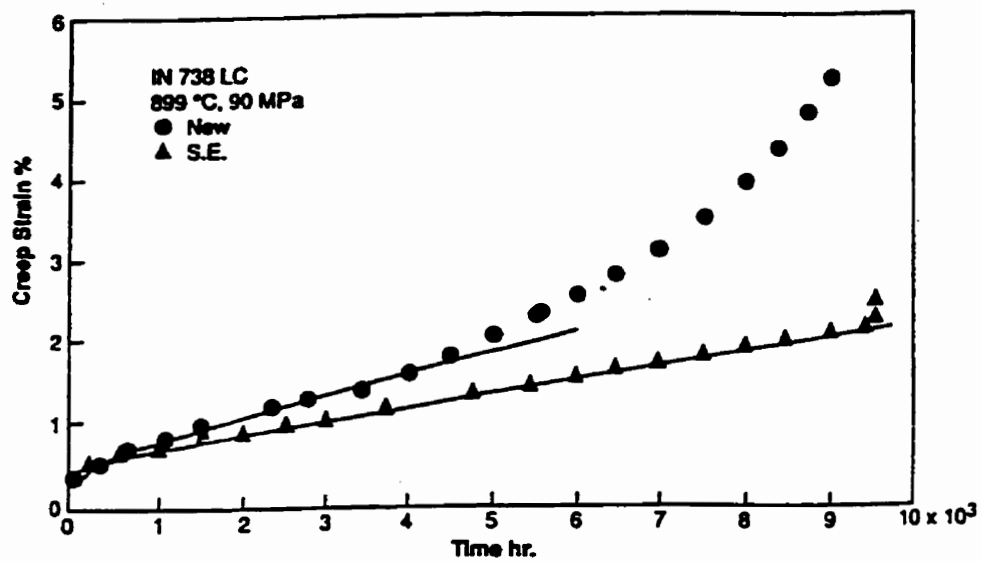


Figure 2.9 Creep strain vs time relationship for new and service exposed IN738LC blades tested at 899° C and 90 MPa. The symbols represent the test data [35]. The solid lines represent the predictions [29].

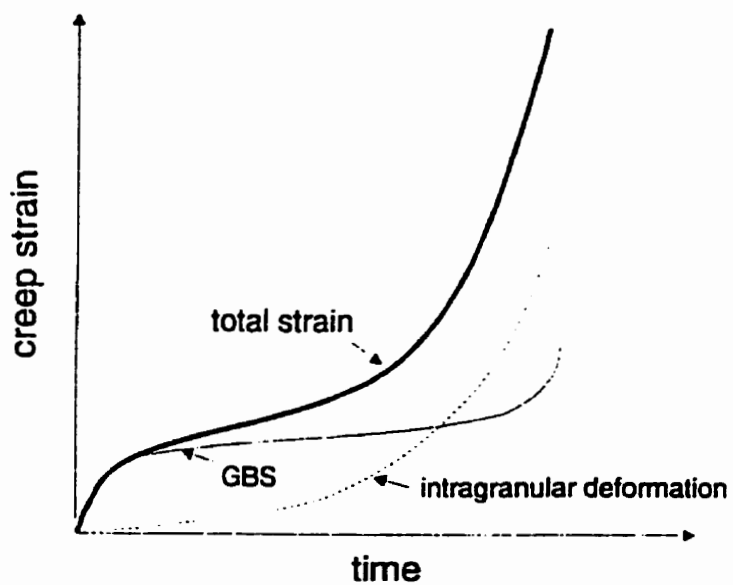


Figure 2.10 Schematics of the creep curve [3].

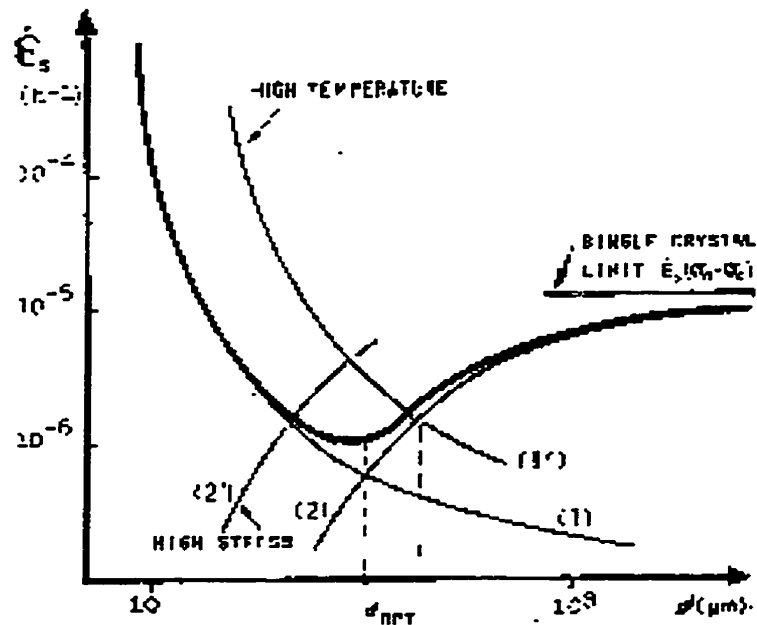


Figure 2.11 Existence of an optimal grain size for which the minimal creep rate is lowest in a superalloy with $f_v = 20\%$ tested at 800°C at a stress 150 MPa [47].

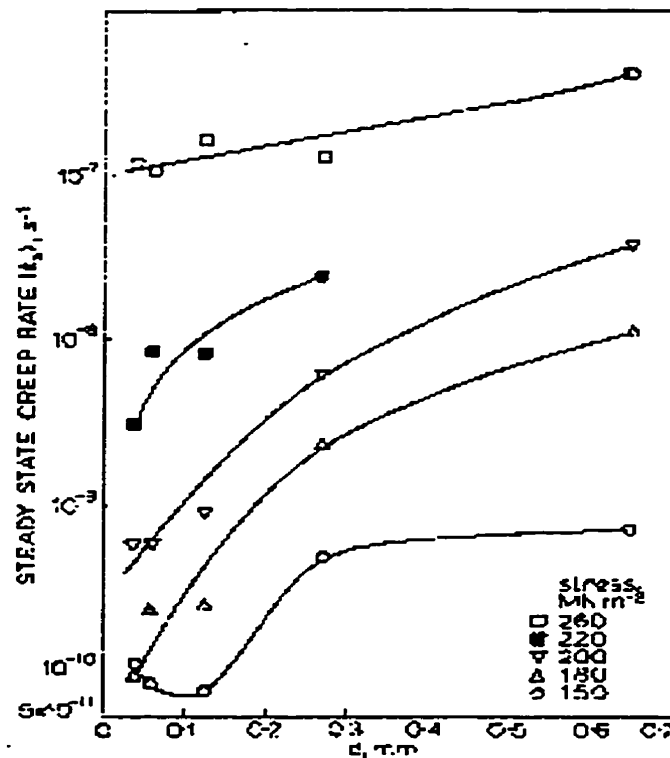


Figure 2.12 Variation of steady state creep rate with grain size at various stresses at 873 K in type 316 stainless steel [49].

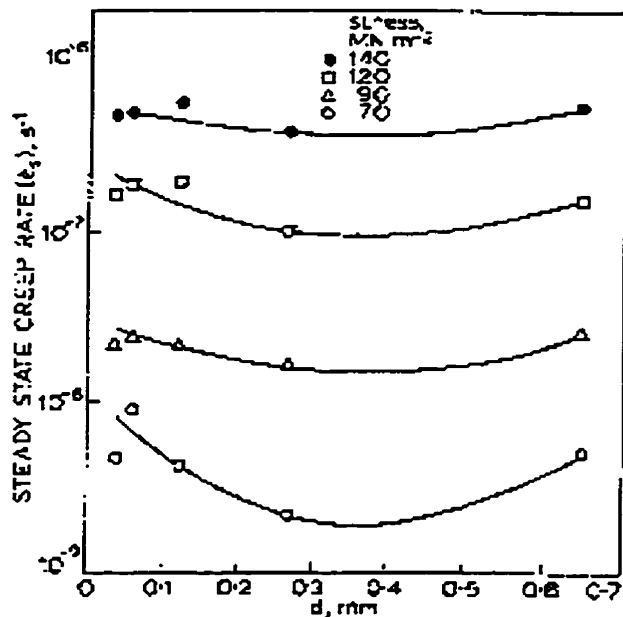


Figure 2.13 Variation of steady state creep rate with grain size at various stresses at 973 K in type 316 stainless steel [49].

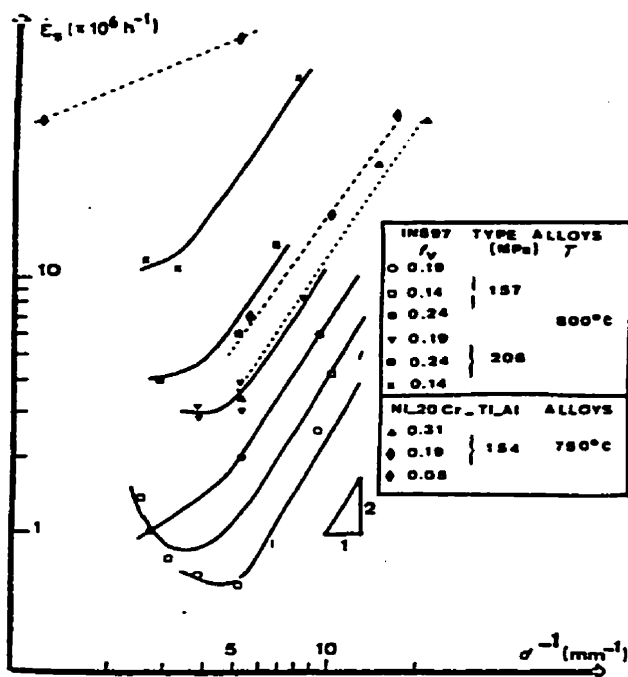


Figure 2.14 The effect of grain size on the minimum creep rate for a series of Ni-based alloys tested at 800°C [50].

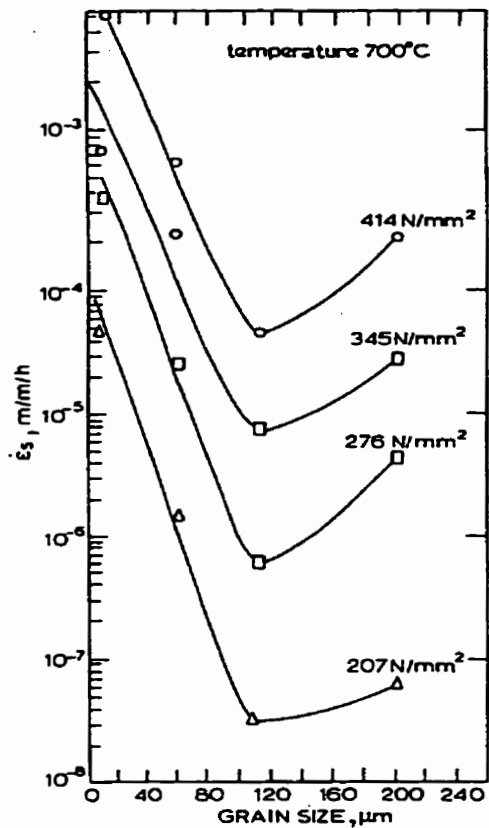


Figure 2.15 The secondary creep rate vs. grain size test at 700°C in Inconel X-750 [51].

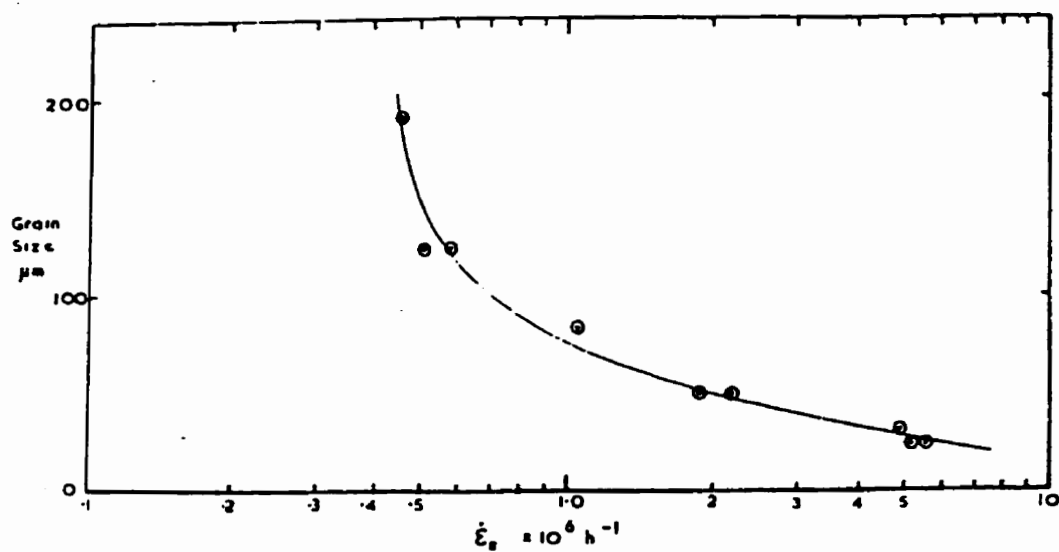


Figure 2.16 The variation of secondary creep rate with average grain diameter tested at 600°C in Nimonic 80A [52].

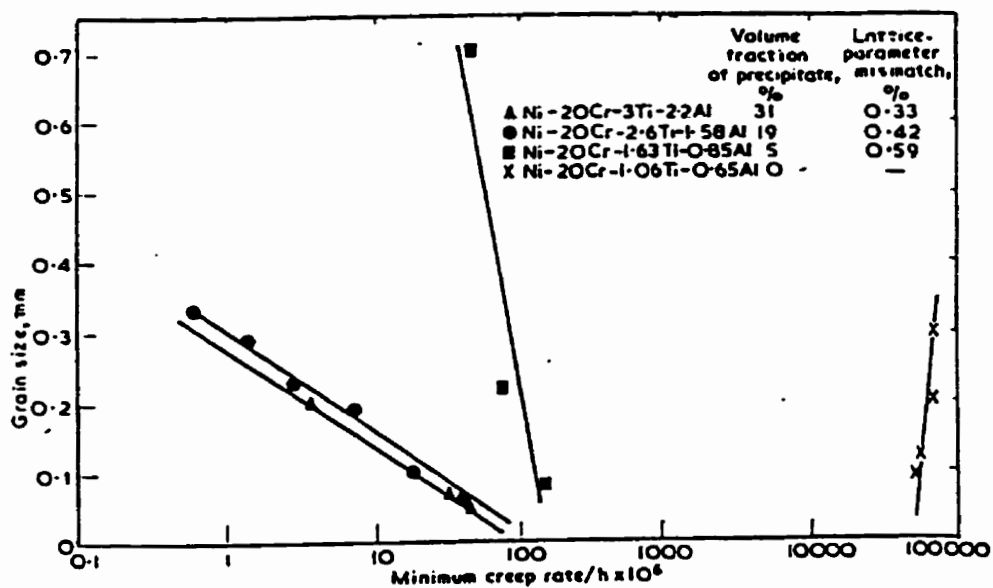


Figure 2.17 The effect of grain size on minimum creep rate for different mismatch and volume fraction of γ' in Ni-20 Cr carbon free alloys. Creep condition: 154.4 MN/m^2 at 750°C [55].

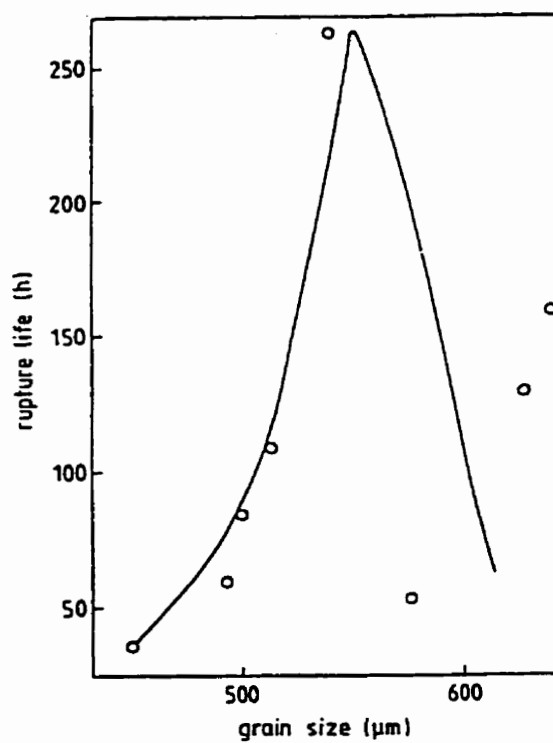


Figure 2.18 Variation of the rupture life as a function of grain size test at 900°C in a cast superalloy IN-100 [58].

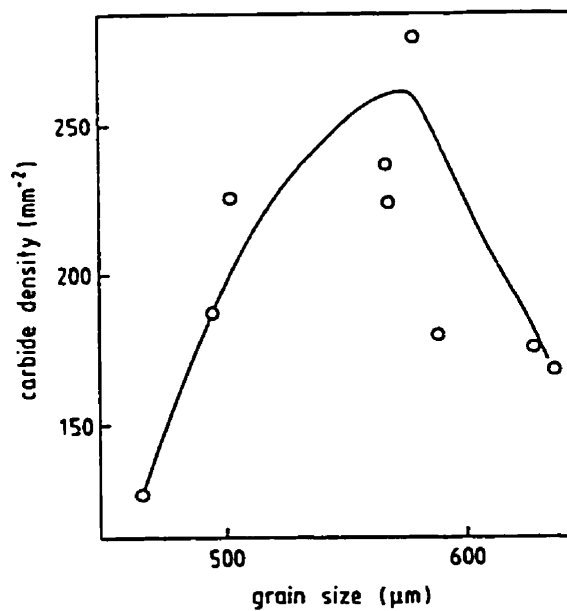


Figure 2.19 Carbide density vs. grain size. Note that this curve is similar to that shown in Fig. 2.18 [58].

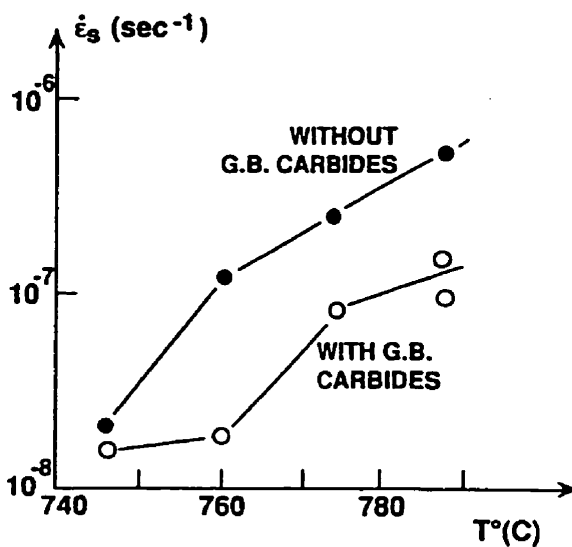


Figure 2.20 Effect of grain boundary carbides on the minimum creep rate of Nimonic 115 over a range of temperatures at 517 MPa [23].

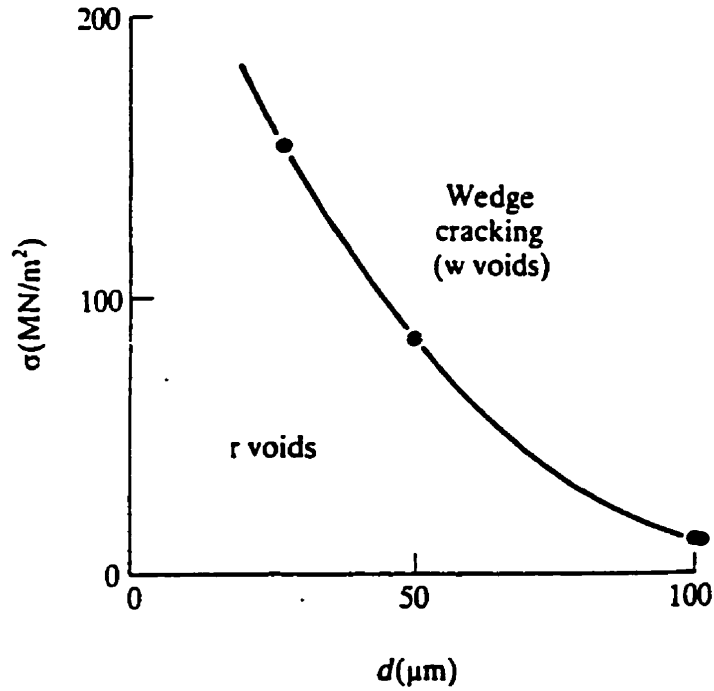


Figure 2.21 Relative tendencies for wedge (w) and cavity (r) voids as a function of stress and grain size [70].

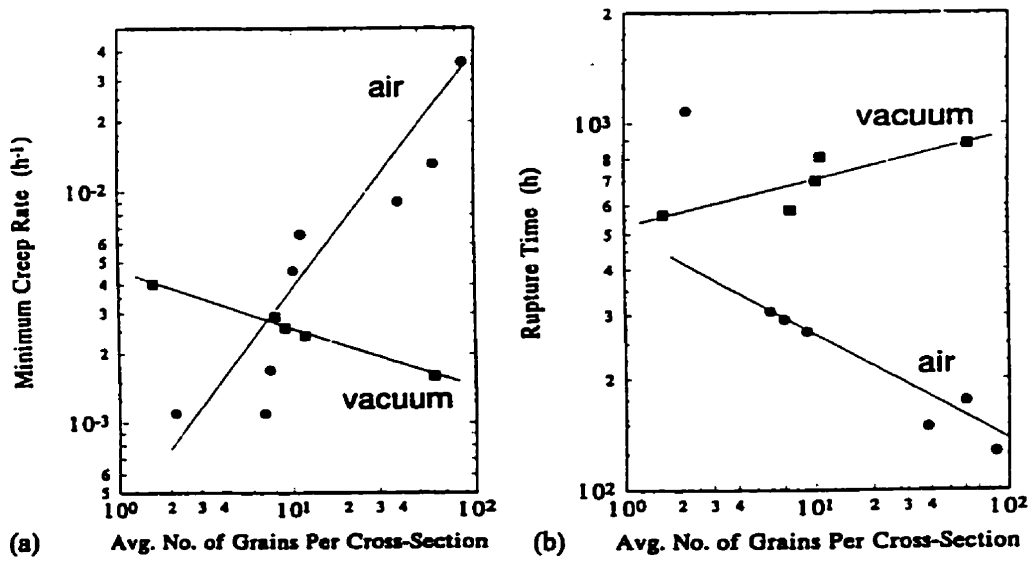


Figure 2.22 (a) Minimum creep rate data and (b) rupture life data for Udimet 700 at 927°C and 172 MPa, in air and vacuum [78] as replotted in ref. [3].

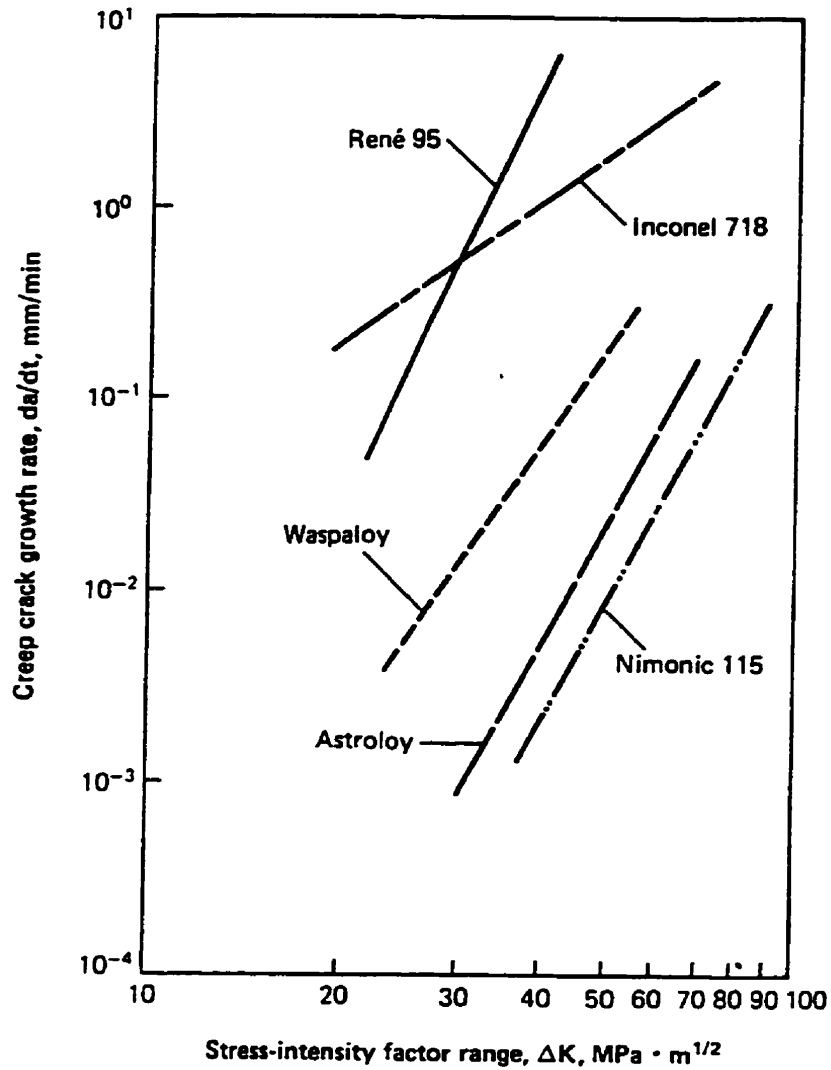


Figure 2.23 Creep crack growth rate data for various superalloys at 704°C [92].

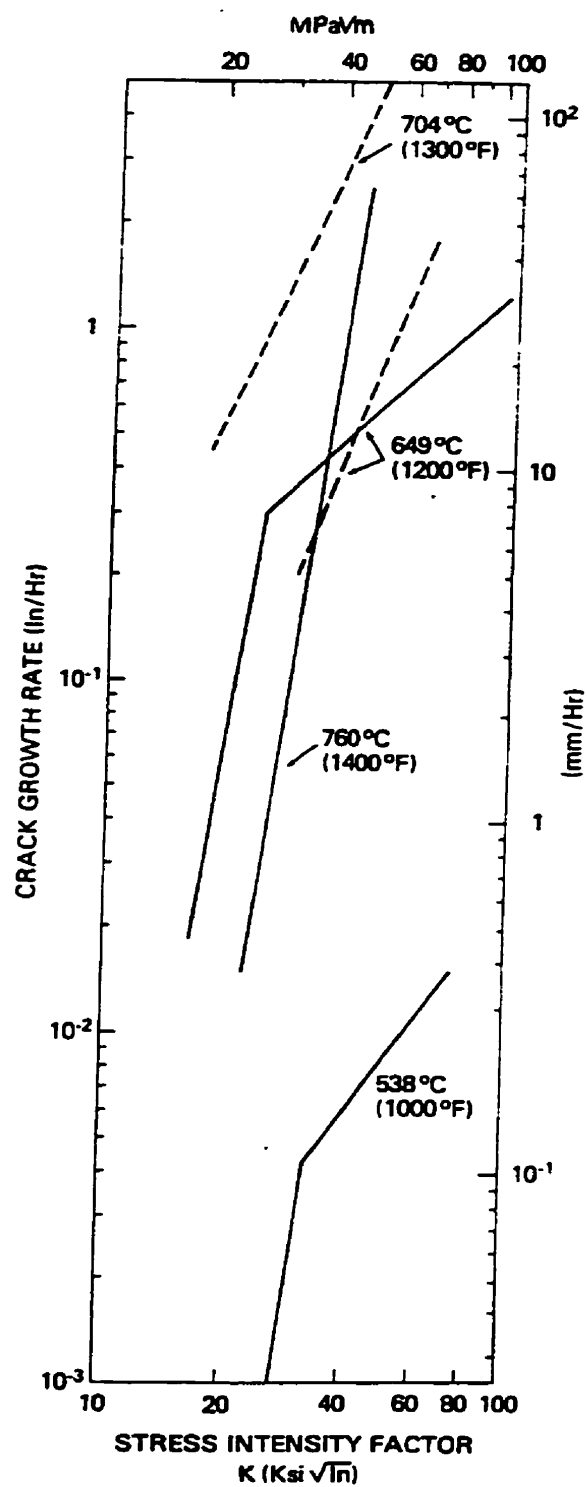


Figure 2.24 Effect of temperature on creep crack growth behavior in Inconel 718 [93].

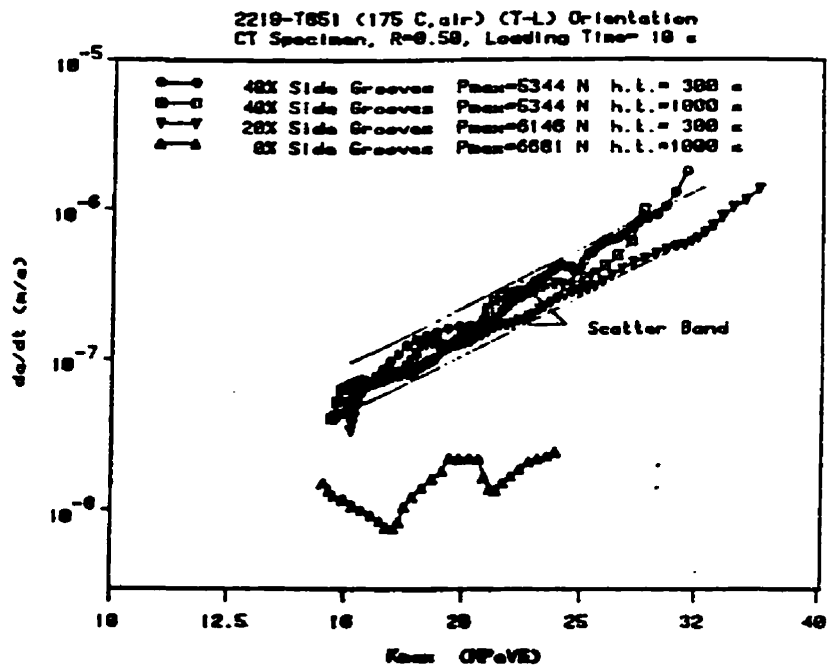


Figure 2.25 Effect of side groove depth on CCGR in an aluminum alloy [116].

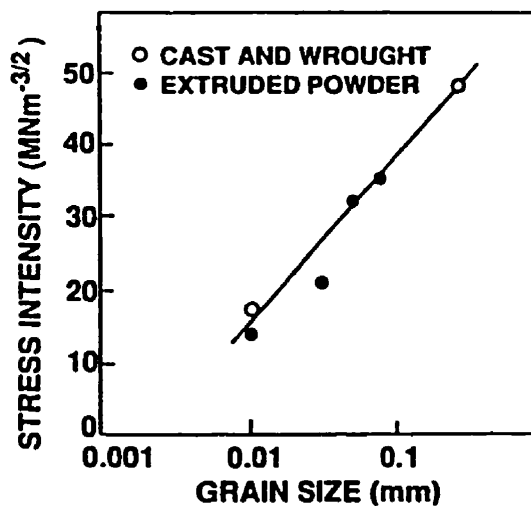


Figure 2.26 Initial stress intensity to produce failure in 100 h at 704°C vs grain size [90].

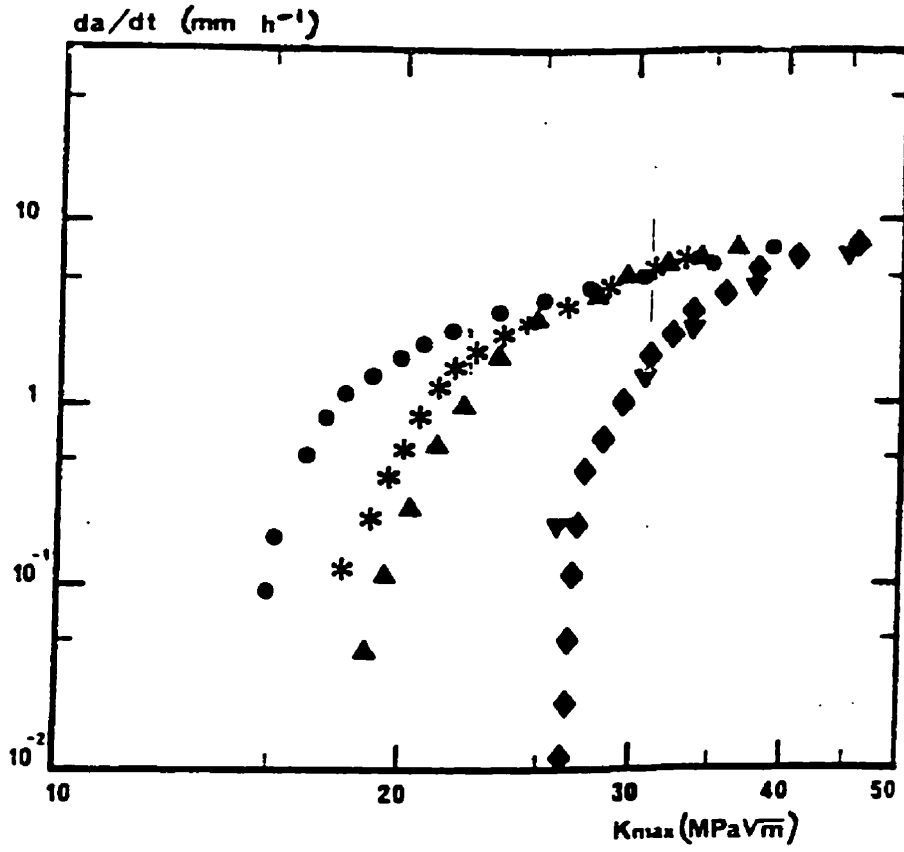
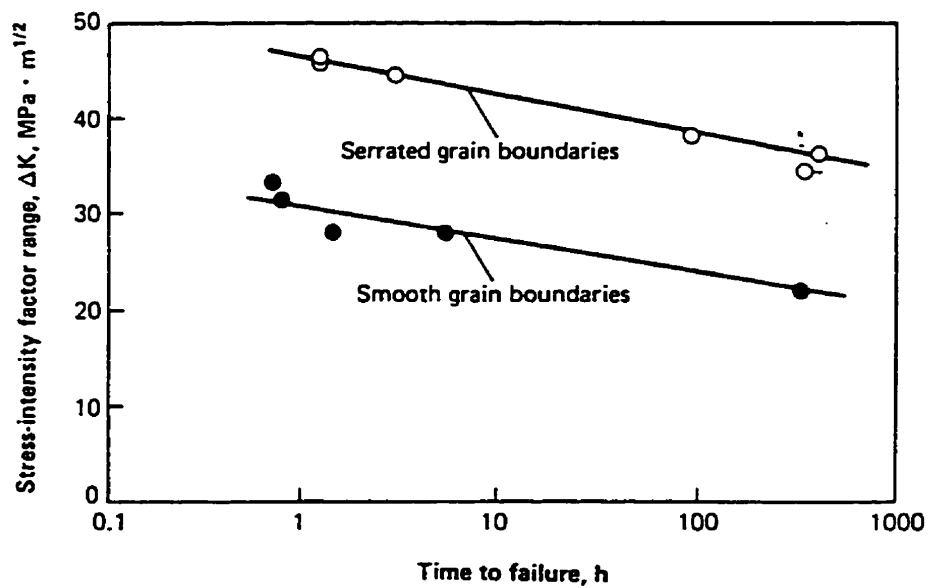


Figure 2.27 Creep crack growth rate as a function of microstructure at 650°C: ◆, necklace structure; ▼, coarse grain (L-S); ▲, coarse grain (S-L) ●, fine grain; *, fine grain (β) [118].



(a) Serrated grain boundary microstructure of IN-792



(b) Time to failure vs stress intensity factor with either smooth or serrated grain boundaries for IN-792 at 704°C

Figure 2.28 Effect of grain boundary structure on CCG [90].

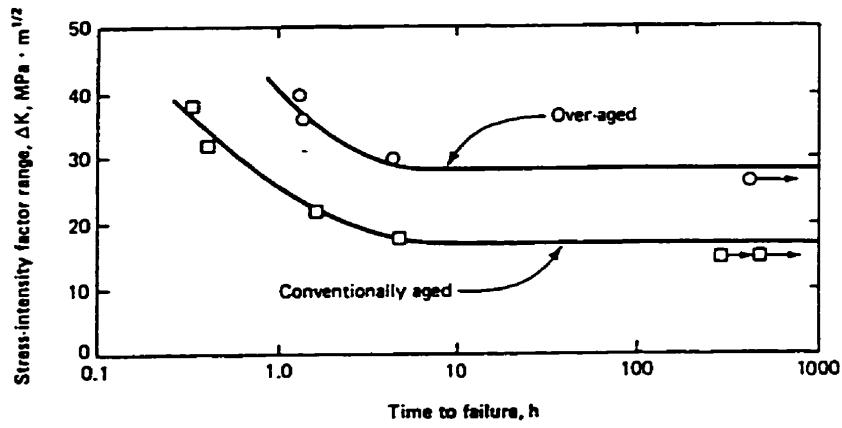


Figure 2.29 Time to failure vs stress intensity factor with various heat treatments for Inconel 718 at 649°C [92].

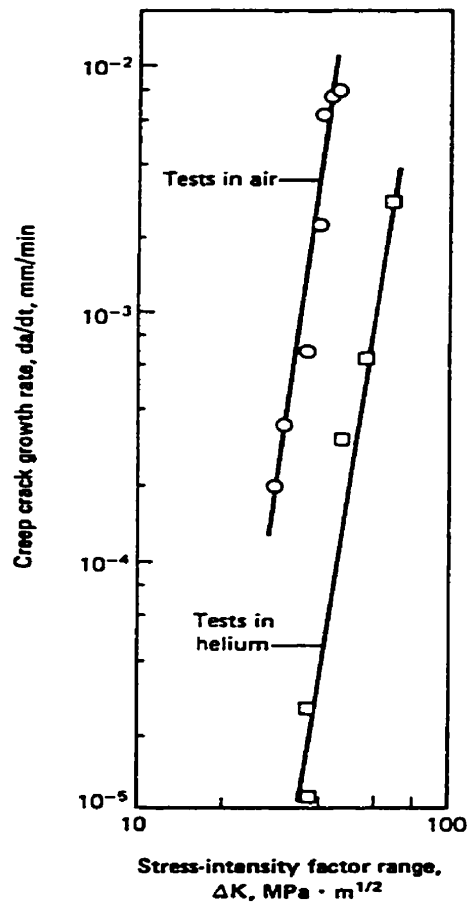


Figure 2.30 Creep crack growth rates in air and helium for Inconel 718 at 650°C [123].

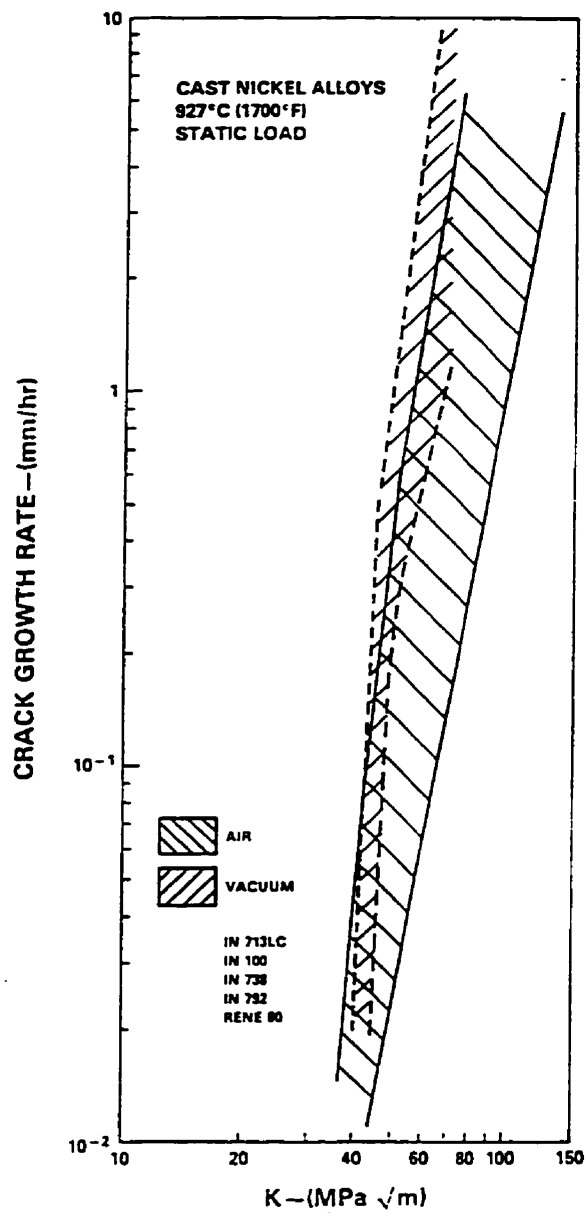


Figure 2.31 Comparison between creep crack growth rates in superalloys in air and in vacuum at 927°C [134].

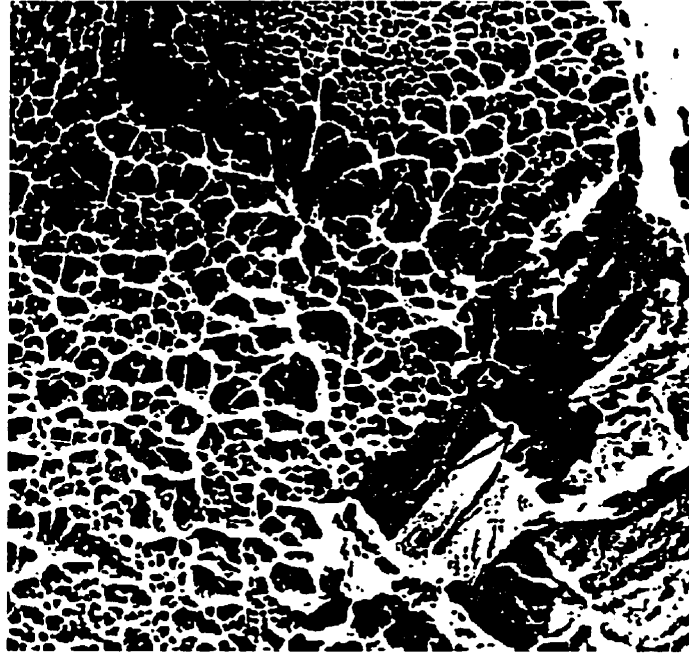


Figure 2.32 Interlinked cavities at the creep crack tip, $\times 720$ [138].

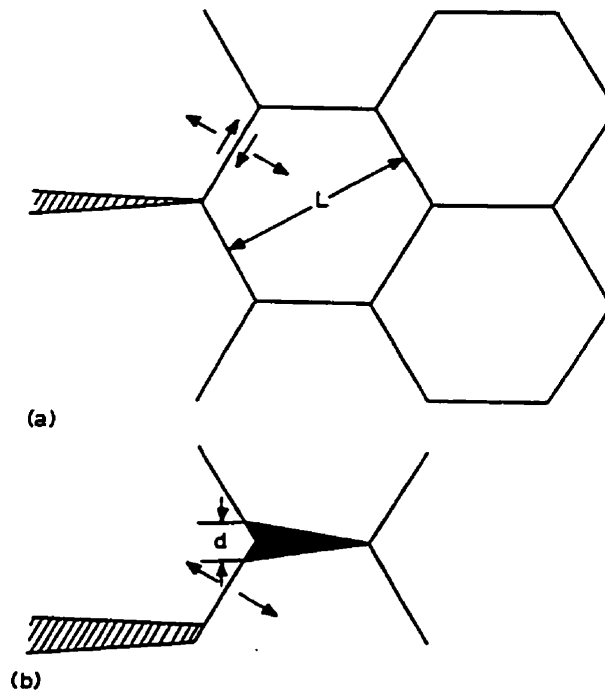


Figure 2.33 Grain boundary sliding contributing to crack growth [152].

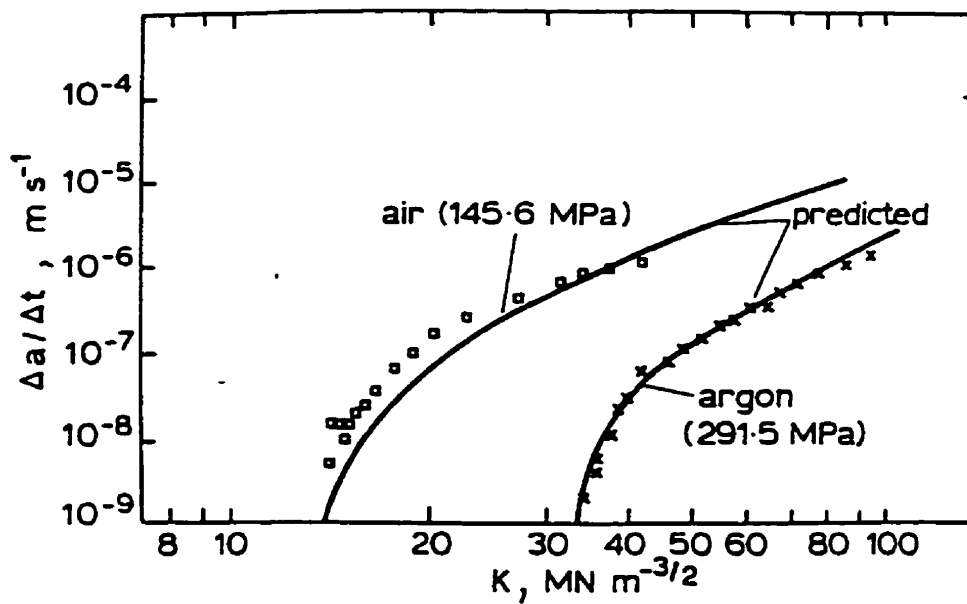
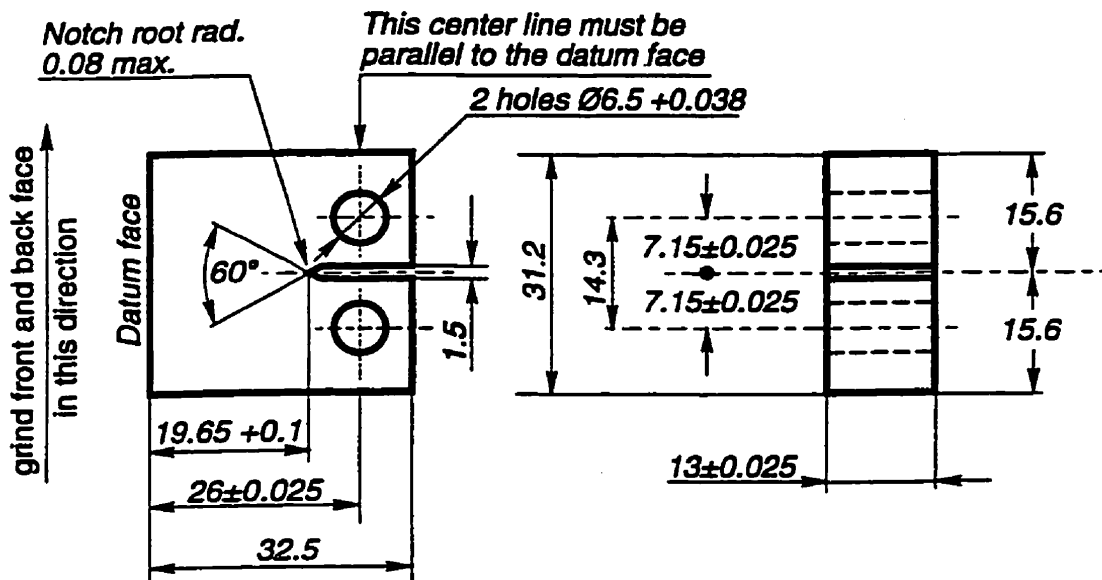
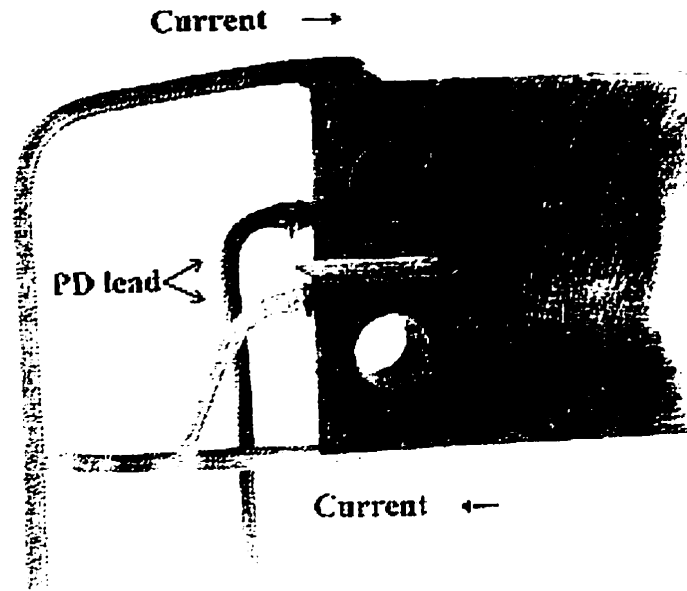


Figure 2.34 Comparison of measured and calculated creep crack growth rates at 704°C of PM HIP MERL 76, an advanced disc alloy [22].

**Note :**

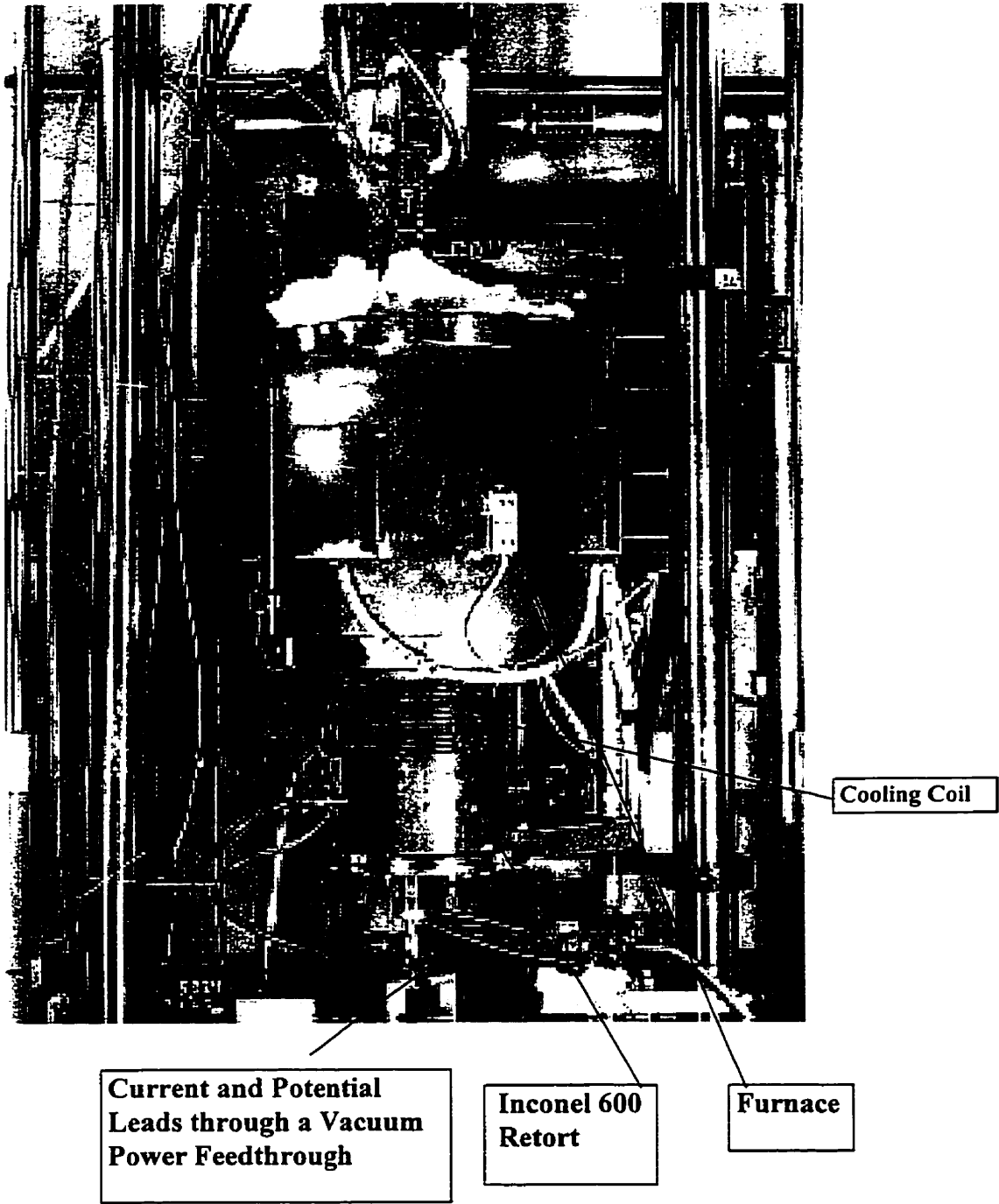
1. Dimensions are in millimeters.
2. Tolerance is ± 0.05 mm unless otherwise specified.

3.1 (a) Specifications of the AGARD CT specimen.



3.1 (b) A CT specimen with current & potential leads attached to it (with fiberglass insulator sleeves around the leads), $\times 1.5$.

Figure 3.1 The CT specimen for CCGR testing.



**Current and Potential
Leads through a Vacuum
Power Feedthrough**

**Inconel 600
Retort**

Furnace

Cooling Coil

Figure 3.2 Test Assembly for Vacuum CCG tests

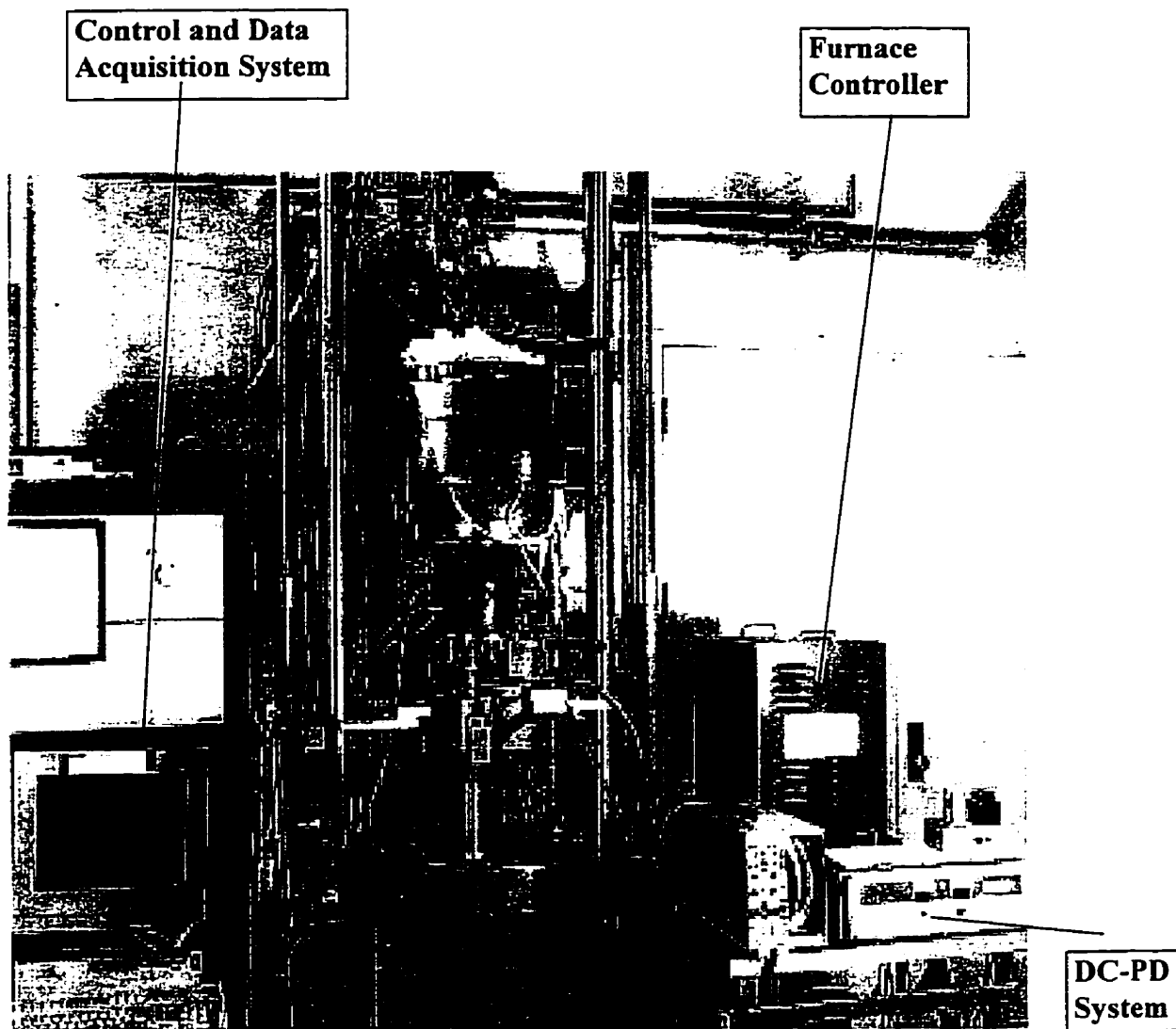


Figure 3.2 (Continued)

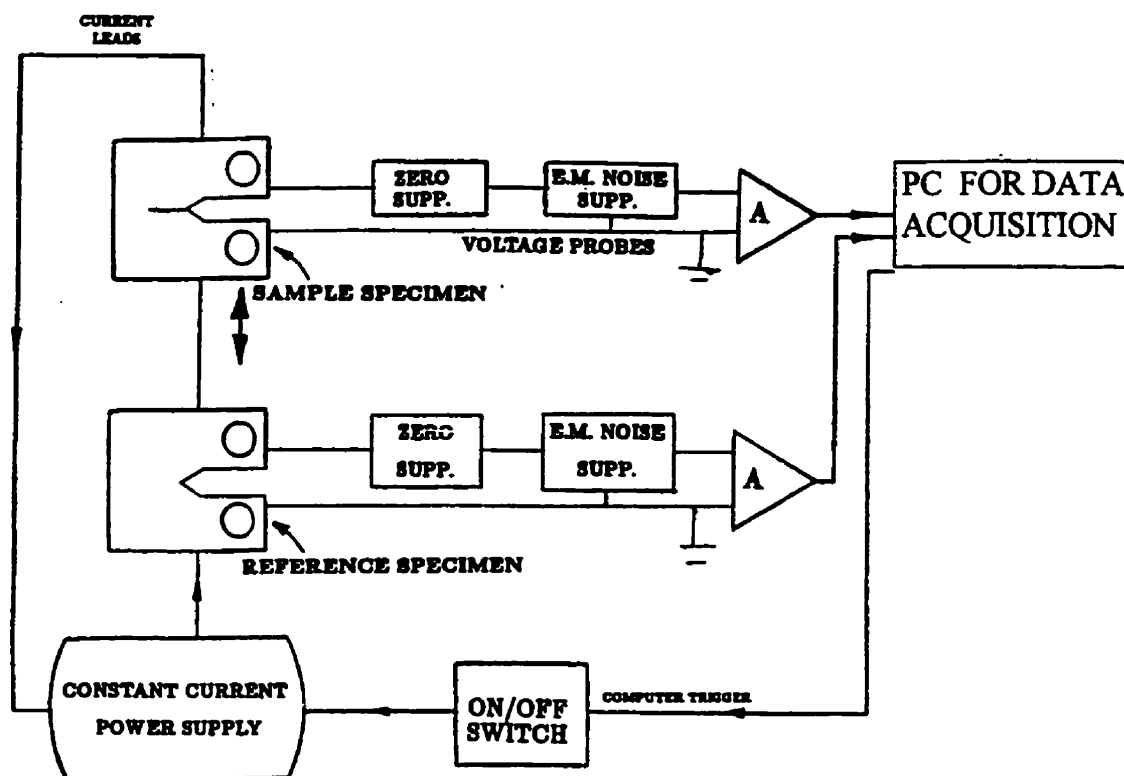


Figure 3.3 Schematic of the DC-PD circuit used to monitor crack length.

ASTM E-139
ASTM E-8

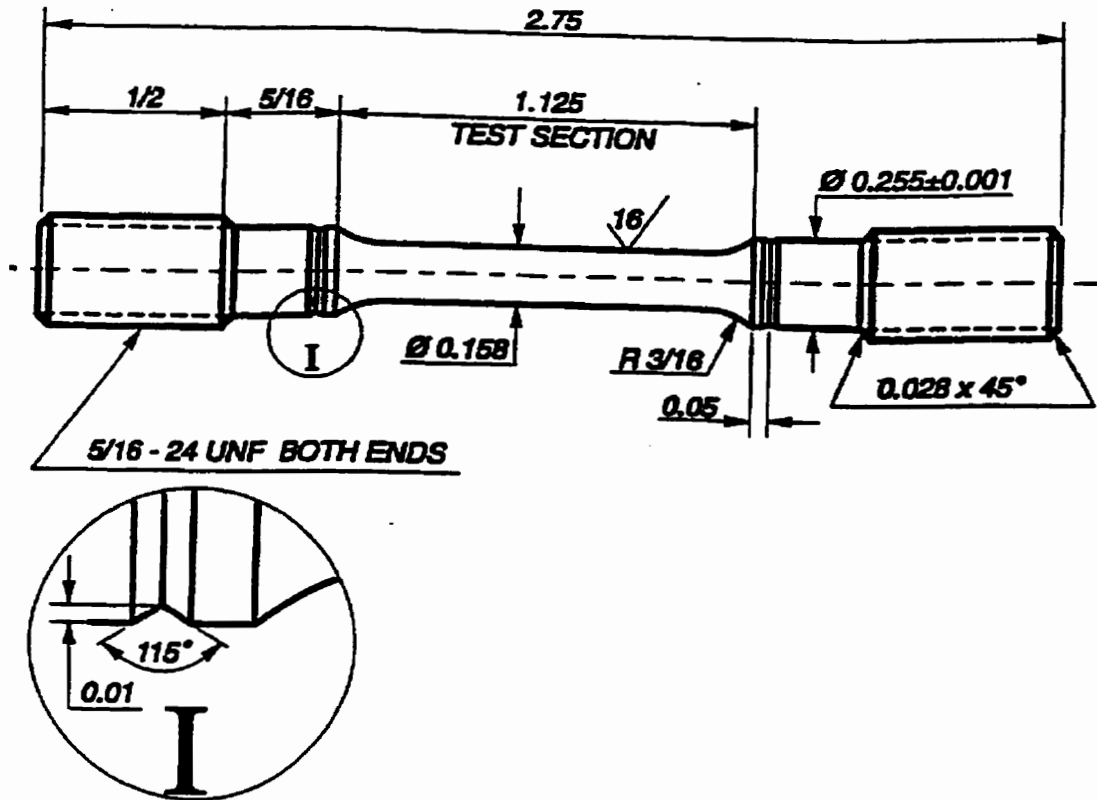


Figure 3.4 The tensile and creep specimen geometries employed.

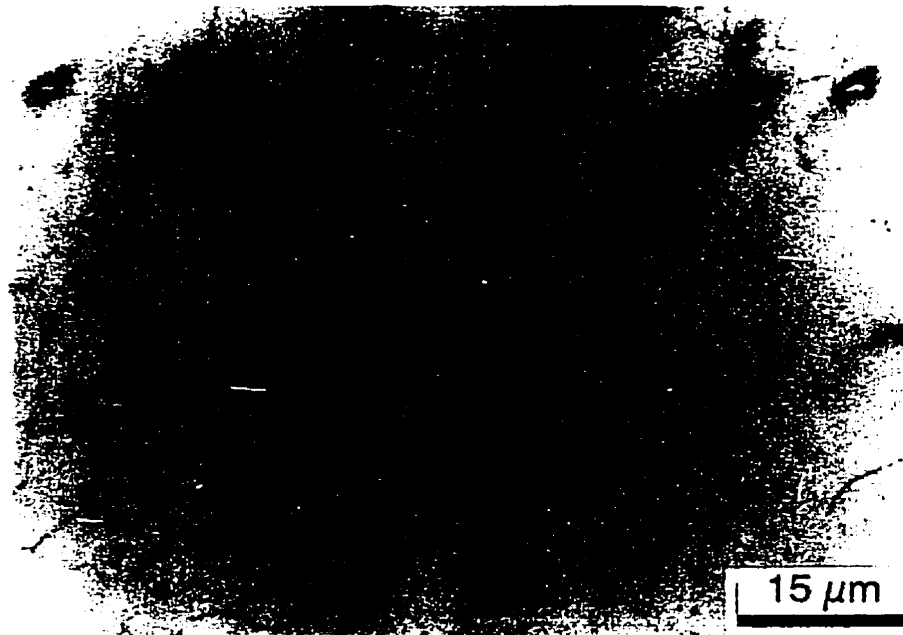


Figure 4.1 Optical microstructure of the forged Udimet 520 (as received).



Figure 4.2 Optical microstructure of an U-520 specimen after 1050°C /4h/AC solution treatment.

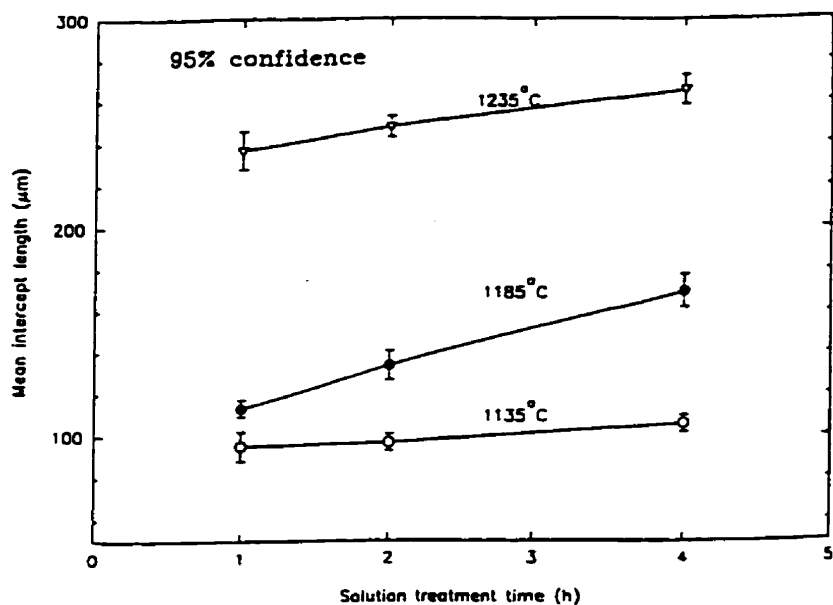


Figure 4.3 Effect of solution treatments on the mean intercept length of grains for U-520.

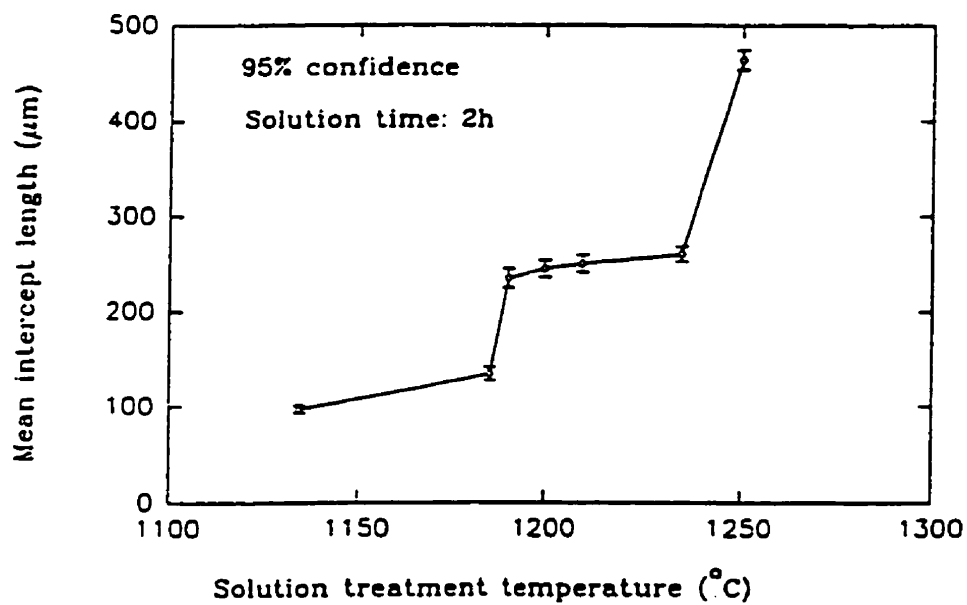


Figure 4.4 Grain coarsening curve for Udimet 520.

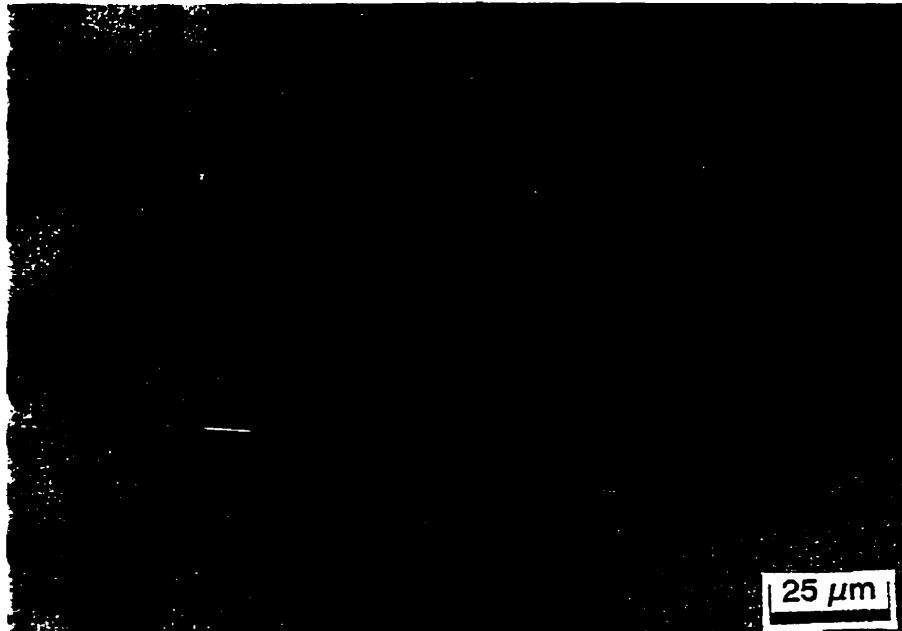


Figure 4.5 Optical microstructure of a specimen after 1090°C /4h/AC solution treatment and the normal two-stage aging treatment.



Figure 4.6 Optical microstructure of a specimen after 1235°C /2h/AC solution treatment and the normal two stage aging treatment.



Figure 4.7 TEM replica micrograph of a specimen after solution treatment at 1135°C for 2 hours and air cooling.

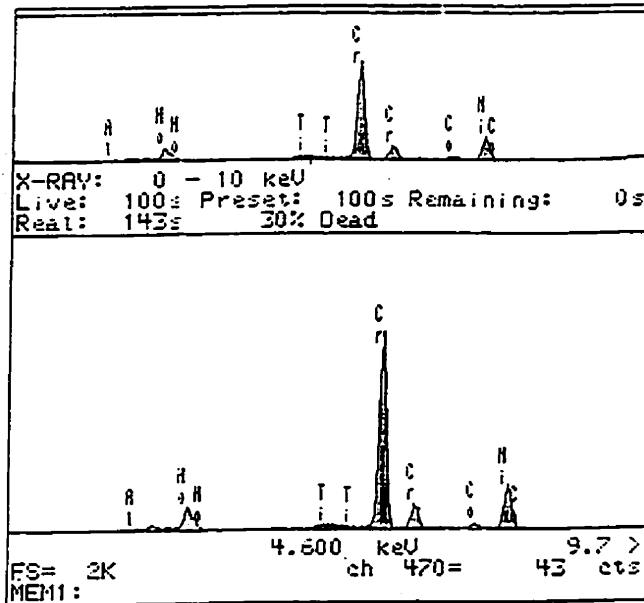
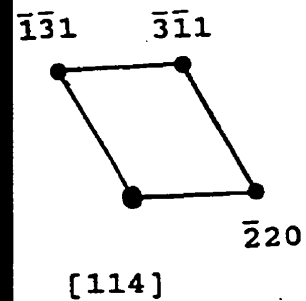
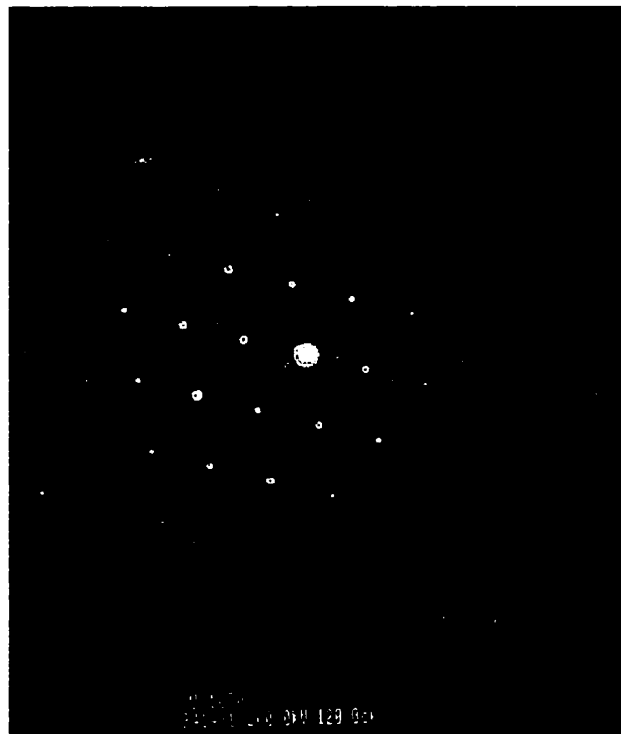


Figure 4.8 A representative X-ray spectrum of $M_{23}C_6$ carbides from a replica.



4.9 (a) Grain boundary $M_{23}C_6$ morphology



4.9 (b) Electron diffraction pattern and index from a carbide in Fig. 4(a)

Figure 4.9 Replica TEM micrograph of a specimen aged at 1050°C for 15 minutes and water quenched, following a solution treatment of 4 hours at 1135°C and air cooled.

ST: ○ 1135°C, 4h, AC (Mean intercept length= 108 μm)
 ● 1250°C, 2h, WC (Mean intercept length= 464 μm)

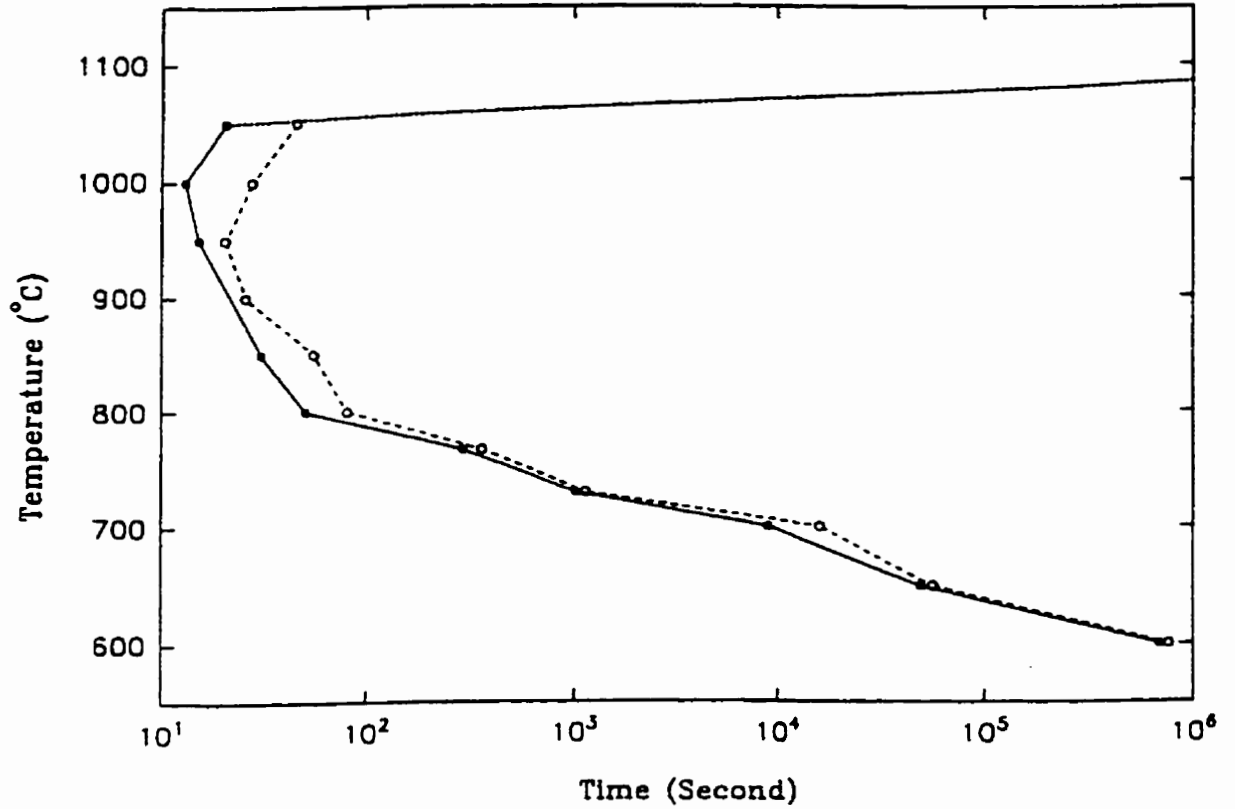


Figure 4.10 The C-curve for the start of the grain boundary $M_{23}C_6$ carbide formation in Udimet 520.

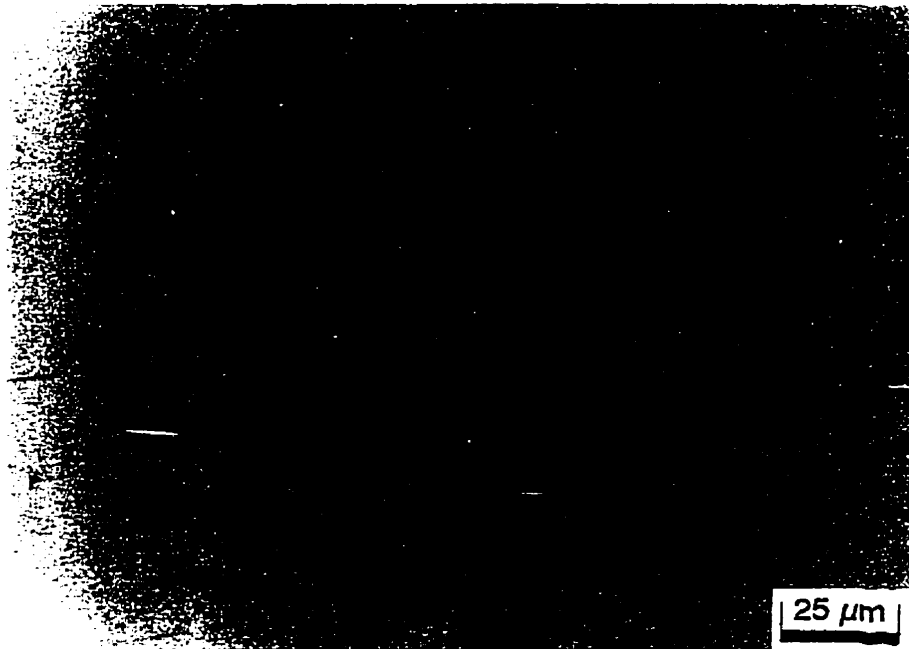


Figure 4.11 Optical microstructure of a specimen annealed for 2 hours at 1100°C, following an aging treatment of 30 minutes at 850°C performed after a first solution treatment at 1250°C for 2 hours.

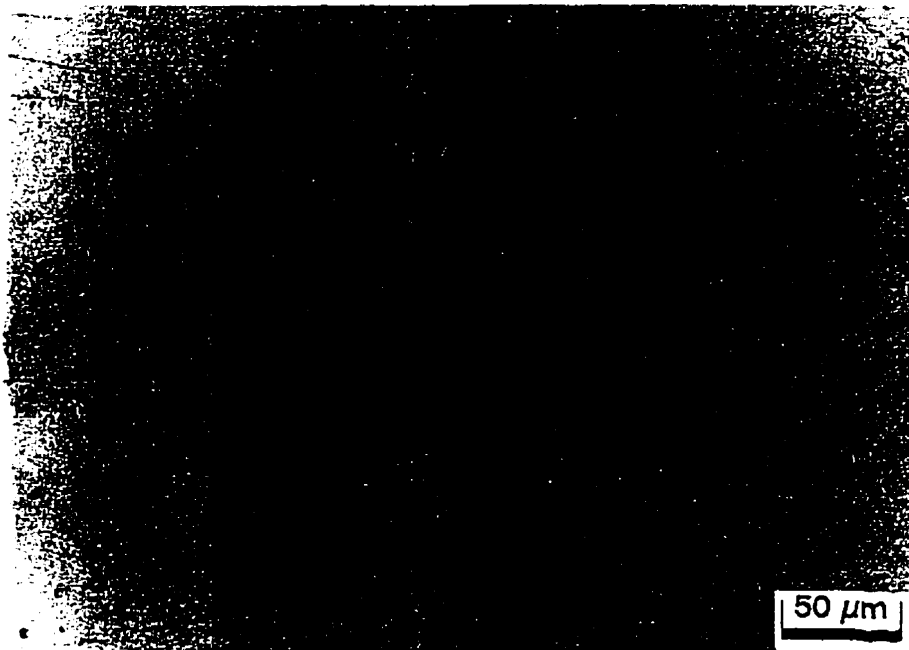


Figure 4.12 Optical microstructure of a specimen aged for 30 minutes at 850°C and water cooled after the 1250°C solution treatment.

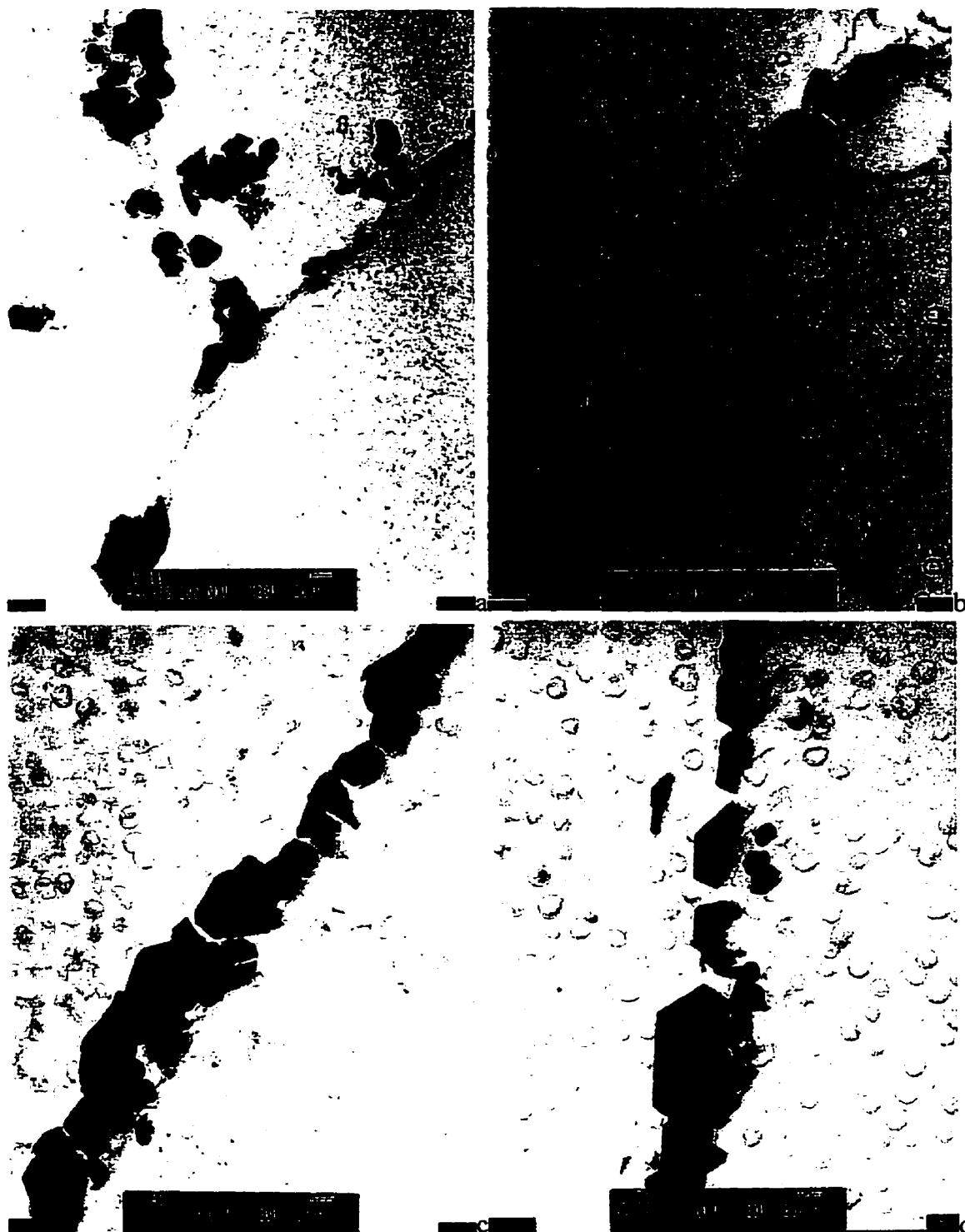


Figure 4.13 Replica TEM micrographs of specimens aged for the indicated time at 900°C after the 1135°C solution treatment. (a) 40 minutes (b) 24 hours (c) 48 hours (d) 90 hours.

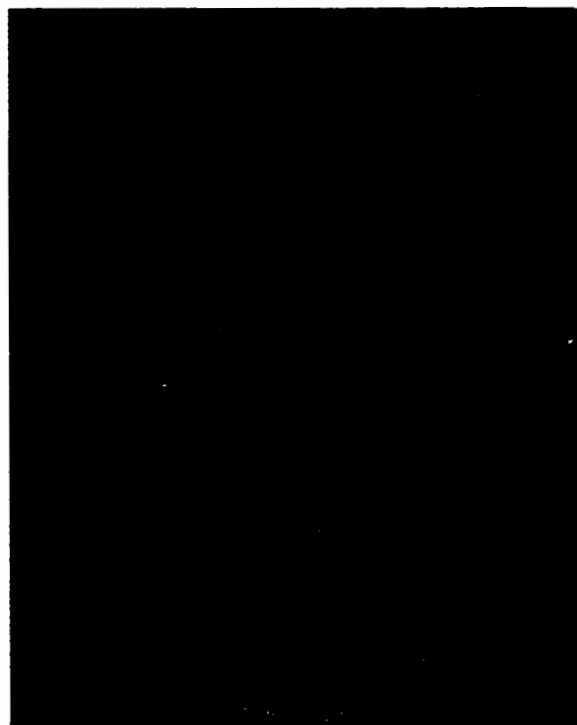


Figure 4.14 Replica TEM micrographs of a specimen aged at 700°C for 100 hours and water cooled after an 1135°C solution treatment.



Figure 4.15 Replica TEM micrograph of a specimen after an 1135°C/4h/AC solution treatment followed by the normal two-stage aging treatment.

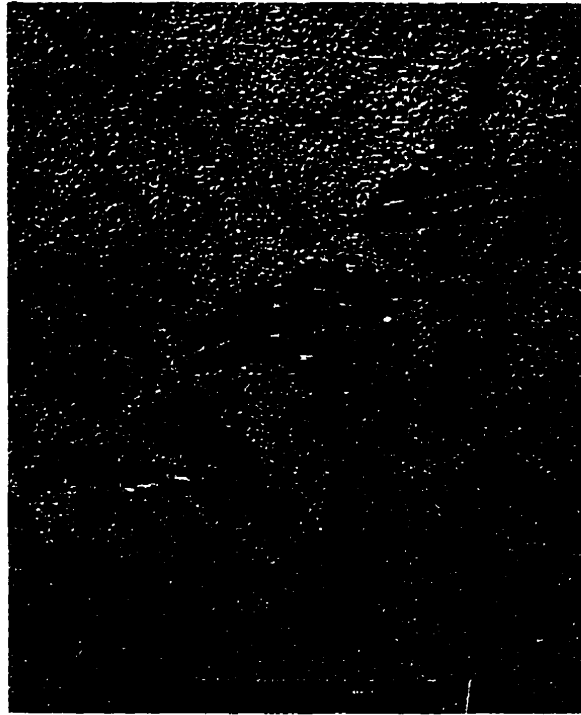


Figure 4.16 TEM replica micrograph showing feather-like grain boundary $M_{23}C_6$ carbides in a specimen aged at 900°C for 40 minutes and water cooled following an 1135°C C/4h/AC solution treatment.



Figure 4.17 Optical microstructure of a specimen annealing at 1177°C for two hours and water cooled after a 1250°C solution treatment (polished only).

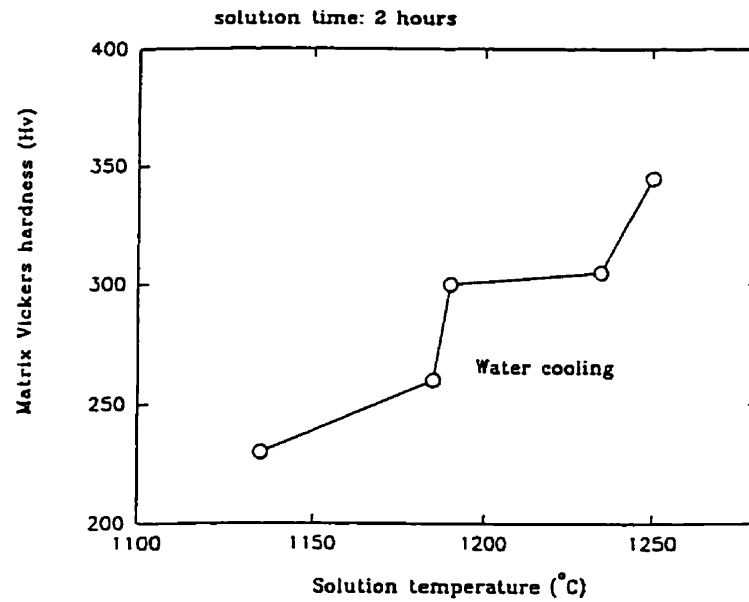


Figure 4.18 Matrix Vicker microhardness vs solution temperature relationship.



Figure 4.19 TEM micrograph of grain boundaries and γ' phases of a specimen solution treated at 1135°C.

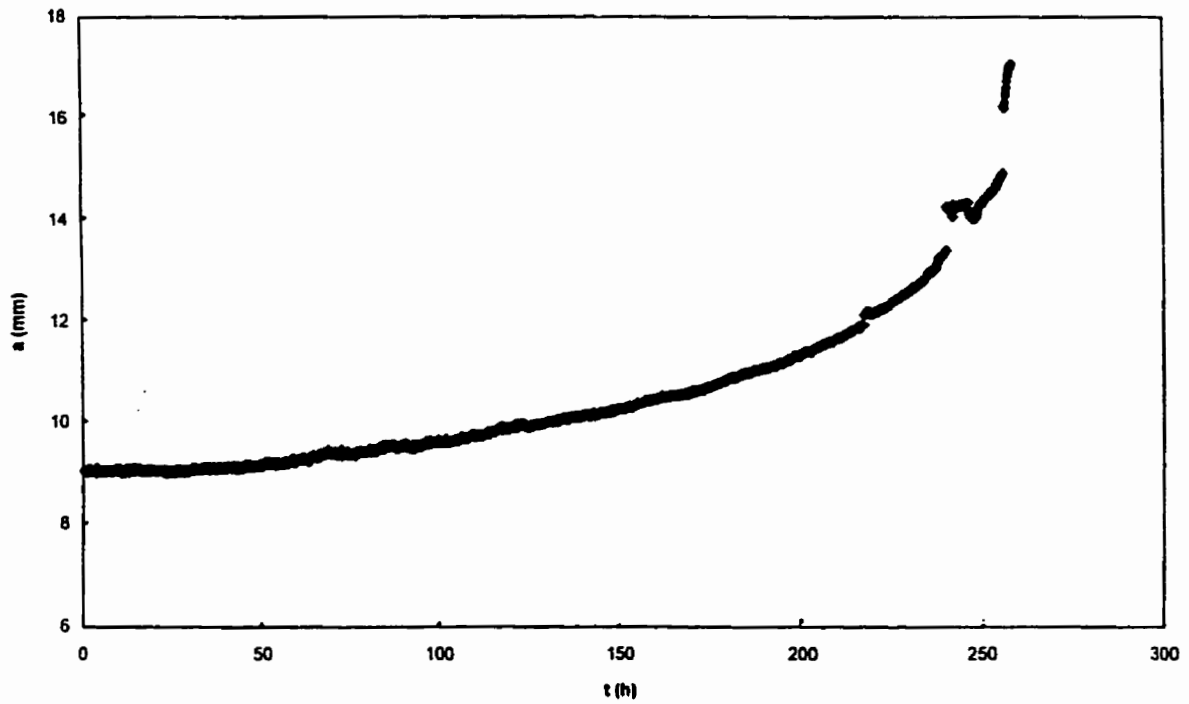


Figure 4.20 Creep crack length vs time relation of an CCG specimen solution treated at 1200°C and CCG tested in air at 540°C.

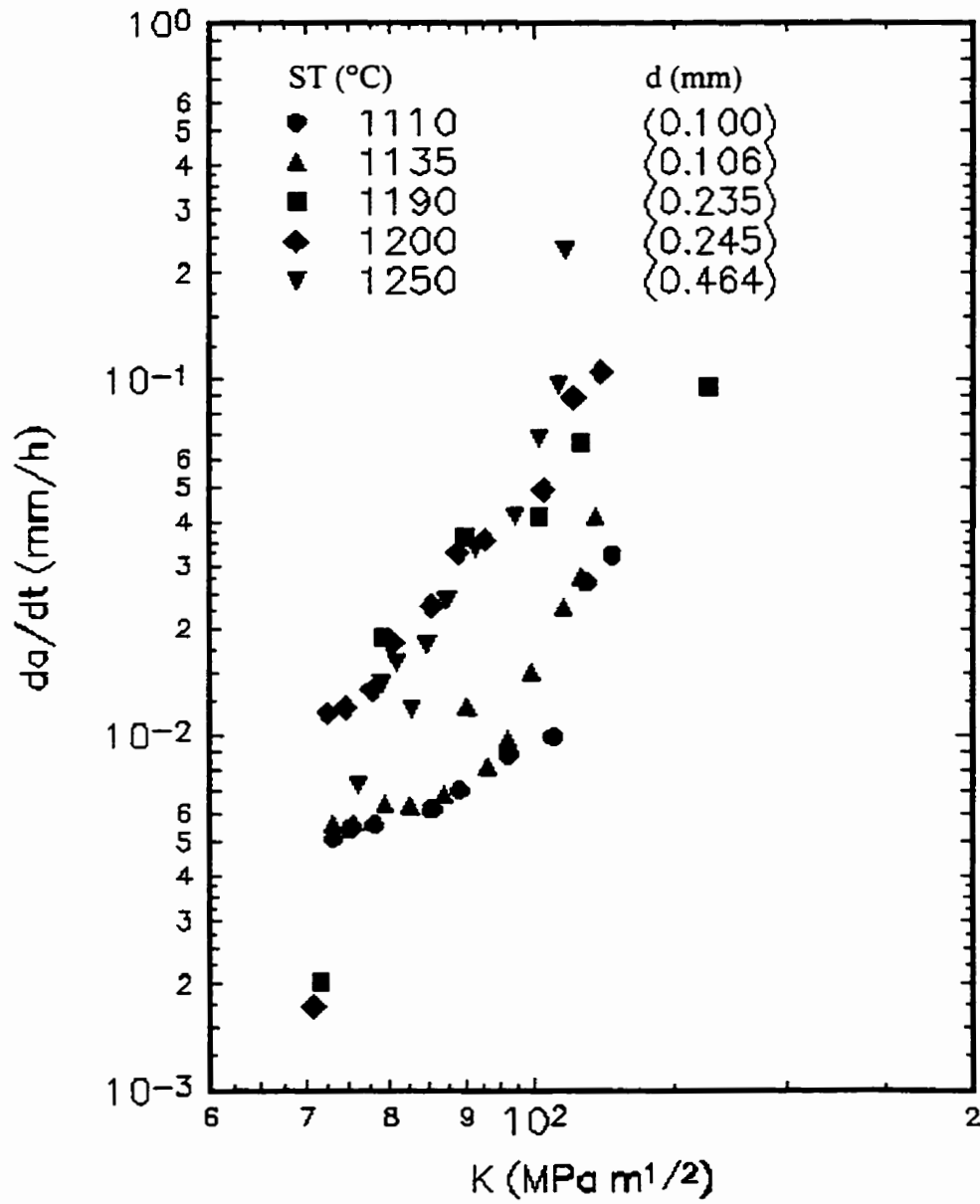


Figure 4.21 CCGR and stress intensity factor relations for specimens subjected to different heat treatments and tested in air at 540°C .

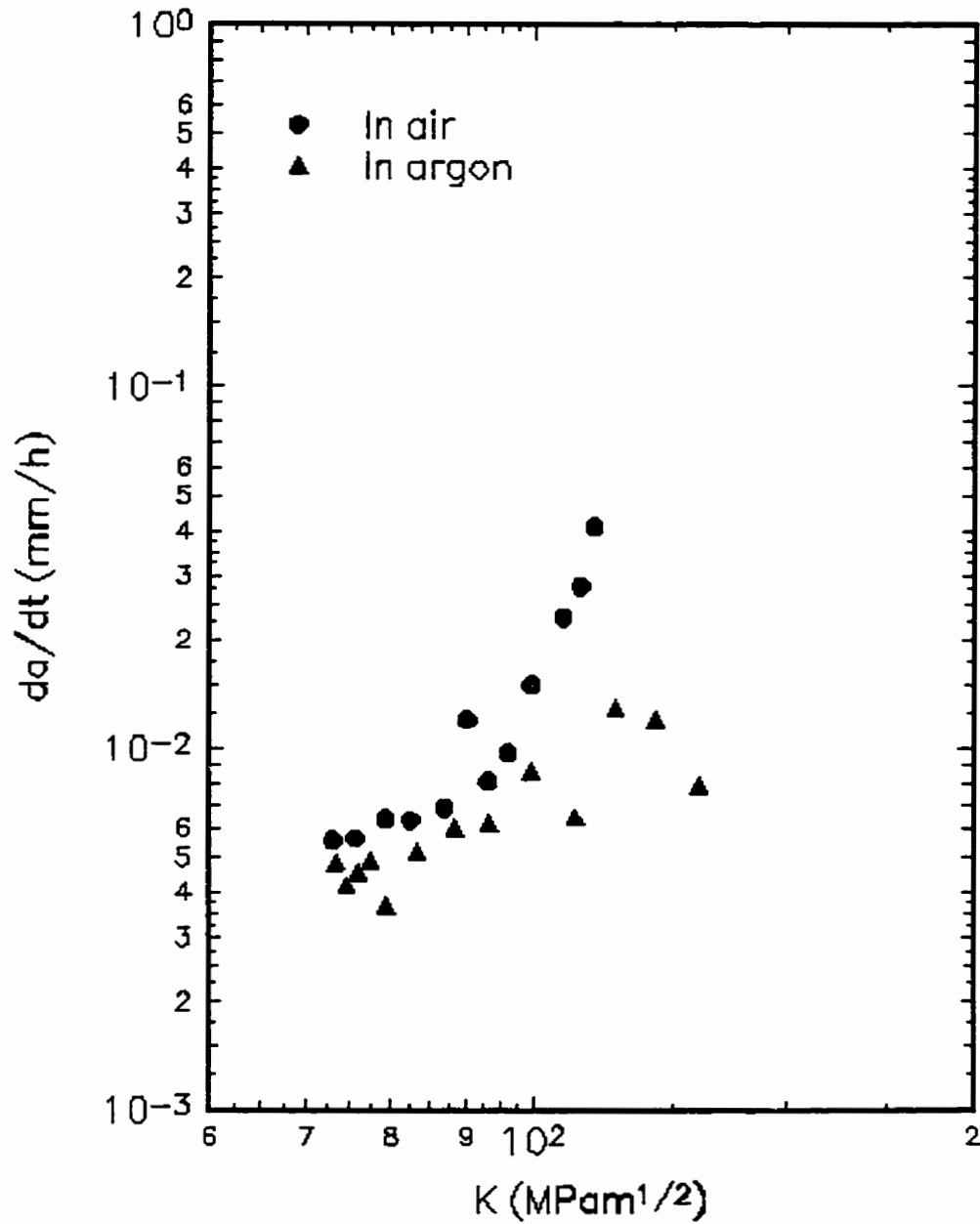


Figure 4.22 CCGR and stress intensity factor relations of the specimens solution treated at 1135°C and tested at 540°C.

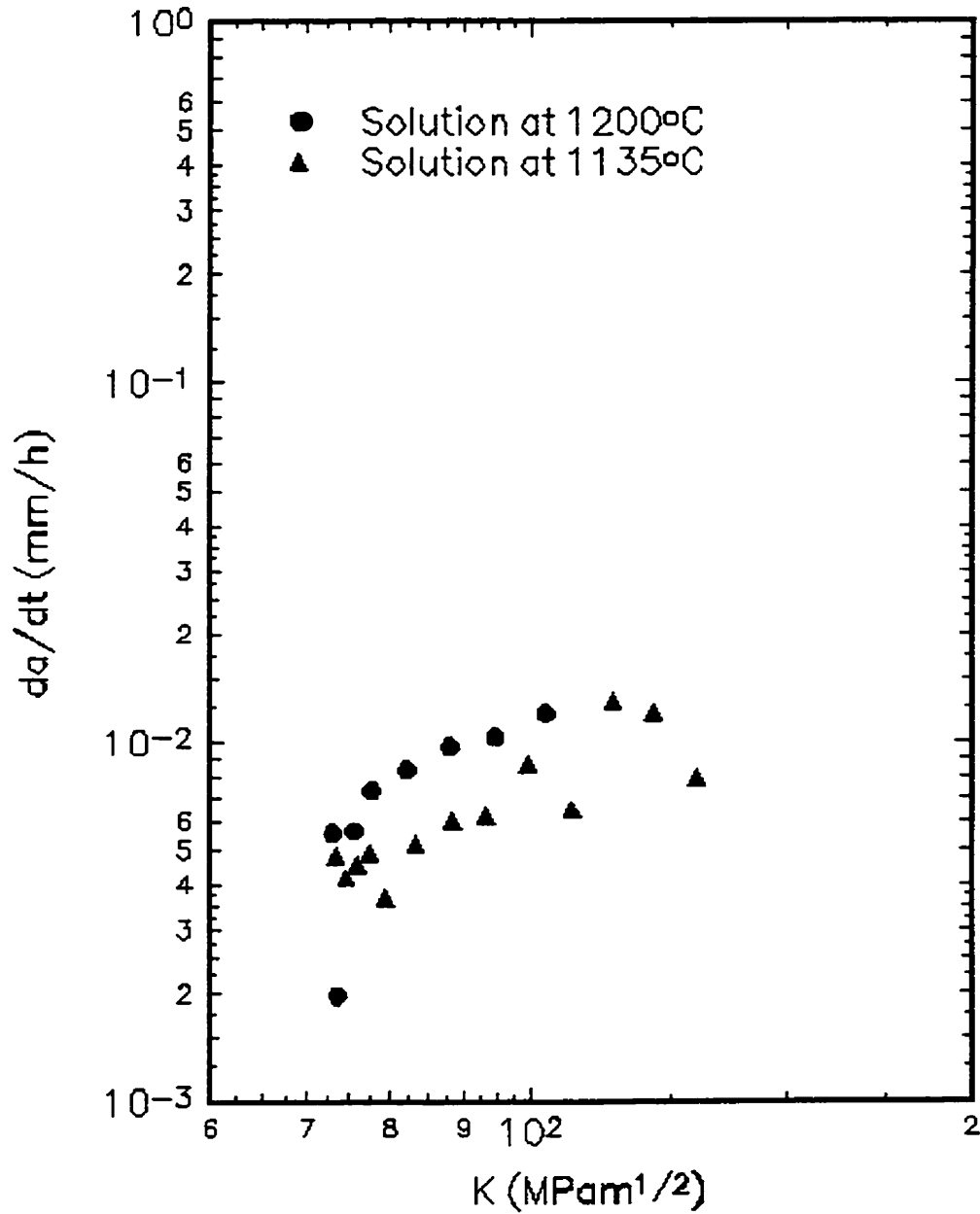


Figure 4.23 CCGR and stress intensity factor relations of the specimens solution treated at 1135°C and 1120°C and tested in argon at 540°C .

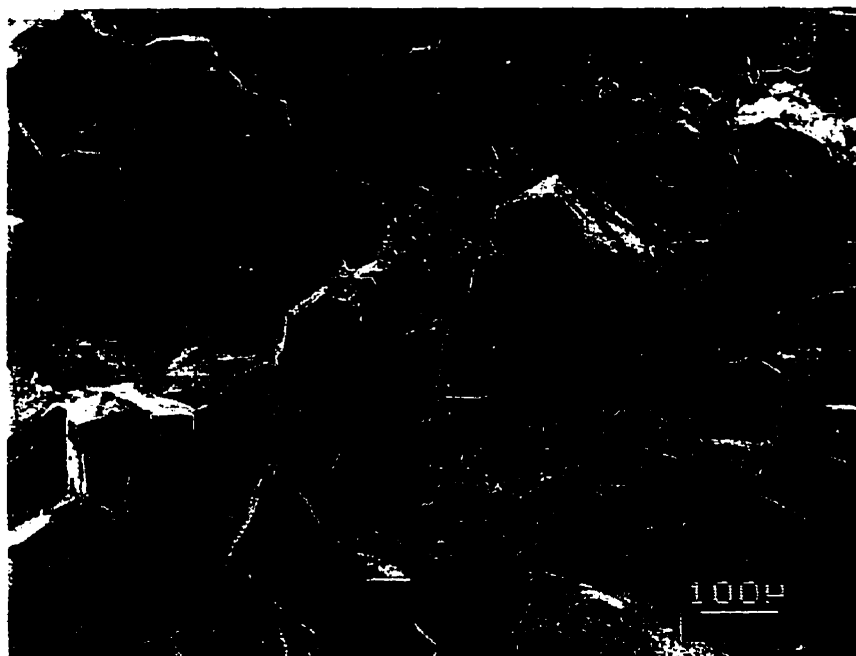


Figure 4.24 Interface of the pre-fatigued region and CCG region of an CCG specimen solution treated at 1135°C and CCG tested in air at 540°C.



Fig. 4.25 (a)



Fig. 4.25 (b)

Figure 4.25 SEM micrographs of CCG region of a specimen solution treated at 1135°C and tested in air at 540°C.



Fig. 4.26 (a)

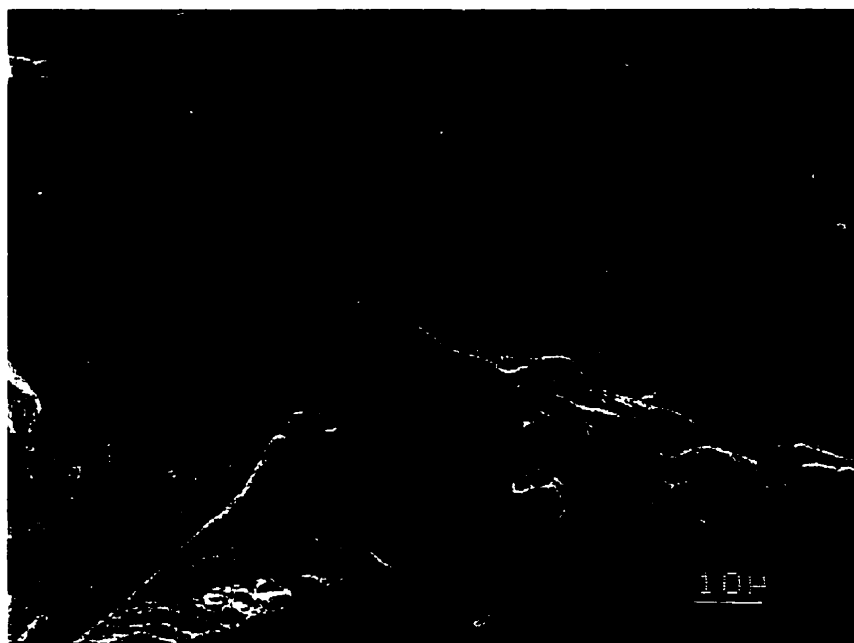


Fig. 4.26 (b)

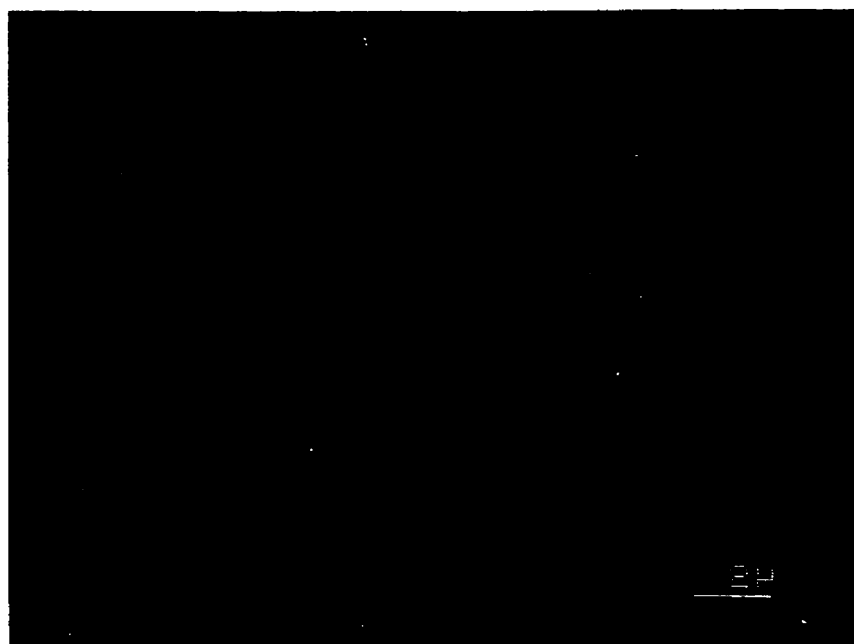


Fig. 4.26 (c)

Figure 4.26 SEM micrographs of CCG region of an CCG specimen solution treated at 1200°C and tested in air at 540°C.



Fig. 4.27 (a)

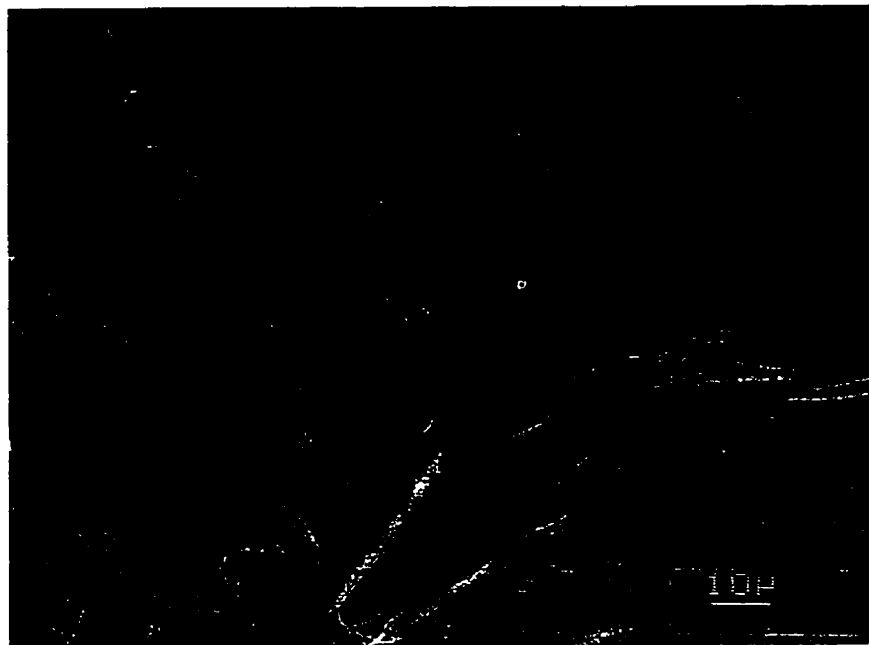


Fig. 4.27 (b)

Figure 4.27 SEM micrographs of CCG region of a specimen solution treated at 1250°C and tested in air at 540°C.



Figure 4.28 Interface of slow CCG region and fast fracture region of an CCG specimen solution treated at 1135°C and tested in air at 540°C.

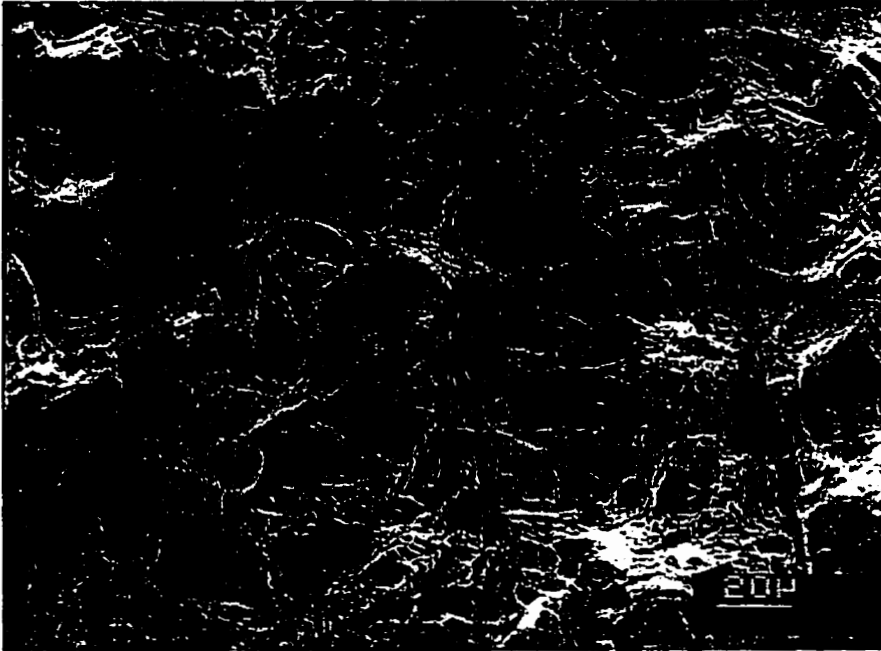


Figure 4.28 SEM micrograph of fast fracture region of a CCG specimen solution treated at 1200°C and tested in air at 540°C.

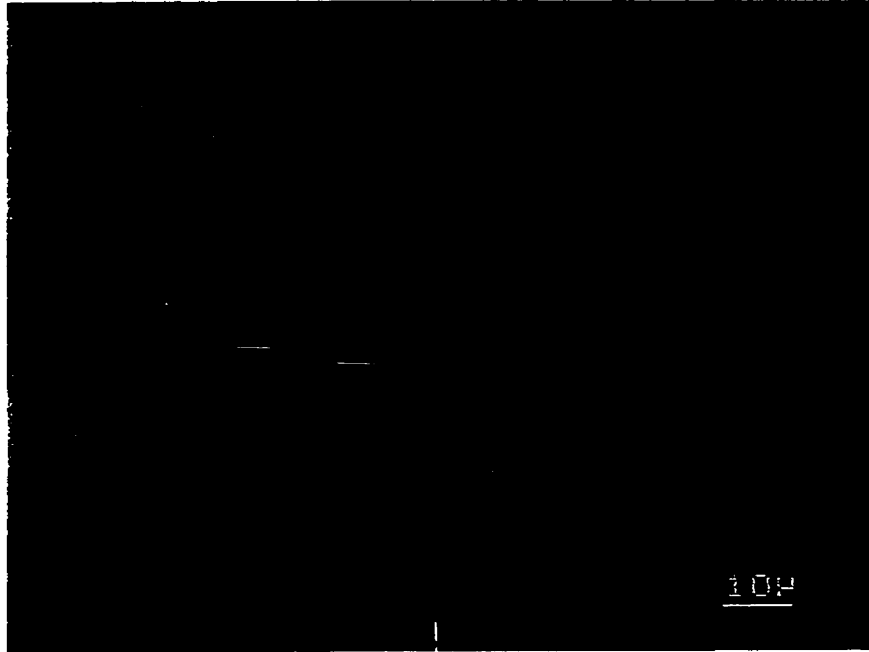


Fig. 4.30 (a) Specimen solution treated at 1135°C



Fig. 4.30 (b) Specimen solution treated at 1200°C

Figure 4.30 SEM micrographs of CCG regions tested in argon at 540°C.



Figure 4.31 Metallographic cross section of a CCG specimen solution treated at 1135°C and tested in air at 540°C (crack propagation from top to bottom).



Figure 4.32 Polished cross section of an interrupted CCG specimen solution treated at 1200°C and tested in air at 540°C (crack propagation from top to bottom).

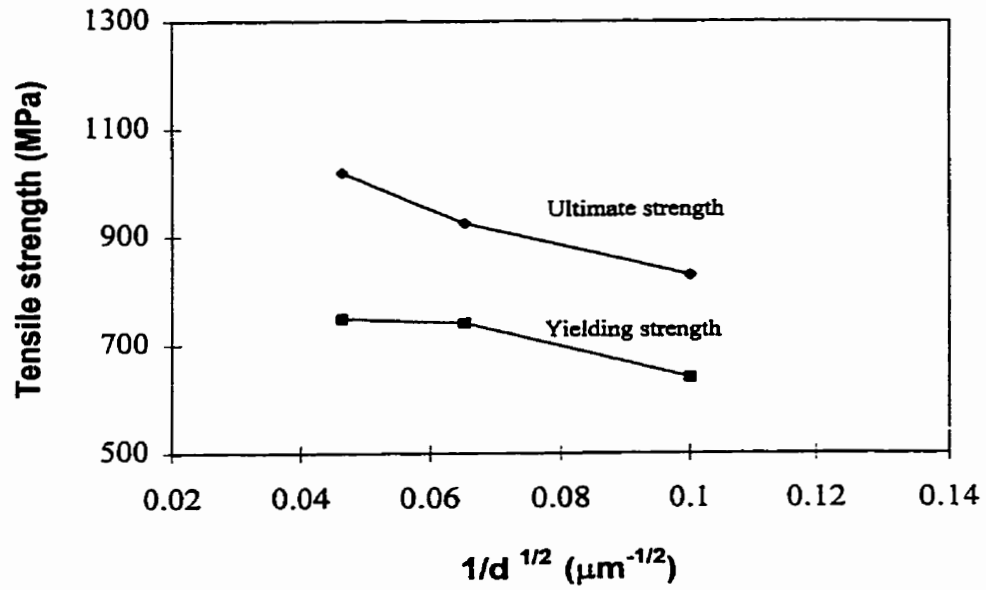
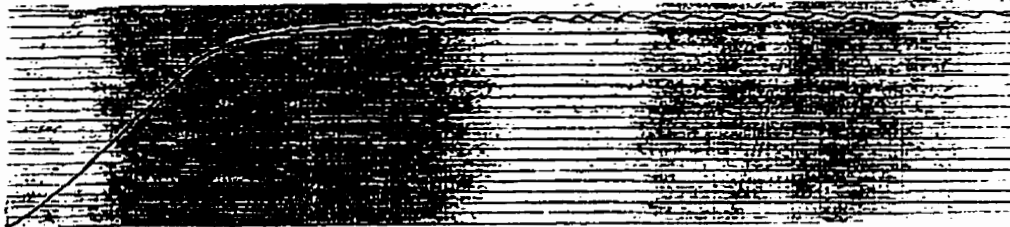


Figure 4.33 Tensile strength vs grain size relationship at 540°C.



(a) "1110" treatment, d : 100 μm



(b) "1190" treatment, d : 235 μm

Figure 4.34 Tensile engineering strain vs load curve (part) at 540°C.

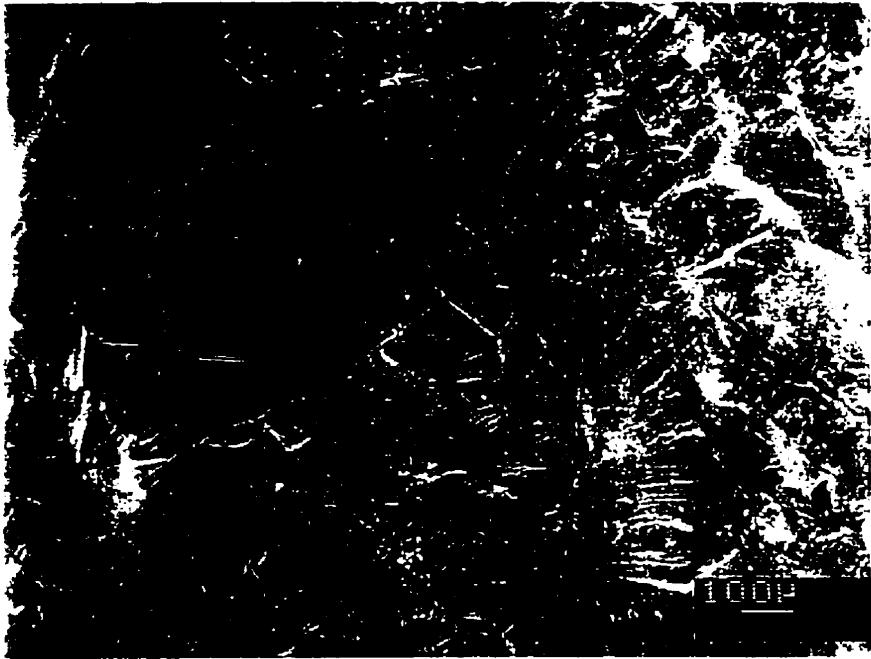


Figure 4.35 (a) Specimen of 1110°C solution treatment



Figure 4.35 (b) Specimen of 1190°C solution treatment

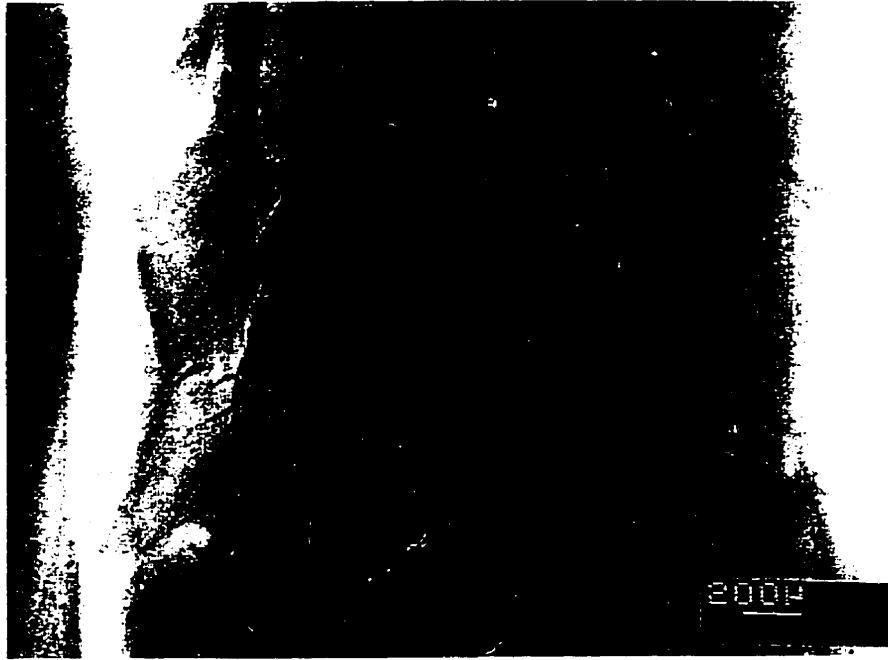


Figure 4.35 (c) Specimen of 1250°C solution treatment
Figure 4.35 Surface morphology after tensile tests at 540°C.

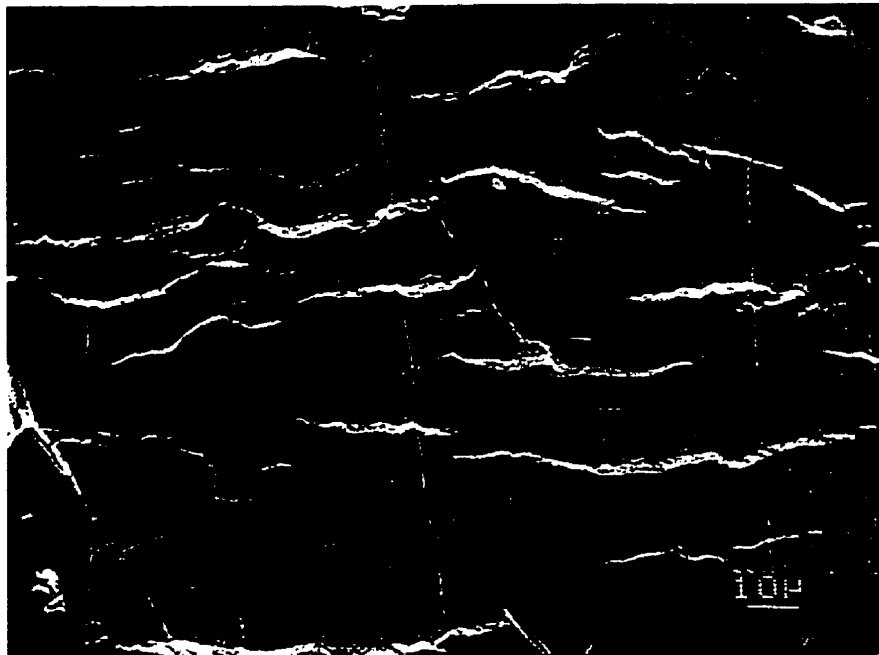


Figure 4.36 (a) Surface microcracks

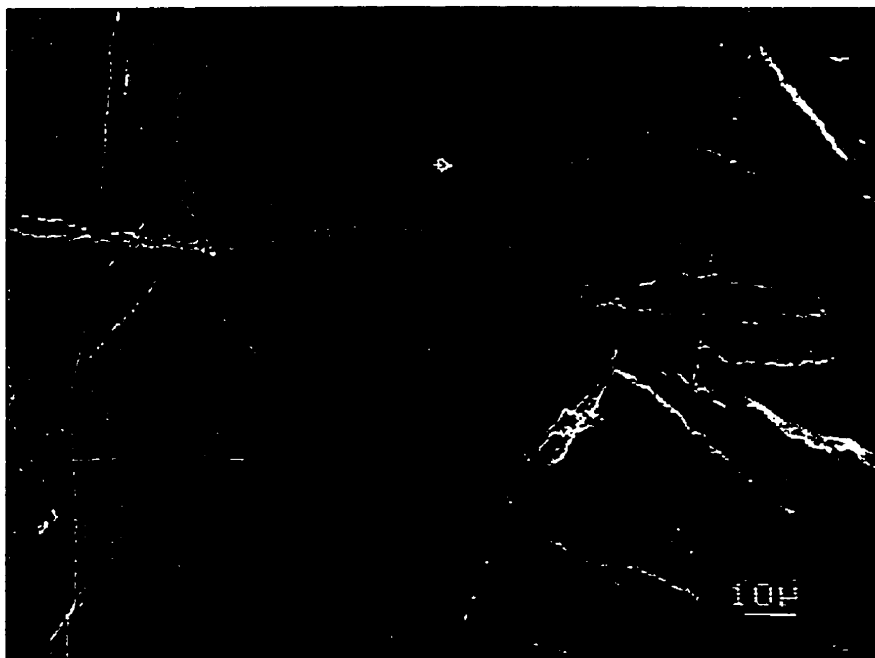


Figure 4.36 (b) Surface deformation bands and microcracks

Figure 4.36 Surface morphology close to the tensile fracture surface of the specimen solution treated at 1250°C.

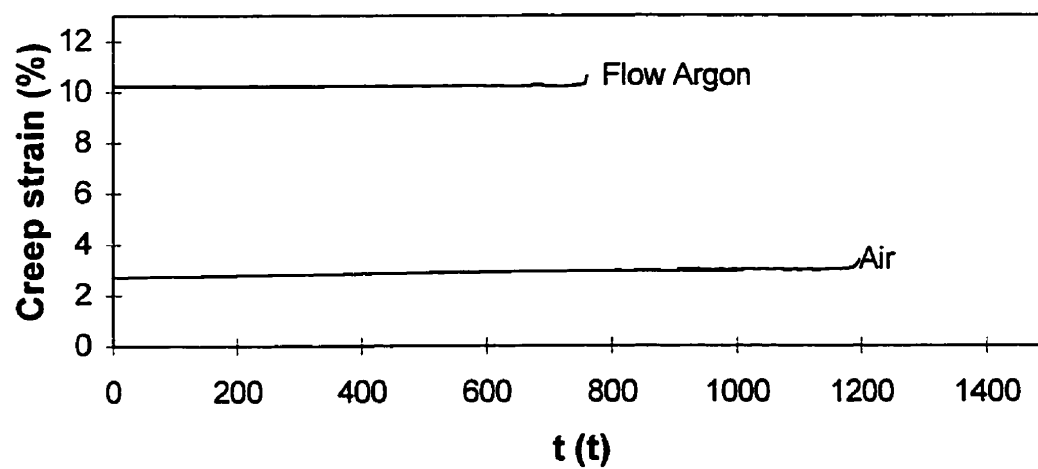


Figure 4.37 Creep strain vs time relationship in Udimet 520 solution treated at 1135°C.

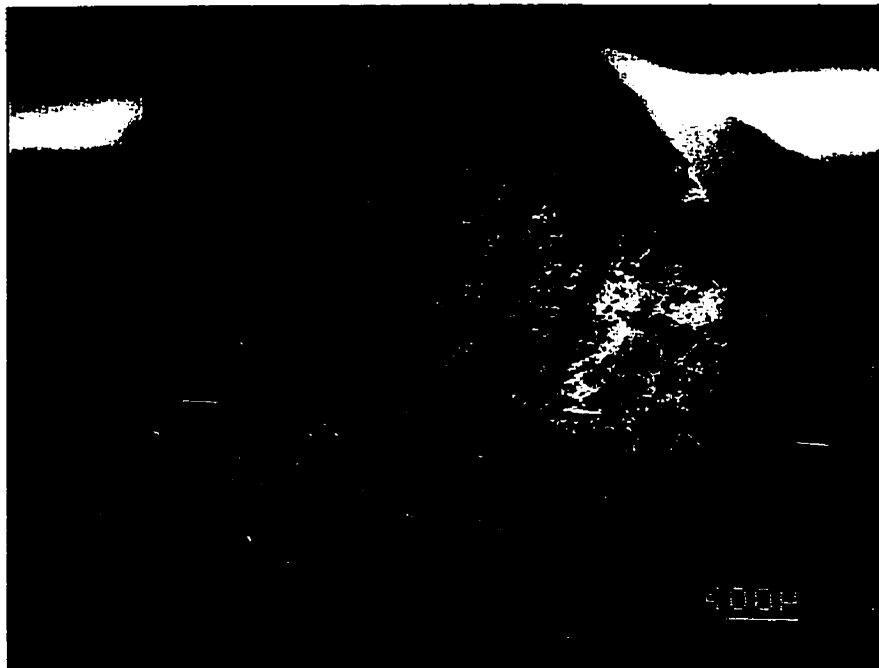


Fig. 4.38 (a)

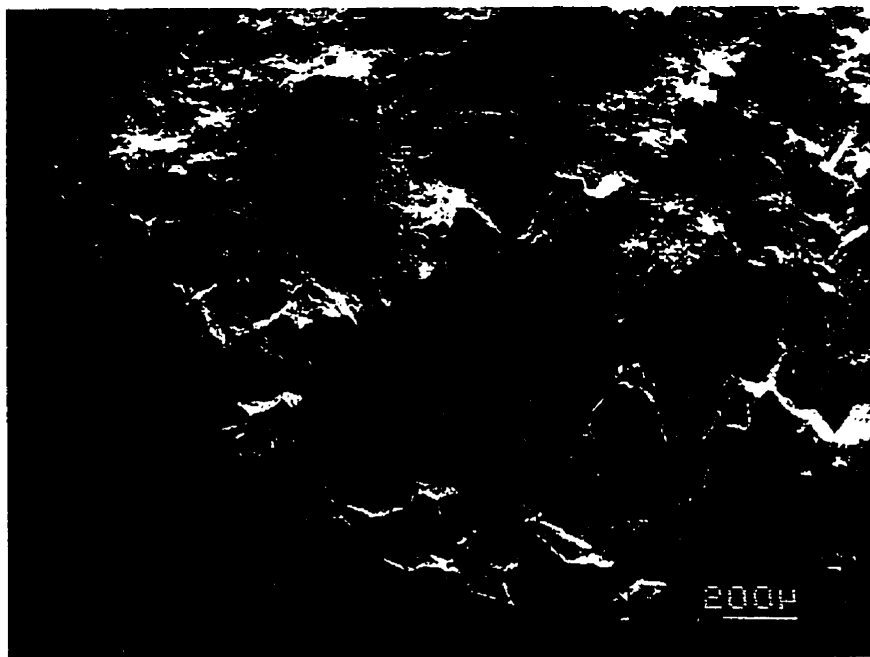


Fig. 4.38 (b)

Figure 4.38 Creep fracture surface of specimen solution treated at 1135°C and tested in air.

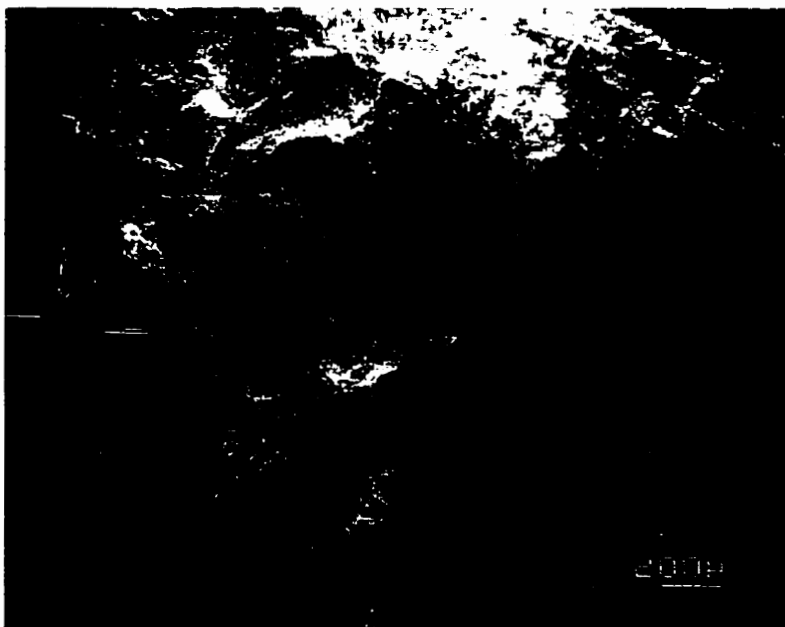


Figure 4.39 Creep fracture surface of specimen solution treated at 1190°C and tested in air.

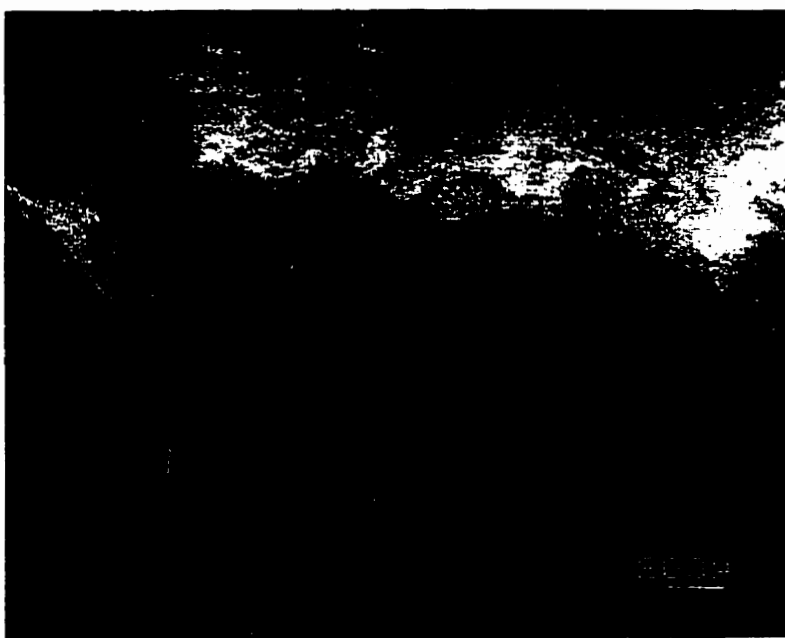


Figure 4.40 Creep fracture surface of specimen solution treated at 1250°C and tested in flowing argon.

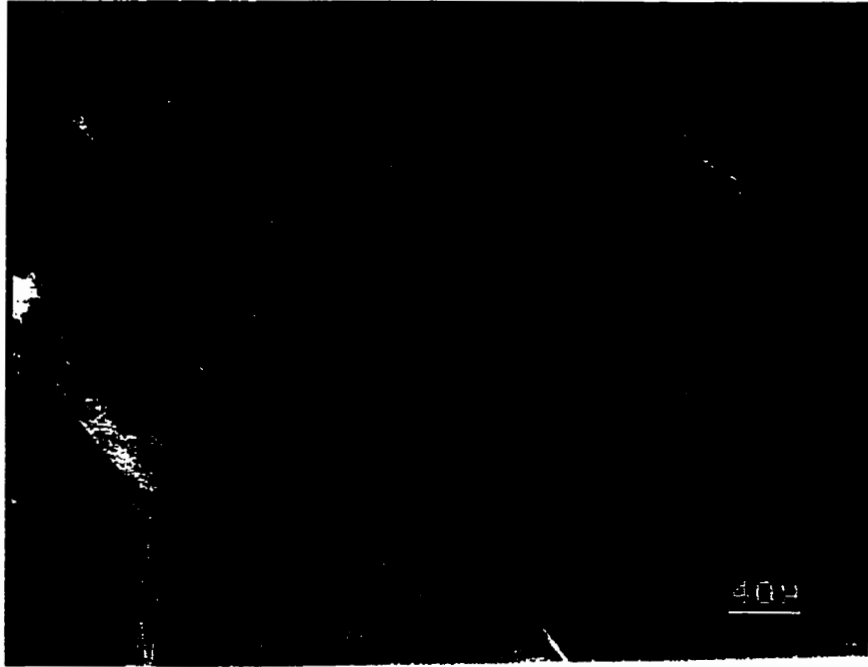


Figure 4.41 Intergranular fracture of creep specimen solution treated at 1135°C and tested in air.

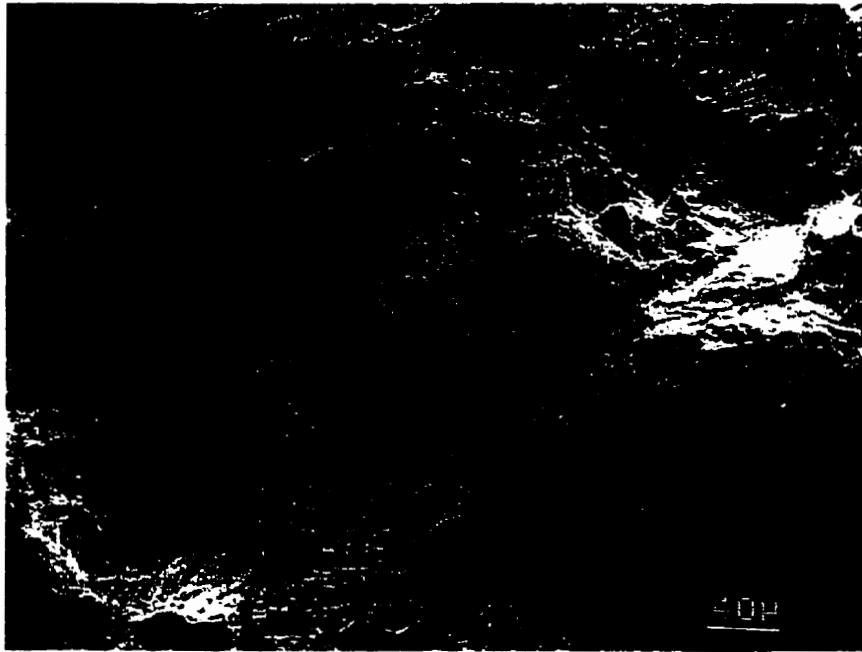


Figure 4.42 Transgranular fracture of creep specimen solution treated at 1135°C and tested in air.



Figure 4.43 Intergranular fracture of creep specimen solution treated at 1135°C and tested in flowing argon.

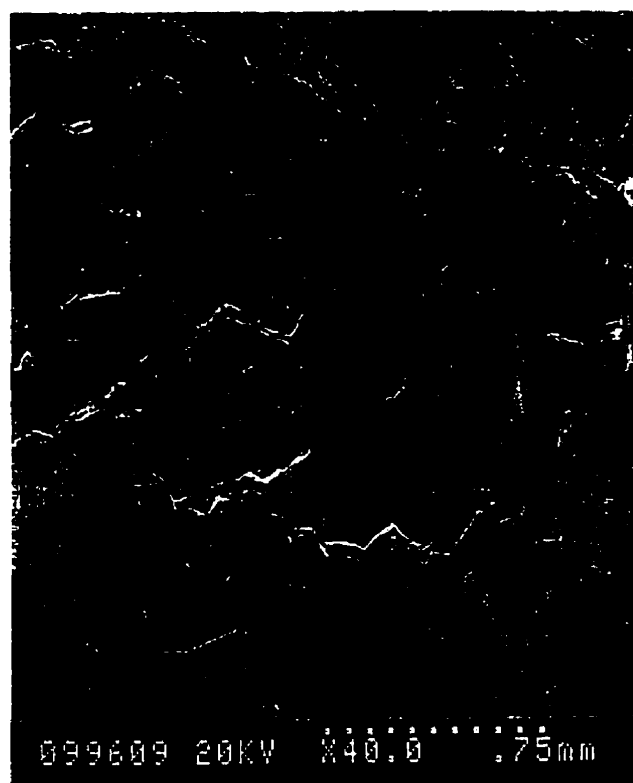


Figure 4.44 Surface of specimen solution treated at 1135°C and creep tested at 540°C.

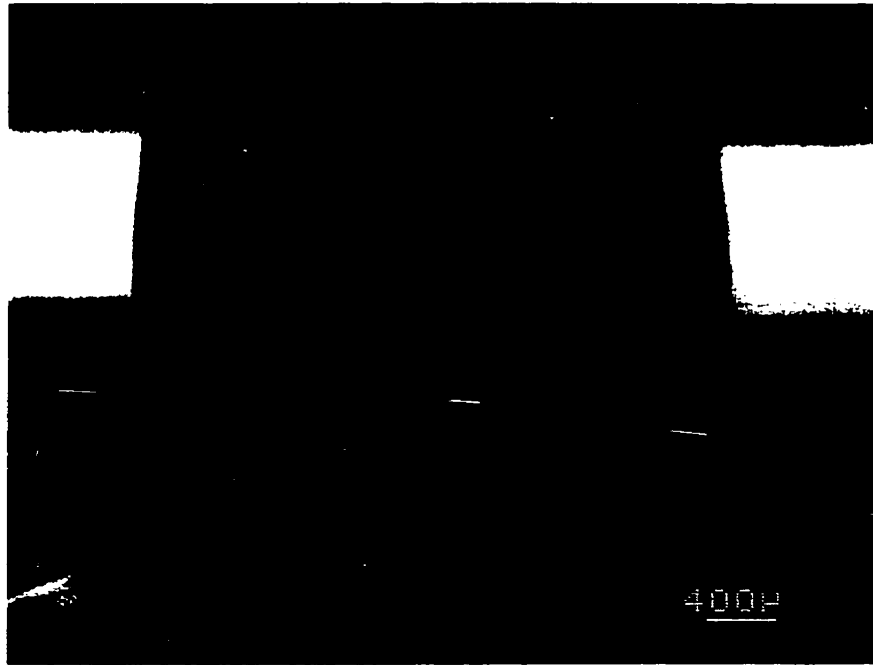


Figure 4.45 Surface of specimen solution treated at 1250°C creep tested at 540°C in air.



Figure 4.46 (a) Tested in air.



Figure 4.46 (b) Tested in flowing argon.

Figure 4.46 Grain boundary cracks at free surface in specimen solution treated at 1135°C and creep tested at 540°C.



Figure 4.47 Profile of fracture surface of specimen solution treated at 1190°C.

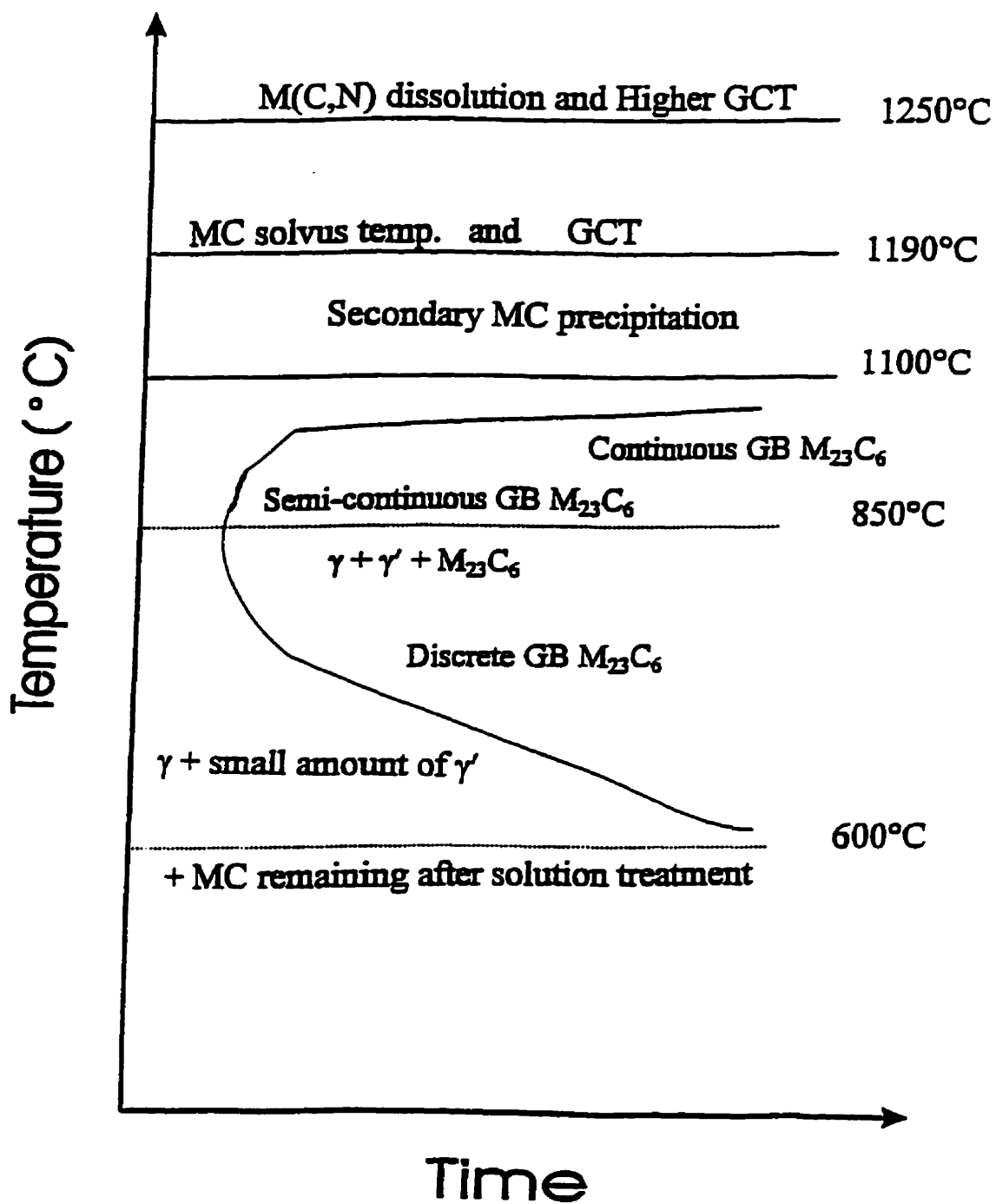
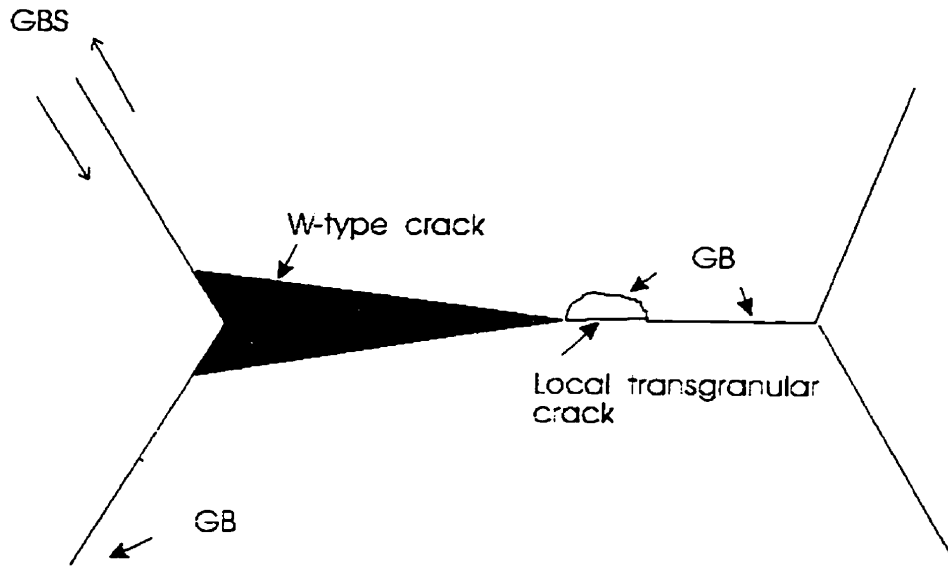
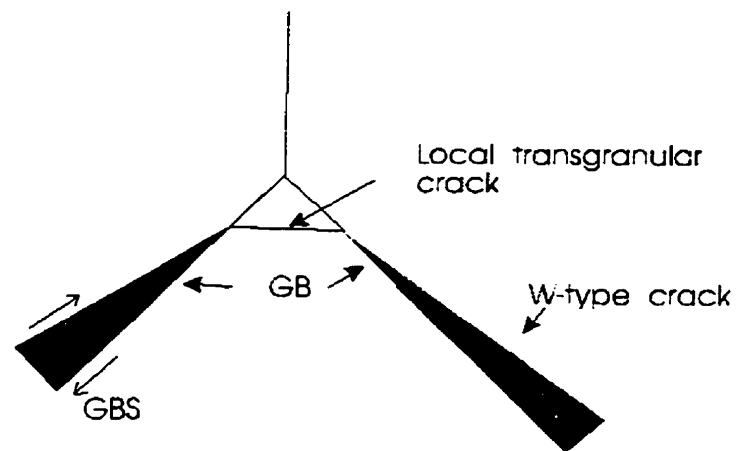


Figure 5.1 A schematic summary of heat treatment time-temperature-microstructure relationship in Udimet 520.



(a) Local transgranular cracking at a grain boundary imperfection



(b) Local transgranular cracking by high local stress

Figure 5.2 Proposed mechanisms for the local transgranular fracture caused by the stress concentration ahead of w-type cracks.

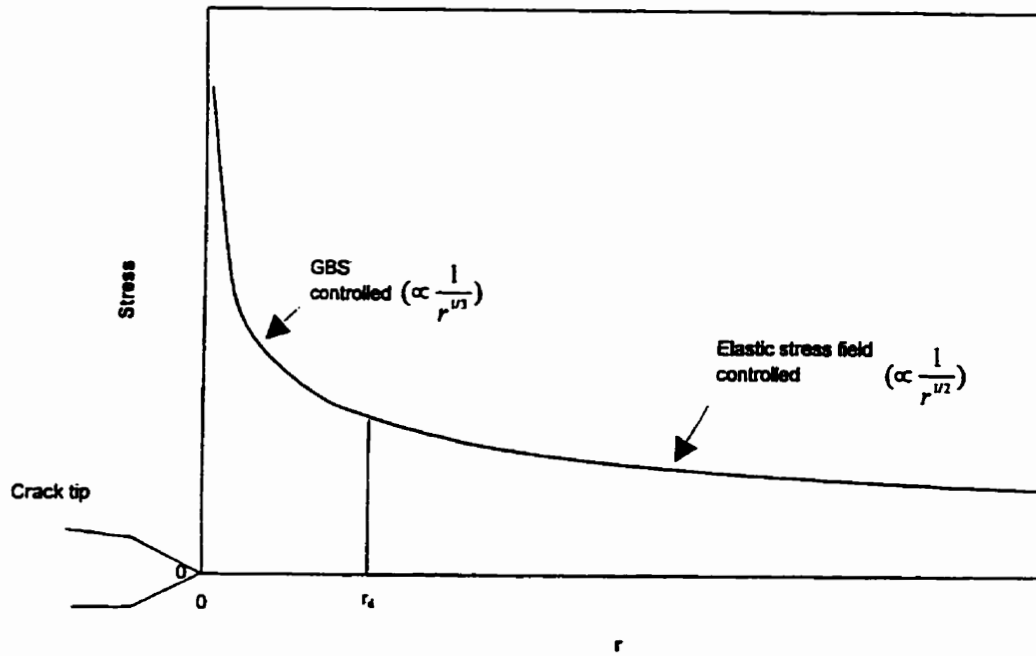


Figure 5.3 Effective stress versus distance ahead of the creep crack tip.

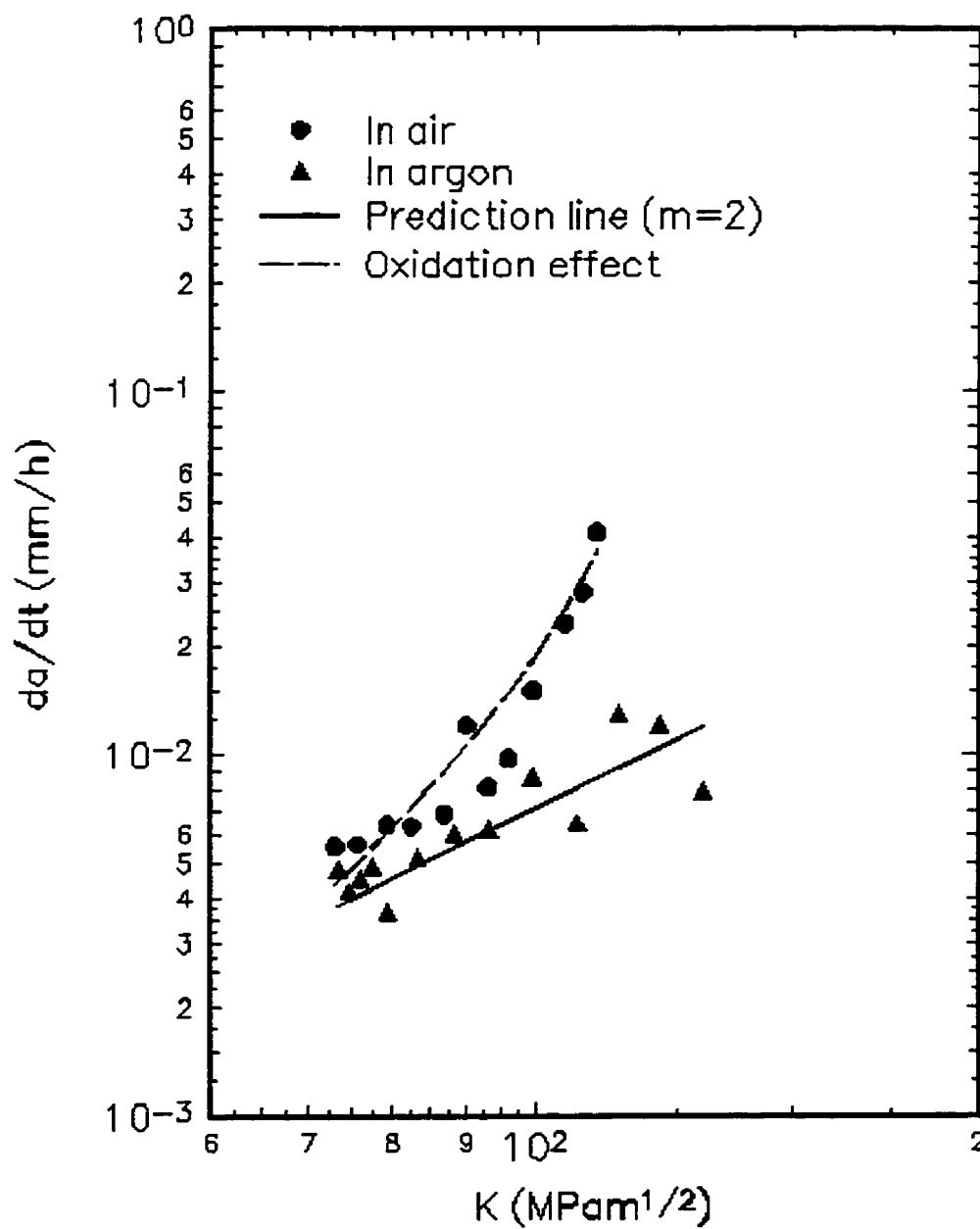


Figure 5.4 The predicted CCGR vs K relation on the specimens solution treated at $1135^{\circ}C$ and tested at $540^{\circ}C$.

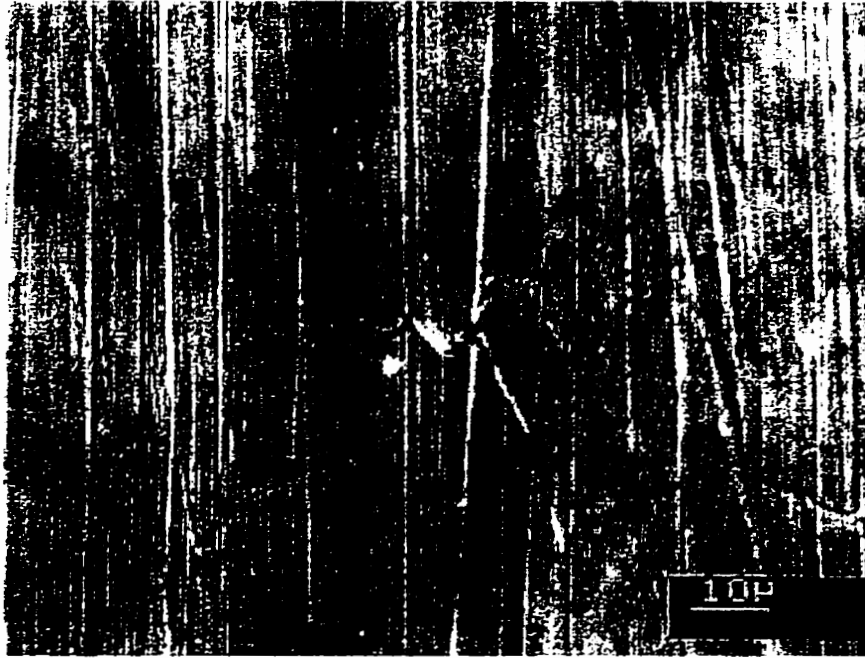


Fig. 5.5 (a)

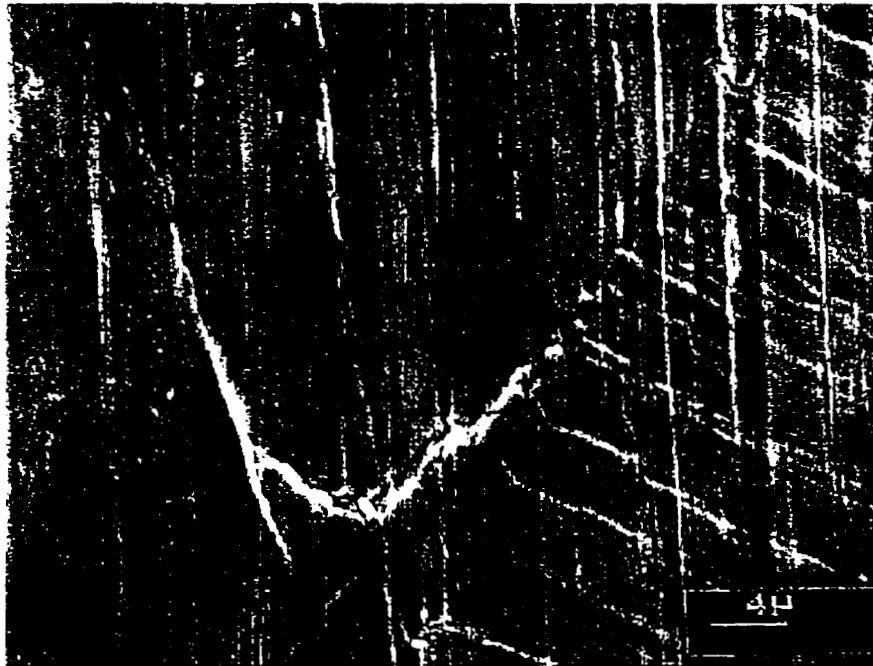


Fig. 5.5 (b)

Figure 5.5 The intergranular cracks on the surface of a specimen interrupted just after creep loading (solution treated at 1110°C).

REFERENCES

1. MIL-STD-1783 (USAF): Military Standard, Engine Structural Integrity Program (ENSIP), by the Department of Defence, USA, Nov. 1984.
2. MIL-STD-1843 (USAF): Military Standard, Reliability-Centred Maintenance for Aircraft, Engine and Equipment, by the Department of Defence, USA, Feb. 1985.
3. WU, X.J. and KOUL, A.K., «Modeling Creep in Complex Engineering Alloys», in «Creep and Stress Relaxation in Miniature Structures and Components», Proceedings of a Symposium of ASM-TMS Materials Week '96, MERCHANT, H. D., Cincinnati, Ohio, October, 1996, pp. 3-19.
4. POWELL, G.W., Metals Handbook, 9th Edn, Ohio: Amer. Soc. Met., Materials Park, vol. 11, 1986, p. 263.
5. SIMS, C.T. and HAGEL, W.C., eds., The Superalloys, New York: John Wiley and Sons, 1972.
6. DODD, A.G., «Mechanical Design of Gas Turbine Blading in Cast Superalloys», J. Mater. Sci. Tech., vol. 2, 1986, pp. 476-485.
7. EVANS, H.E., Mechanism of Creep Fracture, Elsevier Applied Science Publishers, 1984, p. 2.
8. GAROFALO, F., Fundamentals of Creep and Creep-Rupture in Metals, The Macmillan Co., New York, 1965.
9. DYSON, B.F., and McLEAN, D., «Creep of Nimonic 80A in Torsion and Tension», Met. Sci., vol. 11, 1977, pp. 37-45.

10. EL-MAGD, E., NICOLINI, G. and FARAG, M., «Effect of Carbide Precipitation on the Creep Behavior of Alloy 800HT in the Temperature Range 700°C to 900°C», *Metall. Mater. Trans.*, vol. 27A, 1996, pp. 747-756.
11. KOUL, A.K., and CASTILLO, R., «Assessment of Service Induced Microstructural Damage and Its Rejuvenation in Turbine Blades», *Metall. Trans.*, vol. 19A, 1988, pp. 2049-2065.
12. GRANT, N.J., *Deformation and Fracture at Elevated Temperatures*, M.I.T. Press, Cambridge, MA, 1965, pp. 91-105, 165.
13. KOUL, A.K., and PICKERING, F.B., Presented at TMS-AIME fall meeting in Louisville, KY, October 11-15, 1981.
14. NABARRO, F.R.N. and DE VILLIERS, H.L., «Introduction to Creep-Resistant Alloys» (Chapter 1), *The Physics of Creep*, Taylor & Francis Ltd, 1995, p. 47.
15. BEDDOES, J., WALLACE, W. and L. ZHAO, «Current Understanding of Creep Behaviour of near γ -Titanium Aluminides», *Inter. Mater. Rev.*, vol. 40, 1995, pp. 197-217.
16. WU, MU YEH and SHERB, O.D., «Unification of Harper-Dorn and Power Law Creep Through Consideration of Internal Stress», *Acta Metall.*, vol. 32, 1984, pp. 1561-1572.
17. SHERBY, O.D. and BURKE, P.M., «Mechanical Behaviour of Crystalline Solids at Elevated Temperature», *Prog. Mat. Sci.*, vol. 13, 1968, pp. 325-390.
18. CANNON, W.R. and SHERBY, O.D. «High Temperature Creep Behavior of Class I and Class II Solid Solution Alloys», *Metall. Trans.*, vol. 1A, 1970, pp. 1030-1032.
19. See reference 7, p. 6.

20. WANG, J.N., «Harper-Dorn creep in olivine», *Mater. Sci. Eng.*, vol. A183, 1994, pp. 267-272.
21. LANGDON, T.G., «Grain Boundary Sliding as a Deformation Mechanism during Creep», *Phil. Mag.*, vol. 22, 1970, pp. 689-700.
22. PURUSHOTHAMAN, S. and TIEN, J.K., «Role of Back Stress in the Creep Behavior of Particle Strengthened Alloys», *Acta Metall.*, vol. 26, 1978, pp. 519-528.
23. FURILLO, F.T., DAVIDSON, J.M., TIEN, J.K. and JACKMAN, L.A., «The Effect of Grain Boundary Carbides on the Creep and Back Stress of a Nickel-base Superalloy», *Mater. Sci. Eng.*, vol. 39, 1979, pp. 267-273.
24. McLEAN, D., *Rep. Progr. Physics*, vol. 29, 1966, p. 1.
25. See reference 14, p. 34.
26. ASHBY, M.F., «First Report on Deformation-Mechanism Maps», *Acta Metall.*, 1972, vol. 20, pp. 887-897.
27. LUTHY, H., WHITE, R.A., and SHERBY, O.D., «Grain Boundary Sliding and Deformation Mechanism Maps», *Mater. Sci. Eng.*, vol. 39, 1979, pp. 211-216
28. KOUL, A.K., IMMARIGEON, J.P. and WALLACE, W., «Microstructural Control in Ni-base Superalloy», in *Advances in High Temperature Structural Materials and Protective Coatings*, A.K. Koul et al, eds., 1994, p. 107.
29. WU, X-J., and KOUL, A.K., «Grain Boundary Sliding in the Presence of Grain Boundary Precipitates during Transient Creep», *Metall. Mater. Trans.*, vol. 26A, 1995, pp. 905-913.

30. RUANO, O.A., SHERBY, O.D., WADSWORTH, J. and WOLFENSTINE, J., «Rebuttal to 'In defence of diffusional creep' », Mater. Sci. Eng., vol. A211, 1996, pp. 66-71.
31. RUANO, O.A., WADSWORTH, J. and WOLFENSTINE, J. and SHERBY, O.D., «Evidence for Nabarro-Herring Creep in Metals: Fiction or Reality?», Mater. Sci. Eng., vol. A165, 1993, pp. 133-141.
32. WOLFENSTINE, J., RUANO, O.A., WADSWORTH, J., and SHERBY, O.D., «Refutation of the Relationship Between Denuded Zones and Diffusional Creep», Scripta Metall. Mater., vol. 29, 1993, pp. 515-520.
33. BURTON, B. and GREENWOOD, G.W., «Limits of the Linear Relation between Stress and Strain rate in the Creep of Copper and Copper-Zinc Alloys», Acta Metall., vol. 18, 1970, pp. 1237-1242.
34. See ref. 7, pp. 8-10.
35. HOWELL, P.R. and DUNLOP, G.L., «The Role of Grain Boundary Dislocations in High Temperature Deformation», in Creep and Fracture of Engineering Materials and Structures, WILSHIRE, B. and OWEN, D.R.J., eds., 1981, pp. 121-140.
36. CASTILLO, R., KOUL, A.K. and IMMARIGEON, J-P. A., «The Effect of Service Exposure on the Creep Properties of Cast IN-738LC Subjected to Low Stress High Temperature Creep Conditions», in Superalloys 1988, RICHMAN, S., HUAL, D.N., MAUER, G., ANTOLOVICH, S. and LUND, C. eds., The Metallurgical Society, TSM-AIME, Warrendale, NJ, 1988, pp. 805-813.

37. KOUL, A.K. and CASTILLO, R., «Creep Behavior of Industrial Turbine Blade Materials», ASM Materials Congress, Pittsburgh, PA, Oct. 1993.
38. TANAKA, M., «Improvement of Creep-Rupture Properties by Serrated Grain Boundaries in High-Tungsten Cobalt-Base Superalloys», *Z. Metall.*, vol. 84, 1993, pp. 51-56.
39. TAKAHASHI, T., ISHIGURO, T., ORITA, K., TAIRA, J., SHIBATA, T. and NAKATA, S., «Effects of Grain Boundary Precipitation on Creep Rupture Properties of Alloy 706 and 718 Turbine Disk Forgings», in *Superalloys 718, 625, 706 and various Derivatives*, LORIA, E.A., ed., 1994, pp. 557-567.
40. CHANG, M., KOUL, A.K., and COOPER, C., «Damage Tolerance of P/M Turbine Disc», in the *Proceedings of Superalloys 1996*, KISSINGER, R.D., et al eds., 1996, pp. 677-686.
41. WEERTMAN, J., «Theory of Steady-State Creep Based on Dislocation Climb», *J. Appl. Phys.*, vol. 26, 1956, pp. 1213-1217.
42. WEERTMAN, J., «Steady-State Creep through Dislocation Climb», *J. Appl. Phys.*, vol. 28, 1957, pp. 362-364.
43. EVANS, R.W. and WILSHIRE, B., *Creep of Metals and Alloys*, The Institute of Metals, London, 1982.
44. LANGDON, T.G. «The Role of Grain Boundaries in High Temperature Deformation», *Mater. Sci. Eng.*, vol. A166, 1993, pp. 67-79.

45. MALAKONDAIAH, G., PRASAD, N., SUNDARARAJAN, G. and RAMA RAO, P., «An analysis of the Transient Stage in Low Stress Viscous Creep», *Acta Metall.*, Vol. 36, 1988, pp. 2167-2181.
46. LI, P., «On Grain Size Dependence of Minimum Creep Rate», *Chin. J. Met. Sci. Technol.*, vol. 8, 1992, pp. 119-122.
47. LASALMONIE, A. and STRUDEL, J.L., «Influence of Grain Size on the Mechanical Behavior of Some High Strength Materials», *J. Mater. Sci.*, vol. 21, 1986, pp. 1837-1852.
48. KLOC, L., FIALA, J. and CADEK, J., «Creep Behavior of a Ni-15Cr Solid Solution Alloy at Low stresses and Intermediate Temperature», *Mater. Sci. Eng.*, vol. A202, 1995, pp. 11-17.
49. MANNAN, S.L. and RODRIGUEZ, P., «Effect of Grain Size on Creep Rate in Type 316 Stainless Steel at 873 and 973 K», *Met. Sci.*, vol. 17, 1983, pp. 63-69.
50. LUPINC, V. and GIBBONS, T.B., "High Temperature Alloys for Gas Turbines", D. Coutsouradis, FELIX, P., FISCHMEISTER, H., HABRAKEN, L., LINDBLOM, Y. and SPEIDEL, M.O., eds., *Applied Science*, 1978, P. 335.
51. VENKITESWARAN, P.K. and TAPLIN, D.M.R., «Creep Fracture of Inconel X-750 at 700°C», *Met. Sci.*, vol. 8, 1974, pp. 97-106.
52. WHITE, C.H., «The Effect of Cold Work on the Grain Size and Properties of Nimonic Alloy 80A», *J. Inst. Metals*, vol. 97, 1969, pp. 215-220.

53. BROWNSWORD, R. and HOAR, M.R., «The Influence of Grain Size on Secondary Creep Rate in Nimonic 80A Tested at 600°C», *Scripta Metall.*, vol. 7, 1973, pp. 623-646.
54. HAN, Y., CHATURVEDI, M.C., and CAHOON, J.R., «Effect of Grain Size on the Steady State Creep Rate of Inconel 718», *Scripta Metall.*, vol. 22, 1988, pp. 255-260.
55. GIBBONS, T.B., and HOPKINS, B.E., «The Influence of Grain Size and Certain Precipitate Parameters on the Creep Properties of Ni-Cr-Base Alloys», *Met. Sci. J.*, vol. 5, 1971, pp. 233-240.
56. KOUL, A.K. and WALLACE, W., «A Note on the Microstructural Dependence of Creep Strength in Inconel 700», *Metall. Trans.*, vol. 12A, 1981, pp. 673-675.
57. RICHARDS, E.G., «Influence of Specimen Size and Grain Size on the Creep-Rupture Strength of Some Nickel-base High-Temperature Alloys», *J. Inst. Met.*, vol. 96, 1968, pp. 365-370.
58. BALDAN, A. (CSIR), «Effects of Grain Size and Carbides on the Creep Resistance and Rupture Properties of a Conventionally Cast Nickel-Base Superalloy», *Z. Metallkd.*, vol. 83, 1992, pp. 750-757.
59. FELL, E.A., MITCHELL, W.I. and WAKEMAN, D.W., «Interrelation of Structure and Stress-Rupture Properties of Ni-Chromium Alloys Strengthened with Titanium and Aluminium», *Iron Steel Inst. Spec. Rep.*, vol. 70, 1969, pp. 136-146.
60. BELTRAN, A.M., in *Superalloys II*, SIMS, C.T., STOLOFF, N.S. and HAGEL, W.C., eds., Wiley, New York, 1987, pp. 135-162.

61. BETTERIDGE, W. and FRANKLIN, A.W., «The Effect of Heat-Treatment and Structure on the Creep and Stress-Rupture Properties of Nimonic 80A», *J. Inst. Met.*, vol. 85, 1956-57, pp. 473-479.
62. GAROSSHEN, T.J. and McCARTHY, G.P., «Low Temperature Carbide precipitation in a Nickel Base Superalloy», *Metall. Trans.*, vol. 16A, 1985, pp. 1213-1223.
63. HAGEL, W.C. and BEATTIE, H.J., «Aging Reactions in Udimet 500 and M-252», Report No. EF-47-SL-349, Gas Turbine Dept. and Metallurgical Products Dept., General Electric Co., Schenectady, NY, Nov. 1958.
64. PERRY, A. J., «Cavitation in Creep», *J. Mater. Sci.*, vol. 9, 1974, pp. 1016-1039.
65. CHANG, W.H., "Tensile Embrittlement of Turbine Blade Alloys After High Temperature Exposure", in *Superalloys Processing, Section, MCIC-72-10, Metals and Ceramics Information Center, Battelle, Columbus, OH, 1972.*
66. ANGELIU, T.M., and WAS, G.S., «Behavior of Grain Boundary Chemistry and Precipitates Upon Thermal Treatment of Controlled Purity Alloy 690», *Metall. Mater. Trans.*, vol. 21A, 1990, pp. 2097-2107.
67. PANDEY, M.C., SATYANARAYANA, D.V.V., and TAPLIN, D.M.R., «Performance Enhancement of Inconel Alloy X-750 during Creep via Optimal Solution Treatment and Control of Morphology of Grain boundary Carbide», *Mater. Sci. Tech.*, vol. 10, 1994, pp. 936-939.
68. BEDDOES, J. and WALLACE, W., «Heat Treatment of Hot Isostatically Processed IN-738 Investment Castings», *Metallography*, vol. 13, 1980, p. 185.

69. ZHIPING, M., RUIZENG, Y. and Liang, GAO, *Mat. Sci. and Tech.*, vol. 104A, 1988, p. 1.
70. WADDINGTON, J.S. and LOFTHOUSE, K.J., «The Effect of Irradiation on the High Temperature Fracture of Stainless Steel», *J. Nucl. Mater.*, vol. 22, 1967, pp. 205-213.
71. MORRIS, D.G., «Creep Failure in Type 316 Austenitic Steel», *Met. Sci.*, vol. 12, 1978, pp. 19-29.
72. RAO, V. K., TAPLIN, D.M.R. and RAO, P.R., «The Grain Size Dependence of Flow and Fracture in a Cr-Mn-N Austenitic Steel from 300 to 1300K», *Metall. Trans.*, vol. 6A, 1975, pp. 77-86.
73. LINDBORG, U., «Nucleation and Growth of Creep Cracks in an Austenitic Steel», *Acta Metall.*, vol. 17, 1969, pp. 157-165.
74. FLECK, R.G., COCKS, G.J., and TAPLIN, D.M.R., «The Influence of Polycrystal Grain Size upon the Creep Ductility of Copper», *Metall. Trans.*, vol. 1A, 1970, pp. 3415-3420.
75. FLECK, R.G., BEEVERS, C.J. and TAPLIN, D.M.R., «The Hot Fracture of an Industrial Copper-Base Alloy», *Met. Sci.*, vol. 9, 1975, pp. 49-54.
76. CHEN, W. and CHATURVEDI, M.C., «The Influence of Grain Boundary Precipitates on Creep Fracture of Inconel 718», in *Proceedings of the International Symposium on Superalloys 718, 625, 706 and Various Derivatives*, LORIA, E.A., ed., 1994, pp. 567-577.
77. ASHBY, M.F., and DYSON, B.F., «Creep Damage Mechanics and Micromechanisms», in *Advances in Fracture Research (Fracture 84)*, VALLURIA, S.R.,

- TAPLIN, D.M.R., RAMARAO, P., KNOTT, J.F., and DUBEY, R., eds., 1984, pp. 3-30.
78. SESSIONS, M.L., McMAHON, Jr., C.J., and WALKER, J.L., «Further Observations on the Effect of Environment on the Creep/Rupture Behavior of a Nickel-Base High Temperature Alloy: Grain Size Effects», *Mater. Sci. Eng.*, vol. 27, 1977, pp. 17-24.
79. DUQUETTE, D.J., «Effect of High Vacuum on the Creep Properties of a High-Strength Nickel Alloy Single Crystal», *Scripta Metall.*, vol. 4, 1970, pp. 633-636.
80. SHAHINIAN, P. and ACHTER, M.R., «A Comparison of the Creep-Rupture Properties of Nickel in Air and in Vacuum», *Trans. Metall. Soc. AIME*, vol. 215, 1959, pp. 37-41.
81. CHAKU, P.N. and McMAHON, Jr., C.J., «The Effect of an Air Environment on the Creep and Rupture Behavior of a Nickel-Base High Temperature Alloy», *Metall. Trans.*, vol. 5, 1974, pp. 441-450.
82. SHAHINIAN, P., «Effect of Environment on Creep-Rupture Properties of Some Commercial Alloys», *Trans. Am. Soc. Met.*, vol. 49, 1957, pp. 862-882.
83. HENSHALL J.L., and GEE, M.G., «Creep Crack Propagation in a Bainitic 1Cr-0.5Mo Steel between 540 and 590°C», *Mater. Sci. Eng.*, vol. 80, 1986, pp. 49-57.
84. GOOCH, D.J., «The Effect of Cold Work on Low Temperature ($0.35T_M$) Creep Crack Growth in C-Mn Steels», *Mater. Sci. Eng.*, vol. 64, 1984, pp. 183- 196.
85. GOOCH, D.J., «The Effect of Microstructure on Creep Crack Growth in a C-Mn Steel at 360°C», *Mater. Sci. Eng.*, vol. 83, 1986, pp. 17-27.

86. ZHU, S.J., ZHAO, J. and WANG, F.G., «Creep Crack Growth of HK40 Steel: Microstructural Effects», *Metall. Mater. Trans.*, vol. 21A, 1990, pp. 2237-2241.
87. LEE, Y-W. and CHOI, Y-H., «Creep Crack Initiation and Propagation in Type 304 Stainless Steel at 873 K», *Mater. Sci. Eng.*, vol. A131, 1991, pp. 39- 45.
88. JAMES, L., «Some Preliminary Observations on the Extension of Cracks Under Static Loadings at Elevated Temperature», *Int. J. Fract. Mech.*, 1972, vol. 8, pp. 347- 349.
89. NICHOLSON, R.D. and FORMBY, C. L., «Validity of Various Fracture-Mechanics Methods at Creep Temperatures», *Int. J. Fract. Mech.*, 1975, vol. 11, pp. 595-604.
90. LARSON, J.M. and FLOREEN, S., «Metallurgical Factors Affecting the Crack Growth Resistance of a Superalloy», *Metall. Trans.*, vol. 8A, 1977, pp. 51- 55.
91. FLOREEN, S. and KANE, R.H., «A Critical Strain Model for the Creep Fracture of Nickel-Base Superalloys», *Metall. Trans.*, vol. 7A, 1976, pp. 1157-1160.
92. FLOREEN, S., «The Creep Fracture of Wrought Nickel-Base Alloys by a Fracture Mechanics approach», *Metall. Trans.*, vol. 6A, 1975, pp. 1741-1749.
93. SADANANAD, K. and SHAHINIAN, P., «Creep Crack Growth in Alloy 718», *Metall. Trans.*, vol. 8A, 1977, pp. 439-449.
94. DIBOINE, A. and PINEAU, A., «Creep Crack Initiation and Growth in Inconel 718 Alloy at 650°C», *Fatigue Fract. Eng. Mater. Struct.*, vol. 10, No. 2, 1987, pp. 141-151.
95. SADANANDA, K. and SHAHINIAN, P., «The Effect of Environment on the Creep Crack Growth Behavior of Several Structural Alloys», *Mater. Sci. Eng.*, vol. 43, 1980, pp. 159-168.

96. KING, J.E., «Fatigue Crack Propagation in Nickel-Base Superalloys—Effects of Microstructure, Load Ratio, and Temperature», *Mater. Sci. Tech.*, vol. 3, 1987, pp. 750-763.
97. ROBSON, K., "Crack Growth in Two Carbon Steels at 450°C", *International Conference on Creep Resistance in Steel*, Verein Deutscher Eisenhüttenleute, Düsseldorf, 1972.
98. LANDES, J.D. and BEGLEY, J.A., *ASTM STP 590*, 1976, pp. 128-148.
99. HARRISON, C.B. and SANDOR, G.N., «High Temperature Crack Growth in Low-Cycle Fatigue», *Eng. Fract. Mech.*, vol. 3, 1971, pp. 403-420.
100. NICHOLSON, R.D., «Effect of Temperature on Creep Crack Propagation in AISI 316 Stainless Steel», *Mater. Sci. Eng.*, vol. 22, 1976, pp. 1-6.
101. HAIGI, J.R., «The Mechanisms of Macroscopic High Temperature Crack Growth Part I: Experiments on Tempered Cr-Mo-V Steels», *Mater. Sci. Eng.*, vol. 20, 1975, pp. 213-228.
102. PILKINGTON, R., «Creep Crack Growth in Low-Alloy Steels», *Met. Sci. J.*, vol. 13, 1979, pp. 555-564.
103. SAXENA, A., «Mechanics and Mechanisms of Creep Crack Growth», in *Fracture Mechanics: Microstructure and Micromechanisms*, Proceedings of 1987 ASM Materials Science Seminar, NAIR, S.V., TIEN, J.K., BATES, R.C. and BUCK, O., eds., 1987.
104. HUTCHINSON, J.W., «Singular Behaviour at the End of A Tensile Crack in a Hardening Material», *J. Mech. Phys. Solids*, 1968, vol. 16, pp. 13-31.

105. HUTCHINSON, J.W., «Plastic Stress and Strain Fields at a Crack Tip», *J. Mech. Phys. Solids*, vol. 16, 1968, pp. 337-347.
106. RICE, J.R. and ROSENGREN, G.F., «Plane Strain Deformation Near a Crack Tip in a Power-Law Hardening Material», *J. Mech. Phys. Solids*, 1968, vol. 16, pp. 1-12.
107. RIEDEL, H. and RICE, J.R., «Tensile Cracks in Creeping Solids», in *Fracture Mechanics*, ASTM STP 700, 1980, pp. 112-130.
108. FLOREEN, S., «The Creep Fracture Characteristics of Nickel-Base Superalloy Sheet Samples», *Eng. Fract. Mech.*, vol. 11, No. 1, 1979, pp. 55-60.
109. JONES, P.L. and A.S. TETELMAN, «Characterization of the Elevated Temperature Static Load Crack Extension Behavior of Type 304 Stainless Steel», *Eng. Fract. Mech.*, vol. 12, 1979, pp. 79-97.
110. WELLE, A.A. and McBRIDE, F.H., «Application of Fracture Mechanics to High Temperature Creep Rupture», *Can. Met. Quart.*, vol. 8, 1967, pp. 347-368.
111. NEATE, G.J. and SIVERNS, N.J., *Proc. Joint Int. Conf. on Creep and Fatigue in Elevated Temp. App.*, Inst. of Mech. Engrs., London, 1973, p. 234.
112. LENG, Y., *Metall. Mater. Trans.*, «Study of Creep Crack Growth in 2618 and 8009 Aluminum Alloys», vol. 26A, 1995, pp. 315-328.
113. KHOBAIB, M., «Study of Creep Crack Growth Behavior of Ti-24Al-11Nb», in *Titanium '92, Science and Technology*, FROES, F.H. and CAPLAN, I., eds., 1992, pp. 351-365.
114. ZHU, S.J., ZHU, S.M. and WANG, F.G., «Influence of Grain Size on the Creep Crack Growth Behavior of Cr15Ni25 Steel», *Scripta Metall.*, vol. 23, 1989, pp. 1845-1848.

115. BAIN, K.R. and PELLOUX, R.M., «Effect of Environment on Creep Crack Growth in PM/HIP René-95», *Metall. Trans.*, vol. 15A, 1984, pp. 381-388.
116. BENSUSSAN, P.L., JABLONSKI, D. A., and PELLOUX, R.M., «A Study of Creep Crack Growth in 2219-T851 Aluminum Alloy Using a Computerized Testing System», *Metall. Trans.*, vol. 15A, 1984, pp. 107-120.
117. SADANANDA, K. and SHAHINIAN, P., «Creep Crack Growth in Udimet 700», *Metall. Trans.*, vol. 9A, 1978, pp. 79-84.
118. PEDRON, J.P. and PINEAU, A., «The Effect of Microstructure and Environment on the Crack Growth Behaviour of Inconel 718 Alloy at 650°C under Fatigue, Creep and Combined Loading», *Mater. Sci. Eng.*, vol. 56, 1982, pp. 143-156.
119. ZHU, M., WANG, F.G. and ZHU, S.J., «Grain Size Dependence of Creep Crack Growth in Ni-Cr Austenitic Steels», *Mater. Trans., JIM*, vol.15, (3), 1993, pp. 450-54.
120. WILSON, D.J., *J. Eng. Mater. Technol.*, vol. 95, Series H, No. 1, 1973, pp. 15-20.
121. ZHU, S.J., ZHAO, J. and WANG, F.G., «Creep Crack Growth of HK40 Steel: Microstructural Effects», *Metall. Mater. Trans.*, vol. 21A, 1990, pp. 2237-2241.
122. ZHU, S., WANG, F., ZHANG, J. and ZHU, S., «Carbide Effects on Creep Crack Growth of Ni-Cr Austenitic Steels», *Chin. J. Met. Sci. Technol.*, vol. 8, (6), 1992, pp. 391- 396.
123. FLOREEN, S. and KANE, R.H., «An Investigation of the Creep-Fatigue-Environment Interaction in a Ni-Base Superalloy», *Fatigue of Eng. Mater. Struct.*, vol. 2, No. 4, 1979, pp. 401-412.

124. BAIN, K.R. and PELLOUX, R.M., "Effect of Oxygen on Creep Crack Growth in PM/HIP Nickel-Base Superalloys", in *Superalloy 1984*, Maurice Gell et al, eds., 1984, pp. 387-396.
125. PELLOUX, R.M., BAIN, K.R. and BENSUSSAN, P.L., Experimental and Theoretical Studies of Creep Crack Growth, AFOSR-TR84-0387, NTIS AD-A 1984, pp. 141-193.
126. GABRIELLI, F. and PELLOUX, R.M., «Effect of Environment on Fatigue and Creep Crack Growth in Inconel X-750 at Elevated Temperature», *Metall. Trans.*, vol. 13A, 1982, pp. 1083-1090.
127. BRICKNELL, R.H. and WOODFORD, D.A., «The Embrittlement of Nickel Following High Temperature Air Exposure», *Metall. Trans.*, vol. 12A, 1981, pp. 1673-1680.
128. DYSON, B.F., «An Analysis of Carbon/Oxygen Gas Bubble Formation in Some Nickel Alloys», *Acta Metall.*, vol. 30, 1982, pp. 1639-1644.
129. WOODFORD, D.A. and BRICKNELL, R.H., «Grain Boundary Penetration of Oxygen in Nickel and the Effect of Boron Additions», *Metall. Trans.*, vol. 12A, 1981, pp. 1467-1475.
130. BRICKNELL, R.H. and WOODFORD, D.A., «The Embrittlement of Nickel Following High Temperature Air Exposure», *Metall. Trans.*, vol. 12A, 1981, pp. 425-433.
131. WOODFORD, D.A., «Environmental Damage of a Cast Nickel Base Superalloy», *Metall. Trans.*, vol. 12A, 1981, pp. 299-308.
132. KHOBAIB, M., NICHOLAS, T. and SRIVATS, R.V., «Role of Environment in Elevated temperature Crack Growth Behavior of René N4 Single Crystal»,

- Environmentally Assisted Crack: Science and Engineering, ASTM, STP 1049, LISAGER, W.B., CROOKER, T.W. and LEIS, B.N., eds., 1990, pp. 319-333.
133. McVAY, R.V., WILLIAMS, P., MEIER, G.H. and PETTIT, F.S., "Oxidation of Low Sulfur Single Crystal Nickel-Base Superalloys", in Superalloys 1992, ANTOLOVICH, S.D., et al, eds., 1992, pp. 807-811.
134. SHAHINIAN, P. and SADANANDA, K., «Creep an Fatigue Crack Growth Behavior of Some Cast Nickel-base Alloys», Mater. Sci. Eng., vol. A108, 1989, pp. 131-140.
135. PELLOUX, R.M., and HUANG, J.S., "Creep-Fatigue-Environment Interactions in Astroloy", in Creep-Fatigue-Environment Interactions, eds. by PELLOUX, R.M. and STOLOFF, N.S., the Metallurgical Society of AIME, 1980, pp. 151-164
136. TABUCHI, M., KUBO, K. and YAGI, K., «Long-Term Creep Crack Growth Behaviour of 316 Stainless Steeb», J. Soc. Mater. Sci., Japan, vol. 41, (467), 1992, pp. 1255-1260.
137. JASKE, C.E., 'Long-Term Creep-Crack Growth Behavior of Type 316 Stainless Steel', ASTM STP 945, 1988, pp. 867-877.
138. JONES, C.L. and PILKINGTON, R., «The Influence of Microstructure on Creep Crack Growth in 0.5 Pct Cr, 0.5 Pct Mo, 0.25 Pct V Steeb», Metall. Trans., vol. 9A, 1978, pp. 865-871.
139. WU, X.J. and KOUL, A.K., "Modeling Intergranular Creep Crack Growth", Structure & Materials Laboratory, Institute for Aerospace Research, National Research Council of Canada, unpublished research.

140. PURUSHOTHAMAN, S. and TIEN, J.K., «A Theory for Creep Crack Growth», *Scripta Metall.*, 1976, vol. 10, pp. 663-666.
141. DiMELFI, R.I. and NIX, W.D., «The Stress Dependence of the Crack Growth Rate during Creep», *Inter. J. Fract.*, vol. 13, No. 3, 1977, pp. 341-348.
142. BARNBY, J.T., «Crack Propagation during Steady State Creep», *Eng. Fract. Mech.*, vol. 7, 1975, pp. 299-304.
143. McCLINTOCK, F.A. and IRWIN, G.R., ASTM STP 381, Philadelphia, Pa, 1965, pp. 84-113.
144. WALKER, K. P. and WILSON, D. A., "Creep Crack Growth Predictions in INCO 718 Using a Continuum Damage Model", in Proceedings of a symposium held at NASA Lewis Research Center Cleveland, Ohio, June 15-17, 1984, NASA Conference Publication 2369, 1985, pp. 349-372.
145. WALKER, K.P., "Research and Development Program for Nonlinear Structural Modelling with Advanced Time-Temperature Dependent Constitutive Relationships", Final Report NASA CR-165533 on NASA Lewis Contract NAS3-22055, 1981.
146. CHABOCHE, J.L., "Thermodynamic and Phenomenological Description of Cyclic Visoplasticity with Damage", Translation of Publication No. 1978-3 of the Office National d'Etudes et de Recherches Aerospatiale, France, by the European Space Agency Technical Translation Service, Publication No. ESA-TT-548, 1979.
147. VITEK, V., «A Theory of Diffusion Controlled Intergranular Creep Crack Growth», *Acta Metall.*, vol. 13, 1978, pp. 1345-56.

148. GOOCH, D.J., «The Effect of Microstructure on Creep Crack Growth in Notched Bend Tests on 0.5Cr-0.5Mo-0.25V Steel», *Mater. Sci. Eng.*, vol. 27, 1977, pp. 57-68.
149. GOOCH, D.J., «Creep Crack Growth in Variously Tempered Bainitic and Martensitic 0.5Cr-0.5Mo-0.25V Steel», *Mater. Sci. Eng.*, vol. 29, 1979, pp. 227-240.
150. SADANANDA, K., «A Theoretical Model for Creep Crack Growth», *Metall. Trans.*, vol. 9A, 1978, pp. 635-41.
151. BEERE, W. and SPEIGHT, M.V., «Diffusive Crack Growth in Plastically Deforming Solid», *Met. Sci.*, vol. 12, 1978, pp. 593-599.
152. SADANANDA, K. and SHAHINIAN, P., «Creep Crack Growth Behaviour and Theoretical Modelling», *Met. Sci.*, vol. 15, 1981, pp. 425-432.
153. CROSSMAN, F.W. and ASHBY, M.F., «The Non-Uniform Flow of Polycrystals by Grain-Boundary Sliding Accommodated by Power-Law Creep», *Acta Metal.*, vol. 23, 1975, pp. 425-440.
154. VANDER VOORT, G.F., *Metallography: Principles and Practice*, Chapter 6, McGraw-Hill Company, New York, 1984.
155. *The Annual Book of ASTM Standard*, vol. c03.01, 1992, pp. 648-668.
156. AKER, C.F. and TERDAD, T., "The Calibration and Implementation of the Direct Current Potential Drop Technique on CT Specimens", NRCC, NAE LTR-ST-1599, August 1986.
157. PISHVA, M.R., BELLINGER, N.C., TERADA, T. and KOUL, A.K., "DC-PD Technique For Crack Length Measurements at Elevated Temperatures", NRCC, NAE, LTR-ST-1635, October 1987.

158. MOM, A.J.A. and RAIZENNE, M.D., «AGARD Engine Disc Cooperative Test Program», AGARD Report No. 766, 1988, Printed in Specialised Printing Services Limited, 40 Chigwell Lane, Loughton, Essex.
159. SMITH, J.S. and HECK, K.A., «Development of a Low Thermal Expansion, Crack Growth Resistant Superalloy», in the Proceedings of Superalloys 96, KISSINGER, R.D. et al eds., 1996, pp. 91-100.
160. Specification E647-78T, 1979 Annual Book of ASTM Standards, part 10, American Society for Testing and Materials, 1979.
161. KOUL, A.K., IMMARIGEON, J.P. and WALLACE, W., «Microstructural Control in Ni-base Superalloy», in Advances in High Temperature Structural Materials and Protective Coatings, KOUL, A.K., et al, eds., 1994, pp. 96-125.
162. KAUFMAN, M. and PALTY, A.E., «The Relationship of Structure to Mechanical Properties in Udimet 500», Trans. AIME, vol. 218, 1960, pp. 107-116.
163. KOUL, A.K., «Effect of Carbon on Precipitation Reactions in Ni-Fe-Cr Alloys», Met. Sci. J., vol. 16, 1982, pp. 591-592.
164. JANOWSKI, G.M., HECKEL, R.W. and PLETKA, B.J., «The Effects of Tantalum on the Microstructure of Two Polycrystalline Nickel-Base Superalloys: B-1900+Hafnium and Mar-M247», Metall. Trans., vol. 17A, 1986, pp. 1891-1905.
165. FELL, E.A., Scripta Metall., vol. 63, No. 378, 1961, p. 157.
166. GAO, M. and WEL, R.P., «Precipitation of Intragranular $M_{23}C_6$ Carbide in a Nickel Alloy: Morphology and Crystallographic Feature», Scripta Metall. Mater., vol. 30, No. 8, 1994, pp. 1009-1014.

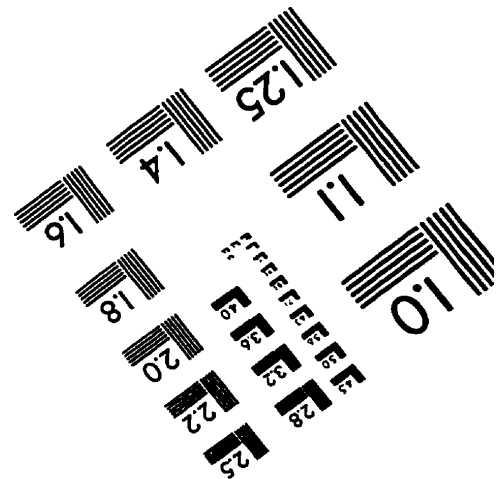
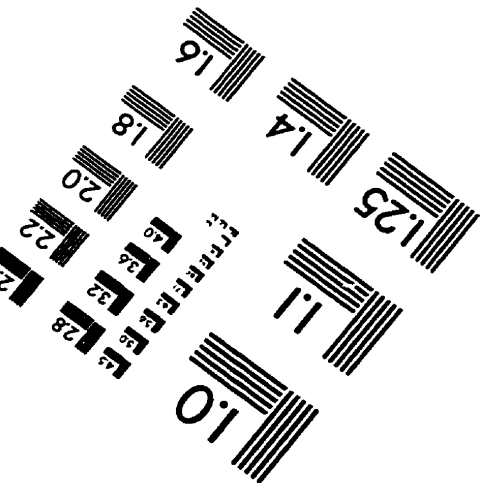
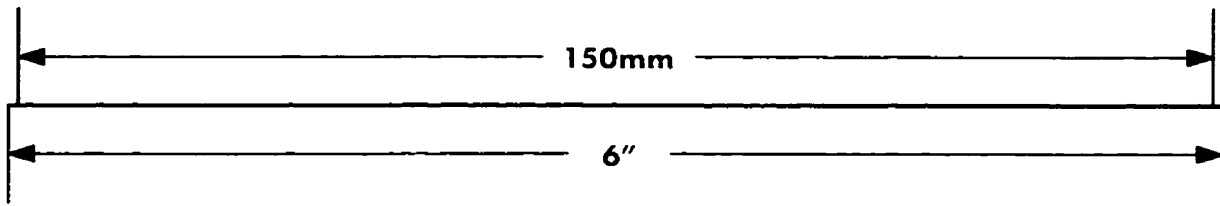
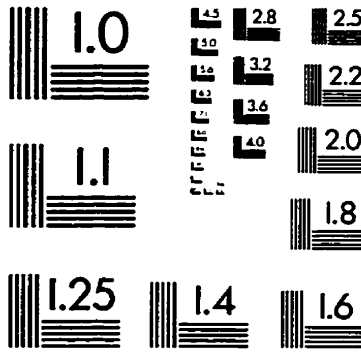
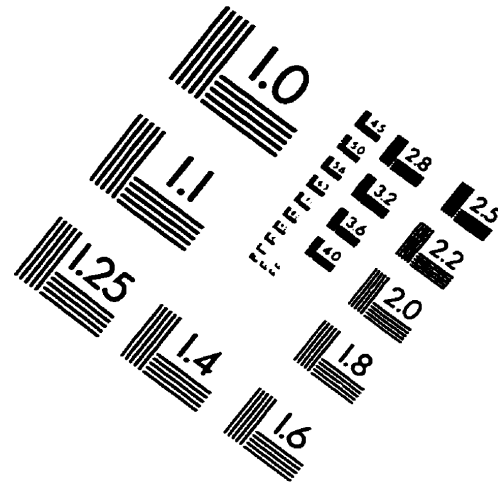
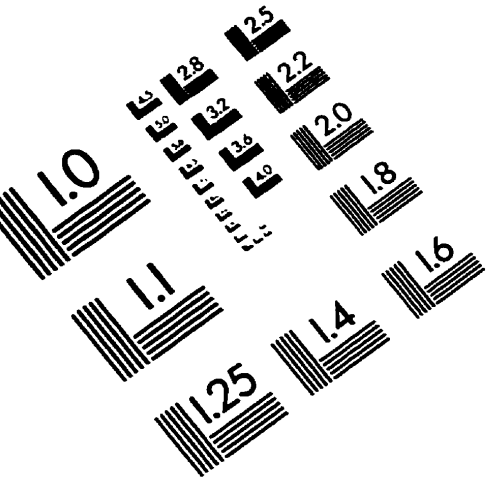
167. ANGELIU, T.M. and WAS, G.S., «Behavior of Grain Boundary Chemistry and Precipitates Upon Thermal Treatment of Controlled Purity Alloy 690», *Metall. Mater. Trans.*, vol. 21A, 1990, pp. 2097-2107.
168. KOTVAL, P.S. and HATWELL, H., «Discontinuous Precipitation of $M_{23}C_6$ Carbide in a Nickel Base Superalloy», *Trans. AIME*, 1969, vol. 245, pp. 1821-1823.
169. WILLIAMS, D.B. and BUTLER, E.P., «Grain Boundary Discontinuous Precipitation Relations», *Int. Met. Rev.*, No. 3, 1981, pp. 153-183.
170. *The Superalloys*, SIMS, C.T., and HAGEL, W.C., eds., Wiley, New York, 1972, pp. 590-596.
171. HAYES, R.W. and HAYES, W.C., «On The Mechanism of Delayed Discontinuous Plasticity in an Age-Hardened Nickel Alloy», *Acta Metall.*, vol. 30, 1982, pp. 1295-1301.
172. SIMS, C.T., STOLOFF, N.S. and HAGEL W.C., eds., *Superalloys II*, 1987, p. 123.
173. MURPHY, H.J., SIMS, C.T. and HECKMA, G.R., «Long-Time Structures and Properties of Three High-Strength, Nickel-Base Alloys», *Trans. AIME*, vol. 239, 1967, pp. 1961-1978.
174. CASTILLO, R. and WILLETT, K.P., «The Effect of Protective Coatings on the High Temperature Properties of a Gamma Prime-Strengthened Ni-base Superalloy», *Metall. Trans.*, vol. 15A, 1984, pp. 229-236.
175. SUSUKIDA, H., TSUJI, I., KAWAI, H. and ITOH, H., «Evaluation of the Properties of Gas Turbine Blade Materials in Long-time Operation», *Proceedings of 1977 Tokyo Joint Gas Turbine Congress*, 1977, pp. 502-510.

176. BECK, C.G., «Factors Controlling the Impact Properties of Nickel Base Superalloy Udimet 520», in Proceedings of Second International Conference on Mechanical Behaviour of Materials, 1976, pp. 476-480.
177. SHUMANUKI, Y. and DOI, H., «Effect of Aging Treatment on Microstructure and Tensile Properties of Udimet 520 and Ni-6.38%Al Alloy», Trans. JIM, vol. 15, 1974, pp. 24-31.
178. SHUMANUKI, Y., MASUI, M. and DOI, H., «The Variation with Aging Condition of the Composition of γ' Phase in a Ni-base Superalloy, Udimet 520», Scripta Metall., vol.10, 1976, pp. 805-808.
179. SUSUKIDA, H., SAKUMOTO, Y., TSUJI, I., and KAWAI, H., «Strength and Microstructure of Ni-base Superalloys after Long Term Heating», Kobe Technical Institute, Akashi, Japan, 1973.
180. LIU, C.D., HAN, Y.F., YAN, M.G. and CHATURVEDI, M.C., «Creep Crack Growth Behavior of Alloy 718», in Proceedings of Superalloys 718, 625 and Various Derivatives, LORIA, E.A., ed., 1991, pp. 537-548.
181. COCKS, A.C.F. and ASHBY, M.F., «The Growth of a Dominant Crack in a Creeping Material», Scripta Metall., vol. 16, 1982, pp. 109-14.
182. MILLER, D.A. and R. PILKINGTON, «Diffusion and Deformation Controlled Creep Crack Growth», Metall. Trans., vol. 1A, 1980, pp. 177-180.
183. SADANANDA, K. and P. SHAHINIAN, «Creep-Fatigue Crack Growth» (Chapter 5), in Cavities and Cracks in Creep and Fatigue, GITTUS, J., ed., Applied Science Publishers, London, 1981, pp. 109-195.

184. EVANS, H.E., *Mechanisms of Creep Fracture*, Elsevier Appl. Sci. Publishers, London, 1984, pp. 234-237.
185. WESTERGAARD, H.M., «Bearing Pressures and Cracks», *Trans. ASME*, vol. 61, 1939, pp. A49-A53.
186. BIRKS, N., and MEIER, G.H., *Introduction to High Temperature Oxidation of Metals*, Pub. Edward Arnold, London, 1983, p.198.
187. NAKADA, Y. and KEH, A.S., «Serrated Flow in Ni-C Alloys», *Acta Metall.*, vol. 18, 1970, pp. 437-443.
188. HONG, S.H., KIM, H.Y., JANG, J.S., and KUK, I.H., «Dynamic Strain Aging Behavior of Inconel 600 Alloy», in the proceedings of *Superalloys 1996*, KISSINGER, R.D., et al eds., 1996, pp. 401-407.
189. VAN DEN BEUKEL, A., «On the Mechanism of Serrated Yielding and Dynamic Strain Ageing», *Acta Metall.*, vol. 28, 1980, pp. 965-969.
190. McCORMICK, P.G., «Model for the Portevin-Le Chatelier Effect in Substitutional Alloys», *Acta Metall.*, vol. 20, 1972, pp. 351-354.
191. MULFORD, R.A. and KOCKS, U.F., *Acta Metall.*, vol. 27, 1979, p. 1125.
192. KOUL, A.K., and PICKERING, F.B., «Serrated Yielding in Ni-Fe Base Superalloys at 700°C», *Scripta Metall.*, vol. 16, 1982, pp. 119-124.
193. JO, C.Y., KIM, S.E., KIM, H.M., PARK, Y.J., and LEE, S.L., «Grain Boundary Crack Initiation and Propagation During Creep of Nickel Base Superalloy René 80», *J. Korean Ins. Met. Mater.* 29, vol. 11, 1991, pp. 1139-1147.

194. PARIS, P.C., and SIH, G.C., «Stress Analysis of Cracks,» Fracture Toughness Testing and Its Applications, ASTM STP 381, ASTM, Philadelphia, 1965, pp. 30-83.

IMAGE EVALUATION TEST TARGET (QA-3)



APPLIED IMAGE, Inc
 1653 East Main Street
 Rochester, NY 14609 USA
 Phone: 716/482-0300
 Fax: 716/288-5989

© 1993, Applied Image, Inc., All Rights Reserved